

**POLYMERS OF INTRINSIC MICROPOROSITY AND
INCORPORATION OF GRAPHENE INTO PIM-1 FOR GAS
SEPARATION**

A thesis submitted to the University of Manchester for the degree of

Doctor of Philosophy

In the Faculty of Engineering and Physical Sciences

2015

By

KHALID ABDULMOHSEN ALTHUMAYRI

SCHOOL OF CHEMISTRY

List of contents

List of Figures	5
List of Schemes.....	9
List of Appendixes	11
List of Publications	14
Acknowledgements	15
Declaration	16
Copyright Statement	16
Chapter 1 Introduction.....	17
1.1 Aims and Objectives	18
1.2 Introduction to membranes	22
1.3 Membrane classification.....	23
1.3.1 Nanoporous membrane materials	26
1.3.2 Microporous organic polymers	27
1.3.2.1 Covalent organic frameworks	28
1.3.2.2 Hypercrosslinked polymers	29
1.3.2.3 Conjugated microporous polymers	30
1.3.3 Zeolites.....	31
1.3.4 Metal-organic frameworks	32
1.4 Attractive membranes for commercialization	34
1.5 References	35
Chapter 2 Synthesis and characterization of PIM-1.....	37
2.1 Introduction to PIMs	38
2.1.1 High and low temperature methods of PIM-1 preparation	47
2.1.2 Characterization of PIM-1 microporosity.....	50
2.2 Experimental	53
2.2.1 Materials	53
2.2.2 Methods.....	53
2.2.3 Synthesis of PIM-1 at low temperature.....	54
2.2.4 Synthesis of PIM-1 at high temperature	55
2.3 Results and discussion	56
2.4 Conclusion.....	61
2.5 References	62

Chapter 3	Preparation and characterization of graphene and GPMMMs	65
3.1	Introduction	66
3.2	Characterization of Graphene by Raman Spectroscopy	70
3.3	Experimental	74
3.3.1	Materials	74
3.3.2	Methods	74
3.3.3	GPMMMs	75
3.3.3.1	Graphene exfoliation in organic solvents (GEOS)	75
3.3.3.2	GPMMMs -1 from graphene dispersion in chloroform	76
3.3.3.3	Graphene exfoliation in PIM-1 solution (GEPS)	77
3.3.3.4	GPMMMs-2 from GEPS-1	78
3.3.3.5	GPMMMs-3 from GEPS-8	79
3.3.3.6	Exfoliation of synthetic multilayer graphene in PIM-1 solution	80
3.3.3.7	GPMMMs-4 from synthetic multilayer graphene	81
3.3.3.8	Incorporating GO, RGO and BWGO in PIM-1 solution	82
3.3.3.8.1	Synthesis of GO	82
3.3.3.8.2	Synthesis of BWGO	83
3.3.3.8.3	Synthesis of RGO	83
3.3.3.9	MMM preparation from graphene derivatives	83
3.4	Results and discussion	84
3.4.1	GPMMMs	84
3.4.2	Graphene exfoliation in organic solvents (GEOS)	84
3.4.3	Graphene exfoliation in PIM-1 solution (GEPS)	86
3.4.4	Exfoliation of synthetic multilayer graphene in PIM-1 solution	87
3.4.5	Incorporating GO, RGO and BWGO in PIM-1 solution	88
3.4.6	Series 1 GPMMMs from graphene dispersion in chloroform	89
3.4.7	GPMMMs from graphene dispersion in PIM-1 solution	92
3.4.8	GPMMMs charactrizations	93
3.5	Conclusions	98
3.6	References	99
Chapter 4	Gas separation by GPMMMs	102
4.1	Gas separation membranes	103
4.1.1	Introduction	103
4.1.2	MMMs in gas separation	108
4.2	Experimental	114
4.2.1	Experimental setup	114
4.2.2	Determination of gas transport coefficients by time lag method	116

4.3 Results and discussion	118
4.3.1 Variation in gas transport properties among PIM-1 membranes	118
4.3.2 Gas transport properties of GPMMs	120
4.4 Conclusion.....	132
4.5 References	133
Chapter 5 New polymers of intrinsic microporosity (PIMs).....	136
5.1 Introduction	137
5.2 Experimental	144
5.2.1 Materials	144
5.2.2 Methods.....	144
5.2.3 Polyphenylene-based polymers of intrinsic microporosity (PP-PIMs) .	
.....	145
5.2.3.1 Synthesis of PP-PIM-1.....	145
5.2.3.1.1 Synthesis of 1,2-dimethoxy-4-(phenylethynyl)benzene (1)	145
5.2.3.1.2 Synthesis of 3,3,3',3'-tetramethyl-2,2',3,3'-tetrahydro-1,1'-	
spirobi[indene]-6,6'-diol (2)	146
5.2.3.1.3 Synthesis of 3,3,3',3'-tetramethyl-2,2',3,3'-tetrahydro-1,1'-	
spirobi[indene]-6,6'-diyl bis(trifluoromethanesulfonate) (3)	146
5.2.3.1.4 Synthesis of 3,3,3',3'-tetramethyl-6,6'-bis(phenylethynyl)-2,2',3,3'-	
tetrahydro-1,1'-spirobi[indene] (4).....	147
5.2.3.1.5 Synthesis of 2,2'-(3,3,3',3'-tetramethyl-2,2',3,3'-tetrahydro-1,1'-	
spirobi[indene]-6,6'-diyl)bis(1-phenylethane-1,2-dione) (5)	148
5.2.3.1.6 Synthesis of 4,4'-(3,3,3',3'-tetramethyl-2,2',3,3'-tetrahydro-1,1'-	
spirobi[indene]-6,6'-diyl)bis(2,3,5-triphenylcyclopenta-2,4-dienone) (6)	148
5.2.3.1.7 Synthesis of 6,6'-bis(6'-(3,4-dimethoxyphenyl)-4',5'-diphenyl-	
[1,1':2'',1''-terphenyl]-3'-yl)-3,3,3',3'-tetramethyl-2,2',3,3'-tetrahydro-1,1'-	
spirobi[indene] (7)	149
5.2.3.1.8 Synthesis of 4',4''''-(3,3,3',3'-tetramethyl-2,2',3,3'-tetrahydro-1,1'-	
spirobi[indene]-6,6'-diyl)bis(3',5',6'-triphenyl-[1,1':2'',1''-terphenyl]-3,4-diol) (8)	150
5.2.3.1.9 Synthesis of PP-PIM-1 from 6,6'-bis(1-(3,4-dihydroxyphenyl)-2,3,5,6-	
tetraphenylbenzyl)-3, 3', 3', 3'-tetramethyl-1, 1'-spirobisindane.....	150
5.2.3.2 Synthesis of PP-PIM-2.....	151
5.2.3.2.1 Synthesis of 1,4-bis (phenylethynyl)benzene (9)	151
5.2.3.2.2 Synthesis of 2,2'-(1,4-phenylene)bis(1-phenylethane-1,2-dione) (10)	
.....	152
5.2.3.2.3 Synthesis of 4,4'-(1,4-phenylene)bis(2,3,5-triphenylcyclopenta-2,4-	
dienone) (11)	152

5.2.3.2.4	Synthesis of 3,3''',4,4'''-tetramethoxy-2',2''',3',3''',5',5''',6',6'''-octaphenyl-1,1':4',1'':4'',1''':4''',1''''-quinquephenyl (12)	153
5.2.3.2.5	Synthesis of 2',2''',3',3''',5',5''',6',6'''-octaphenyl-[1,1':4',1'':4'',1''':4''',1''''-quinquephenyl]-3,3''',4,4'''-tetraol (13).....	153
5.2.3.2.6	Synthesis of PP-PIM-2 from 2',2''',3',3''',5',5''',6',6'''-octaphenyl-[1,1':4',1'':4'',1''':4''',1''''-quinquephenyl]-3,3''',4,4'''-tetraol	154
5.2.3.3	Biphenyl-based polymer of intrinsic microporosity (BP-PIM-1).....	154
5.2.3.3.1	Synthesis of 6,6'-bis(3,4-dimethoxyphenyl)-3,3,3',3'-tetramethyl-2,2',3,3'-tetrahydro-1,1'-spirobi[indene] (14)	154
5.2.3.3.2	Synthesis of 4,4'-(3,3,3',3'-tetramethyl-2,2',3,3'-tetrahydro-1,1'-spirobi[indene]-6,6'-diyl)bis(benzene-1,2-diol) (15).....	155
5.2.3.3.3	Synthesis of BP-PIM-1 from 4,4'-(3,3,3',3'-tetramethyl-2,2',3,3'-tetrahydro-1,1'-spirobi[indene]-6,6'-diyl)bis(benzene-1,2-diol)	156
5.2.3.4	Synthesis of PP-PIM-3.....	156
5.2.3.5	Synthesis of PP-PIM-4.....	157
5.2.3.6	Synthesis of PP-PIM-5.....	158
5.2.3.6.1	Synthesis of 1,3-bis(phenylethynyl)benzene (16)	158
5.2.3.6.2	Synthesis of PP-PIM-5	158
5.2.3.7	Synthesis of PP-PIM-6.....	159
5.3	Results and discussion	159
5.3.1	Synthesis of polyphenylene-based polymers of intrinsic microporosity (PP-PIMs).....	159
5.3.1.1	PP-PIMs via condensation polymerization	160
5.3.1.1.1	Synthesis of PP-PIM-1	160
5.3.1.1.2	Synthesis of PP-PIM-2	165
5.3.1.1.3	Synthesis of BP-PIM-1	169
5.3.1.2	PP-PIMs via Diels-Alder polymerization.....	174
5.4	Conclusions	179
5.5	References	179
Chapter 6	Conclusions.....	181
Chapter 7	Appendixes	183

List of Figures

Figure 1-1. General classification of membranes.....	23
Figure 1-2. Correlations between pore diameter, separation processes and potential substrates for membrane separation.....	24
Figure 1-3: Different types of pore that can exist in general porous materials (classification based on pore accessibility or interconnectivity).....	24
Figure 1-4: Classification of pores by their dimensional structures. ⁹	25
Figure 1-5. Various separation mechanisms can operate, depending on the porous properties of the membrane. ¹	26
Figure 1-6: Organic reactions recently used in microporous polymer synthesis. ⁴	28
Figure 1-7. Two examples of the formation of COFs: COF-1 and COF-5. ⁵	29
Figure 1-8. Preparation of HCP from a styrenic polymer. ⁸	30
Figure 1-9. Examples of monomers which can undergo direct polymerization for the preparation of HCPs.....	30
Figure 1-10. Several examples of CMPs. ⁴	31
Figure 1-11. Representative framework structure of zeolite A, illustrating how micropores are formed. Adapted from ref. ¹⁸	32
Figure 1-12. Various MOF framework topologies, prepared from different metals and organic geometries. ¹⁹	33
Figure 1-13. Comparison between angles of imidazole silicate bridges. ²³	34
Figure 1-14. ZIF-8. a) Preparation by mechanosynthesis; b) Crystal structure. ²⁵	34
Figure 2-1. An industrial respirator that contains PIM-1 as a key component in its sensor. The green area indicates the sensor part in whose fabrication PIM-1 is used. ³⁴	46
Figure 2-2. Hypothetical routes of PIM-1 polymerization.....	49
Figure 2-3. Potential formation of branched centres in PIM-1 polymerization.....	49
Figure 2-4. Six types of sorption isotherms giving the IUPAC classification of porous materials. Adapted from Barton et al. ⁴⁵	52
Figure 2-5. Proposed reaction mechanism of dibenzodioxane linkages in PIM-1 synthesis.....	57
Figure 2-6. GPC traces of KA1-1, KA1-4 and KA1 polymers.	58
Figure 2-7. MALDI-ToF spectrum of PIM-1 produced by LTM (Batch KA1), showing cyclic-PIM-1 oligomers. Cyclic-PIM-1 = $C_n = 460$ (repeating-unit mass of PIM-1) \times n (number of repeating units) + 23 (Na^+ mass).	59
Figure 2-8. MALDI-ToF spectrum of PIM-1 produced by HTM (Batch KA1-4), showing cyclic-PIM-1 Oligomers. Cyclic-PIM-1 = $C_n = 460$ (repeating-unit mass of PIM-1) \times n (number of repeating units) + 23 (Na^+ mass).	59
Figure 2-9. 1H NMR spectroscopy of PIM-1.	60
Figure 2-10. TGA thermogram of KA1-4.	60

Figure 2-11. Nitrogen sorption isotherm of PIM-1 at 77 K; nitrogen adsorption (filled squares) and desorption (empty circles).	61
Figure 3-1. Typical Raman spectra of species obtained by liquid phase exfoliation of graphite in N-methyl-2-pyrrolidone (NMP), showing the differences in the shape of the 2D peak for single-layer graphene, few-layer graphene and graphitic species. Data were provided by Shin.	72
Figure 3-2. Jablonski energy diagram illustrating the different quantum descriptions of Raman scattering, Rayleigh scattering, infrared and fluorescence. ⁴³	73
Figure 3-3: Digital image of GPMMMs-3 series dispersions before membrane casting.	80
Figure 3-4. Proposed mechanism for epoxide reduction with hydrazine. ⁴⁹	88
Figure 3-5. Graphene concentrations obtained by LPE of synthetic graphene, exfoliated graphene, r-GO, BWGO and GO. All dispersions were centrifuged at 10,000 rpm and concentrations were determined by UV-Vis.....	89
Figure 3-6. Different MMM preparation methods (adapted from ref. ⁵⁰).	90
Figure 3-7. Digital image of Series 1 GPMMMs with graphene loading of 0.4 and 0.18 wt.%. a) wet composite of GPMMM-1 (0.38 wt.%), b) GPMMM-1 (0.38 wt.%), c) GPMMM-1 (0.18 wt.%).	91
Figure 3-8. Raman spectra of graphene exfoliated in chloroform drop-cast on silica substrate, performed with a laser of 513 nm wavelength, a) is FLG and b) is graphite flake. Data were provided by Yuyoung Shin.	91
Figure 3-9. Digital image of Series 2 GPMMMs and its dispersion, a) dispersion of GEPS-1, b) free-standing GPMMM-2 (5).	92
Figure 3-10. GPMMM-2 (6) (0.18 wt%) after dissolution and before, showing good graphene dispersion.....	92
Figure 3-11. Raman spectrum of GPMMM with laser wavelength of 533 nm. Data was provided by Zhou.....	93
Figure 3-12. Raman spectra of pure PIM-1 compared with Raman spectra of graphene/PIM-1 MMM. The PIM-1 peaks overlapped with the G and D peaks, requiring a normalization process. The 2D peak was clearly visible without normalization. Data were provided by Yuyoung Shin.....	94
Figure 3-13. Lorentzian fitting of the 2D peak of a GPMMM, typically confirming a restacked FLG content. Data were provided by Yuyoung Shin.	94
Figure 3-14. SEM images of pristine PIM-1 (KA1-4) and GPMMMs-3 (1). a) and b) are SEM images at two different magnifications of pristine PIM-1 membrane (d); e) and f) are the equivalent SEM images of GPMMM (g). Data were provided by Gonciaruk.	95
Figure 3-15. SEM image of pristine epoxy resin (a), graphene/epoxy composite (b) and a large block of aggregated graphene (c). ⁵¹	96
Figure 3-16. GPC graph of PIM-1 before and after ultrasonic treatment for 84 h. Before sonication, M_w , M_n and PDI were $78 \times 10^3 \text{ g mol}^{-1}$, $32 \times 10^3 \text{ g mol}^{-1}$ and 2.4; respectively. After sonication, M_w , M_n and PDI were $77 \times 10^3 \text{ g mol}^{-1}$, $22 \times 10^3 \text{ g mol}^{-1}$ and 3.4.	97
Figure 3-17. GPC graphs of KA1-4 (PIM-1) that was tested before and after ultrasonic treatment for various lengths of time.	97

Figure 4-1. Robeson plots illustrating the correlation of permeability and permselectivity for various industrially important gas pairs: (a) CO ₂ /CH ₄ , (b) O ₂ /N ₂ , (c) CO ₂ /N ₂ and (d) H ₂ /N ₂ . The solid brown line is the 1991 upper bound, the dashed blue line is the 2008 upper bound, filled green triangles indicate PIMs, non-filled red squares indicate thermal-rearranged polymers, non-filled circles indicate other high free-volume polymers and asterisks indicate various polymers. ⁷ ...	104
Figure 4-2. Examples of glassy polymers with high gas permeability.....	107
Figure 4-3. Examples of TR polymer preparation from polyimides. These examples are subjected to thermal treatment conditions with lower relative temperature, potential structural rearrangement from distinctive incorporation of –OH or –SH groups.	108
Figure 4-4. Schematic representation of an ideal MMM.	109
Figure 4-5. Six possible interfacial morphologies influencing gas transport properties.	110
Figure 4-6. Plot adapted from Moore and Koros, ²⁰ summarizing the relationship between various MMM morphologies and transport properties. Circles indicate predicted values; squares show experimental results. Filled markers are 35 vol.% Zeolite A4; non-filled markers are 15 vol.% 4A.	111
Figure 4-7: Schematic presentation of the permeation experiments performed at ITM.	114
Figure 4-8. Time lag measurements on perforated aluminium foil for H ₂ , He, CH ₄ and CO ₂ . ³²	115
Figure 4-9. Permeate pressure versus time of various gases tested on a PIM-1 membrane as cast, determining the time lag for each gas.	115
Figure 4-10. a) Illustration of the use of a permeation curve to find the permeation coefficient (P) and diffusion coefficient (D) from time lag (θ), as well as the indirect determination of solubility coefficient (S). b) Shows how the concentration profile can develop over time. This figure was produced by Johannes Jansen at ITM.	117
Figure 4-11. ¹ H NMR spectra of low- and high- permeability PIM-1 batches (as powder in chloroform) (KA1-1 and KA1-4, respectively), showing a significant difference in water content.	120
Figure 4-12. Permeability of several gases (CO ₂ , H ₂ , He, O ₂ , CH ₄ and N ₂) in correlation with weight percent of graphene loading.....	124
Figure 4-13. Correlation of CO ₂ permeability and the loading of fused silica fillers for MMMs of PIM-1. The dashed line indicates the predication of the Maxwell model for an impermeable filler.	125
Figure 4-14. A graph shows the CO ₂ permeability vs volume percent filler of graphene and f-MWCNTs, ⁴⁰ each comprising PIM-1 membranes.....	126
Figure 4-15. Correlations of CO ₂ permeability and volume percent of graphene fillers of all samples as cast. Methanol treated are also included for most samples. Lines indicate Permeability of starting PIM-1.....	128
Figure 4-16. Correlation of O ₂ permeability and O ₂ /N ₂ selectivity for two series of GPMMMs, f-MWCNTs-MMMs and fused silica-MMMs. (b) is a zoomed-in image of (a) with highlighted regions for each series. Arrows indicate increased loading of nanofillers.....	130

Figure 4-17. Effects of graphene fillers on CO ₂ /CH ₄ separation of PIM-1. Filled squares indicate neat PIM-1 membrane measured as cast; unfilled squares indicate as-cast Series 3 GPMMMs; filled circles indicate PIM-1 membrane after methanol treatment; unfilled circles are Series 3 GPMMMs after methanol treatment.	131
Figure 4-18. Effects of synthetic graphene fillers on CO ₂ /CH ₄ separation of PIM-1. Filled square indicates neat PIM-1 membrane (as cast); unfilled squares indicate Series 4 GPMMMs (as cast). Arrows indicate increased filler.	131
Figure 4-19. Effects of ageing for ca. 8 months on the CO ₂ permeability of PIM-1 (■) and GPMMMs (Series 2) at nanofiller loadings of 0.046 vol.% (●), 0.088 vol.% (◆) and 0.164 vol.% (▲). The lines are guides to the eye.	132
Figure 5-1. Illustrative examples of hexaphenylbenzene compounds (HPBs) that can construct pores by self-assembly: a) HPB with terminal functional groups, b) functional groups that facilitate hydrogen bond interactions, c) network structure of HPBs from self-assembly. ⁴	138
Figure 5-2. Chemical structures of HPOP-1 and HPOP-2.	142
Figure 5-3. The relationship between porous properties and structure of HEX-POPs and HBC-POPs varying in structure, planarization and functional groups. ¹⁵	143
Figure 5-4. GPC plots of three batches of PP-PIM-1 polymerization. PP-PIM-1 (1) was via LTM, PP-PIM-1 (2) and PP-PIM-1 (3) via HTM, at 125 °C and 145 °C respectively.	163
Figure 5-5. ¹ H NMR spectroscopy of PP-PIM-1 in CDCl ₃	163
Figure 5-6. MALDI-ToF spectrum of PP-PIM-1 produced by HTM (batch PP-PIM-1 (3)), showing cyclic-PP-PIM-1 oligomers. Cyclic-PP-PIM-1 = C _n = 1373.6 × n + 23.	164
Figure 5-7. Nitrogen sorption isotherm of PP-PIM-1 at 77 K; nitrogen adsorption (filled squares) and desorption (empty circles).	164
Figure 5-8. Nitrogen sorption isotherm of PP-PIM-2 at 77 K; nitrogen adsorption (filled squares) and desorption (empty circles).	166
Figure 5-9. Photograph of PP-PIM-2 powder (a) and oligomer solution in chloroform under a UV lamp at 365 nm (b).	167
Figure 5-10. ¹ H NMR spectroscopy of soluble fractions of PP-PIM-2 in d ₆ -DMSO.	168
Figure 5-11. ¹³ C solid-state NMR spectroscopy of PP-PIM-1 (top) and PP-PIM-2 (bottom). Data provided by Bann Dawood.	168
Figure 5-12. ATR-IR spectra of PP-PIM-2 (top) and PP-PIM-1 (bottom).	168
Figure 5-13. Photograph of BP-PIM-1 powder (a) and oligomer solution in chloroform under UV lamp at 365 nm (b).	170
Figure 5-14. MALDI-ToF spectrum of BP-PIM-1, showing peaks of cyclic-PP-PIM-1 oligomers. Cyclic-PP-PIM-1 = C _n = 612.2 × n + 23.	170
Figure 5-15. ¹ H NMR spectroscopy of BP-PIM-1 in CD ₂ Cl ₂	171
Figure 5-16. ¹³ C solid-state NMR spectra of BP-PIM-1 (top) and PIM-1 (bottom). Data provided by Bann Dawood.	172
Figure 5-17. ATR-IR spectrum of BP-PIM-1.	172

Figure 5-18. Nitrogen sorption isotherm of BP-PIM-1 at 77 K; nitrogen adsorption (filled squares) and desorption (empty circles).	173
Figure 5-19. UV-Vis spectra of PP-PIMs from condensation polymerization.....	173
Figure 5-20. TGA thermogram of PP-PIMs from condensation polymerization.	174
Figure 5-21. Nitrogen adsorption isotherm at 77 K; for PIM-1, PP-PIM-3, PP-PIM-4 and PP-PIM-6.	176
Figure 5-22. ¹ H NMR (a) and ¹³ C NMR (b) spectra of PP-PIM-3, PP-PIM-5, PP-PIM-6 (in CDCl ₃) and PP-PIM-4 (in CD ₂ Cl ₂). In ¹ H NMR solvent traces were labelled as follows: 1) CHCl ₃ , 2) CH ₂ Cl ₂ 3) acetone, 4) <i>n</i> -hexane, 5) H ₂ O.....	177
Figure 5-23. TGA thermogram of PP-PIMs from Diels Alder polymerization.....	177
Figure 5-24. UV-Vis spectra of PP-PIMs from Diels Alder polymerization.	178
Figure 5-25. MALDI-ToF spectrum of PP-PIM-4, showing cyclic-PP-PIM-4 oligomers. Cyclic-PP-PIM-4 = C _n = 1111.45 × n + 23.....	178

List of Schemes

Scheme 1-1. Schematic route of PP-PIM-1 synthesis, i) PdCl ₂ (PPh ₃) ₂ , CuI, DMF, Amine, Δ; ii) CH ₃ SO ₃ H, RT, 4 days; iii) (CF ₃ SO ₂) ₂ O, DCM, Pyridine; iv) Phenylacetylene, PdCl ₂ (PPh ₃) ₂ , CuI, DMF, Amine, Δ; v) I ₂ , DMSO, Δ; vi) 1,3-diphenyl-2-propanone, KOH, EtOH; vii) Diphenyl ether, 3 days; viii) BBr ₃ , DCM, RT; ix) K ₂ CO ₃ , DMF, Toluene, Δ. Compounds 5, 6, 7 and 8 were prepared by Alkabli.....	20
Scheme 1-2. Schematic route of PP-PIM-2 synthesis, i) PdCl ₂ (PPh ₃) ₂ , CuI, DMF, Et ₃ N, Δ; ii) I ₂ , DMSO, Δ; iii) 1,3-diphenyl-2-propanone, KOH, EtOH; iv) Compound 1 , Diphenyl ether, 3 days, Δ; v) BBr ₃ , DCM, RT; vi) K ₂ CO ₃ , DMF, Toluene, Δ. Compounds 9-13 were prepared by Alkabli.	21
Scheme 1-3. Schematic route of BP-PIM-1 synthesis, i) Pd(PPh ₃) ₄ , K ₂ CO ₃ , H ₂ O, Aliquat336, Δ; ii) BBr ₃ , DCM, RT; iii) K ₂ CO ₃ , DMF, Toluene, Δ.	21
Scheme 1-4. [4+2]-cycloaddition Diels-Alder polymerization of novel PP-PIMs, i) Diphenyl ether, Δ. Polymerizations performed by Jafar Alkabli.	22
Scheme 2-1. The synthesis of phthalocyanine-based network polymer with microporosity. i) K ₂ CO ₃ , DMF, 100° C; ii) metal cation (M) incorporation to template phthalocyanine formation at 200° C. Adapted from McKeown. ²	38
Scheme 2-2. The synthesis of a porphyrin-based network polymer with microporosity. i) K ₂ CO ₃ , NMP, 170°, 5 h; ii) Fe ₂ Cl ₃ , NMP, 120° C, 24 h. Adapted from McKeown et al. ⁷	39
Scheme 2-3. Synthesis of PIMs based on Tröger's Base (TB) formation, using dimethoxyethane (DMM) and trifluoroacetic acid (TFA).	45
Scheme 5-1. Preparation of cyclic (top) and linear (bottom) HPB-PIMs. i) diphenyl ether, 250 °C; ii) BBr ₃ , DCM, 20 °C; (iii) tetrafluoroterephthalonitrile, DMF, K ₂ CO ₃ , 65 °C, 96 h. ¹⁴	139

Scheme 5-2. Two different approaches for HPB monomer preparation, a) non-regioselective approach, b) regioselective approach. Adapted from McKeown et al. ¹⁴	139
Scheme 5-3. Synthesis of [6] CCHPB 2 from HPB derivatives, i) Suzuki coupling reaction (Pd(PPh ₃) ₄ , Cs ₂ CO ₃ , 100 °C), ii) demethoxylation under reductive conditions (TiCl ₄ , LiAlH ₄ , 80 °C). ¹⁶	140
Scheme 5-4. Synthesis of GNRs from polyphenylene-based polymer. ¹⁷	141
Scheme 5-5. Preparation of HTP and HP. i = 1,5-cyclooctadiene, bis(1,5-cyclooctadiene) nickel(0), 2,20- bipyridyl, DMF, 85 °C, 96 h. ¹⁸	142
Scheme 5-6. Synthesis of PP-PIM-1 from 8 . i) K ₂ CO ₃ , DMF, toluene, 145 °C, 30 min.	161
Scheme 5-7. Synthesis of 8 . i) PdCl ₂ (PPh ₃) ₂ , CuI, DMF, diisopropylamine, 60 °C, 24 h; ii) CH ₃ SO ₃ H, RT, 4 days; iii) (CF ₃ SO ₂) ₂ O, DCM, pyridine, RT, 18 h; iv) Phenylacetylene, PdCl ₂ (PPh ₃) ₂ , CuI, DMF, Et ₃ N, 80 °C, 17 h; v) I ₂ , DMSO, 155 °C, 18 h; vi) 1,3-diphenyl-2-propanone, KOH, EtOH, 80 °C, 2 h; vii) Diphenyl ether, 255 °C, 3 days; viii) BBr ₃ , DCM, RT, 18 h.	161
Scheme 5-8. Synthesis of PP-PIM-2 from 13 , i) K ₂ CO ₃ , DMF, 65 °C, 48 h.	165
Scheme 5-9. Synthesis of 13 , i) PdCl ₂ (PPh ₃) ₂ , CuI, DMF, Et ₃ N, 50 °C, 18 h; ii) I ₂ , DMSO, 155 °C, 18 h; iii) 1,3-diphenyl-2-propanone, KOH, EtOH, 80 °C, 2 h; iv) Diphenyl ether, 255 °C, 3 days; v) BBr ₃ , DCM, RT, 18 h.	166
Scheme 5-10. Synthesis of BP-PIM-1 from 15	169
Scheme 5-11. Synthesis of compound 15 . i) Pd(PPh ₃) ₄ , K ₂ CO ₃ , toluene/H ₂ O, aliquat 336 [®] , 75 °C, 18 h; ii) BBr ₃ , DCM, RT, 18 h.	169
Scheme 5-12. Synthesis of PP-PIMs from Diels Alder polymerization. i) diphenyl ether, 255 °C, 8 days. These polymerizations were performed by Alkabli.	175

List of Tables

Table 2-1. Selected non-network PIMs based on dibenzodioxin formation, including selected data of solubility, name and quoted BET surface area. Adapted from McKeown. ²	41
Table 2-2. PIMs from postsynthesis reactions of PIM-1.....	42
Table 2-3. Non-network PIMs based on imide formation, including data of solubility, name and quoted BET surface area, the table adapted from ref. ²	43
Table 3-1 Graphene exfoliation parameters: solvent, sample volume, sonication time, initial graphite concentration, centrifuge speed and final graphene concentrations that were determined by UV-Vis spectroscopy at 660 nm.	76
Table 3-2: Experimental details for GPMMMs-1: sample name based on graphene loading (wt.%), added mass of PIM-1, added mass of graphene, dispersion volume of graphene in chloroform and diameter of petri dish that was used for the casting process.	77
Table 3-3: Experimental details for graphene/PIM-1 dispersion: sample volume, sonication time, initial PIM-1 concentration, initial graphite concentration, centrifuge speed and final graphene concentrations that were determined by UV-Vis spectroscopy at 660 nm.	78

Table 3-4. GPMMMs-2 preparation parameters and obtained C_{graphene} and graphene:PIM-1 wt.% determined by UV-Vis measurement.	79
Table 3-5. Preparation details of GPMMMs-3.....	79
Table 3-6: Preparation details of GPMMMs-4 samples.....	82
Table 3-7. GPC data of KA1-4 (PIM-1) that was tested before and after ultrasonic treatment for various lengths of time.	97
Table 4-1. Several MMM examples from the literature with improved O_2/N_2 separation. ¹⁸	112
Table 4-2. Several MMM examples from the literature with improved CO_2/CH_4 separation. ¹⁸	113
Table 4-3. Variation of gas transport properties from different PIM-1 preparation conditions, using the example of O_2/N_2 separation. Data adapted from ref.....	118
Table 4-4. Permeation data of Series 2 GPMMMs as cast.	121
Table 4-5. Permeation data of Series 2 GPMMMs after methanol treatment.	121
Table 4-6. Permeation data of Series 2 GPMMMs after ageing.	121
Table 4-7. Permeation data of Series 3 GPMMMs as cast.	122
Table 4-8. Permeation data of Series 3 GPMMMs after methanol treatment.	122
Table 4-9. Permeation data of Series 4 GPMMMs as cast.	123
Table 5-1. Properties of PP-PIMs prepared via Diels Alder polymerization.	176
Table 7-1. Permeation data of Series 2 GPMMMs as cast.	184
Table 7-2. Permeation data of Series 2 GPMMMs after methanol treatment.	185
Table 7-3. .Permeation data of Series 2 GPMMMs after ageing.	185
Table 7-4. Permeation data of Series 3 GPMMMs as cast.	186
Table 7-5. Permeation data of Series 3 GPMMMs after methanol treatment.	187
Table 7-6. Permeation data of Series 4 GPMMMs as cast.	188

List of Appendixes

Appendix A. Permeation data of GMMMs.	184
Appendix B. Effects of graphene (GPMMMs-3)) in the permeability (O_2 , CO_2 , CH_4 , N_2 H_2 and He). Squares as casted membranes, circles indicate methanol treated membranes, line indicates PIM-1 as casted membrane, and dashed line indicates PIM-1 methanol treated membrane.....	189
Appendix C. Effects of graphene (GPMMMs-3) in the selectivity (CO_2/N_2 , CO_2/CH_4 , O_2/N_2 and H_2/N_2). Squares as casted membranes, circles indicate methanol treated membranes, line indicates PIM-1 as casted membrane, and dashed line indicates PIM-1 methanol treated membrane.	190
Appendix D. Robeson plots of GPMMMs Series 3.	191
Appendix E. Robeson plots of GPMMMs Series 4.....	192
Appendix F. Effects of graphene (GPMMMs -4) in the permeability (O_2 , CO_2 , CH_4 , N_2 H_2 and He). Squares as casted membranes, line indicates PIM-1 as casted membrane.....	193

Appendix G. Effects of graphene (GPMMMs-4) in the selectivity (CO_2/N_2 , CO_2/CH_4 , O_2/N_2 and H_2/N_2). Squares as casted membranes, circles indicate methanol treated membranes, line indicates PIM-1 as casted membrane.	194
Appendix H. Digital images of Series 3 and 4 GPMMMs.	195
Appendix I. Digital images of GPMMMs that made from Graphene exfoliation of various sources, a) from natural graphite, b) from synthetic multilayers graphene, c) from reduced graphene oxide (<i>r</i> -GO), d) from base washed graphene oxide (BWGO), e) from pristine PIM-1 and f) from graphene oxide (GO).	196
Appendix J. Sample names and Experimental codes	197

Abstract

Membrane-based gas separation processes are an area of interest owing to their high industrial demand for a wide range of applications, such as natural gas purification from CO₂ or H₂, and N₂ or O₂ separation from air. This thesis is focused on developing and investigating polymeric-based membranes. Firstly, novel mixed matrix membranes (MMMs) were prepared, incorporating few-layer graphene in the polymer of intrinsic microporosity PIM-1. Secondly, novel polyphenylene-based polymers of intrinsic microporosity (PP-PIMs) were synthesised.

An optimum preparation method of graphene/PIM-1 MMMs (GPMMMs) was established from numbers of experiments. In this study, graphene exfoliation was a step towards GPMMM preparation. Starting from graphene exfoliation in chloroform, as a good solvent for PIM-1, enhancement in graphene dispersibility was obtained with addition of PIM-1. This result helped in GPMMM preparation with high graphene content (up to 4 wt.%). Characterizations techniques such as Raman spectroscopy and scanning electron microscopy (SEM) of GPMMMs, confirmed the few layer graphene content, with morphology changes in the polymeric matrix compared to pure PIM-1.

Gas permeability results of GPMMMs showed an enhancement in permeability with low loading graphene (0.1 wt.%) using a relatively low permeability PIM-1 batch, due to high water content. However, less influence of graphene incorporation on permeability was observed with a highly permeable PIM-1 batch. Reduction in permeability over time, termed an ageing effect, is known for a polymer of high-free volume like PIM-1. However, the enhancement of GPMMMs permeability after eight months storage was shown to be retained.

Novel PP-PIMs were prepared from novel precursors using a series known organic reactions. PP-PIMs were divided into two groups of polymers based on their polymerization reactions. A group of polymers were prepared from condensation polymerization between bis-catechol monomers and tetrafluoroterephthalonitrile (TFTPN). Another group of polymers were prepared from Diels Alder polymerization between monomers of terminal bisphenylacetylene groups and bis tetraphenylcyclopentadienones (TPCPDs). All of which yielded polymers with apparent BET surface area in the range 290-443 m² g⁻¹.

List of Publications

1. Gonciaruk, A.; Althumayri, K.; Harrison, W. J.; Budd, P. M.; Siperstein, F. R. Microporous Mesoporous Mater. **2015**, 209, 126.
2. K. Althumayri, W.J. Harrison, Y. Shin, J.M. Gardiner, C. Casiraghi, P.M. Budd, P. Bernardo, G. Clarizia and J.C. Jansen, The influence of few-layer graphene on the gas permeability of the high-free-volume polymer PIM-1, *Phil. Trans. R. Soc. A*, accepted.

Acknowledgements

I owe my deepest gratitude to Prof. Peter Budd for giving me the opportunity to work in his group, and let me be the first one in his group that involved in graphene-based membrane project. I would like also acknowledge the support from EPSRC (grant no. EP/K016946/1), and Taibah University in Saudi Arabia

During PhD study, I have been kindly introduced by Prof. Peter Budd to very cooperative and helpful number of people from different disciplinary, who participated in regular progress meetings. Thus, I would also like to express my gratitude to all of them for their support, especially, who measured GPMMMs in ITM-CNR, Dr. Paola Bernardo, Dr. Gabriele Clarizia and Dr. Johannes Jansen, also to who helped or characterized GPMMMs, Dr. Cinzia Casiraghi, Dr. Kai-Ge Zhou, Yuyoung Shin, Dr. Sarah Haigh, Dr. Eric Prestat.

I thank Prof Ian Kinloch and his group, and Dr. Rahul Nair for permission to use their lab.

I would like to show my greatest appreciation to Muhanned Khdayyer, Bann Dawood, Keith Nixon, Gareth Smith, who have been a great help in sample measurements.

I would also thank Dr. John Gardner and his wonderful group for their kindness and friendship, all of them, and especially, Jafar Alkabli and Issa Issa, Mostafa Mahmoud.

All Prof. Budd Group have been extraordinarily tolerant and supportive, Dr. Wayne Harrison, Muhanned Khdayyer, Bann Dawood, Bekir Satilmis, Peter Youle, Lei Gao, Rebecca Dey, Tom Raine, Dr. Hosna Shamsipur, Dr. Louise Maynard-Atem, Dr. Chris Mason, Dr. Rupesh Bhavsar.

I owe my deepest gratitude to Mohammed Al Najrani, Eufemio Moreno and Sultan Alshimiri for their support and encouragement.

My Parents and all my Family Support encouragement were invaluable during my PhD time.

Declaration

No portion of the work referred to in the thesis has been submitted in support of an application for another degree or qualification of this or any other university or other institute of learning.

Copyright Statement

The following four notes on copyright and the ownership of intellectual property rights must be included as written below:

i. The author of this thesis (including any appendices and/or schedules to this thesis) owns certain copyright or related rights in it (the “Copyright”) and he has given The University of Manchester certain rights to use such Copyright, including for administrative purposes.

ii. Copies of this thesis, either in full or in extracts and whether in hard or electronic copy, may be made **only** in accordance with the Copyright, Designs and Patents Act 1988 (as amended) and regulations issued under it or, where appropriate, in accordance with licensing agreements which the University has from time to time. This page must form part of any such copies made.

iii. The ownership of certain Copyright, patents, designs, trade marks and other intellectual property (the “Intellectual Property”) and any reproductions of copyright works in the thesis, for example graphs and tables (“Reproductions”), which may be described in this thesis, may not be owned by the author and may be owned by third parties. Such Intellectual Property and Reproductions cannot and must not be made available for use without the prior written permission of the owner(s) of the relevant Intellectual Property and/or Reproductions.

iv. Further information on the conditions under which disclosure, publication and commercialisation of this thesis, the Copyright and any Intellectual Property and/or Reproductions described in it may take place is available in the University IP Policy (see <http://documents.manchester.ac.uk/DocuInfo.aspx?DocID=487>), in any relevant Thesis restriction declarations deposited in the University Library, The University Library’s regulations (see <http://www.manchester.ac.uk/library/about-tus/regulations>) and in the university’s policy, and in the presentation of thesis.

Chapter 1 Introduction

1.1 Aims and Objectives

Owing to their solution processability, their ability to form membranes with high intrinsic surface areas and their permselectivity, polymers of intrinsic microporosity (PIMs) are of interest to researchers seeking to develop polymeric membranes for gas separation purposes. PIM-1 is a well-characterized glassy, spirobisindane-based polymer. Its contorted structure and the space-inefficient packing of the polymer backbone provide PIM-1 with intrinsic microporosity and enable its possible use in molecular separation applications. Additive fillers may increase the extent of inefficient packing, thereby increasing the free volume of PIM-1. Graphene is an interesting candidate as an additive filler due to its stiffness, nanoscale features and high surface area. For this reason, materials incorporating graphene have become a hot topic in science.

The overall goal of this project was to develop a novel polymeric membrane for gas separation. In the first part of the study, the effect of graphene incorporation into PIM-1 was examined. The theoretical basis for this was the idea that using graphene as an additive would increase the free volume in the polymer, leading to higher gas permeability of the membrane. Despite the fact that graphene is impermeable even to small gas molecules such as helium, graphene exhibits a high-surface area. This high-surface area is expected to be reflected in graphene-based materials. The second part of this project involved the comparison of features of novel PIMs with those of PIM-1. Features investigated include polymerization and other physical properties, such as the Brunauer-Emmett-Teller (BET) surface area and sorption. Moreover, several PIMs contain polyphenylene fragments that can be transformed to novel graphene fragments via chemical oxidation reactions.

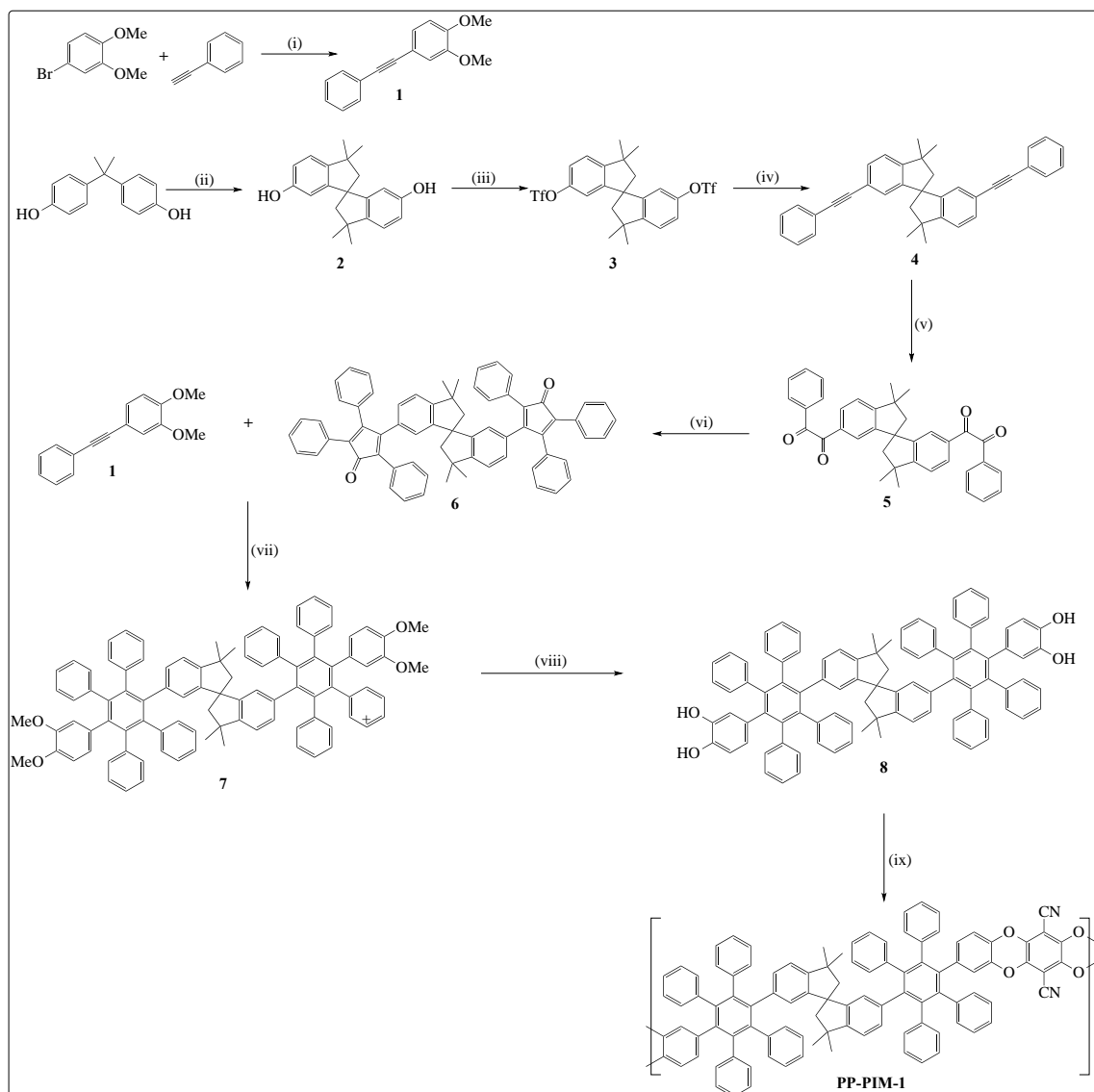
For the first part of this project, methods for preparing graphene/PIM-1 mixed matrix membranes (GPMMMs) were developed. These methods incorporated common approaches to graphene preparation, such as top-down and bottom-up methods. The objectives of GPMMM preparation were as follows:

1. Graphene dispersion via liquid phase exfoliation (LPE) from natural graphite (top-down approach):
 - a. Exfoliation of graphene in organic solvents and in a solution of PIM-1.

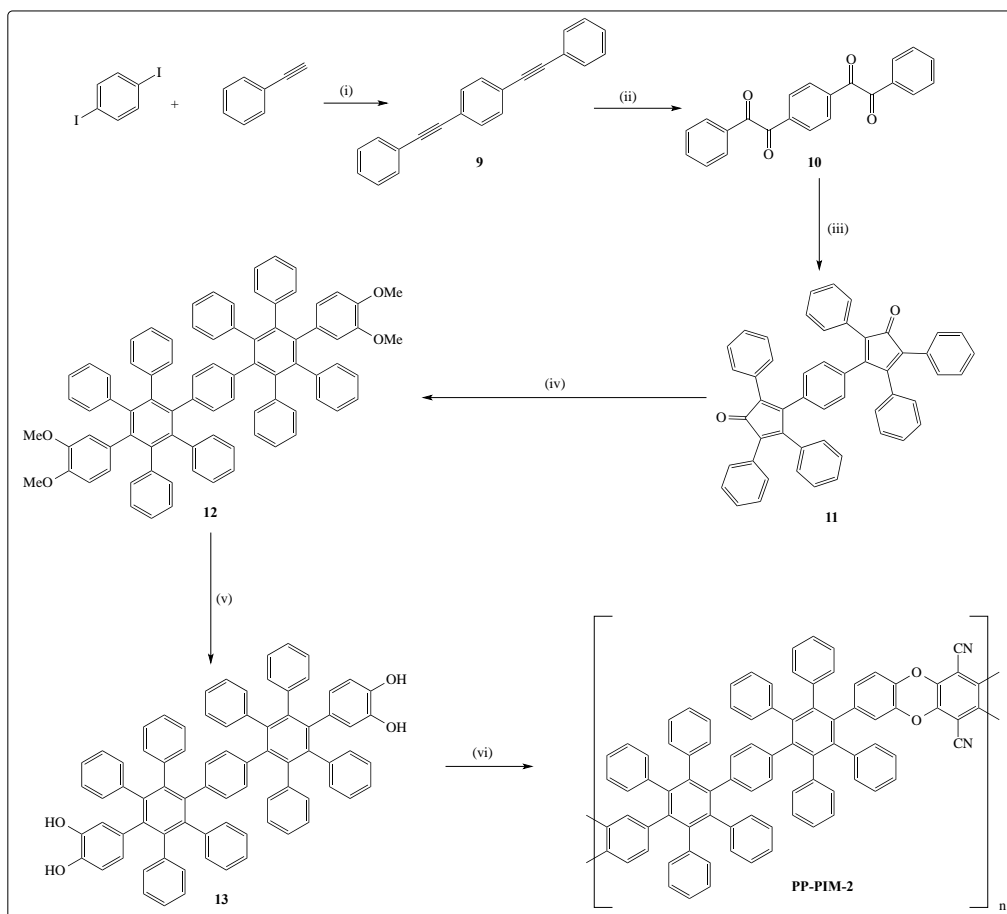
- b. Determination of the graphene concentration by ultraviolet-visible (UV-Vis) spectroscopy.
 - c. Addition of a dispersion of graphene in organic solvent (i.e. chloroform) to PIM-1 and casting of GPMMMs via solvent evaporation.
 - d. Dispersion of graphene in a PIM-1 solution, to be cast as GPMMMs with high graphene content, and preparation of other GPMMMs of lower graphene content from the addition of pure PIM-1 solution.
2. Preparation of synthetic multilayer graphene from dry ice via a reduction chemical reaction (bottom-up approach), which was performed by Dr. Frank Mair:
 - a. Exfoliation of the multilayer graphene by an LPE process in PIM-1 solution.
 - b. Casting of the dispersion of graphene in PIM-1 solution as GPMMMs of high graphene content, and preparation of GPMMMs with lower graphene content by addition of pure PIM-1 solution.
3. Obtainment of other graphene derivatives (e.g. graphene oxide [GO], base-washed graphene oxide [BWGO] and chemically reduced graphene oxide [RGO]) from Dr. Patricia Gorgojo, and utilization in GPMMM preparation by using LPE in PIM-1 solution.
4. Characterization of GPMMMs by scanning electron microscopy (SEM) (by Aleksandra Gonciaruk) and Raman spectroscopy (by Yuyoung Shin).
5. Measurement of the permeability of GPMMMs to different gases, such as CO₂, H₂, He, O₂, CH₄ and N₂, which were performed by Dr. Paola Bernardo, Dr Gabriele Clarizia and Dr. Johannes Jansen at the Institute on Membrane Technology (ITM), Italy.

For the second part of this work, PIMs were prepared from novel monomers, which were synthesized via common organic reactions. PIM preparations were divided into two groups of novel polymers. One group concerned polymers that can be prepared by forming dibenzodioxane linkages. This group of polymers required the polymerization of bis-catechol monomers with another monomer, tetrafluoroterephthalonitrile (TFTPN), as illustrated in Scheme 1-1, 1-2 and 1-3. The other group of polymers was prepared from A-A and B-B monomers via [4+2]-

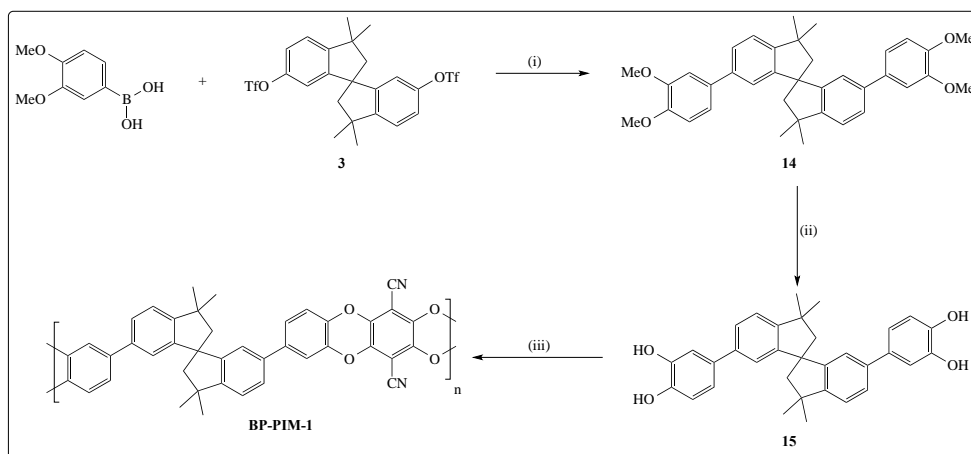
cycloaddition Diels-Alder polymerization, as shown in Scheme 1-4. A-A is a monomer with two terminal alkyls, and B-B is a monomer with two terminal tetraphenylcyclopentadienone (TPCPDs). In each scheme, compounds and polymers were synthesized by Jafar Alkabli, under the supervision of Gardiner were indicated.



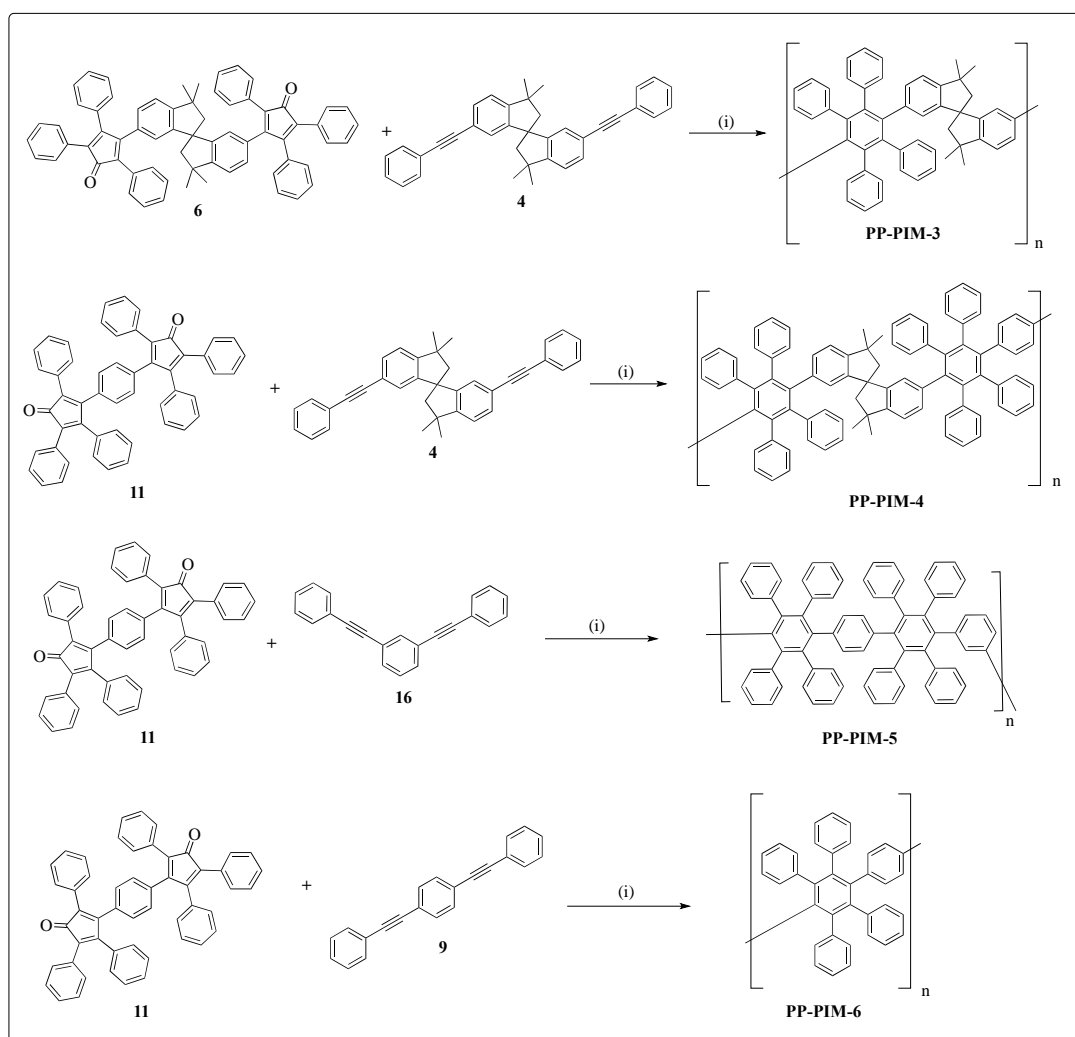
Scheme 1-1. Schematic route of PP-PIM-1 synthesis, i) $\text{PdCl}_2(\text{PPh}_3)_2$, CuI, DMF, Amine, Δ ; ii) $\text{CH}_3\text{SO}_3\text{H}$, RT, 4 days; iii) $(\text{CF}_3\text{SO}_2)_2\text{O}$, DCM, Pyridine; iv) Phenylacetylene, $\text{PdCl}_2(\text{PPh}_3)_2$, CuI, DMF, Amine, Δ ; v) I_2 , DMSO, Δ ; vi) 1,3-diphenyl-2-propanone, KOH, EtOH; vii) Diphenyl ether, 3 days; viii) BBr_3 , DCM, RT; ix) K_2CO_3 , DMF, Toluene, Δ . Compounds 5, 6, 7 and 8 were prepared by Alkabli.



Scheme 1-2. Schematic route of PP-PIM-2 synthesis, i) $\text{PdCl}_2(\text{PPh}_3)_2$, CuI , DMF, Et_3N , Δ ; ii) I_2 , DMSO, Δ ; iii) 1,3-diphenyl-2-propanone, KOH , EtOH; iv) Compound 1, Diphenyl ether, 3 days, Δ ; v) BBr_3 , DCM, RT; vi) K_2CO_3 , DMF, Toluene, Δ . Compounds 9-13 were prepared by Alkabli.



Scheme 1-3. Schematic route of BP-PIM-1 synthesis, i) $\text{Pd}(\text{PPh}_3)_4$, K_2CO_3 , H_2O , Aliquat336, Δ ; ii) BBr_3 , DCM, RT; iii) K_2CO_3 , DMF, Toluene, Δ .



Scheme 1-4. [4+2]-cycloaddition Diels-Alder polymerization of novel PP-PIMs, i) Diphenyl ether, Δ . Polymerizations performed by Jafar Alkabli.

1.2 Introduction to membranes

Membranes are important structures which have gained considerable attention in the development of chemical technologies. The ability to control the rate of transport of a chemical species from one side of a membrane to the other can be beneficial in drug delivery applications, where regulation of the drug's passage from a reservoir to the body is important. In separation applications, membranes are applied to extract one component from a mixture by facilitating the exclusive transport of this component through the membrane. Thus, there is increasing interest in membrane development.¹

As this work is concerned with gas separation membranes, this introduction outlines the most relevant aspects of membrane development such as classification, applications, porosity and associated transport mechanisms. Nanotechnology is also mentioned, as an overlapping topic in porous materials.

1.3 Membrane classification

Membranes can be classified in a general context by a wide range of characteristic differences such as chemical and physical composition. In terms of porosity, there are two main classes: porous and nonporous membranes. The former can be further classified by pore size; the International Union of Pure and Applied Chemistry (IUPAC) distinguishes between micropores (< 2 nm), mesopores (2-50 nm) and macropores (> 50 nm). Structurally, membranes can be either symmetric or asymmetric, as shown in Figure 1-1. Finally, they can be classified by the material of which they are composed as either organic, inorganic or hybrid. All of these classifications help developers to convey a clear vision of membrane properties and performance. For example, organic polymer membranes can generally resist thermal conditions from 100 to 300 °C, whereas inorganic ones (e.g. ceramic membranes) can operate at temperatures above 250 °C. Knowledge of the advantages and disadvantages of each class of membrane allows developers to innovate and invent productively.¹

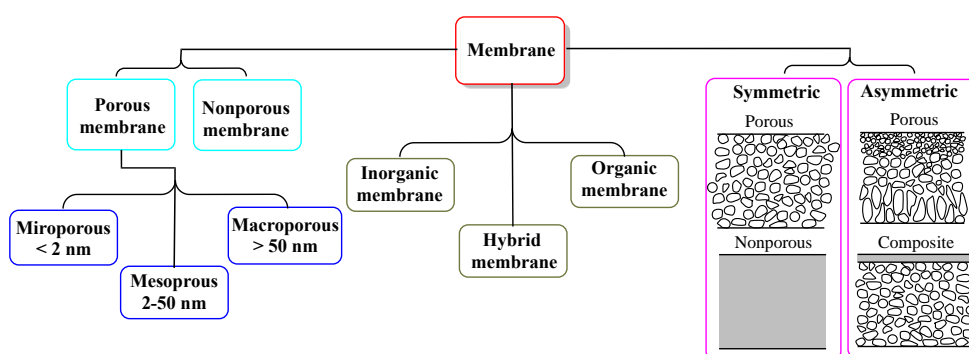


Figure 1-1. General classification of membranes.

Properties that depend on pore size, for instance, can be used in mapping current or potential applications involving separation processes and the materials separated (Figure 1-2). Membranes in the microporous region, for example, have been

considered for many separation processes and materials, reflecting the strong industrial demand for microporous materials.

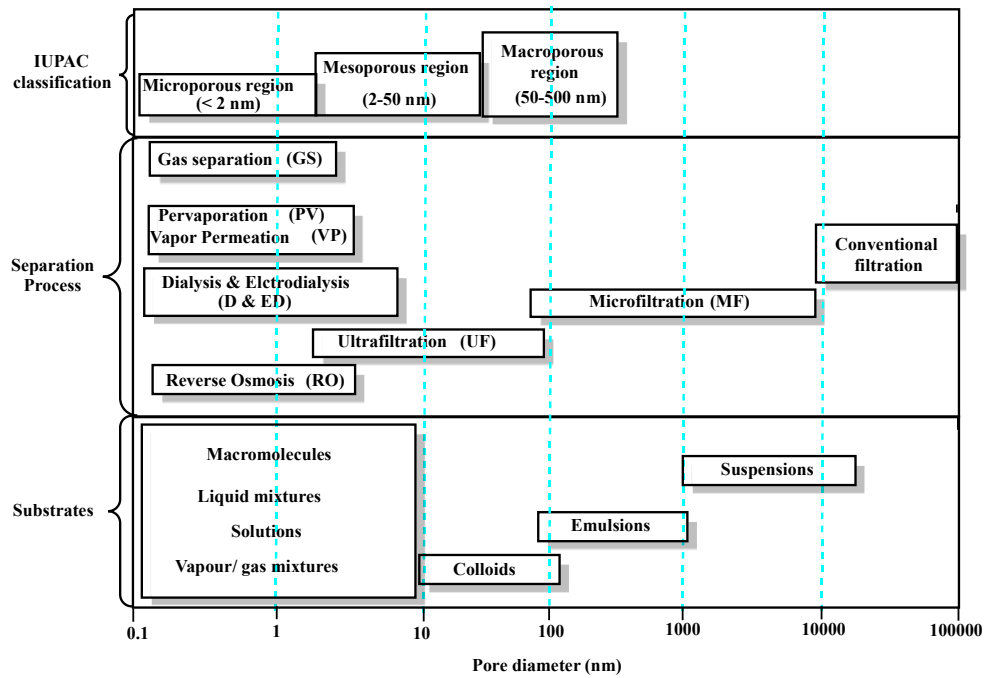


Figure 1-2. Correlations between pore diameter, separation processes and potential substrates for membrane separation.

Effective pores, which allow components to penetrate through the membrane, are usually deep and connecting, and can be found in different shapes such as cavities or channels. Inaccessible pores, on the other hand, do not contribute to separation and transport. Figure 1-3 illustrates different types of pore that can be found in a membrane cross section.

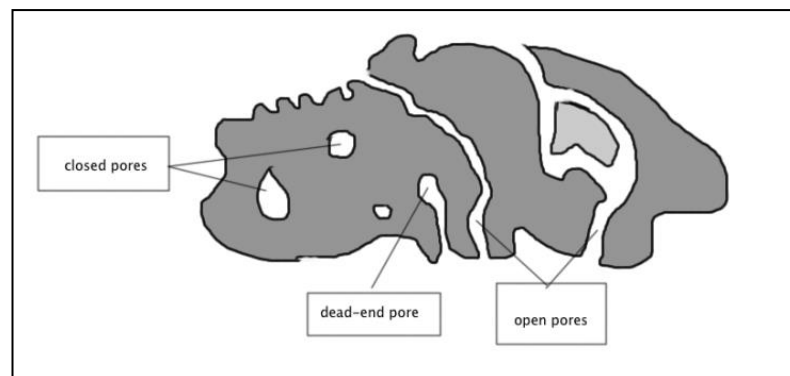


Figure 1-3: Different types of pore that can exist in general porous materials (classification based on pore accessibility or interconnectivity).

Pore dimension is an important factor that can determine membrane performance. In the case of well-engineered structures, pores can be divided into four classes, as shown in Figure 1-4. Membranes with one- and two-dimensional pores can be used in directed transport. They are known as active components in the separation mechanism, as are three-dimensional pores. Zero-dimensional pores can be isolated from the transport process, which make them less attractive in porous separation membranes.

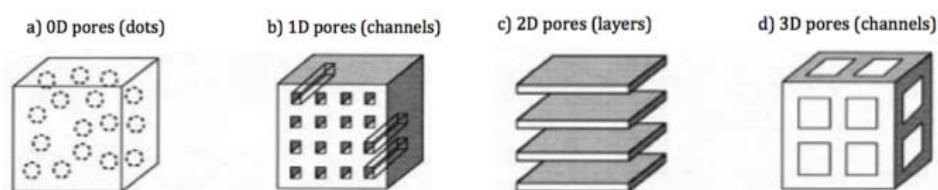


Figure 1-4: Classification of pores by their dimensional structures.⁹

Transport mechanisms are associated with pore sizes. Relatively large macropores, in the diameter range of 100-10000 nm, have low separation efficiency, as a result of the convective flow, which takes place within them. When the pore diameter is less than 100 nm, in the same order as the mean free path or smaller of penetrate molecules, the Knudsen diffusion mechanism dominates and the transport rate is determined by the inverse square root ratio of the molecular weights of the penetrant species. Very small pores (0.5-20 nm) facilitate the molecular sieving mechanism, or surface diffusion in the case of adsorbed penetrants, with the result that strong separation occurs. In the case of dense membranes, separation occurs by the solution-diffusion mechanism (Figure 1-5). Further detail will be given later in this work. In well-structured microporous materials (such as crystalline ones), molecular sieving can be more defined. In the case of polymer-based membranes, both molecular sieving and solution-diffusion mechanisms have to be considered, because they usually overlap.

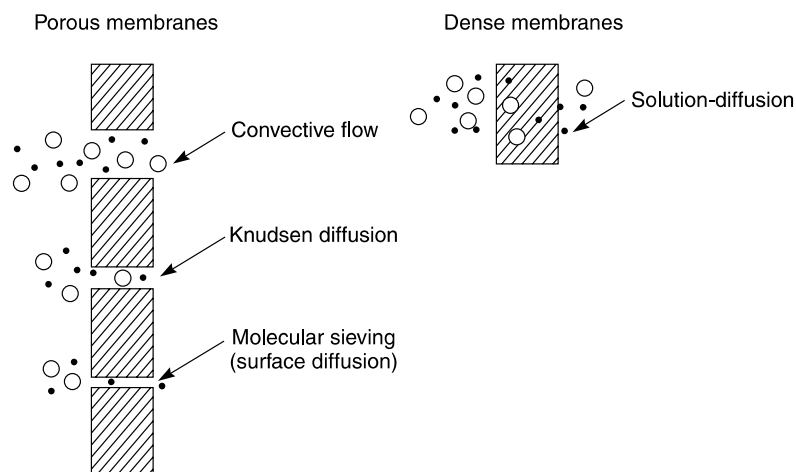


Figure 1-5. Various separation mechanisms can operate, depending on the porous properties of the membrane.¹

1.3.1 Nanoporous membrane materials

Nanomaterials are of major interest because of their potential for widespread use in advanced applications. Nanoporous materials, in particular, exhibit unique properties, dependent on their surface features, structure and bulk. These properties are relevant in several important applications such as purification, catalysis, separation and ion exchange. From the scientific and technological perspectives, nanoporous materials are important because of their sophisticated ability to interact and adsorb, based on their nanoscale properties.²

Nanomaterials, defined as having particles or pores of diameter ranging between 1 and 100 nm, have properties which are nanoscale dependent. Materials containing nanopores are termed nanoporous. Their nanoscale properties can be tailored at the scale of atoms, molecules or their assembly, giving them unique properties different from those of conventional materials. These underlie nanomaterial technologies and developments.³ Nanoporous materials can be classified as either microporous or mesoporous; the focus of this review is on microporous materials, particularly polymers.

1.3.2 Microporous organic polymers

The family of microporous organic polymers (MOPs) is attractive in the development of porous materials. MOPs are composed of light elements in the periodic table such as carbon, nitrogen, boron and oxygen, which means that they are usually of low density.⁴ In MOPs, covalent bonds can form various classes of polymers, such as polymers of intrinsic microporosity (PIMs), hypercrosslinked polymers (HCPs) and conjugated microporous polymers (CMPs).

Organic reactions have the potential to form large numbers of structures and there is thus significant scope for the exploitation of synthetic organic polymers, which may have crystalline or amorphous structures. Moreover, organic reactions can facilitate sophisticated functionalization and the tailoring of materials to fit their performance to given applications.⁴ This gives microporous organic polymers their characteristic advantage. Figure 1-6 shows a number of common organic reactions that can be utilized in the synthesis of organic polymers.

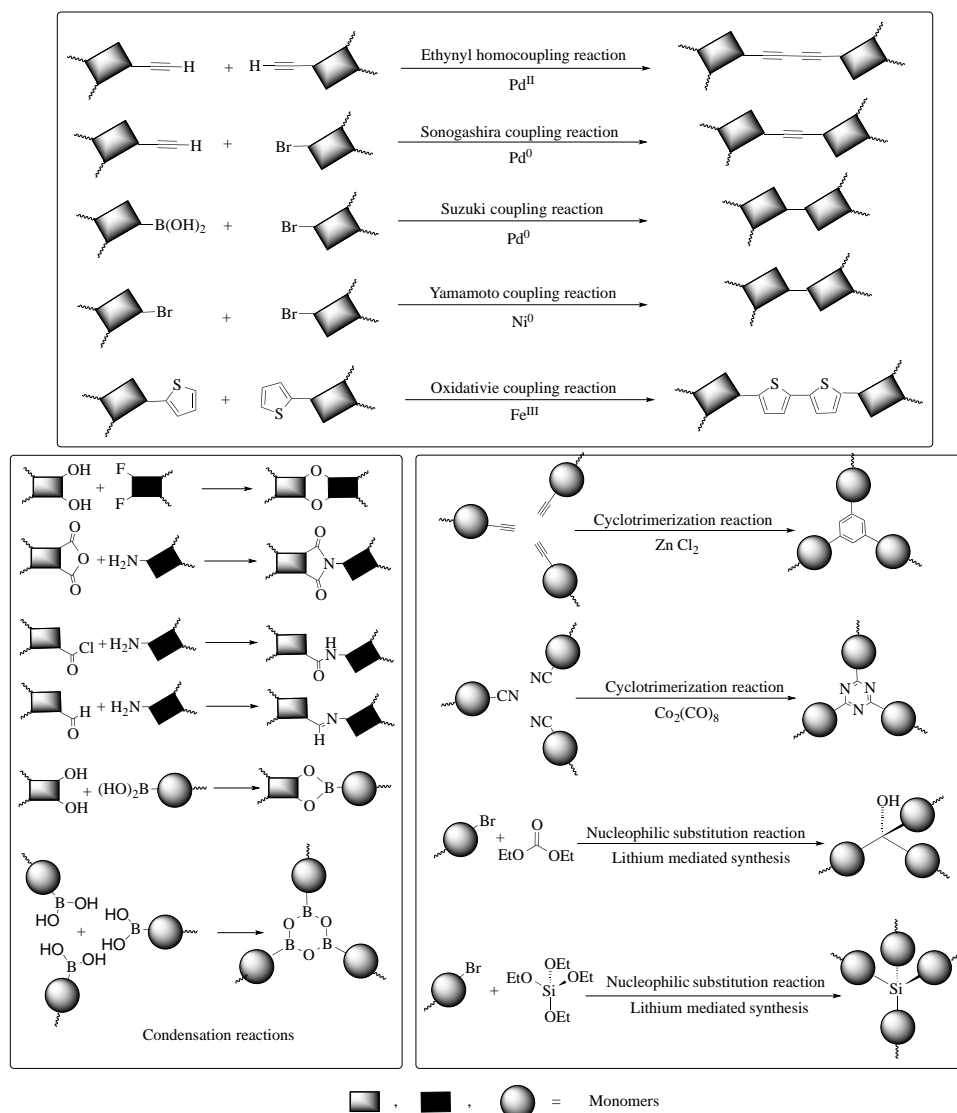


Figure 1-6: Organic reactions recently used in microporous polymer synthesis.⁴

1.3.2.1 Covalent organic frameworks

Covalent organic frameworks (COFs) are a group of MOPs that were first reported by Yaghi *et al.*⁵ In COFs, organic monomers form crystalline structures with a scaffolding of strong covalent bonds. Their crystallinity is attributed to their formation by reversible reactions, making their structures thermodynamically stable and ordered. COF-1 and COF-5 are examples of two-dimensional COFs.⁵ COF-1 is a boroxine-ring forming polymer prepared from benzene 1,4-diboronic acid, which undergoes self-condensation (Figure 1-7). COF-5 is prepared from a condensation reaction between catechol derivatives and boronic acid, forming boronate ester linkages (Figure 1-7). The respective BET surface areas of COF-1 and COF-5 are

reported to be 711 and 1590 m² g⁻¹ (further details of this measurement are given in Chapter 2).⁶ Other COFs with three-dimensional structures have higher BET surface areas, up to 4210 m² g⁻¹.⁷

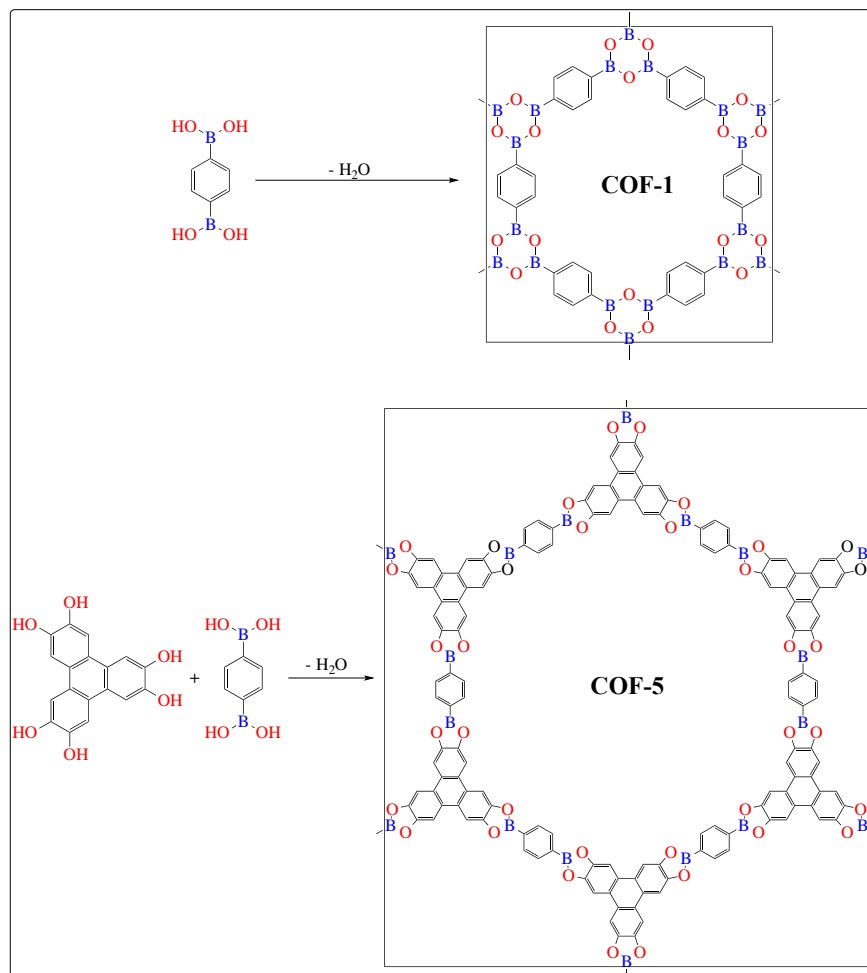


Figure 1-7. Two examples of the formation of COFs: COF-1 and COF-5.⁵

1.3.2.2 Hypercrosslinked polymers

Hypercrosslinked polymers (HCPs) are a broad class of polymers that can be porous. Microporous HCPs can be prepared from styrene-based polymers, in which crosslinking can be processed with a Lewis acid such as iron(III) chloride via Friedel-Crafts alkylation (Figure 1-8).⁸

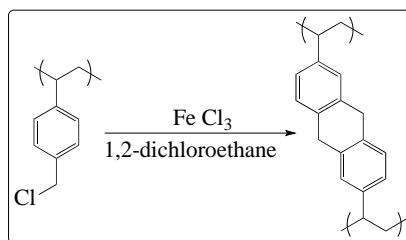


Figure 1-8. Preparation of HCP from a styrenic polymer.⁸

Another approach to HCP preparation is the direct polymerization of bisvinylchloride-based monomers, such as 1,4-bis(chloromethyl)benzene (BCMB), 4,4'-bis(chloromethyl)-1,1'-biphenyl (BCMBP) and 9,10-bis(chloromethyl)anthracene (BCMA) (Figure 1-9).⁹ These materials have relatively high BET surface areas, ranging from 600 to 2000 m² g⁻¹.⁴

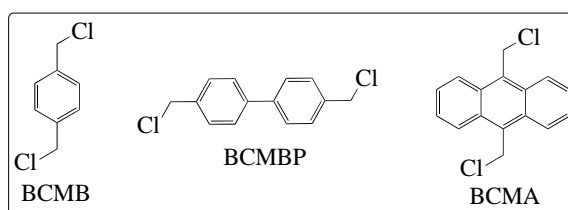


Figure 1-9. Examples of monomers which can undergo direct polymerization for the preparation of HCPs.

1.3.2.3 Conjugated microporous polymers

Conjugated microporous polymers (CMPs) can be considered to be hypercrosslinked polymers. However, a distinguishing feature of CMPs is that the whole polymer network comprises conjugated carbon-carbon bonds. This class of polymer has been successfully prepared by combining conjugated polymers with nanoporous components, which can take place in catalytic and energy-harvesting applications.^{4,10,11,12}

CMPs are a recent class of polymers, having first been studied in 2007.¹³ They were originally prepared by the palladium-mediated Sonogashira-Hagihara reaction, involving carbon-carbon coupling between arylhalides and arylalkyls. These studies led to a series of poly(arylene ethynylene) networks.^{6,14} In general, CMPs have average apparent BET surface areas from 520 to 830 m² g⁻¹.¹⁵ Interestingly, among

the large number of CMPs, those with short strut length, such as CMP-0 and CMP-1 (Figure 1-10), have been found to have a high BET surface area. In the case of CMP-0, this was reported to be $1018 \text{ m}^2 \text{ g}^{-1}$.¹⁵ This phenomenon is attributed to the fact that long struts can provide greater flexibility and conformation freedom.¹⁵ Greater strut length can also favour self-interpenetration, resulting in the filling of more free space and thus a lower BET surface area.⁴

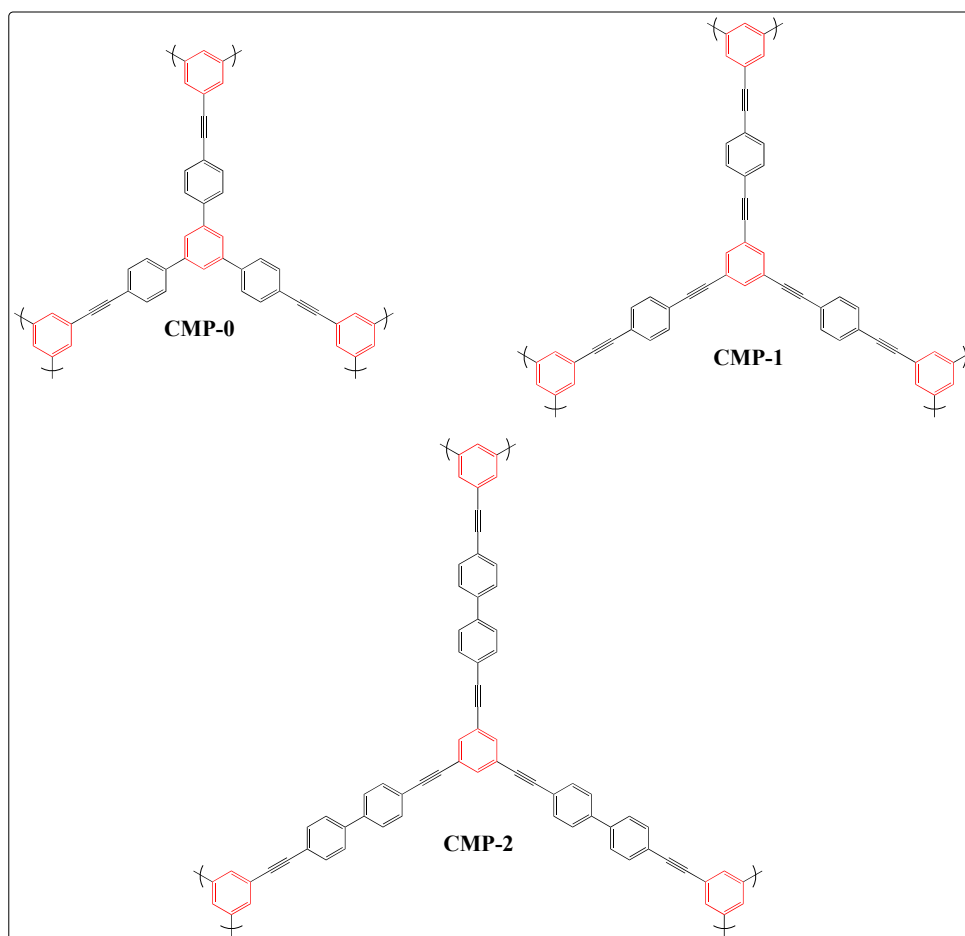
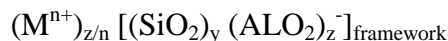


Figure 1-10. Several examples of CMPs.⁴

1.3.3 Zeolites

Zeolites are microporous crystalline materials that can be obtained naturally or synthetically and are known for their hydrophilic features. They are basically aluminosilicate minerals, with unique separation properties. Zeolites can be used to separate mixed components according to size and shape. Therefore, they are considered to be molecular sieves. Defined sizes and shapes of pores and channels

result from the building of regular structures.^{16,17} Zeolite frameworks can be defined as follows:



There are also structurally similar materials termed ‘zeolite-like materials’ and sometimes ‘zeolite-type framework structures’. These have chemical compositions other than aluminosilicate, such as aluminophosphate (ALPO) and silica-aluminophosphate (SAPO).¹⁶

In general, Zeolites are constructed from oxygen bridges and tetrahedral networks, resulting in well-defined sizes and shapes of pores and channels. Figure 1-11 shows zeolite A as an example.

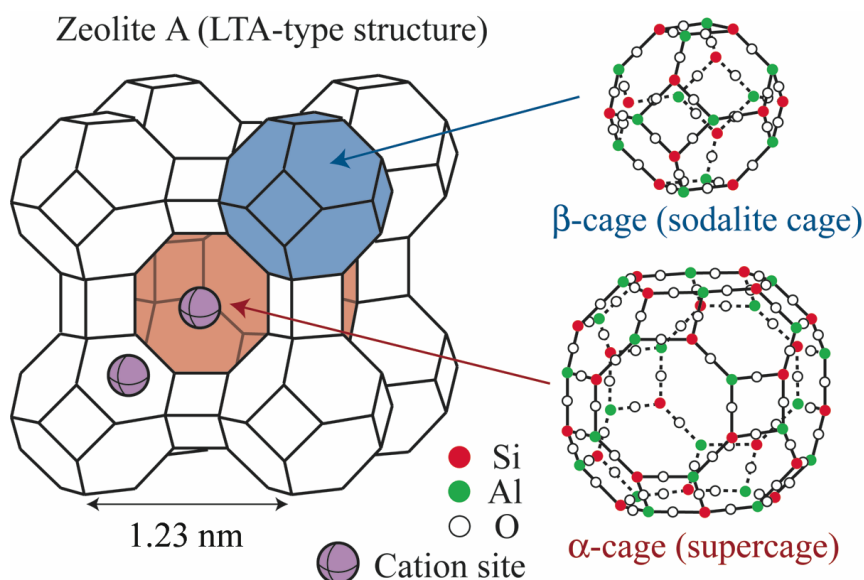


Figure 1-11. Representative framework structure of zeolite A, illustrating how micropores are formed. Adapted from ref.¹⁸.

1.3.4 Metal-organic frameworks

Metal-organic frameworks (MOFs) are crystalline frameworks consisting of metal ions or clusters and organic linkers, coordinated to form polymer networks. The literature reports the investigation of more than 20,000 MOFs,¹⁹ because they have ultrahigh porosity and a resultant free volume up to 90%, with apparent BET

surface area exceeding $6000 \text{ m}^2 \text{ g}^{-1}$. MOFs thus have high potential in many applications usually associated with microporous materials.^{20, 21}

In general, MOFs can be prepared from a variety of metals and organic linkers, the selection of which will determine the resultant framework topology. Figure 1-12 illustrates some possible MOF frameworks that can be obtained by selecting certain types of component.

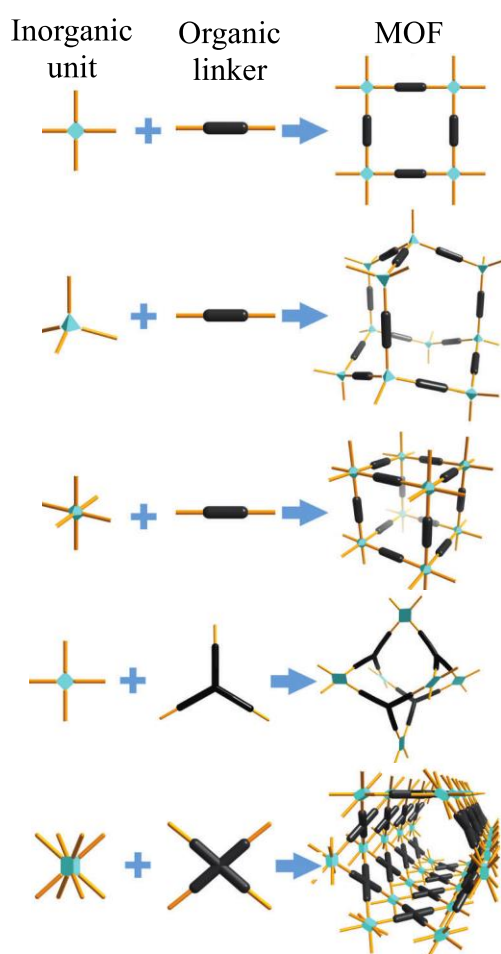


Figure 1-12. Various MOF framework topologies, prepared from different metals and organic geometries.¹⁹

An important group of MOFs are the zeolitic imidazolate frameworks (ZIFs), which consist of imidazolate (im) bridges and metals of tetrahedral geometry, such as Zn, Co and Cu, with the formula $[\{M(im)_2\}_\infty]$.²² Thus, ZIFs are zeolite-type materials, because their frameworks have similar tetrahedral topologies. This similarity arises because the metal-imidazolate linkages have similar angles to the Si-O-Si bridges in zeolites (Figure 1-13).²³ Recently, more than 100 different ZIFs have

been reported with various structures.²⁴ Figure 1-14 shows the illustrative example of ZIF-8.²⁵

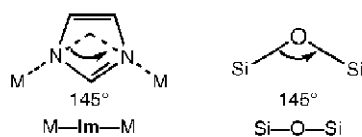


Figure 1-13. Comparison between angles of imidazole silicate bridges.²³

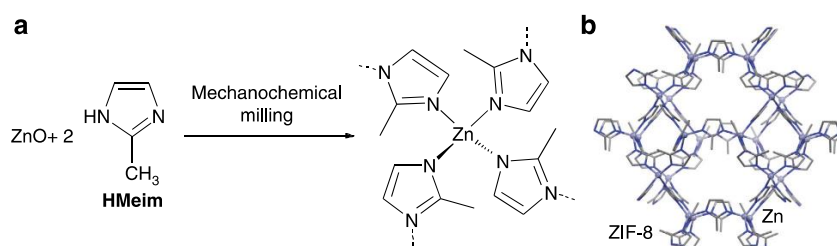


Figure 1-14. ZIF-8. a) Preparation by mechanochemical synthesis; b) Crystal structure.²⁵

1.4 Attractive membranes for commercialization

Membrane science dates back to the discovery of biological membranes, which can be considered to offer examples of optimum membrane performance, in the sense that most commercial developers today attempt to simulate the operation of biological membranes for industrial purposes. However, biological membranes cannot usually be operated at high temperatures and they tend not to have the chemical resistance or stability under changing physical conditions that are required for industrial applications. Moreover, biological membranes are known for their complex structures, whereas in industry there is a need for simplicity and low capital costs while retaining optimum performance. All of these requirements pose challenges to developers of commercial membrane systems, which must offer high performance with chemical and physical stability. While polymeric membranes, in particular, are utilized in large-scale commercial applications, rapid developments are also underway in the search for novel membrane materials, because of the limited scope for improvements in the properties of polymeric membranes. Furthermore, the

conditions of manufacture are important, since improved fabrication can lead to superior separation properties.^{26,27}

Properties of particular interest in membrane commercialization include reliable and efficient separation under adverse pressure, thermal and chemical conditions.²⁶ From a general perspective, the use of nanoporous materials is an area of active research and development.²⁸ In this work, several attractive emergent properties are considered as part of membrane development and studies.

1.5 References

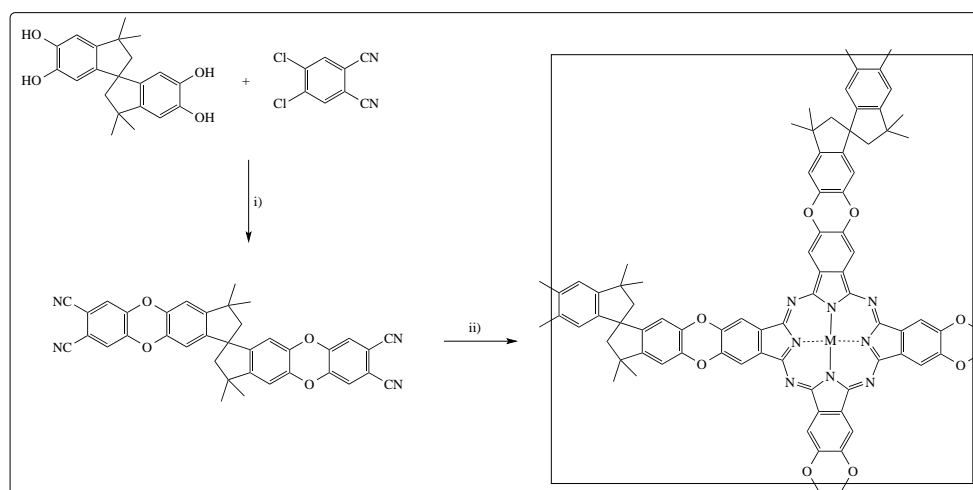
- (1) Baker, R. W. *Membrane Technology and Applications*; Second Eds, John Wiley & Sons, Ltd, Chichester, UK, pp 1-90.
- (2) Kenneth, J. *Nanoscale Materials in Chemistry*, Second Eds, John Wiley & Sons, Inc., New York, USA, 2009, pp 1-13.
- (3) Lu, G. Q.; Zhao, X. S. *Nanoporous Materials: Science and Engineering*, Imperial College Press, London, 2004, pp 1-47.
- (4) Dawson, R.; Cooper, A. I.; Adams, D. J. *Prog. Polym. Sci.* **2012**, *37*, 530.
- (5) Ockwig, N. W.; Co, A. P.; Keeffe, M. O.; Matzger, A. J.; Yaghi, O. M. *Science*. **2005**, *310*, 1166.
- (6) Jiang, J. X.; Su, F.; Trewin, A.; Wood, C. D.; Campbell, N. L.; Niu, H.; Dickinson, C.; Ganin, A. Y.; Rosseinsky, M. J.; Khimyak, Y. Z.; Cooper, A. I. *Angew. Chemie Int. Ed.* **2007**, *46*, 8574.
- (7) El-Kaderi, H. M.; El-Kaderi, H. M.; Hunt, J. R.; Hunt, J. R.; Mendoza-Cortés, J. L.; Mendoza-Cortés, J. L.; Côté, A. P.; Côté, A. P.; Taylor, R. E.; Taylor, R. E.; O’Keeffe, M.; O’Keeffe, M.; Yaghi, O. M.; Yaghi, O. M. *Science* **2007**, *316*, 268.
- (8) Lee, J. Y.; Wood, C. D.; Bradshaw, D.; Rosseinsky, M. J.; Cooper, A. I. *Chem. Commun.* **2006**, *25*, 2670.
- (9) Wood, C. D.; Bien, T.; Trewin, A.; Hongjun, N.; Bradshaw, D.; Rosseinsky, M. J.; Khimyak, Y. Z.; Campbell, N. L.; Kirk, R.; Stöckel, E.; Cooper, A. I. *Chem. Mater.* **2007**, *19*, 2034.
- (10) Chen, L.; Honsho, Y.; Seki, S.; Jiang, D. *J. Am. Chem. Soc.* **2010**, *132*, 6742.
- (11) Jiang, J. X.; Wang, C.; Laybourn, A.; Hasell, T.; Clowes, R.; Khimyak, Y. Z.; Xiao, J.; Higgins, S. J.; Adams, D. J.; Cooper, A. I. *Angew. Chemie Int. Ed.*

- 2011**, 50, 1072.
- (12) Vilela, F.; Zhang, K.; Antonietti, M. *Energy Environ. Sci.* **2012**, 5, 7819.
 - (13) Chinchilla, R.; Nájera, C. *Chem. Rev.* **2007**, 107, 874.
 - (14) Weder, C. *Angew. Chemie - Int. Ed.* **2008**, 47, 448.
 - (15) Jiang, J. X.; Su, F.; Trewin, A.; Wood, C. D.; Niu, H.; Jones, J. T. a; Khimyak, Y. Z.; Cooper, A. I. *J. Am. Chem. Soc.* **2008**, 130, 7710.
 - (16) Meier, W. M. *Stud. Surf. Sci. Catal.* **1986**, 28, 13.
 - (17) Fedosov, D. a.; Smirnov, a. V.; Knyazeva, E. E.; Ivanova, I. I. *Pet. Chem.* **2011**, 51, 657.
 - (18) Duan, T.; Nakano, T.; Nozue, Y. *e-Journal Surf. Sci. Nanotechnol.* **2007**, 5, 6.
 - (19) Lu, W.; Wei, Z.; Gu, Z. Y.; Liu, T. F.; Park, J.; Park, J.; Tian, J.; Zhang, M.; Zhang, Q.; Gentle III, T.; Bosch, M.; Zhou, H. C. *Chem. Soc. Rev.* **2014**, 43, 5561.
 - (20) Zhou, H. C.; Long, J. R.; Yaghi, O. M. *Chem. Rev.* **2012**, 112, 673.
 - (21) Zhou, Joe, H. C.; Kitagawa, S. *Chem. Soc. Rev.* **2014**, 43, 5415.
 - (22) Huang, X. C.; Lin, Y. Y.; Zhang, J. P.; Chen, X. M. *Angew. Chemie Int. Ed.* **2006**, 45, 1557.
 - (23) Phan, A.; Doonan, C. J.; Uribe R. F. J.; Knobler, C. B.; Okeeffe, M.; Yaghi, O. M. *Acc. Chem. Res.* **2010**, 43, 58.
 - (24) Ortiz, A. U.; Freitas, A. P.; Boutin, A.; Fuchs, A. H.; Coudert, F. X. *Phys. Chem. Chem. Phys.* **2014**, 16, 9940.
 - (25) Katsenis, A. D.; Puškarić, A.; Štrukil, V.; Mottillo, C.; Julien, P. a; Užarević, K.; Pham, M. H.; Do, T. O.; Kimber, S. a J.; Lazić, P.; Magdysyuk, O.; Dinnebier, R. E.; Halasz, I.; Frišćić, T. *Nat Commun* **2015**, 6.1
 - (26) Pushpinder S. Puri.; Membrane Engineering for the Treatment of Gases **2011**, 1, 215-244
 - (27) Strathmann, H.; Giorno, L.; Drioli, E. *CNR-Servizio Pubblicazioni* **2006**, 10, 8.
 - (28) Salim, W.; Ho, W. W. *Curr. Opin. Chem. Eng.* **2015**, 8, 76.

Chapter 2 Synthesis and characterization of PIM-1

2.1 Introduction to PIMs

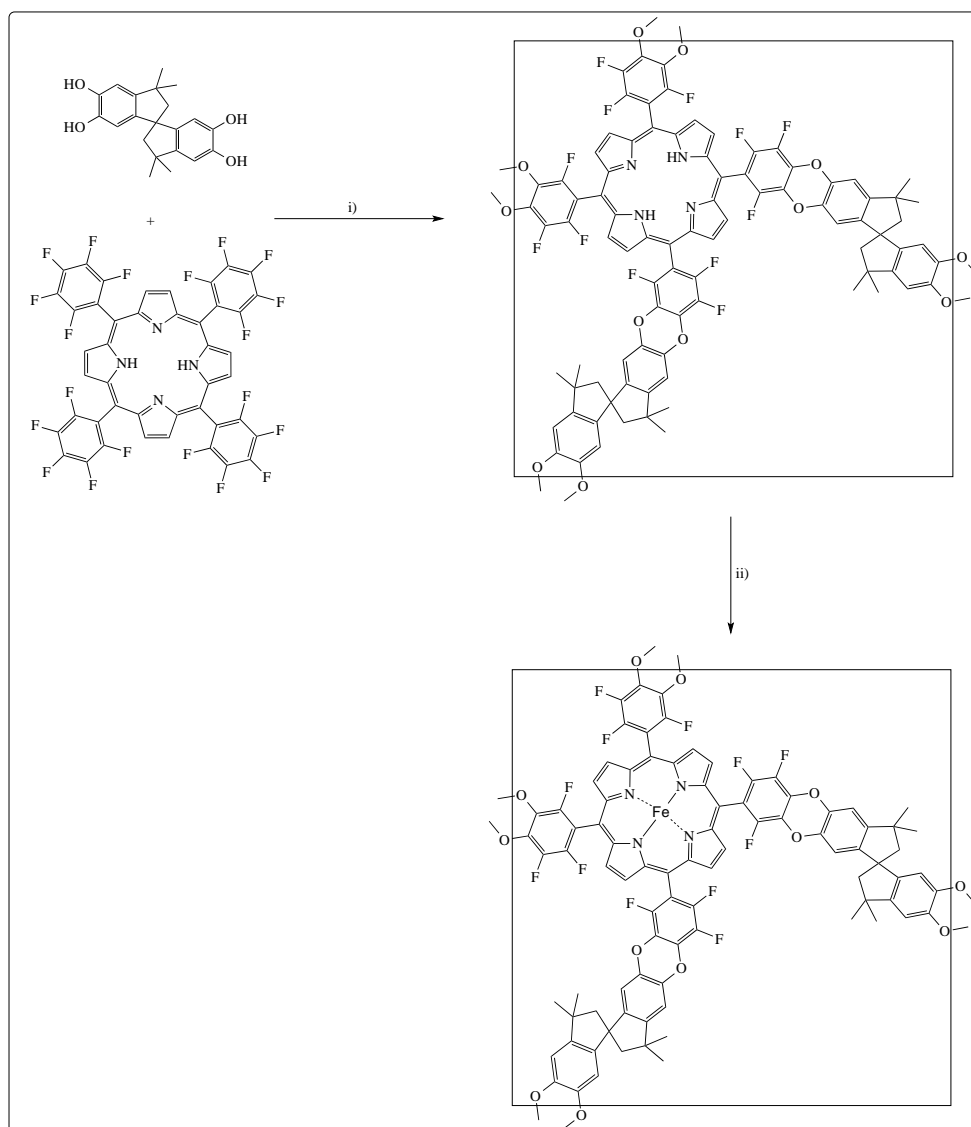
PIMs are a family of high free-volume polymers which were first described at the University of Manchester by McKeown and colleagues.^{1,2} The idea of PIMs was developed from a study of phthalocyanine materials for catalytic applications. Phthalocyanine materials were known to be catalytically active, especially in oxidation reactions, but their catalytic activity was reduced by the phenomenon of aggregation. In 2001, there was a successful attempt to synthesize a network polymer incorporating both phthalocyanine and a spirobisindane derivative in its structure.³ This work yielded a highly porous material with orthogonal orientation of each macrocycle component in respect to its neighbour. The synthesis of this network polymer was easily achieved by phthalocyanine linkage from a spirocyclic bisphthalonitrile monomer, which was prepared by the reaction of 5,5',6,6'-tetrahydroxy-3,3',3',3'-tetramethyl-1,1'-spirobisindane (TTSBI) with 4,5-dichlorophthalonitrile (Scheme 2-1). This network polymer had a BET surface area of over 750 m² g⁻¹ as measured by its nitrogen adsorption isotherm.⁴ It was successfully used to catalyze oxidation reactions.^{5, 6}



Scheme 2-1. The synthesis of phthalocyanine-based network polymer with microporosity. i) K₂CO₃, DMF, 100° C; ii) metal cation (M) incorporation to template phthalocyanine formation at 200° C. Adapted from McKeown.²

Thereafter, the same concept of incorporating a catalytically active macrocycle and spiro-based components in a network polymer was also achieved with the reaction between cheap and commercially available compounds (*tetrakis-meso-*

(pentafluorophenyl) porphyrin and TTSBI) to give a network polymer with high BET surface area (up to $1000 \text{ m}^2 \text{ g}^{-1}$) (Scheme 2-2).⁷



Scheme 2-2. The synthesis of a porphyrin-based network polymer with microporosity. i) K_2CO_3 , NMP, 170° , 5 h; ii) Fe_2Cl_3 , NMP, 120° C , 24 h. Adapted from McKeown et al.⁷

Thereafter, the preparation of high surface area polymers was framed within a general strategy based on the reaction of an appropriate fluorinated or chlorinated monomer with its complementary monomer of multiple catechol components, such as TTSBI. This opened a wide range of studies and investigations, involving high hydrogen storage and heterogeneous catalysts.^{8, 2}

In parallel, non-network polymers were also explored. Most of these were found to have advantages of solubility and membrane formation, as well as high surface area from their intrinsic microporosity. Solution-based characterization was achievable. Thus, these studies also supported the efficiency of dibenzodioxin formation in network polymers.²

PIM-1 was the first polymer which was prepared in this work. A high yield was obtained of this fluorescent yellow polymer with high molar mass. A high BET surface area was also obtained (up to $800 \text{ m}^2 \text{ g}^{-1}$), which established a new approach to the preparation of microporous materials.² Notably, the non-network approach allows microporosity to be achieved with less covalent bonds, as in the case of PIM-1. In other words, intrinsic microporosity can be atomically engineered by carefully selecting appropriate monomers that prevent effective packing of the polymer chains and create interconnected cavities throughout the block volume. One member of the team doing this work at the University of Manchester was Peter Budd, who pointed to a potential use of PIM-1 in membrane fabrication.² This idea began to be transformed into a concrete concept, with an initial experiment to separate phenol from water using a PIM-1 membrane in pervaporation.^{9, 10}

Thereafter, a number of non-network PIMs were also investigated. Table 2-1 illustrates a selection of these soluble PIMs, which were constructed from various monomer architectures with various BET surface area values.

Table 2-1. Selected non-network PIMs based on dibenzodioxin formation, including selected data of solubility, name and quoted BET surface area. Adapted from McKeown.²

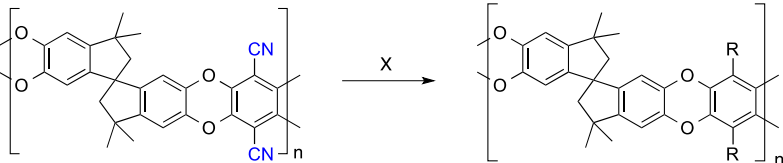
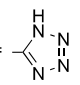
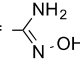
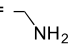
<p style="text-align: center;">(PIM)</p>				
<p style="text-align: center;">AB1</p>				
Monomers ^a	Solubility	Name ^b	Surface area (BET; m ² g ⁻¹)	Reference
A1 + B1	THF, CHCl ₃	PIM-1	760-850	10,11
A1 + B2	THF	PIM-2	600	11
A1 + B3	THF	PIM-3	560	11
A2 + B1	THF	PIM-4	440	11
A2 + B2	THF	PIM-5	540	11
A3 + B2	THF	PIM-6	430	11
A1 + B4	CHCl ₃	PIM-7	680	12
A4 + B4	CHCl ₃	PIM-8	677	12
A1 + B5	CHCl ₃	PIM-9	661	12
A4 + B5	<i>m</i> -cresol	PIM-10	680	12
A4 + B1	Insoluble	PIM-CO-100	680	12
A8 + B1	THF	Polymer from 7	895	13
A10 + B1	THF	Polymer from 5	432	14

^a See structures above.

^b As given in reference.

Strong interest in PIM-1 as a membrane material led to several studies of the modification of its structure by postsynthesis reactions involving the nitrile group. These reactions were achieved with simple hydrolysis to give carboxylic acids, with P_2S_5 to give thioamides, or with sodium nitrile to yield tetrazole substituents, as shown in Table 2-2 with other examples of modifications.

Table 2-2. PIMs from postsynthesis reactions of PIM-1.

<div style="display: flex; align-items: center; justify-content: space-around;">  <div style="margin-left: 20px;"> <p>$R = R_1, R_2 \text{ and } R_3$</p> <p>$R_1 = -CO_2H$</p> <p>$R_2 = -CSNH_2$</p> <p>$R_3 =$</p> <p>$R_4 =$</p> <p>$R_5 =$</p> </div> </div>				
Substituents, (R)	Reagents (X)	Solubility	Names ^a	Reference
Carboxylic acid, (R_1)	$NaOH_{aq}, H^+$	THF, $CHCl_3$	cPIM-1	15
Thioamide, (R_2)	P_2S_5/Na_2SO_3	$CHCl_3$	Thioamide-PIM-1	16
Tetrazole, (R_3)	$NaN_3/ZnCl_2$	$CHCl_3$	TZ-PIM-2	17
Amidoxime, (R_4)	NH_2OH	DMSO, DMF, DMAc, NMP	Amidoxime-PIM-1	18
Thioamide, (R_5)	$(CH_3)_2S-BH_3$	Insolubility	Amine-PIM-1	19

A number of additional studies also reflect interest in the area of PIMs. Classical polymerization by forming imide linkages instead of benzodioxin was investigated, producing a new series of PIMs named PIM-PIs. Table 2-3 shows how several polymers were prepared from selected monomers to form imide linkages. However, PIM-PIs do not have the same potential conformation as in the case of benzodioxin linkages. Imide linkages are characterized by rotation about the single bond linkages, which may yield less free volume than in benzodioxin-based polymers. This general disadvantage can be mitigated by the selection of appropriate diamine aromatic monomers, such as D1, D6 or D9. These have methyl groups adjacent to the reactive sites, thus restricting possible rotation around C-N single bonds and conferring significant intrinsic microporosity.

Table 2-3. Non-network PIMs based on imide formation, including data of solubility, name and quoted BET surface area, the table adapted from ref.².

Monomers	Solubility	Name ^a	Surface area (BET; m ² g ⁻¹)	References
C1 + D1	CHCl ₃	PIM-PI-1	680	20, 21
C1 + D2	CHCl ₃	PIM-PI-2	500	21
C1 + D3	CHCl ₃	PIM-PI-3	471	20, 21
C1 + D4	CHCl ₃	PIM-PI-4	486	21
C1 + D5	CHCl ₃	PIM-PI-7	485	21
C1 + D6	CHCl ₃	PIM-PI-8	683	20, 21
C2 + D7	CHCl ₃	P4	551	22
C3 + D1	THF	6FDAm4	-	23
C4 + D9	THF	6FDAm3	-	23
C2 + D10	THF	PIM-6FDA-OH	255	24
C3 + 10	THF	PIM-PMDA-OH	190	24

^a As given in reference.

An advantage of network polymers is that they offer porosity in a more stable form, because their scaffold is relatively rich in covalent bonds compared with non-network polymers. This explains discrepancies in the characterization values of intrinsic microporosity between different non-network polymer forms (i.e. film or powder) and different history, such as exposure to heat, vacuum or vapour, reprecipitation procedure or casting solution. Furthermore, the micropore structure

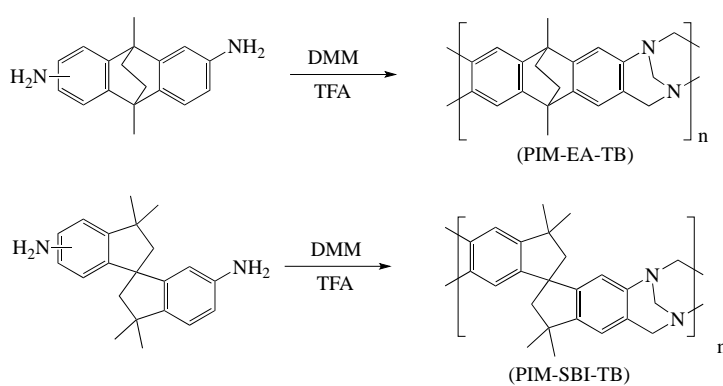
may undergo some changes during the analysis itself, depending on its physical properties. For example, in the adsorption step of the analysis procedure, swelling may occur due to the adsorption of gas molecules.

PIMs derive several characteristic properties from their structure, including solubility. Broadly speaking, ladder polymers are insoluble, although long aliphatic substituents can occasionally induce solubility. Thus, PIMs have been found to have the unusual property of solubility in common organic solvents, as can be seen in Table 2-1 and Table 2-2. The combination of contortion and rigid components in their structure minimizes intermolecular cohesive interactions within the polymer chains, promoting good solvation. In addition, the relative flexibility of the spirobisindane and benzodioxin components helps to induce solubility. In contrast, some PIMs, including PIM-CO-100, are insoluble because of the greater rigidity of the ethanoanthracene monomer (A4) (Table 2-1). Insolubility can also be attributed to the two-dimensional contortion of the ethanoanthracene component, which provides more interactions of polar groups (i.e. CN substituents), as a result of which more cohesive interactions of polymer chains may occur. Notably, soluble PIMs exhibit random coils in three dimensions.

The structural properties of PIMs affect not only their solubility but also their microporosity. PIMs vary in their apparent BET surface area values, as Table 2-1 shows. PIM-1 was found to be within the range of $720\text{--}875\text{ m}^2\text{ g}^{-1}$. The significant diversity of PIM-1 values seems to arise from different measurement conditions or sample history.²⁵ It is noticeable that few PIMs are close to or higher than PIM-1 in BET surface area. A general comparison indicates that PIMs with aromatic monomers of greater rigidity, such as A8, tend to have higher apparent BET surface areas.^{25, 26, 13} On the other hand, PIMs with more flexible components, such as tetrahydronaphthalene-based polymers prepared from A10 and B1 monomers (Table 2-1), seem to have lower permeability and microporosity than the equivalent PIMs with spirobisindane units.¹⁴

Scheme 2-3 shows PIM-EA-TB, which contains relatively more rigid components and exhibits more significant microporosity (BET surface area = $1038\text{ m}^2\text{ g}^{-1}$) than PIM-SBI-TB (BET surface area = $700\text{ m}^2\text{ g}^{-1}$), which is constructed from more flexible spirobisindane units.²⁷ Broadly speaking, it is difficult to predict

the microporosity that will be obtained by adding such substituents.²⁵ Indeed, adding substituents occasionally reduces microporosity, as they tend to fill the micropores and contribute to the packing of the polymer chains, rather than improving the microporosity. For example, post-modification of PIM-1 by converting nitrile groups to different groups such as carboxylic, thioamide and tetrazole substituents has been found to reduce the apparent surface area significantly.^{15,16,17} However, replacing nitrile groups with amidoxime substituents in PIM-1 led to a significant increase in the BET surface area, as these are termed “non-invasive” substituents.²⁸



Scheme 2-3. Synthesis of PIMs based on Tröger's Base (TB) formation, using dimethoxyethane (DMM) and trifluoroacetic acid (TFA).

Most of the above-mentioned PIMs have been considered for use as gas separation membranes. However, there are various other interesting applications for which PIMs are suitable, including as pervaporation membranes. For instance, PIM-1 forms a hydrophobic membrane which facilitates the separation of organic solvents such as alcohols and phenol from an aqueous-feed mixture.^{10, 29} Furthermore, these materials exhibit both high selectivity and high flux, which are attractive features for advanced applications in pervaporation technologies.²

Organic solvent nanofiltration membranes (OSNMs) are another application that has been investigated using PIMs.² PIM-1 and PIM copolymers have shown promising performance in OSNM studies.³⁰

PIMs have been also considered for use in sensors, where their properties of porosity, solution processability and optical clarity are all attractive. For instance, PIM-3, a fluorescent polymer, can be used to make an optical sensor for ethanol,

while fluorescent PIM-1 has been applied in laser sensor fabrication with significant sensitivity in the detection of nitrated aromatics.³¹ An investigation was conducted into the fabrication of a colorimetric optical sensor for organic vapour detection,^{32,33} using the phenomenon of rapid change in the reflective index of a thin PIM-1 film, combined with its rapid change in colour from green to red. This technique facilitates the visual sensing of the concentration of organic vapour in air down to 50 ppm, which can be enhanced using a fibre-optic spectrometer to be sensitive at 50 ppb.

Recently, PIM-1 has been marketed by the 3M company, as a key component in the sensor of an industrial respirator (Figure 2-1). This innovation helps the user to know when the respirator is no longer safe for use and should be changed.³⁴



Figure 2-1. An industrial respirator that contains PIM-1 as a key component in its sensor. The green area indicates the sensor part in whose fabrication PIM-1 is used.³⁴

A conventional sensor has been also designed, using PIM-1 as preconcentrator medium to adsorb organic vapour from air, which can then be desorbed by external heating.^{35, 36} This application requires high thermal stability, which is a property of PIMs.

In conclusion, there are more significant and promising developments to be explored in the future, using PIMs in such technologies, especially in the area of gas separation, as PIMs show advanced performance among the available polymers. Furthermore, different preparation methods are associated with variations in membrane performance, all of which has established significant knowledge for developing the area of membrane applications. State-of-the-art performance can be determined with Robeson plots, which include empirical upper bounds. However, simple comparison of gas transport properties is not the only important measure, as

properties such as solubility, stability and preparation costs are crucial considerations in membrane commercialization.

PIM-1 can be prepared from commercially available monomers and contributes to drawing the 2008 upper bounds of a number of Robeson plots (more details in Chapter 4). This project is concerned with the synthesis of PIM-1 and studying the potential enhancement of its gas transport properties by the mixed matrix membrane (MMM) preparation approach.

2.1.1 High and low temperature methods of PIM-1 preparation

Two methods have been devised to prepare ladder PIM-1. The first, established by Budd *et al.*,¹¹ is known as the low-temperature method (LTM). This was carried out using equimolar quantities of monomers and a fine dry base of potassium carbonate dissolved in anhydrous DMF under inert condition at 65 °C for 75 h. It was shown to be a successful method of preparing PIM-1 and it is worth noting its strong influence in investigating novel PIMs for membrane studies via dibenzodioxin-forming polymerization. Both linear and network polymers have been investigated using this polymerization method.^{9,11} The LTM is designed to be performed under relatively diluted conditions and over a long time; the polymerization reaction takes several days to complete.

The second technique, referred to as the high-temperature method (HTM), was developed at the Canadian NRC laboratories by Michael Guiver *et al.*³⁷ This involves rapid stirring of a monomer mixture in dimethyl acetamide at a temperature of 160 °C for only between eight and 40 minutes.³⁷ However, polymerization <40 minutes seems not to be scalable, as controlling the reaction conditions becomes complicated.² Toluene also has to be added to facilitate continued stirring, as the mixture becomes viscous with time. The addition of toluene is believed to be sufficient to remove any water produced, using a Dean-Stark apparatus, and to enhance monomer salt compatibility during polymerization. The concentration is also determined to be relatively high, at 1 mmol: 3 mL (monomer:solvent).³⁸

Both LTM and HTM show good production of high average molecular mass and film-forming capability. McKeown states that the concentration factor needs to

be considered as a high concentration reaction in the LTM can lead to crosslinked product.² On the other hand, a low-concentration reaction can yield a majority of cyclic product.^{39, 40} Therefore, the concentration of monomers in DMF have to be relatively low (0.2 mmol:1mL) for an optimum condition in the LTM.²

Guiver claims that the HTM is preferable because the short polymerization time enhances the mechanical properties of the polymer, with much smaller microcyclic, oligomeric and crosslinked fractions.³⁸ The presence of crosslinked product in this method is attributed to the dissolution of an intermediate salt, which is made worse by insufficient stirring; therefore, the addition of toluene seems to solve the problem. Also, under an intensive mixing process, the concentration of initial mediated salt is high, which helps to prevent the formation of cyclic products and leads to the production of soluble oligomer salts. The claim that Guiver's method reduces the likelihood of the production of both cyclic and crosslinked material is supported by GPC, which shows the absence of a shoulder attached to the main peak in either high or low-molecular-weight regions.³⁷ Further development of this method yielded PIM-1 after only 8 minutes of polymerization, but with additional critical steps.³⁷ However, McKeown states that the LTM is favoured because of its ease of processing and scalability.²

Ideally, ladder PIM-1 should be free of branched, cyclic and crosslinked material. Nevertheless, this type of polymerization has the potential to form cyclic and branched moieties as well as linear polymers, due to the complexity of the polymerization reaction, which involves monomers with multiple reactive groups. Figure 2-2 demonstrates schematically the routes of polymerization, where cyclic and various terminating sites can take place. This polymerization can also involve the formation of branched centres to give branched and crosslinked polymers (Figure 2-3).

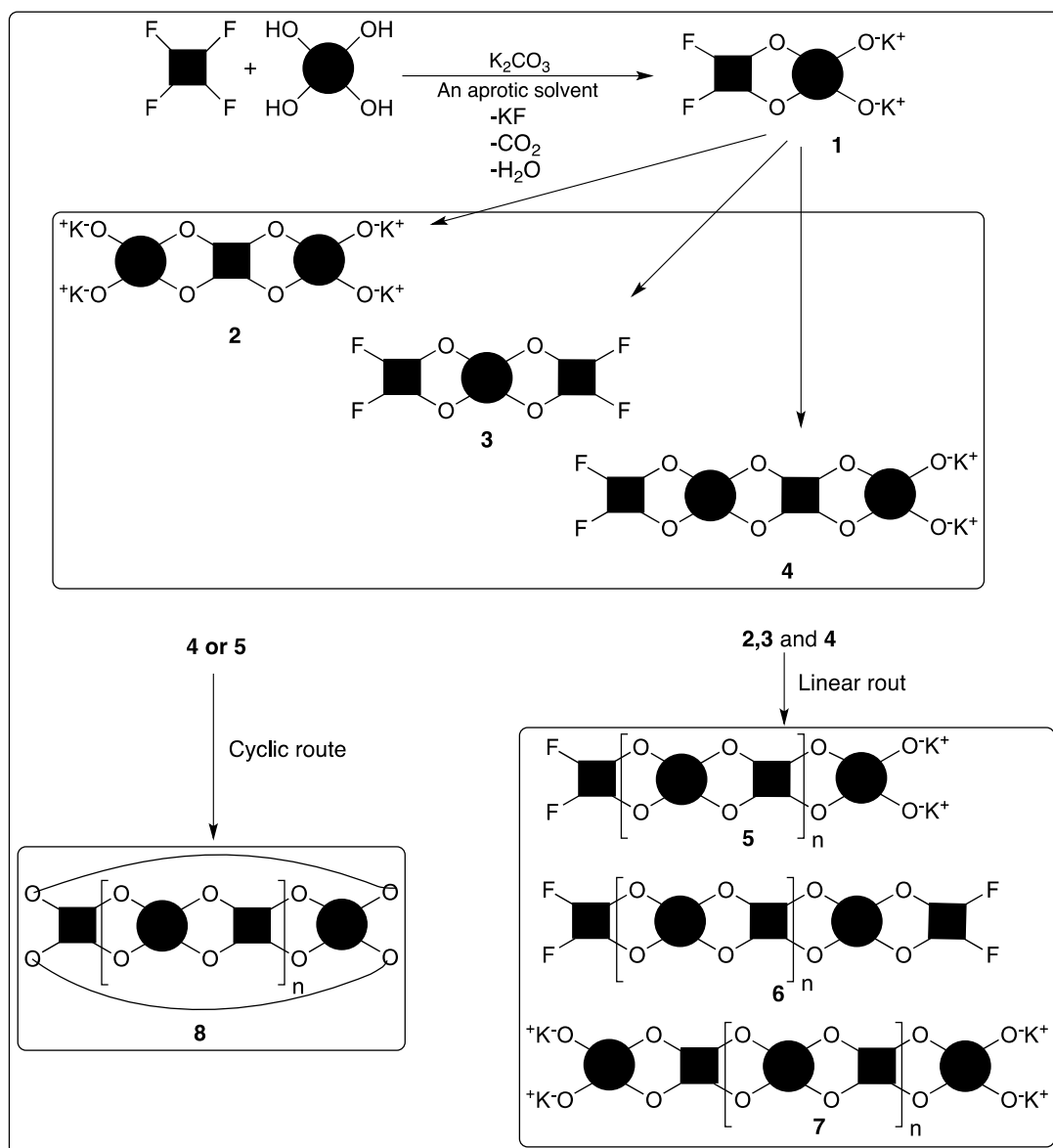


Figure 2-2. Hypothetical routes of PIM-1 polymerization.

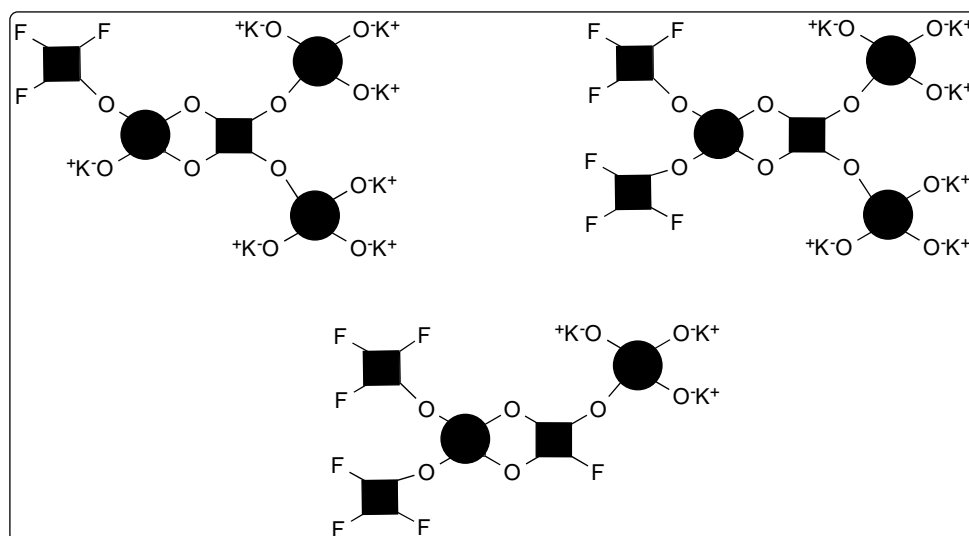


Figure 2-3. Potential formation of branched centres in PIM-1 polymerization.

A suitable characterization method to assign cyclic and terminal ends is MALDI-ToF spectroscopy. However, MALDI-ToF is used to characterize only low-molecular weight regions (up to ca. 10000 m/z).

The Ruggli-Ziegler dilution principle states that the average molecular weight values of cyclic polymers decrease as the dilution of the mixture increases in the case of high conversion.⁴¹ Moreover, the participation of cyclic polymerization can be attributed to the flexibility of the polymer, as more rigid polymers tend to undergo cyclic-free polymerization.⁴⁰ In addition, polycondensation of high conversion (*i.e.* > 99%) tends to produce a majority of cyclic polymer, which is a concentration-independent phenomenon.⁴²

Kricheldorf states that cyclization competes with linear-ladder polymer formation at any step of polymerization and any concentration. This cyclic polymerization can affect methods of synthesis of two types: kinetically controlled polycondensation (KCP) and thermodynamically controlled polycondensation (TCP). KCP is polymerization associated with non-equilibrium reactions and rapid product formation. The alternative, TCP, is associated with rapid equilibrium reactions of polycondensation. However, Kricheldorf concludes that in the case of high conversion, neither TCP nor KCP is able to prevent cyclization occurring at any concentration.^{40–44}

2.1.2 Characterization of PIM-1 microporosity

Generally, porous materials have been considered in terms of their adsorption properties. Adsorption is simply the condensation of a gas on the accessible free surface of a bulk volume. However, a common measurement of adsorption or simply sorption is the gas uptake, which does not take account of the physical mechanism of uptake.⁴⁵

The sorption of N₂ in PIM-1 can be quantified through its sorption isotherm, which shows the amount of N₂ uptake at constant temperature and measured pressure, after the sample has been prepared by degassing. The adsorption isotherm

is commonly used in surface area calculations, because adsorption is considered to be more sensitive than desorption.

This is a volumetric technique by which the number of moles of adsorbed molecules (n_m) required to cover in a monolayer the surface of the adsorbent is simply multiplied by the area occupied by the adsorbed molecules (A_m) (which is 0.162 nm for N₂) and the Avogadro number (N). Thus, the surface area (S_A) is given Equation 2-1:

$$S_A = n_m * A_m * N \quad (2-1)$$

Therefore, the specific surface area (S_{SA}) can be found by normalizing the (S_A) to the sample mass, as shown in Equation 2-2:

$$S_{SA} = \frac{n_m * A_m * N}{m} \quad (2-2)$$

In this volumetric technique, the adsorbed molecules form layers which cover the surface of the adsorbent material. The number of layers increases as the pressure is increased.

The BET surface area can be determined by this method. The BET model is derived from Langmuir theory, which quantifies the adsorption of monolayer coverage. It is based on multilayer adsorption on a homogeneous surface, as represented by Equation 2-3

$$v = \frac{v_m * c * p}{(p_0 - p) * (1 + (c - 1) * (\frac{p_0}{p}))} \quad (2-3)$$

This can be rearranged to the following linear form:

$$\frac{p}{v * (p_0 - p)} = \frac{1}{v_m * c} + \frac{c - 1}{v_m * c} * \frac{p}{p_0} \quad (2-4)$$

where v is the adsorbed volume at a specific pressure, v_m is the adsorbed volume that is required to form a monolayer, c is the BET constant, p_0 and p are the saturation and equilibrium pressures respectively.

It is worth mentioning that the Langmuir theory is applied here to each individual layer, whereas no interactions between layers are involved. In addition, note that the BET equation shows a linear relationship when $p/v * (p_0 - p)$ is plotted against p/p_0 only when the relative pressure remains within a particular range of fairly low values.⁴⁶

Furthermore, gas sorption data can be used to classify materials in terms of their porosity. The IUPAC convention classifies six possible types of porous material by their sorption isotherms (Figure 2-4).⁴⁷

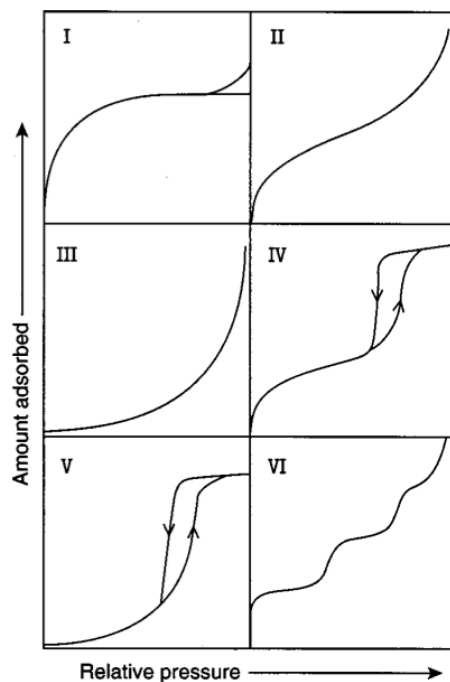


Figure 2-4. Six types of sorption isotherms giving the IUPAC classification of porous materials. Adapted from Barton et al.⁴⁵

Types I, II and IV shown in Figure 2-4 are associated with microporous materials, nonporous or macroporous materials, and mesoporous materials respectively. Types III and V are associated with macroporous and mesoporous materials; these phenomena are attributed to the higher interaction energy between

adsorbate and adsorbent molecules than the interaction energy between adsorbate molecules. Type VI is associated with uniform nonporous materials.

Budd *et al.*^{2, 48} also investigated the high free volume properties of PIM-1, using various measurement techniques such as positron annihilation lifetime spectroscopy (PALS), ¹²⁹Xe NMR, N₂ sorption and Xe sorption. In this work, N₂ sorption at 77 K was used to calculate the BET surface area.

2.2 Experimental

2.2.1 Materials

Tetrafluoroterephthalonitrile (TFTPN, 98%, Aldrich) was purified by sublimation; it was heated to around 150 °C and the pure product collected without vacuum was used in the preparation of PIM-1 batches KA1 and KA1-3. Another batch of TFTPN (98%, Aldrich) was used as received to prepare PIM-1 batch KA1-4. 5,5',6,6'-Tetrahydroxy-3,3,3',3'-tetramethyl-1,1'-spirobisindane (TTSBI, 98%, Alfa Aesar) was dissolved in methanol and reprecipitated from dichloromethane before use. Anhydrous K₂CO₃ (99.0%, Fisher) was dried in an oven at 110 °C overnight before use. Anhydrous dimethylformamide (DMF), anhydrous dimethylacetamide (DMAc), toluene and methanol (MeOH) were purchased from Sigma-Aldrich and used as received.

2.2.2 Methods

Gel-permeation chromatography (GPC) measurements were carried out on a Viscotek GPC max VE 2001 instrument, with tetrahydrofuran as solvent at a flow rate of 1 cm³ min⁻¹ and injection volume of 100 µL, using two PL mixed-B columns and a Viscotek VE3580 refractive index detector. Calibration was performed with polystyrene standards of known molar mass.

All NMR spectra were recorded at 400 MHz using a Bruker 400 MHz spectrometer and CDCl₃ as solvent. For NMR sample preparation, PIM-1 (≈ 5 mg) was dissolved in CDCl₃ (Aldrich, 99.8% atom D) and transferred into a 5 mm NMR tube.

UV-Vis absorption measurements were recorded on a Cary 60 UV-Vis spectrophotometer, in chloroform at room temperature.

Elemental analysis was performed on a Carlo Erba Instruments EA1108 elemental analyzer.

Matrix-Assisted Laser Desorption/Ionisation – Time of Flight (MALDI-TOF) spectroscopy was performed on a Shimadzu Axima Confidence instrument using dithranol as the matrix by Mr. Gareth Smith at the University of Manchester, School of Chemistry.

N₂ adsorption/desorption isotherms and BET surface areas were obtained from powders at 77 K, using a Micromeritics ASAP 2020 instrument. Samples were degassed before measurement for 16 h at 120 °C under high vacuum. After cooling, degassed samples were reweighed, and placed in the analysis port. Further degassing was performed at sample run under high vacuum at 120 °C for 2 h. The apparent surface area was calculated from N₂ adsorption data by multi-point Brunauer-Emmet-Teller (BET) analysis. The free space of the samples tube was measured after analysis.

All infrared spectra were recorded for solid samples using a Biorad FTS 6000 spectrometer with an attenuated total reflectance (ATR) accessory. Samples were measured with 16 times scans.

Thermogravimetric analysis (TGA) was carried out on a TGA Q5000 V3.15 Build 263, under atmospheric nitrogen at a heating rate of 10.00 °C min⁻¹ from 30 to 800 °C, using a pan of Platinum-HT.

2.2.3 Synthesis of PIM-1 at low temperature

Batch KA1

The monomers TTSBI (29.32 mmol, 9.98 g) and TFTPn (29.33 mmol, 5.87 g) were transferred into a three-necked round-bottomed flask and dissolved in dry DMF (200 mL) in the presence of potassium carbonate (10.20 g). The reaction mixture was heated to 65 °C for 75 h under an inert atmosphere of nitrogen, then cooled to room temperature for half an hour. The crude polymer was poured into water (300 mL). Following this, the polymer was filtered and washed with 1,4-

dioxane (500 mL), acetone (100 mL), water (100 mL) and finally acetone (100 mL). The final product was then dried at 110 °C overnight under vacuum. A yellow solid was obtained (12.56 g, 93%). ¹H NMR (400 MHz, CDCl₃): δ 6.74 (br. s, 2H), 6.35 (br. s, 2H), 2.26-2.09 (br. m, 4H), 1.53-1.23 (br. m, 12H). GPC: conc. 1 mg mL⁻¹, $M_w = 76 \times 10^3$ g mol⁻¹, $M_n = 22 \times 10^3$ g mol⁻¹, $M_w/M_n = 3.4$. IR (ATR; cm⁻¹): 3000-2800, 2238, 1443, 1262, 1107, 1009, 751.

2.2.4 Synthesis of PIM-1 at high temperature

Batch KA1-1

TFTPN (2 g, 1 mmol), TTSEBI (3.4 g, 1 mmol), anhydrous K₂CO₃ (4.14 g, 3 mmol), DMAc (20 mL) and toluene (10 mL) were added to a round-bottomed flask with mechanical stirrer, nitrogen inlet and a Dean-Stark trap. After the solution mixture had been refluxed at 155 °C for 40 min, the viscous solution obtained was added to methanol. The yellow product was dissolved in chloroform and reprecipitated from methanol. Further purification was carried out by refluxing the precipitate in deionized water overnight, then drying out overnight in a vacuum oven at 110° C to give PIM-1 (4.2 g, 91%). GPC: $M_w = 170 \times 10^3$ g mol⁻¹, $M_n = 43 \times 10^3$ g mol⁻¹, $M_w/M_n = 3.8$. ¹H NMR (400 MHz; CDCl₃): δ 6.81 (br, s, 2H), 6.42 (br, s, 2H), 2.33 (br, s, 2H), 2.17 (br, s, 2H), 1.36 (br, s, 6H), 1.31 (br, s, 6H). IR (ATR; cm⁻¹): 3000-2800, 2238, 1443, 1262, 1107, 1009, 751. Elemental analysis, calculated for C₂₉H₂₀N₂O₄ (wt.%): C, 75.64; H, 4.38; N, 6.08. Found: C, 71.99; H, 4.17; N, 6.02.

Batch KA1-4

To a 1000 mL round-bottomed flask TFTPN (40.02 g, 0.2 mol), TTSEBI (68.08 g, 0.2 mol) and potassium carbonate (82.8 g, 0.6 mol) were added. The mixture was stirred mechanically under nitrogen for one hour. Thereafter, DMAc (400 mL) and toluene (200 mL) were added to the mixture, before it was refluxed at 160 °C for 40 min. After polymerization, the hot mixture was poured into 1500 mL of methanol to precipitate the product, which was filtered and dissolved in chloroform, then reprecipitated from methanol twice to give 75 g of PIM-1 (82%). To remove low-molecular-weight polymer, a 1,4-dioxane wash (200 mL) was applied. GPC: $M_w = 92 \times 10^3$ g mol⁻¹, $M_n = 23 \times 10^3$ g mol⁻¹, $M_w/M_n = 3.9$. ¹H NMR

(400 MHz; CDCl₃): δ 6.81 (s, 2H), 6.42 (s, 2H), 2.32 (s, 2H), 2.15 (s, 2H), 1.36 (s, 6H), 1.30 (s, 6H). IR (ATR; cm⁻¹): 3000-2800, 2238, 1443, 1262, 1107, 1009, 751. Elemental analysis, calculated for C₂₉H₂₀N₂O₄ (wt.%): C, 75.64; H, 4.38; N, 6.08. Found: C, 74.03; H, 4.34; N, 5.89.

2.3 Results and discussion

PIM-1 was prepared via step-growth polymerization, which is carried out with the use of four functional groups of each monomer (i.e. four fluorines or four hydroxyls as functional groups). This requires the systematic reactivity of a pair of functional groups on each monomer to ensure that a double aromatic nucleophilic substitution (S_NA_r) takes place, in order to form dibenzodioxane linkages. The presence of a base promotes the deprotonation of a hydroxyl group to give an oxyanion, which attacks a fluorine-attached carbon atom. This step is facilitated by an electron-withdrawing group (i.e. CN), which is attached to the aryl ring, via stabilization of the intermediate compound. Therefore, S_NA_r is proposed to occur in two steps (Figure 2-5).

Forming dibenzodioxane linkages demonstrates successful PIM-1 construction. However, it is important to consider the influence on high-molecular-weight PIM-1 preparation of several factors, such as the presence of the relevant base, temperature, polymerization time and monomer purity. The presence of an aprotic solvent also plays a key role in the solvation of intermediate salts. However, DMF is shown to be an optimum solvent system that produces high average-molar mass polymer and higher yield over other solvents such as NMP, DMSO and sulfolane.⁴⁰ In the HTM, DMAc has a similar efficiency to that of DMF in the polymerization, but with more thermal stability. The small amount of water as a by-product can also enhance the solubility of intermediate salts. It is believed that initial dimer salts are more reactive than monomer salts due to the dissolution effect.³⁷ Therefore, optimization conditions were studied to produce high-quality PIM-1 at low preparation cost.

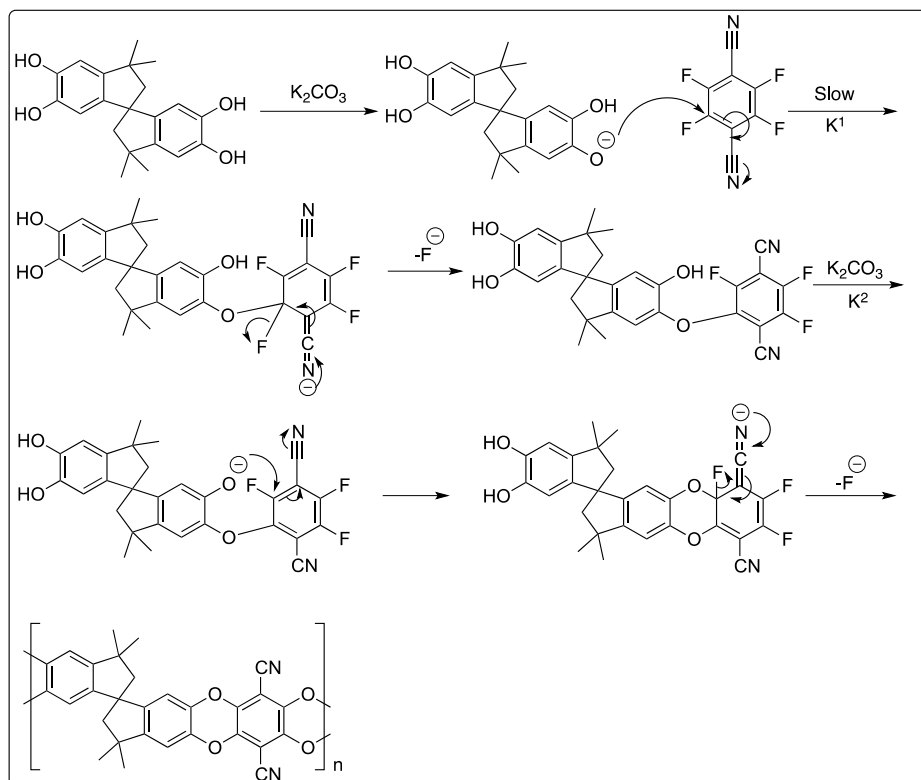


Figure 2-5. Proposed reaction mechanism of dibenzodioxane linkages in PIM-1 synthesis.

The LTM was used to prepare PIM-1 (KA1) using a magnetic bar stirrer to take advantage of the dilute condition. The polymer was washed with 1,4-dioxane to remove low molecular weight and cyclic polymers. However, GPC results show a shoulder on the molecular weight distribution (Figure 2-6), which is attributed to the presence of some low molecular weight and cyclic polymers. Nevertheless, this polymer was found to be capable of forming film by slow evaporation (for three days) of polymer solution in chloroform.

KA1-1 and KA1-4 were prepared by the HTM. In the preparation of the latter batch, any water produced from carbonic acid decomposition was not removed from the reaction mixture, but this did not prevent the production of high-molecular-weight polymer. This can be attributed to the fact that the polymerization is not strongly influenced by the extraction of water. In both batches, yellow and film-forming polymers were obtained, and GPC results for both batches revealed high-molecular-weight polymers (Figure 2-6).

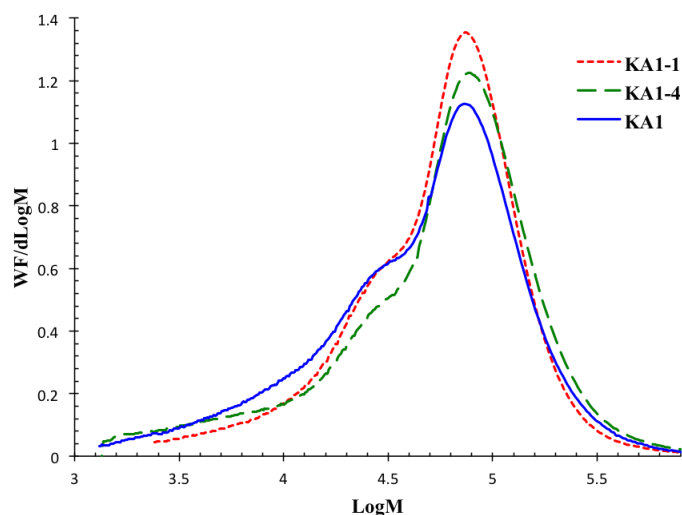


Figure 2-6. GPC traces of KA1-1, KA1-4 and KA1 polymers.

Overall, both methods seem to provide high values of polydispersity index ($PDI = M_w/M_n$). In order to reduce the PDI, 1,4-dioxane washing is required to remove low-molecular-weight polymers. 1,4-Dioxane washing was performed for KA1 and KA1-4, but not for the KA1-1 batch.

For these batches, the LTM produced polymer of lower average molecular weight ($M_w < 80 \times 10^3 \text{ g mol}^{-1}$) than the HTM ($M_w > 90 \times 10^3 \text{ g mol}^{-1}$).

MALDI-Tof mass spectrometry showed the presence of cyclic PIM-1 in polymer produced by both methods (Figure 2-7 and Figure 2-8). These cyclic polymers were observed in mixtures of two different dilutions: KA1 monomer concentration ≈ 0.15 molar; KA1-4 monomer concentration ≈ 0.3 molar.

The high PDI values of all polymers produced by both methods might be ascribed to the presence of cyclic polymerization competing with linear polymerization.

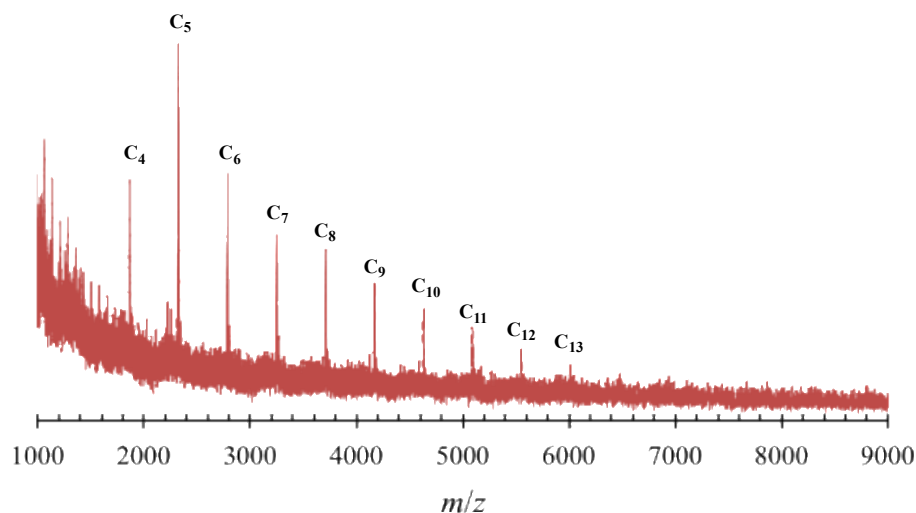


Figure 2-7. MALDI-ToF spectrum of PIM-1 produced by LTM (Batch KA1), showing cyclic-PIM-1 oligomers. Cyclic-PIM-1 = $C_n = 460$ (repeating-unit mass of PIM-1) \times n (number of repeating units) + 23 (Na^+ mass).

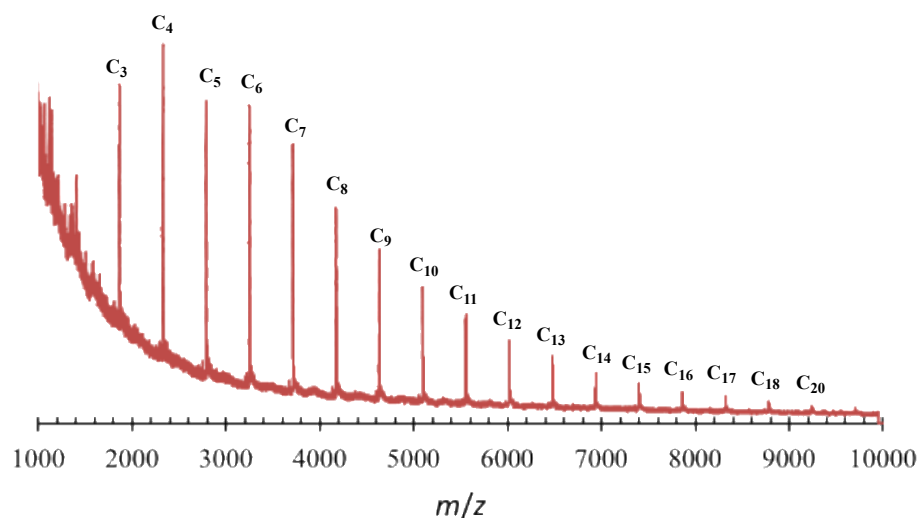


Figure 2-8. MALDI-ToF spectrum of PIM-1 produced by HTM (Batch KA1-4), showing cyclic-PIM-1 Oligomers. Cyclic-PIM-1 = $C_n = 460$ (repeating-unit mass of PIM-1) \times n (number of repeating units) + 23 (Na^+ mass).

^1H NMR spectroscopy for all batches confirmed typical PIM-1 polymer, as shown in Figure 2-9. The methyl groups in the repeating unit (H^a) represent two different peak environments and show two singlets peaks of six aliphatic protons. H^b have two singlet peaks are correlated with two different proton environments of

methylene groups. Finally, H^c are aromatic protons of two different chemical environments. The integration of each peak also quantifies the proton number in the PIM-1 backbone.

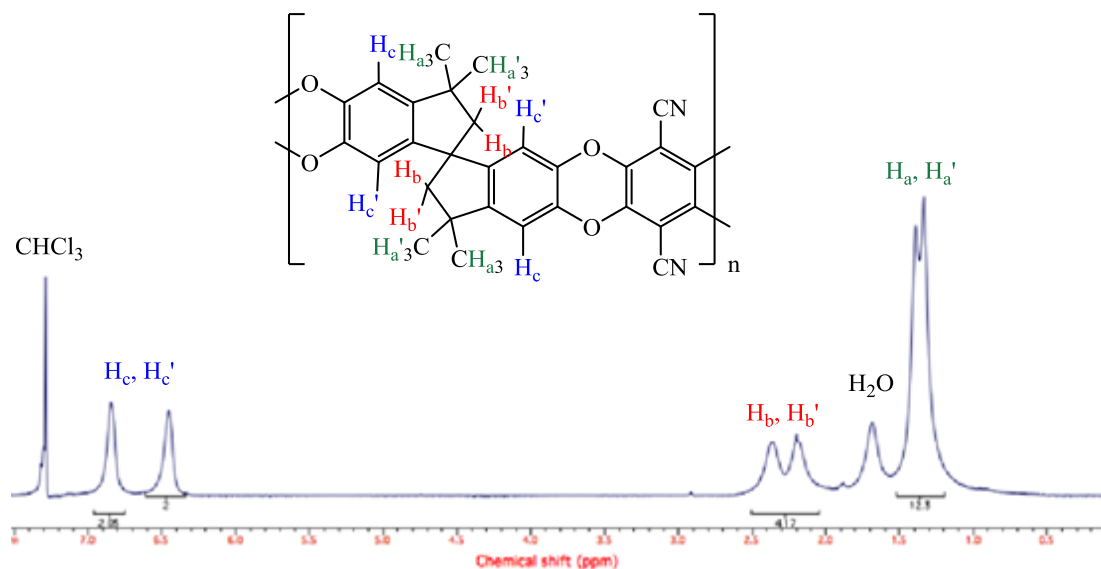


Figure 2-9. ¹H NMR spectroscopy of PIM-1.

The TGA thermogram (Figure 2-10) shows a weight loss of about 4.7% below 160 °C, which is attributed to moisture or residual solvent. The polymer degrades above *ca.* 450 °C.

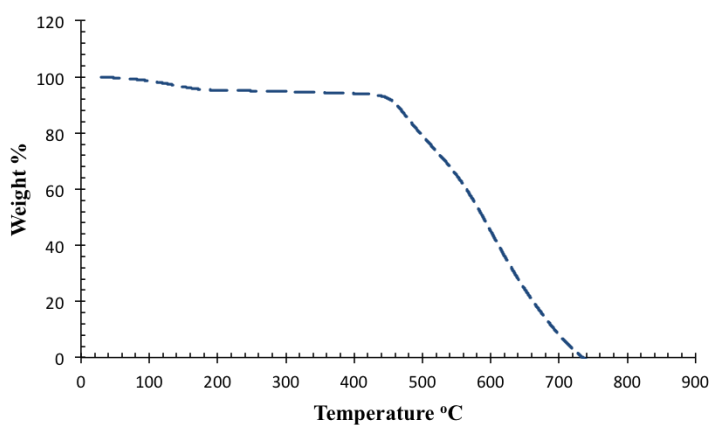


Figure 2-10. TGA thermogram of KA1-4.

The surface area of KA1-4 was measured via its nitrogen adsorption/desorption isotherm (Figure 2-11). Its BET surface area of approximately $700 \text{ m}^2 \text{ g}^{-1}$ is in the typical range of PIM-1 surface area.

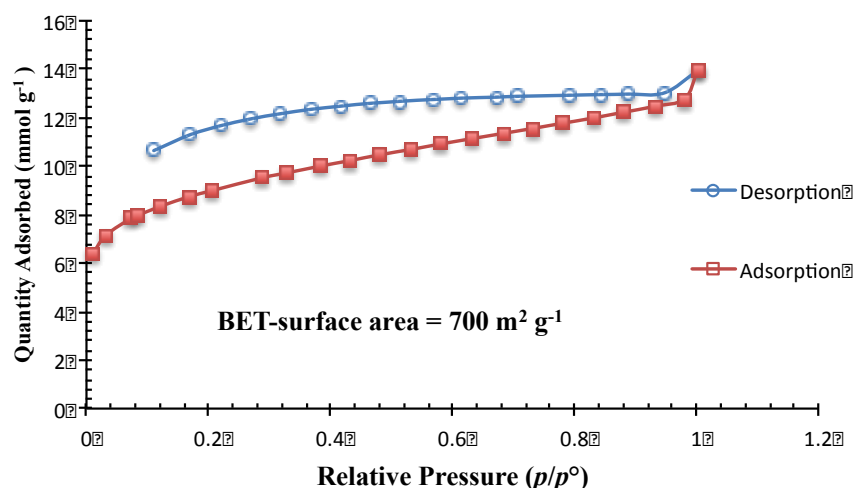


Figure 2-11. Nitrogen sorption isotherm of PIM-1 at 77 K; nitrogen adsorption (filled squares) and desorption (empty circles).

2.4 Conclusion

Both high and low temperature methods can be used to produce film-forming PIM-1. The HTM, which was performed successfully in large-scale production without using a Dean-Stark trap, has advantages over the LTM, such as taking less time and consuming less solvent.

Overall, the divergent conditions of both methods towards optimum temperature and concentration can be established via close consideration of the nature and complexity of polymerization, such as the relative involvement of cyclization or crosslinking products and inactive low-molecular-weight PIM-1. For instance, compatible solvents were chosen for each temperature: DMAc for the HTM and DMF for the LTM. Both solvents effectively maintained the sufficient solubility of intermediate salts during polymerization.

It is suggested that an optimum method to reduce PDI may be several washings with 1,4-dioxane. On the other hand, avoiding cyclic production can be an inefficient approach to polymerization, as illustrated by the work of Kricheldorf.

Despite those problematic aspects of PIM-1 preparation, PIM-1 is still believed to be a competitive candidate in the area of porous polymeric materials and membranes, owing to its properties such as high surface area, high thermal stability, membrane formation, easy processability and promising permselectivity, as will be shown in the following chapters.

2.5 References

- (1) McKeown, N. B., *Phthalocyanine Materials: Synthesis, Structure and Function*; CUP: Cambridge, UK, 1998, pp 12-144.
- (2) McKeown, N. B. *ISRN Mater. Sci.* **2012**, 2012, 16.
- (3) McKeown, N. B.; Li, H.; Makhseed, S. In *Supported Catalysts and Their Applications*; Royal Society of Chemistry: Cambridge, 2001, pp 214–218.
- (4) McKeown, N. B.; Budd, P. M. *Chem. Commun.* **2002**, 44, 2780.
- (5) Makhseed, S.; Al-Kharafi, F.; Samuel, J.; Ateya, B. *Catal. Commun.* **2009**, 10, 1284.
- (6) Mackintosh, H. J.; Budd, P. M.; McKeown, N. B. *J. Mater. Chem.* **2008**, 18, 573.
- (7) McKeown, N. B.; Hanif, S.; Msayib, K.; Tattershall, C. E.; Budd, P. M. *Chem. Commun.* **2002**, 44, 2782.
- (8) McKeown, N. B.; Budd, P. M. *Chem. Soc. Rev.* **2006**, 35, 675.
- (9) Budd, P. M.; McKeown, N. B.; Fritsch, D. *J. Mater. Chem.* **2005**, 15, 1977.
- (10) Budd, P. M.; Elabas, E. S.; Ghanem, B. S.; Makhseed, S.; McKeown, N. B.; Msayib, K.; Tattershall, C. E.; Wang, D. *Adv. Mater.* **2004**, 5, 2002.
- (11) Budd, P. M.; Ghanem, B. S.; Makhseed, S.; McKeown, N. B.; Msayib, K. J.; Tattershall, C. E. *Chem. Commun. (Camb)*. **2004**, 2, 230.
- (12) Du, N.; Robertson, G. P.; Pinnau, I.; Guiver, M. D. *Macromolecules* **2009**, 42, 6023.
- (13) Carta, M.; Msayib, K. J.; Budd, P. M.; McKeown, N. B. *Org. Lett.* **2008**, 10, 2641.
- (14) Carta, M.; Msayib, K. J.; McKeown, N. B. *Tetrahedron Lett.* **2009**, 50, 5954.
- (15) Du, N.; Robertson, G. P.; Song, J.; Pinnau, I.; Guiver, M. D. *Macromolecules* **2009**, 42, 6038.
- (16) Mason, C. R.; Maynard-Atem, L.; Al-Harbi, N. M.; Budd, P. M.; Bernardo,

- P.; Bazzarelli, F.; Clarizia, G.; Jansen, J. C. *Macromolecules* **2011**, *44*, 6471.
- (17) Du, N.; Park, H. B.; Robertson, G. P.; Dal-Cin, M. M.; Visser, T.; Scoles, L.; Guiver, M. D. *Nat. Mater.* **2011**, *10*, 372.
- (18) Patel, H. A.; Yavuz, C. T. *Chem. Commun.* **2012**, *48*, 9989.
- (19) Mason, C. R.; Maynard-Atem, L.; Heard, K. W. J.; Satilmis, B.; Budd, P. M.; Friess, K.; Lanč, M.; Bernardo, P.; Clarizia, G.; Jansen, J. C. *Macromolecules* **2014**, *47*, 1021.
- (20) Ghanem, B. S.; McKeown, N. B.; Budd, P. M.; Selbie, J. D.; Fritsch, D. *Adv. Mater.* **2008**, *20*, 2766.
- (21) Ghanem, B. S.; McKeown, N. B.; Budd, P. M.; Al-Harbi, N. M.; Fritsch, D.; Heinrich, K.; Starannikova, L.; Tokarev, A.; Yampolskii, Y. *Macromolecules* **2009**, *42*, 7881.
- (22) Weber, J.; Su, Q.; Antonietti, M.; Thomas, A. *Macromol. Rapid Commun.* **2007**, *28*, 1871.
- (23) Tanaka, K.; Okano, M.; Toshino, H.; Kita, H.; Okamoto, K. I. *J. Polym. Sci. B*. **1992**, *30*, 907.
- (24) Ma, X.; Swaidan, R.; Belmabkhout, Y.; Zhu, Y.; Litwiller, E.; Jouiad, M.; Pinnau, I.; Han, Y. *Macromolecules* **2012**, *45*, 3841.
- (25) McKeown, N. B.; Budd, P. M. *Encycl. Membr. Sci. Technol.* **2012**, *14*, 1.
- (26) Bezzu, C. G.; Carta, M.; Tonkins, A.; Jansen, J. C.; Bernardo, P.; Bazzarelli, F.; McKeown, N. B. *Adv. Mater.* **2012**, *24*, 5930.
- (27) Carta, M.; Malpass-Evans, R.; Croad, M.; Rogan, Y.; Jansen, J.; Bernardo, P.; Bazzarelli, F.; McKeown, N. B. *Science*. **2013**, *339*, 303.
- (28) Patel, H. a.; Yavuz, C. T. *Chem. Commun.* **2012**, *48*, 9989.
- (29) Adymkanov, S. V.; Yampol'skii, Y. P.; Polyakov, a. M.; Budd, P. M.; Reynolds, K. J.; McKeown, N. B.; Msayib, K. *J. Polym. Sci.* **2008**, *50*, 444.
- (30) Priske, M.; Baumgarten, G.; Lueken, H. G., Method for enriching a homogeneous catalyst from a process flow. US 0046503A1, 2012.
- (31) Wang, Y.; McKeown, N. B.; Msayib, K. J.; Turnbull, G. a.; Samuel, I. D. W. *Sensors* **2011**, *11*, 2478.
- (32) Rakow, N. a; Wendland, M. S.; Trend, J. E.; Poirier, R. J.; Paolucci, D. M.; Maki, S. P.; Lyons, C. S.; Swierczek, M. J. *Langmuir* **2010**, *26*, 3767.
- (33) Thomas, J. C.; Trend, J. E.; Rakow, N. a; Wendland, M. S.; Poirier, R. J.; Paolucci, D. M. *Sensors* **2011**, *11*, 3267.

- (34) Manchester polymer helps protect people at work <http://umip.com/manchester-polymer-helps-protect-people-work/> (accessed Sep 15, 2015).
- (35) Cox, T. I.; Gb, M.; Ian, C. (12) United States Patent. US 08137979, 2012.
- (36) Hobson, S. T.; Cemalovic, S.; Patel, S. V. *Analyst* **2012**, *137*, 1284.
- (37) Naiying, D.; Jingshe, S.; Robertson, G. P.; Pinnau, I.; Guiver, M. D. *Macromol. Rapid Commun.* **2008**, *29*, 783.
- (38) Du, N.; Robertson, G. P.; Song, J.; Pinnau, I.; Thomas, S.; Guiver, M. D. *Macromolecules* **2008**, *41*, 9656.
- (39) Kricheldorf, H. R.; Fritsch, D.; Vakhtangishvili, L.; Lomadze, N.; Hamburg, D. *Society* **2006**, 4990–4998.
- (40) Kricheldorf, H. R.; Lomanze, N.; Fritsch, D.; Schwarz, G. *J. Polym. Sci. Part A-Polymer Chem.* **2006**, *44*, 5344.
- (41) Kricheldorf, H. R.; Schwarz, G. *Macromol. Rapid Commun.* **2003**, *24*, 359.
- (42) Kricheldorf, H. R.; Fritsch, D.; Vakhtangishvili, L.; Schwarz, G. *Macromol. Chem. Phys.* **2005**, *206*, 2239.
- (43) Kricheldorf, H. R. *Macromol. Rapid Commun.* **2008**, *29*, 1695.
- (44) Kricheldorf, H. R. *J. Polym. Sci. Part A-Polymer Chem.* **2010**, *4*, 251.
- (45) Barton, T. J.; Bull, L. M.; Klemperer, W. G.; Loy, D. a.; McEnaney, B.; Misono, M.; Monson, P. a.; Pez, G.; Scherer, G. W.; Vartuli, J. C.; Yaghi, O. M. *Chem. Mater.* **1999**, *11*, 2633.
- (46) Brunauer, S.; Emmett, P. H.; Teller, E. *J. Am. Chem. Soc.* **1938**, *60*, 309.
- (47) Sing, K. S. W.; Everett, D. H.; Haul, R. a. W.; Moscou, L.; Pierotti, R. a.; Rouquérol, J.; Siemieniewska, T. *Pure Appl. Chem.* **1985**, *57*, 603.
- (48) Emmmler, T.; Heinrich, K.; Fritsch, D.; Budd, P. M.; Chaukura, N.; Ehlers, D.; Rätzke, K.; Faupel, F. *Macromolecules* **2010**, *43*, 6075.

Chapter 3 Preparation and characterization of graphene and GPMMMs

3.1 Introduction

Graphene has been the subject of widespread interest because of its superior properties. It has become a major area of study for developers of electronic devices because of its high conductivity, transparency and sheet flexibility, as well as its high thermal and chemical stability. Moreover, single layer graphene has high surface area (theoretically $2630 \text{ m}^2 \text{ g}^{-1}$) and strong adsorption of gases, organic molecules or metallic ions.^{1,2,3} These characteristic properties are also important for developing composite materials.^{4,5} Graphene composites have many potential environmental applications.^{6,7}

Graphene is defined as individual sheets of sp^2 -bonded carbon forming two-dimensional lattices of honeycomb structure. It is also known as the thinnest material that could exist in the universe, because it is only one atom thick.^{8,9} Since graphene is a crystalline form of carbon, which can pack together through π - π bond interaction to form natural graphite, a common method of preparing graphene is via exfoliation from natural graphite. The exfoliation concept is based on disturbing the π - π interaction between individual layers among three-dimensional graphite lattices in order to obtain individual graphene layers.

This is known as a top-down approach to preparation, because it starts with large units of graphite, which are fractionated into subunits of graphene. This approach was demonstrated in 2004 by Novoselov and his co-workers and named “micromechanical cleavage”.^{10,11} Their method successfully extracts single layers of graphene from graphite. This observation confirms that graphite is constructed from graphene layers that are packed together via weak physical interactions (i.e.; π - π interactions). The slippery nature of graphite layers on paper is also attributed to the weakness of these interactions between layers.

Based on the same concept by which graphene can be obtained from natural graphite, by overcoming the interlayer interactions, several preparation methods have been developed and investigated.

Recent research has investigated the surface modification of graphene to prevent agglomeration, which can impair its preparation, and to enhance the stability of graphene and polymer/graphene compatibility.¹² This approach of surface

modification can be achieved through the direct modification of graphene or graphene oxide, which can be performed via covalent bonds.¹³ GO can also undergo chemical conversion to give functionalized graphene.⁴⁴ Much work has been carried out to functionalize graphene, such as amination, esterification and isocyanate modification.^{14,15,13}

Other methods of graphene preparation are concerned with the incorporation of small molecules, charged ions or macromolecules like polymers in order to weaken the interactions between graphene layers and produce them in appropriate stable forms with higher graphene content.^{16,17,18,19,20} These methods are based on utilizing non-covalent bonds to make surface modifications. The most prominent method that can be applied is the liquid phase exfoliation (LPE). This method is typically aided by sonication. In general, this process undergoes three steps. The first is graphite dispersion in a solvent. The second, graphene exfoliation and finally purification.²¹

It is worth considering the application of solubility theory to LPE. According to solubility theory, graphene layers can be dispersed in the liquid phase when the free energy of mixing is negative. The free energy of mixing $\Delta\bar{G}_{mix}$ can be calculated from Equation 3-1:

$$\Delta\bar{G}_{mix} = \Delta\bar{H}_{mix} - T\Delta\bar{S}_{mix} \quad (3-1)$$

Where $\Delta\bar{H}_{mix}$ is the enthalpy of mixing, T is the absolute temperature and $\Delta\bar{S}_{mix}$ is the entropy of mixing.

The increase of entropy on LPE can help to increase the degree of dispersion. However, the entropy contribution of large graphene layers can be small, which would not minimize the free energy of mixing.²² Therefore, the enthalpy of mixing should be small, to ensure the desired dispersion of the graphene layers.²² This can be achieved with a good liquid phase of correct Hansen parameters. These three parameters are dispersive (δ_D), polar (δ_P) and hydrogen bonding (δ_H). The sum of the squares of each of the parameters gives the square of the Hildebrand solubility parameter, δ_T (Equation 3-2). The square root of the Hildebrand solubility parameter is expressed as cohesive energy density per unit volume, which means the energy per

unit volume of a component that is needed to disassociate components from each other. In other words, the solubility parameters of all components in the LPE system must match or be close to each other in order to minimize the energy cost of dispersion.

$$\delta_T^2 = \delta_D^2 + \delta_P^2 + \delta_H^2 \quad (3-2)$$

The enthalpy of mixing graphene per volume of liquid phase can be expressed as in Equation 3-3:

$$\frac{\Delta \bar{H}_{mix}}{V_{mix}} \approx \frac{4}{D} (\delta_{graphene} - \delta_{liquid\ phase})^2 \phi \quad (3-3)$$

where D is the diameter of the graphene molecule and ϕ is the volume fraction of graphene. δ of graphene or liquid phase is equal to the square root of surface energy.²³ The surface energy can determine the surface tension (γ) parameter, as can be found from the solubility Equation 3-1 and expressed as Equation 3-4:

$$\gamma = \delta_{surface} - TS_{surface} \quad (3-4)$$

The surface tension of graphene was determined to be 40 mJ.m⁻².²³ Therefore, the optimum liquid phase for high graphene dispersibility should have a surface tension close to this value in order to ensure high stability and productivity. There are several solvents of matched or close surface tension values, such as *N*-methyl-2-pyrrolidone (NMP), DMF and DMAc, which are more favourable than other poorly dispersive solvents. Furthermore, in addition to solvents, other components can contribute to effective exfoliation and should be considered in this process, such as molecules, ions or polymers as solvent-enhanced additives and stabilizers.

In this project, chloroform is of interest owing to the processability requirements of PIM-1-based MMM preparations. PIM-1 can be dissolved in chloroform and the

solution used to exfoliate graphene via the LPE process. Therefore, the use of other solvents can be limited.

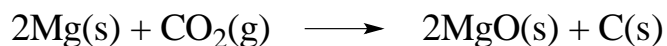
The discussion of Equations 3-4 makes it clear that in order to exfoliate graphene, an external energy source is required. Commonly, graphene is exfoliated with the aid of ultrasonic power; ultrasonic probes have been used in graphene preparation.^{24,25} LPE can also be performed in an ultrasonic bath. Researchers are well aware of the effect of intense cavitation during sonication.¹⁶ Therefore, it is necessary to consider sample shape, volume and position to ensure sufficient exfoliation.¹

However, graphene can also be exfoliated via non-ultrasonic processes. For example, various mixing processes have been used, such as wet or dry ball milling, electrochemical treatment and fluid dynamics.¹

As a consequence of the strong interest in graphene studies, a number of alternative methods have been developed to prepare graphene from non-graphite sources, most of which have taken a bottom-up approach. One attractive method of graphene preparation is chemical vapour deposition (CVD).²⁶ By this means, a relatively large area of pristine monolayer graphene is produced as a continuous lattice, which is attractive for electronic device applications. Graphene produced by the CVD method takes the form of a transparent film of high conductivity.²⁷ However, CVD is relatively costly, limiting its use in large-scale applications.

A number of other methods of graphene preparation that take a bottom-up approach involve the reduction of carbon-containing materials to produce few-layer graphene. Examples are igniting magnesium in dry ice, calcining aluminium sulphide (Al_2S_3) in carbon monoxide, and reducing calcium carbonate with magnesium powder.^{28,29,30}

Igniting magnesium in dry ice, first reported by Chakrabarti and his co-workers,²⁸ is a method of interest because it is cost effective and provide few-layer graphene as a major product. The proposed reaction of this conversion can be illustrated in the following scheme.



The mechanism of graphene formation by this method is still not entirely clear. Nonetheless, the high temperature that is generated during the reaction plays an undoubted role. It is believed that the retention time of forming sp^2 carbon prevents the formation of multi-layered graphene (i.e. graphite). In addition, few-layer graphene is kinetically favored.²⁸ Kelber et al.³¹ report an associated mechanism, growing graphene on MgO (111) by physical vapour deposition. Another model of graphene formation, proposed by King,³² states that the reaction may occur in two reaction zones of magnesium. The first is the outer shell, which converts the carbon dioxide to carbon monoxide and yields magnesium oxide. The second is the inner zone, which converts the carbon monoxide to graphene and gives magnesium oxide as a by-product.

In this work, we explored the exfoliation of graphene in organic solvents, particularly chloroform as a good solvent for PIM-1. In addition to the exfoliation of graphite, we exfoliated synthetic graphene (made by carbon dioxide conversion), graphene oxide (GO), base-washed graphene oxide (BWGO) and chemically reduced graphene oxide (r-GO) in PIM-1 solution.

3.2 Characterization of Graphene by Raman Spectroscopy

Precise nomenclature of graphene products must be addressed, before the introducing the use of Raman spectroscopy in graphene characterization. In the literature, the term ‘graphene’ has been applied to a wide range of graphitic materials. This uncertainty of nomenclature can cause confusion and raise problems in graphene applications. An approach to the nomenclature of graphene-based materials has recently been established.³³ The present work adopts this recommended classification.³⁴ Thus, graphene-based terminology is applied to all graphitic materials of 5 or fewer graphene layers. However, for greater precision, graphene whose flakes contain between two and ten layers is designated few-layer graphene (FLG), while single-layer graphene (SLG) is also known as monolayer graphene.

This approach to terminology allows a clear distinction between graphene and graphite composites, such as those using graphite nanoplatelets or exfoliated graphite, which consist of more than 10 graphene layers and whose thickness is less than 100 nm. Subsequently, classifying graphenic carbon materials enables us to examine the huge potential differences in their properties and applications. One important parameter which varies among such species is their obtainable surface area. For example, natural graphite has a lower specific surface area ($\approx 0.6 \text{ m}^2.\text{g}^{-1}$) than its modified derivatives, whereas SLG has the highest surface area ($\approx 2040 \text{ m}^2.\text{g}^{-1}$).^{35, 36, 37, 38}

Raman spectroscopy is among the more powerful techniques that can be used to characterize graphene samples, whether in pristine or functionalized form. This technique can determine layer number, functionality, defects and stacking order, which are important properties affecting the suitability of graphene for different applications. The Raman spectrum is highly sensitive to preparation conditions and provides an inexpensive, simple and useful quality control tool. Moreover, Raman spectroscopy can be used to follow the deformation of graphene in nanocomposite films.³⁹

A strong Raman spectrum is yielded even by monolayer graphene, as a result of the absence of a band gap, leading to the resonance of all incident wavelength radiation.³⁹ The spectrum can also be differentiated for monolayer graphene or some other determined number of stacked layers. Furthermore, Raman spectra can provide detailed information about atomic structure and electronic properties.

Generally, the Raman spectrum consists of three main bands: the 2D band (around 2650 cm^{-1}), the G band (around 1580 cm^{-1}) and the D band (around 1325 cm^{-1}). The D band corresponds to the presence of defects, which may be due to the edges, notches or functionality of graphene flakes as a result of the one-phonon process. The G band corresponds to vibration of the lattice of sp^2 carbon atoms, which increases in intensity as the number of layers increases. The 2D band is the second order of D, which corresponds to the dispersion of two phonons. All Raman signals are considered to be fingerprints that reflect structure and electronic properties. These signals can be evaluated according to their change in shape, position and relative intensity. However, the characteristic signals of materials are

commonly sensitive to charge impurities and induced strain in the case of composite fabrication.⁴⁰

Figure 3-1 offers an example of how clearly distinguishable are the spectra of graphene and graphite from NMP dispersion, demonstrating several characteristic differences along the spectra. It can be seen from this example that the 2D peaks of SLG and FLG are blueshifted relative to graphite and that reducing the number of layers gives narrower 2D signals, as a consequence of less splitting occurring from the phonon branches or electronic bands.²⁸ The intensity ratio between the D and G peaks is usually considered to correspond to the defect level. However, the defect signal can be associated either with basal-plane defects or with the formation of new edges, which is proportional to a reduction of flake size. Thus, the distinction between these forms of defect can be size dependent.⁴¹

More information can be obtained based on the 2D symmetry. SLG should show a highly symmetric and narrow 2D peak. The symmetry also should be found for FLG of restacked layers or random stacking, but with a broader 2D peak. In contrast, FLG of regular stacking (known as A-B stacking or Bernal stacking) is associated with an asymmetric and broad 2D peak.⁴² In order to distinguish between two different stacking orders, the 2D peak can be fitted with a Lorentzian lineshape and the coefficient of determination (R^2) can be calculated.

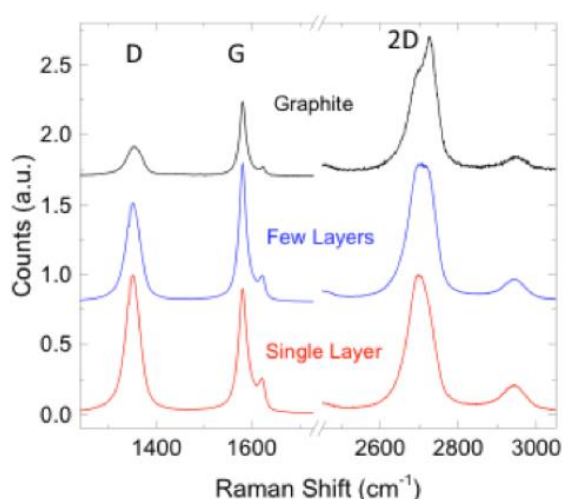


Figure 3-1. Typical Raman spectra of species obtained by liquid phase exfoliation of graphite in N-methyl-2-pyrrolidone (NMP), showing the differences in the shape of the 2D peak for single-layer graphene, few-layer graphene and graphitic species. Data were provided by Shin.

It is important to note that Raman spectroscopy is based on energy changes in a system which results from the interaction of incident photons with the system. Therefore, an external energy source is required to elicit such energy changes. This takes the form of a monochromatic light source, usually a laser.

Raman spectra are generated in particular by light scattering that is classified as inelastically scattered radiation, which can occur in two forms. One of these has lower energy relative to Rayleigh (elastic) scattering and is called Stokes Raman scattering, while the form which has higher energy is known as anti-Stokes Raman.

If the energy of the incident photon is insufficient to excite a molecule from the ground state to an electronic state, it will be excited to a virtual state. In this case, there are three possible phenomena: Rayleigh scattering occurs when the photon is scattered with no energy loss; in Stokes scattering the molecule loses the energy of the photon; alternatively, a small number of molecules which occupy higher vibrational levels can cause photon scattering with higher energy, i.e. anti-Stokes scattering (Figure 3-2).⁴³

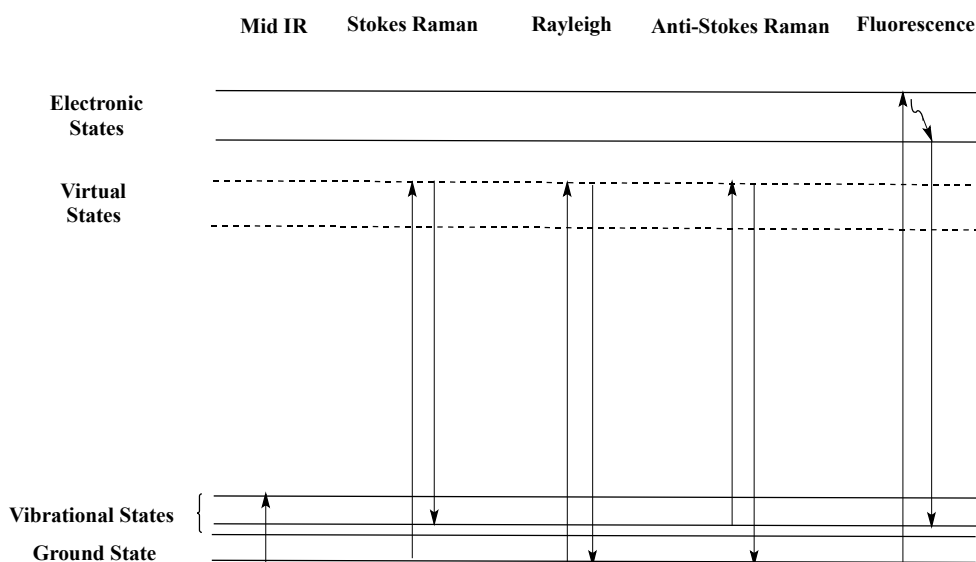


Figure 3-2. Jablonski energy diagram illustrating the different quantum descriptions of Raman scattering, Rayleigh scattering, infrared and fluorescence.⁴³

It is important to choose the appropriate laser wavelength for a Raman experiment. For instance, many organic-based materials are fluorescent in nature and the use of a green laser (533 nm) will essentially increase their fluorescence, creating

a background against which Raman spectra are impossible to detect. The solution is to use a laser of a different wavelength, such as 633 nm (red) or 785 nm (near-infrared). While these lasers have lower photon energy, there is not enough energy for electronic transitions to another electronic state, which makes Raman detection easier by avoiding fluorescence.

3.3 Experimental

3.3.1 Materials

Natural graphite was purchased from NGS Naturgraphite GmbH. Chloroform (CHCl_3), dimethylformamide (DMF), *N*-methyl-2-pyrrolidone (NMP) and hydrazine monohydrate ($\text{NH}_2\text{NH}_2 \cdot \text{H}_2\text{O}$) were purchased from Sigma-Aldrich. Hydrochloric acid (HCl), sulphuric acid (H_2SO_4) and sodium hydroxide (NaOH) were purchased from Fisher Scientific. All materials were used as received.

3.3.2 Methods

All dispersions were prepared in glass-capped bottles (50-, 150- and 500-mL bottles were used, as appropriate for each sample volume). Each bottle was washed with acetone and dried in an oven at 100 °C. The paper was removed from the cap of each bottle and the cap was washed with acetone until no glue remained. Aluminium foil was placed under the cap to ensure a good seal.

Sonication was carried out with an ultrasonic water bath (Elmasonic P70H, 220-W effective ultrasonic power, 37-kHz ultrasonic frequency), which was equipped with an external water pipe as a chiller to keep the bath at about room temperature (RT) and to prevent any significant increase in temperature due to sonication. The instrument was set to work over a 12-h period, so it was manually switched on after each 12-h session. The interval between experiments generally did not exceed 2 h. All reported sonication times are the actual times that samples were exposed to ultrasonic power.

Centrifugation was carried out with an Eppendorf Centrifuge 5804, using a 50-mL disposable polypropylene tube, which was washed with acetone and dried before use.

UV-Vis spectroscopy and the Beer-Lambert law (Equation 3-5) were used to measure the graphene concentrations of graphene/PIM-1 composites.

$$A = \epsilon * C * l \quad (3-5)$$

Here, A is absorbance, ϵ ($\text{mg mL}^{-1} \cdot \text{cm}^{-1}$) is the extinction coefficient, C (mg mL^{-1}) is concentration, and l is the length pathway of the cuvette (usually 1 cm). Coleman and co-workers determined the extinction coefficient of graphene at 660 nm (ϵ) to be $36.2 \text{ mg mL}^{-1} \cdot \text{cm}^{-1}$.⁴¹ The absorption spectrum of graphene at 660 nm is always flat and featureless. Therefore, the graphene concentration can be found by the Beer-Lambert (Equation 3-6):

$$C = \frac{A}{l * \epsilon} \quad (3-6)$$

All Raman samples were prepared by drop-casting of dispersions on a silica substrate. Raman measurements were carried out with a Renishaw instrument at a wavelength of 533 (with and 2400 grooves/mm grating, objective 100X NA0.85 lens) or 633 nm (with 1200 grooves/mm grating, objective 50x, and three integrations over 90 s), and a laser power of 1.0 mW.

SEM images were performed on a FEI Quanta 200 ESEM. For films, samples were coated with thin layer gold using an Emitech sputter coater.

3.3.3 GPMMMs

3.3.3.1 Graphene exfoliation in organic solvents (GEOS)

All samples were prepared as shown in Table 3-1, which lists the sample name, solvent, sample volume, sonication time, initial graphite concentration ($C_{\text{graphite},i}$) and

centrifugation settings (speed and time). Centrifugation time was divided into 10-min sessions. Between sessions, each dispersion was carefully transferred to a new centrifuge tube (50 mL) using plastic pipettes to remove the remaining graphite from the sample. Final dispersions were black and homogeneous. High-concentration dispersions were noticeably darker in colour than low-concentration ones. Concentrations were determined by UV-Vis spectroscopy.

Table 3-1 Graphene exfoliation parameters: solvent, sample volume, sonication time, initial graphite concentration, centrifuge speed and final graphene concentrations that were determined by UV-Vis spectroscopy at 660 nm.

Sample	Solvent	Vol. (mL)	Sonic. time (h)	$C_{\text{graphite,i}}$ (mg mL ⁻¹)	Centrifuge speed (rpm) (time)	$C_{\text{graphene,f}}$ (mg mL ⁻¹)
GEOS-1	CHCl ₃	120	24	3.3	6000 (20 min)	0.002
GEOS-2	CHCl ₃	120	48	5	9000 (20 min)	0.0015
GEOS-3	CHCl ₃	120	29	3.3	2000 (20 min)	0.111
GEOS-4	CHCl ₃	120	29	3.3	2000 (20 min)	0.108
GEOS-5	CHCl ₃	120	75	3.3	6000 (20 min)	0.011
GEOS-6	CHCl ₃	120	75	3.3	2000 (20 min)	0.056
GEOS-7 ^a	CHCl ₃	120	40	3.3	6000 (30 min)	0.0111
GEOS-8 ^a	CHCl ₃	120	40	3.3	6000 (30 min)	0.0129
GEOS-9	CHCl ₃	400	31	3.3	6000 (30 min)	0.0055
GEOS-10	CHCl ₃	400	31	3.3	6000 (30 min)	0.0027
GEOS-11	CHCl ₃	400	73	3.3	8000 (30 min)	0.029
GEOS-12	NMP	30	12	5	6000 (20 min)	0.107
GEOS-13	DMF	100	84	6	9000 (20 min)	0.039

^a Sample was stored for 3 weeks before UV measurements.

3.3.3.2 GPMMMs -1 from graphene dispersion in chloroform

Various GPMMMs were prepared from graphene dispersions in chloroform, by mixing a portion of the GEOS series with a determined mass of PIM-1. Dispersion volumes of less than 13 mL were added to PIM-1 solution (10 mL). Other samples were used to dissolve PIM-1 without the addition of chloroform. Table 3-2 shows all of the experimental details for the GPMMMs. ‘Solution volume’ refers to the volume of graphene dispersion (GEOS). All graphene dispersions were coded to previously described samples and PIM-1 batches. Membranes were cast on flat Petri dishes, with slow evaporation over 3 days, then removed using an ethanol/water mixture (1:1).

Table 3-2: Experimental details for GPMMMs-1: sample name based on graphene loading (wt.%), added mass of PIM-1, added mass of graphene, dispersion volume of graphene in chloroform and diameter of petri dish that was used for the casting process.

Membrane (wt%)	PIM-1 mass (mg)	Graphene mass (mg)	Solution vol. (mL)	Petri dish diam. (cm)
GPMMM-1 (0.02%)	113 (KA1)	0.0226 (GEOS-7)	2	6.8
GPMMM-1 (0.05%)	113 (KA1)	0.0565 (GEOS-7)	5	6.8
GPMMM-1 (0.08%)	113 (KA1)	0.0904 (GEOS-7)	8.1	6.8
GPMMM-1 (0.1%)	113 (KA1)	0.113 (GEOS-7)	10.2	6.8
GPMMM-1 (0.12%)	113 (KA1)	0.1356 (GEOS-7)	12.2	6.8
GPMMM-1 (0.15%)	113 (KA1)	0.1695 (GEOS-7)	15.2	6.8
GPMMM-1 (0.18%)	113 (KA1)	0.2034 (GEOS-7)	18.3	6.8
GPMMM-1 (0.2%)	113 (KA1)	0.226 (GEOS-7)	20.32	6.8
GPMMM-1 (0.22%)	113 (KA1)	0.2486 (GEOS-7)	22.4	6.8
GPMMM-1 (0.28%)	113 (KA1)	0.3164 (GEOS-8)	24.4	6.8
GPMMM-1 (0.3%)	113 (KA1)	0.339 (GEOS-8)	26.2	6.8
GPMMM-1 (0.32%)	113 (KA1)	0.3616 (GEOS-8)	27.9	6.8
GPMMM-1 (0.35%)	113 (KA1)	0.3955 (GEOS-9)	70.7	6.8
GPMMM-1 (0.38%)	113 (KA1)	0.4294 (GEOS-9)	76.8	6.8
GPMMM-1 (0.45%)	113 (KA1)	0.5085 (GEOS-10)	186.3	6.8
GPMMM-1 (0.48%)	113 (KA1)	0.5424 (GEOS-10)	198.7	6.8
GPMMM-1 (0.1%)	28 (KA1)	0.028 (GEOS-2)	20	5
GPMMM-1 (0.03%)	299 (KA1)	0.102 (GEOS-2)	68	9
GPMMM-1 (0.01%)	50.9 (KA1)	0.0056 (GEOS-6)	4	5
GPMMM-1 (0.18%)	113(KA1-1)	0.2034 (GEOS-5)	18.3	6.8

3.3.3.3 Graphene exfoliation in PIM-1 solution (GEPS)

GEPSs were prepared as shown in Table 3-3, which contains experimental details such as sample name, sample volume, sonication time, initial PIM-1 concentration ($C_{\text{PIM-1,i}}$), initial graphite concentration ($C_{\text{graphite,i}}$), centrifugation time and speed, as well as the graphene concentration obtained ($C_{\text{graphene,f}}$). Centrifugation was performed as described in Section 4.2.3.1. Graphene concentrations were determined by UV-Vis spectroscopy at a wavelength of 660 nm and molar absorptivity coefficient of $36.3 \text{ mg mL}^{-1} \cdot \text{cm}^{-1}$. PIM-1 showed no obvious absorption in the visible regime above 550 nm. Therefore, the graphene concentration was measured without considering the presence of polymer.

Table 3-3: Experimental details for graphene/PIM-1 dispersion: sample volume, sonication time, initial PIM-1 concentration, initial graphite concentration, centrifuge speed and final graphene concentrations that were determined by UV-Vis spectroscopy at 660 nm.

Sample	Vol. (mL)	Sonic. time (h)	$C_{\text{PIM-1,i}}$ (mg mL ⁻¹)	$C_{\text{graphite,i}}$ (mg mL ⁻¹)	Centrifuge speed (rpm) (time)	$C_{\text{graphene,f}}$ (mg mL ⁻¹)
GEPS-1	100	84	14	6	6000 (20 min)	0.349
GEPS-2	100	84	35	6	8000 (20 min)	0.2
GEPS-3	100	84	3	6	8000 (20 min)	0.2
GEPS-4	100	84	14	6	6000 (20 min)	0.1
GEPS-5	100	84	14	6	6000 (20 min)	0.18
GEPS-6	100	84	14	6	10000 (30 min)	0.12
GEPS-7	100	84	14	6	10000 (30 min)	0.15
GEPS-8	100	84	14	6	10000 (30 min)	0.14
GEPS-9	100	84	14	6	10000 (30 min)	0.14

3.3.3.4 GPMMMs-2 from GEPS-1

GEPS-1, as previously mentioned, was made from PIM-1 (KA1-1) and used to prepare a series of membranes. The first membrane GPMMM-2 (1), which was intended to have the highest graphene content, was cast from 5 mL of the original stock sample of GEPS-1. This volume was transferred into a 7.8-cm-diameter flat-bottomed glass Petri dish and the solvent was evaporated slowly over 3 days.

Membranes with lower graphene content were prepared by mixing portions of the stock GEPS-1 sample with a pure PIM-1 (KA1-1) solution of 35 mg mL⁻¹. For samples GPMMM-2 (2), GPMMM-2 (3) and GPMMM-2 (4), 2 mL of stock solution were mixed with 2, 5 and 10 mL, respectively, of PIM-1 solution. For samples GPMMM-2 (5) and GPMMM-2 (7), 4 mL of stock solution were mixed with 20 and 40 mL, respectively, of PIM-1 solution. A 7.8-cm-diameter Petri dish was used for samples GPMMM-2 (2) and GPMMM-2 (6), and a 6.8-cm-diameter dish was used for other samples.

Graphene concentration was determined for GPMMM-2 (5) (0.23 g) in 23 mL chloroform, giving 0.018 mg mL⁻¹. This determined the graphene concentration (C_{graphene}) and wt.% for GPMMM-2 (1), GPMMM-2 (2), GPMMM-2 (3), GPMMM-2 (4), GPMMM-2 (5) and GPMMM-2 (6), as shown in Table 3-4.

Table 3-4. GPMMMs-2 preparation parameters and obtained C_{graphene} and graphene:PIM-1 wt.% determined by UV-Vis measurement.

Membrane	Stock GEPS-1 (mL)	PIM-1 (mL) ^a	Total Vol. (mL)	C_{graphene} (mg mL ⁻¹)	Wt.%
GPMMM-2 (1)	5	0	5	0.349	2.43
GPMMM-2 (2)	2	2	4	0.174	0.71
GPMMM-2 (3)	2	5	7	0.1	0.34
GPMMM-2 (4)	2	10	12	0.058	0.18
GPMMM-2 (5)	4	20	24	0.058	0.18
GPMMM-2 (6)	4	40	44	0.032	0.1

^a PIM-1 (KA1-1) concentration was 35 mg mL⁻¹.

3.3.3.5 GPMMMs-3 from GEPS-8

GEPS-8 was used to prepare GPMMMs-3. Various graphene-loaded membranes were prepared from a pure PIM-1 (KA1-4) (2.014 g) solution in chloroform (134.3 mL). This stock PIM-1 solution was filtered through a cotton band before use. Each loading system was prepared by adding a determined volume of PIM-1 to the stock solution, as shown in Table 3-5 and Figure 3-3. All additions were carried out with a 20 mL graduated syringe and a micropipette. All samples were cast in flat, 6.7 cm diameter Petri dishes, covered and slowly evaporated over 3 days. Membranes were removed from the dishes using a 1:1 ethanol/water mixture and dried under a vacuum dissector overnight.

Table 3-5. Preparation details of GPMMMs-3.

Membrane	Stock GEPS-8 (mL) ^a	Added PIM-1 (mL) ^b	Total PIM-1 (mg)	Graphene content (mg)	wt%
GPMMM-3 (1)	14.29	0	200	1.86	0.92
GPMMM-3 (2)	10.7	3.3	200	1.39	0.7
GPMMM-3 (3)	8.04	5.8	200	1.04	0.5
GPMMM-3 (4)	6.03	7.7	200	0.78	0.4
GPMMM-3 (5)	4.52	9.1	200	0.59	0.3
GPMMM-3 (6)	3.40	10.2	200	0.44	0.2
GPMMM-3 (7)	2.50	11	200	0.33	0.17
GPMMM-3 (8)	1.91	11.6	200	0.25	0.13
GPMMM-3 (9)	1.43	12	200	0.19	0.1
GPMMM-3 (10)	1.07	12.3	200	0.14	0.07
GPMMM-3 (11)	0.81	12.6	200	0.10	0.05
GPMMM-3 (12)	0.60	12.8	200	0.08	0.04
GPMMM-3 (13)	0.45	12.9	200	0.06	0.03
GPMMM-3 (14)	0.34	13	200	0.04	0.02

^a PIM-1 and graphene concentrations in stock GEPS-8 were 14 and 0.13 mg mL⁻¹, respectively. ^b PIM-1 concentration was 15 mg mL⁻¹.



Figure 3-3: Digital image of GPMMS-3 series dispersions before membrane casting.

3.3.3.6 Exfoliation of synthetic multilayer graphene in PIM-1 solution

Dr. Frank Mair prepared multilayer graphene samples via a reaction between magnesium and dry ice. Magnesium turnings were placed in a Buchner funnel and washed sequentially with HCl and acetone. Turnings were left for about 30 min, as air was drawn through them with a diaphragm vacuum pump. Dry turnings, free of oxide coating, were then ready for use.

To make the reaction vessel, a block of dry ice was purchased from Air Liquide. The block was cut in half to obtain the largest cut surface. A well (~5 cm in depth \times 15 cm in diameter) was made in the block. First, a 5-cm-deep circular cut was made by a cylindrical cutter mounted on an electric drill. The central portion of the dry ice was removed with a chisel. A heated brass block was placed in the hole, to sublime prominent lumps on the bottom surface, such that a reasonably flat surface remained.

The prepared block was placed in a fume hood equipped with heat-resistant mats and cleared of all other contents. Magnesium turnings (20 g) were placed in the hole in the block. The other half of the block was placed adjacent to the first, to act as a lid for the reaction vessel. The magnesium turnings were heated with a butane gas torch until intense white combustion ensued, at which point the lid was quickly placed on the block. Violent and intense combustion ensued, with emission of UV light. When the block no longer emitted light or heat, the remaining grey/black

residue was removed, weighed, placed in concentrated HCl (150 mL) and left overnight. The residue in acid solution was treated in an ultrasound bath for 30 min, filtered, washed until the washings were free of chloride (determined qualitatively with silver nitrate solution) and oven-dried (80 °C) overnight.

3.3.3.7 GPMMMs-4 from synthetic multilayer graphene

Synthetic multilayer graphene was used as received from Dr. Mair. Stock PIM-1 solution was prepared from PIM-1 powder (1.27 g) dissolved in 100 mL chloroform and filtered through a cotton band. Multilayer graphene (0.6 g) was added to the PIM-1 solution, sonicated for 24 h and centrifuged at 10,000 rpm for 30 min. The centrifugation time was divided into 10 min sessions. Between sessions, the dispersion was carefully transferred to a new centrifuge tube (50 mL) by plastic pipette. Finally, the dispersion GEPS-10 was filtered through a cotton band. The graphene concentration was determined by UV-Vis spectrometry to be 0.53 mg mL⁻¹.

GEPS-10 was used to prepare GPMMMs-4. Various graphene-loaded membranes were prepared from another pure PIM-1 (KA1-4) (2.606 g) solution in chloroform (205.2 mL) as shown in Table 3-6.

Table 3-6: Preparation details of GPMMMs-4 samples.

Membrane	Stock GEPS-10 (mL) ^a	Added PIM-1 (mL) ^b	Total PIM-1 (mg)	Total graphene content (mg)	wt%
GPMMM-4 (1)	15.75	0	200	8.35	4
GPMMM-4 (2)	11.81	3.94	200	6.26	3.03
GPMMM-4 (3)	8.86	6.89	200	4.69	2.30
GPMMM-4 (4)	6.64	9.10	200	3.52	1.73
GPMMM-4 (5)	4.98	10.77	200	2.64	1.30
GPMMM-4 (6)	3.74	12.01	200	1.98	0.98
GPMMM-4 (7)	2.80	12.95	200	1.49	0.74
GPMMM-4 (8)	2.10	13.65	200	1.11	0.55
GPMMM-4 (9)	1.58	14.18	200	0.84	0.42
GPMMM-4 (10)	1.18	14.567	200	0.63	0.31
GPMMM-4 (11)	0.89	14.86	200	0.47	0.23
GPMMM-4 (12)	0.67	15.08	200	0.35	0.18
GPMMM-4 (13)	0.5	15.25	200	0.26	0.13
GPMMM-4 (14)	0.37	15.37	200	0.20	0.10
GPMMM-4 (15)	0.28	15.47	200	0.15	0.07
GPMMM-4 (16)	0.21	15.54	200	0.11	0.06
GPMMM-4 (17)	0.16	15.59	200	0.08	0.04

^a PIM-1 and graphene concentrations in stock GEPS-10 were 12.7 and 0.53 mg mL⁻¹ respectively.

^b Concentration of added PIM-1 was 12.7 mg mL⁻¹

3.3.3.8 Incorporating GO, RGO and BWGO in PIM-1 solution

GO, RGO and BWGO were prepared by Dr. Patricia Gorgojo.

3.3.3.8.1 Synthesis of GO

GO was prepared by a modified Hummers' method.⁴⁴ Briefly, natural graphite (5 g) and potassium nitrate (4.5 g) were stirred in concentrated H₂SO₄. The mixture was cooled in an ice bath with the addition of potassium permanganate (22.5 g) over 70 min. The mixture was stirred continuously at RT for 7 days, during which time the mixture thickened, and no efficient stirring was achieved after 3 days.

The dark mixture obtained was diluted slowly with 550 mL of H₂SO₄ solution (5 wt.%) over about 1 h with continuous stirring, followed by stirring for an additional 3 h. Hydrogen peroxide (H₂O₂; 15 g, 30 mL) was carefully added while being mindful of effervescence. The mixture was stirred for 2 h as it turned into a yellow suspension, then 500 mL of H₂SO₄ (3 wt.%) and H₂O₂ (0.5 wt.%) were added and the mixture stirred overnight.

The mixture was centrifuged for 20 min at 8000 rpm. Two separate phases were obtained. The top phase was a clear solution, which was removed. The other

was a viscous dark yellow solution, which was further dispersed into 500 mL of H_2SO_4 (3 wt.%) and H_2O_2 (0.5 wt.%) with the aid of shaking for 5 to 10 min. Further washing was repeated until the dispersion darkened and became less glittery. After four washes, no glitter was observed.

Final washing was carried out with deionised water (500 mL), followed by centrifugation to remove the colourless top solution. This step was repeated several times until the top solution was neutralized (pH \sim 7). The GO obtained was collected by filtration and vacuum dried.

3.3.3.8.2 Synthesis of BWGO

GO (1.8 g) was stirred vigorously in deionised water (1.8 L) for 24 h, then sodium hydroxide (12 g) was added slowly. The solution was stirred for 24 h and then filtered. The solid obtained was treated with 1 M HCl, stirred for 24 h, filtered and washed with water until it became neutral (pH \sim 7). The BWGO obtained was dried under vacuum at RT.

3.3.3.8.3 Synthesis of RGO

GO (1.8 g) was dispersed in deionised water (1.8 L) by stirring for 24 h. Hydrazine monohydrate (3.6 mL, 65 wt.%) was added and the mixture stirred for 24 h. The resulting RGO was filtered and dried under vacuum at RT.

3.3.3.9 MMM preparation from graphene derivatives

BWGO (0.240 g), PIM-1 (KA1-4) (0.6 g) and chloroform (40 mL) were added to a 50-mL bottle, sonicated for 84 h and centrifuged at 10,000 rpm for three 10-min sessions. Each session was followed by removal of the dispersion to a new centrifuge tube (50 mL) by plastic pipette. A homogeneous dispersion was successfully obtained as a greenish BWGO suspension (KA18). The same procedure was applied to prepare the RGO suspension (KA19) and GO suspension (KA20).

BWGO-MMM, RGO-MMM and GO-MMM were prepared by adding 14 mL of each composite to a 7.6-cm-diameter Petri dish. Samples were evaporated slowly over 3 days. BWGO-MMM and RGO-MMM were removed from dishes by using a

1:1 mixture of ethanol and water. These two membranes were successfully obtained as intact films, whereas the GO-MMM film was cracked and discontinuous after the evaporation process.

3.4 Results and discussion

3.4.1 GPMMMs

3.4.2 Graphene exfoliation in organic solvents (GEOS)

A number of experiments were performed to assess graphene exfoliation in organic solvents, particularly chloroform, as a good solvent for PIM-1. A number of other solvents such as NMP and DMF have high graphene dispersibility, but chloroform has a low boiling point and has the advantages of easy removal, better polymer dissolution and fewer problems in composite fabrications. Graphene dispersion in a low-boiling point solvent can facilitate the spray casting of graphene flakes onto appropriate substrates. Coleman and his co-workers have reported that chloroform shows good graphene dispersibility and stability, with half of the graphene concentration that can be obtained with high-boiling point solvents such as NMP.⁴⁵

A number of exfoliations using chloroform were observed to have failed. These failures are attributed to inadequate sealing or exposure to contaminants. Therefore, all samples listed in Table 3-1 were processed in carefully designed conditions of good sealing and bottle cleaning.

The main focus of these experiments was to identify preparation conditions that would yield graphene of high concentration in order to carry out large-scale production of MMMs and then to investigate the effect of graphene loading on gas permeation for a series of MMMs. The ideal product that the experiments aimed to produce was a stable batch of few-layer graphene dispersion on a gram scale, suitable for MMM preparation. A narrow flake size distribution is also favourable in the composite formation.

Our understanding of graphene LPE is that as long as the sonication conditions are constant, long-time sonication should yield a high graphene concentration. However, long-time, high-power sonication can lead to a low average flake size. Moreover, average flake size and concentration depend on centrifugation speed. Therefore, there is a trade-off between large graphene flake production and concentration.⁴⁶

Size-selective conditions can be achieved by programming sequences of LPE with controlled centrifugation, as reported by Coleman et al.⁴⁶

From Table 3-1, it can be seen that GEOS-1 gave a graphene concentration of 0.002 mg mL^{-1} with 24 h sonication and centrifugation at 6000 rpm. GEOS-2 yielded a lower graphene concentration, despite 100% longer sonication time and 50% higher centrifugation speed. This can be attributed to a higher initial graphite concentration, as high graphite content can require extra sonication power. The higher centrifugation speed also reduced the graphene concentration.

GEOS-3 and GEOS-4 were subject to the same conditions of sample volume, sonication time, initial graphite concentration and centrifugation speed, to give similar graphene concentrations of 0.11 mg mL^{-1} . However, a low centrifugation speed and short sonication time can lead to a majority yield of few-layer rather than monolayer graphene. Coleman et al. were able to obtain <10 layers with average length of $0.84 \text{ }\mu\text{m}$ under conditions of $\sim 16 \text{ W}$, 2000 rpm and 48 h sonication.⁴⁵ Our experiments were carried out with significantly higher input power, which can produce smaller flakes.

Two other samples, GEOS-5 and GEOS-6, differed only in centrifugation speed and show that faster centrifugation leads to lower graphene concentration.

GEOS-7 and GEOS-8, with less sonication time, gave graphene concentration values ($\approx 0.01 \text{ mg mL}^{-1}$) closest to GEOS-5, which had more sonication time. It is notable that the graphene concentration was stable even after three weeks storage at room temperature, when samples were measured by UV-Vis.

GEOS-9 and GEOS-10 were processed in high volume and yielded lower graphene concentrations than samples of lower volume but otherwise identical conditions. This demonstrates the role of energy cost in graphene exfoliation. In

order to overcome the poor yield at high volume, sonication was performed for a longer time on GEOS-11. This gave a much higher graphene concentration than GEOS-9 and GEOS-10, even with a slightly higher centrifugation speed.

Two other high-boiling-point solvents, NMP (GEOS-12) and DMF (GEOS-13), were also tested. NMP yielded a high graphene concentration of 0.1 mg mL^{-1} , even with the shortest sonication time. This matched our expectation that NMP would be a good solvent for LPE. DMF also demonstrated a significantly better ability to exfoliate graphene than chloroform, giving a high graphene concentration at the highest centrifugation speed (9000 rpm).

3.4.3 Graphene exfoliation in PIM-1 solution (GEPS)

Based on the principle that polymers can enhance LPE, and also because a computational study of GPMMMs by Gonciaruk illustrates potential Graphene-PIM-1 interactions,⁴⁷ PIM-1 was used as a solvent-enhancing additive and stabilizer. All dispersions yielded higher graphene concentrations than those for the pure organic solvents of both high and low boiling points, as shown in Table 3-3.

All experiments used 100 mL samples, sonicated for 84 h. As to the initial concentrations of PIM-1 and graphite, most samples had a 1:2 graphite:PIM-1 ratio. However, GEPS-2 and GEPS-3 had ratios of 1:5.8 and 1:0.5 respectively. No difference in graphene concentration resulted. However, a high concentration of PIM-1 may not be ideal to prepare a composite of high graphene content. On the other hand, a small amount of PIM-1 may not ensure graphene stability.

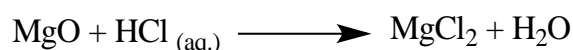
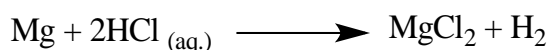
Our first successful preparation (GEPS-1) gave a high graphene concentration. The variation in graphene concentration between GEPS-1, GEPS-4 and GEPS-5 can be attributed to the influence of intense cavitation during sonication. Centrifugation speed was increased to ensure high production of monolayer graphene, albeit by sacrificing the concentration.

3.4.4 Exfoliation of synthetic multilayer graphene in PIM-1 solution

Synthetic multilayer graphene is composed of smaller flakes than can be obtained from natural graphite by LPE. This can be assumed from the proposed preparation mechanisms. The higher capability of synthetic multilayer graphene to exfoliate is obvious from the GEPS-10 (4 wt. %). It is believed that smaller graphene flakes have higher dispersibility, which may be due to both entropy and enthalpy effects. It is worth mentioning that using synthetic multilayer graphene does reduce the energy cost, as this dispersion was prepared by short-time sonication (24 h).

The dispersion was filtered through a cotton band before the graphene concentration was determined, because some small grey particles were observed during and after the centrifugation process. This may have been residual MgO which was not removed by sedimentation or centrifugation.

The dispersion was first subjected to hydrochloride treatment in an attempt to remove any Mg or MgO. This method uses hydrochloric acid to convert any residual Mg or MgO to MgCl₂ as follows:



The Mair group, however, has reported that hydrochloride treatment did not entirely remove MgO, so that even after overnight treatment, the MgO:C ratio was 0.54, only slightly lower than the ratio after 2 h of treatment (0.59).⁴⁸

Residues can be problematic in GPMMM formation and filtration through a cotton band can be a powerful technique to remove them and to purify the graphene dispersion. Therefore, this method was applied successfully.

High graphene concentrations allowed the exploration of a wide range of GPMMMs with different loadings, whereas exfoliated graphene is limited, with relatively low graphene concentrations.

3.4.5 Incorporating GO, RGO and BWGO in PIM-1 solution

GO is graphene decorated with oxygen-containing groups such as carboxyl, hydroxyl and epoxy groups. The oxidation process leads to random functionalization either on the edge or in the continuous lattice of graphene flakes. It also causes indiscriminate defects, holes and cut-offs in graphene layers.

As a consequence of its functionality, GO is hydrophilic and water dispersible. This can limit its incorporation in PIM-1. However, GO is an attractive material because of its easy preparation and scalability.

The ratio of carbon to oxygen varies with the preparation method. The chemical composition of GO can range from $C_8O_2H_3$ to $C_8O_4H_5$, corresponding to a C:O ratio from 4:1 to 2:1.⁴⁹

LPE was applied to GO and the dispersion obtained was found to have a low graphene concentration when it was measured by UV-Vis.

Washing GO with a base such as sodium hydroxide can reduce the oxide groups and tune its hydrophilicity. This method can be used to produce BWGO, which has better compatibility with PIM-1; thus, enhanced dispersibility is expected with BWGO compared with GO.

r-GO is obtained from the chemical reduction of GO via hydrazine monohydrate to remove the major oxygen-containing groups, as shown in Figure 3-4. This method can improve the C:O ratio in most cases to approximately 12:1.⁴⁹

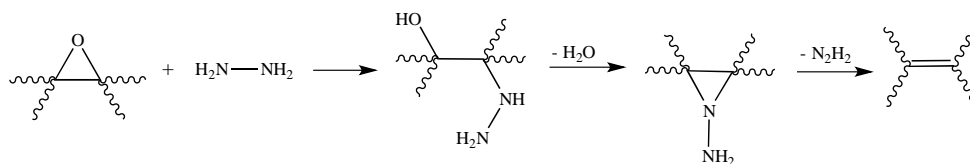


Figure 3-4. Proposed mechanism for epoxide reduction with hydrazine.⁴⁹

Applying LPE to a solution of r-GO with PIM-1 gave a higher graphene content than for GO or BWGO as a consequence of the difference in hydrophilicity. Figure

3-5 illustrates the effect of hydrophilicity on graphene content for different graphene sources in hydrophobic PIM-1 solution.

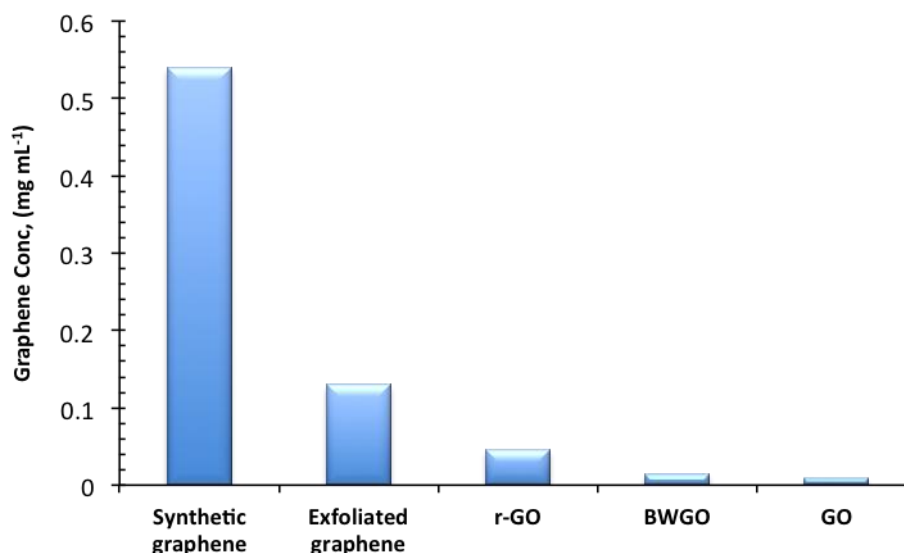


Figure 3-5. Graphene concentrations obtained by LPE of synthetic graphene, exfoliated graphene, r-GO, BWGO and GO. All dispersions were centrifuged at 10,000 rpm and concentrations were determined by UV-Vis.

3.4.6 Series 1 GPMMMs from graphene dispersion in chloroform

In MMM preparation, we were concerned with the compatibility, size and distribution of fillers in the continuous polymer matrix. Preparation difficulties varied among the different MMM components. In general, three preparation methods are utilized in MMM fabrication. One method begins with the dispersion of fillers in an appropriate solvent, followed by polymer addition, then casting, as shown in Figure 3-6a. The method shown in Figure 3-6b starts with dissolution of the polymer in a solvent, followed by the addition of fillers and casting of the homogenous mixture. Finally, the fillers can be dispersed and the polymer dissolved separately, then the two are mixed before casting as a homogenous mixture (Figure 3-6c). The first and third methods are commonly used for optimum distribution and to minimise aggregation.⁵⁰ The second method is not applicable to GPMMM preparation, unless external energy, such as ultrasonic power, is introduced to incorporate graphene, which will be demonstrated later.

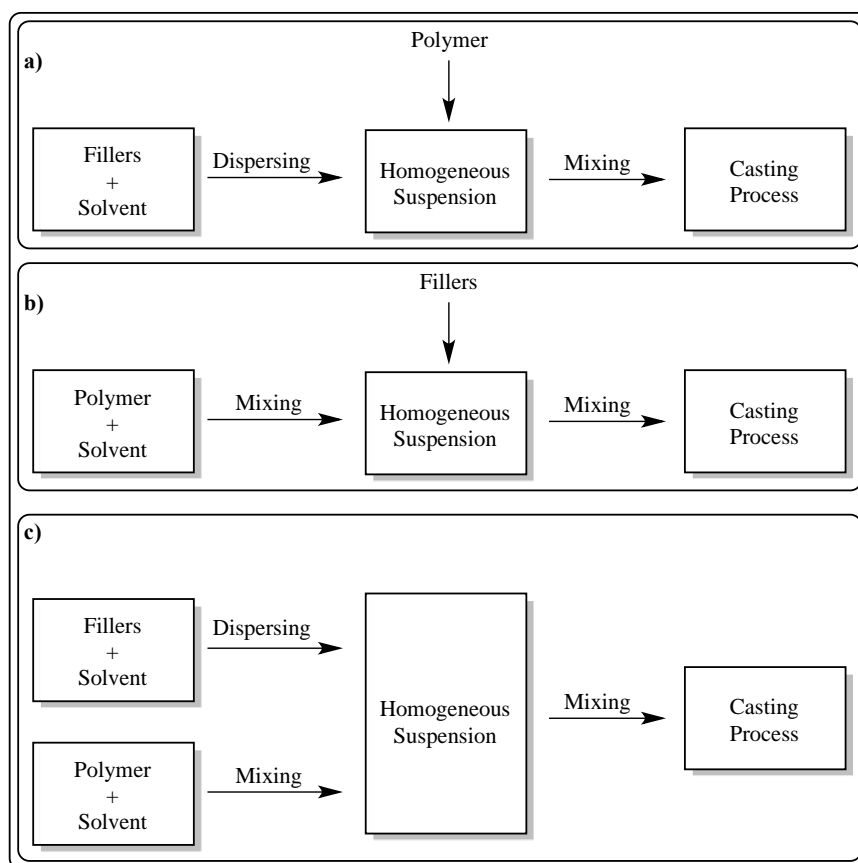


Figure 3-6. Different MMM preparation methods (adapted from ref.⁵⁰).

Series 1 GPMMMs were prepared by either the first or third methods. The third method was used for graphene dispersions of <13 mL. Thus, PIM-1 was dissolved separately in 10 mL before mixing. Most of the used graphene dispersions were >13 mL; therefore, predetermined masses of PIM-1 powder were added to graphene dispersion with the aid of vigorous stirring, before they were cast. In these samples, no additional chloroform was used, in order to not increase dilution. Highly dilute mixtures can be disadvantageous for casting optimum GPMMMs.

From a number of experiments of Series 1 GPMMMs, It shows those membranes with graphene loadings >0.18 wt.% look less homogeneous, as can be seen in Figure 3-7b, even though exfoliated products looked well dispersed before solvent removal (Figure 3-7a). In contrast, Series 1 GPMMMs with graphene loadings <0.18 wt.% seem more homogeneous (Figure 3-7c).

Raman tests were carried out by Yuyoung Shin on samples obtained by drop casting of graphene dispersions in chloroform. No single-layer graphene was

observed. About 50% of flakes were few-layer graphene with AB stacking and 50% were graphite (Figure 3-8, a and b).

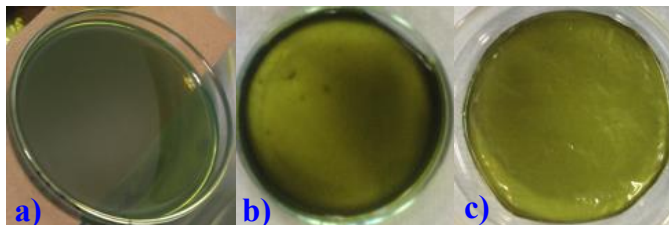


Figure 3-7. Digital image of Series 1 GPMMMs with graphene loading of 0.4 and 0.18 wt.%. a) wet composite of GPMMM-1 (0.38 wt.%), b) GPMMM-1 (0.38 wt.%), c) GPMMM-1 (0.18 wt.%).

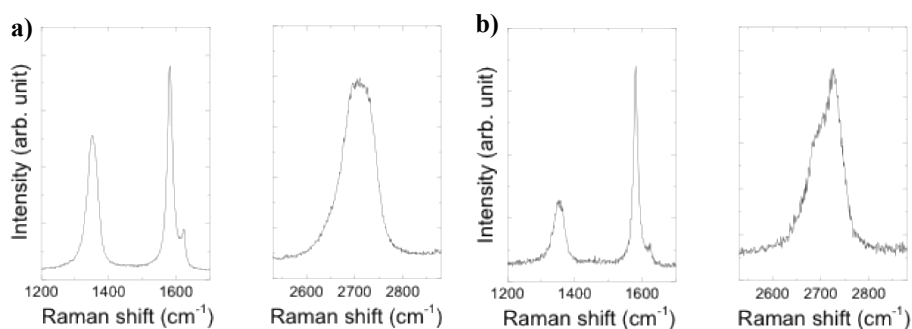


Figure 3-8. Raman spectra of graphene exfoliated in chloroform drop-cast on silica substrate, performed with a laser of 513 nm wavelength, a) is FLG and b) is graphite flake. Data were provided by Yuyoung Shin.

Combining both experimental observations and Raman measurements on Series 1 GPMMMs, one can suggest reasons why dark regions were observed in MMMs. It is owing to graphene dispersibility in pure chloroform. In other words, poor graphene dispersibility in chloroform has an influence on obtaining desirable GPMMMs. Moreover, graphene concentration in chloroform was found to be relatively low. Therefore, the applicability of this method can be limited to produce GPMMMs.

3.4.7 GPMMMs from graphene dispersion in PIM-1 solution

A number of GPMMMs were prepared from natural graphite via LPE, typically from GEPS-1 and GEPS-8. A series of different graphene loadings were also prepared with the addition of a predetermined mass of PIM-1 to the stock dispersions. Graphene appeared better dispersed in those membranes where graphene loading was high (i.e. >0.18 wt.%) than in Series 1 GPMMMs (Figure 3-9). This confirms that direct graphene exfoliation in PIM-1 solution can be an appropriate method of GPMMM preparation. In addition, the GPMMMs showed solution processability, which means that membranes are able to undergo dissolution without graphene sedimentation (Figure 3-10). This can be attributed to good graphene distribution, which is crucial in order to fulfil the demands of membrane applications.

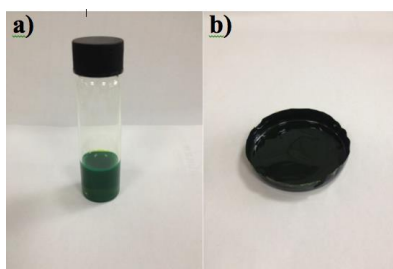


Figure 3-9. Digital image of Series 2 GPMMMs and its dispersion, a) dispersion of GEPS-1, b) free-standing GPMMM-2 (5).

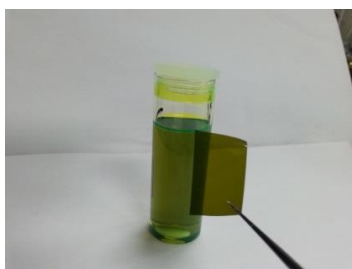


Figure 3-10. GPMMM-2 (6) (0.18 wt%) after dissolution and before, showing good graphene dispersion.

The highest graphene content of Series 2 GPMMMs (wt.% = 2.43) was significantly higher than that of Series 3 GPMMMs (wt.% = 0.92). This results from the different preparation conditions of associated dispersions. Notably, Series 3 GPMMMs were centrifuged at a higher speed, giving a lower graphene

concentration. UV-Vis measurement to determine concentration does not classify the product as monolayer, few-layer or multilayer graphene. Therefore, further characterization is needed for more information on graphene content.

Another series of Series 4 GPMMMs were prepared by exfoliation of synthetic multilayer graphene in PIM-1 solution. These membranes covered graphene loading up to 4 wt.%.

3.4.8 GPMMMs charactrizations

In GPMMMs, polymer fluorescence was found to be an obstacle to obtaining Raman signals using a green laser, as PIM-1 is too fluorescent (Figure 3-11). Therefore, as explained above, a red laser was used to obtain a Raman spectrum of the graphene content of a graphene/PIM-1 composite. However, PIM-1 was found to give Raman signals which overlapped with the graphene G and D peaks, so a subtracted process was needed to resolve these (Figure 3-12 and Figure 3-13). Fortunately, the 2D peak was free of any signals from the polymer. This 2D peak is associated with FLG of random stacking order, which means that FLG was obtained by SLG reassembly after they were obtained from LPE.

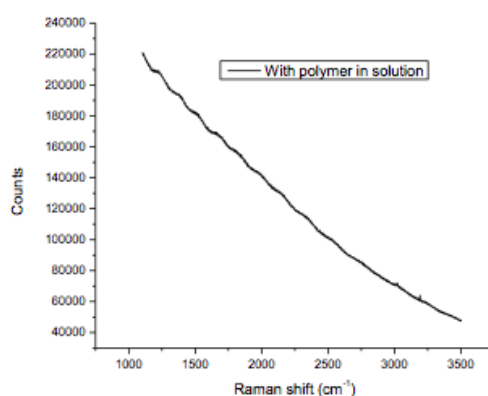


Figure 3-11. Raman spectrum of GPMMM with laser wavelength of 533 nm. Data was provided by Zhou.

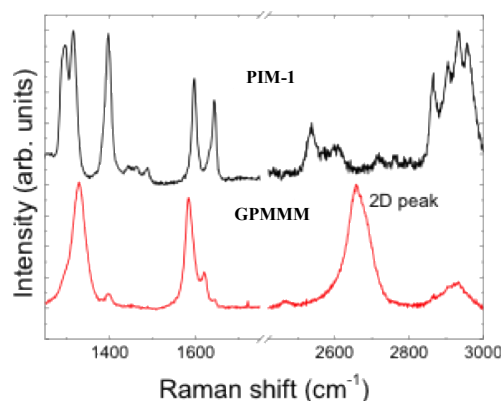


Figure 3-12. Raman spectra of pure PIM-1 compared with Raman spectra of graphene/PIM-1 MMM. The PIM-1 peaks overlapped with the G and D peaks, requiring a normalization process. The 2D peak was clearly visible without normalization. Data were provided by Yuyoung Shin.

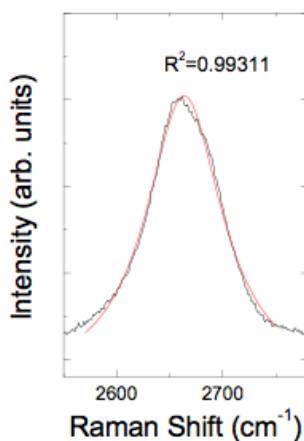


Figure 3-13. Lorentzian fitting of the 2D peak of a GPM-MMM, typically confirming a restacked FLG content. Data were provided by Yuyoung Shin.

Exfoliated graphene in chloroform gives similar Raman spectra of the FLG 2D peak (Figure 3-8a). However, the level of defects or disorders in GEOS samples can be found from low intensity ratio of D and G bands (I_D/I_G), which are usually small for unfunctionalized and relatively big average flack size. In contrast, the levels of defects or disorders in GPM-MMMs are difficult to be evaluated, due to overlapping polymer peaks.

In summary, from various graphene exfoliations in different solvents and exfoliating enhancements (like PIM-1), SLG is obtained from a good solvent like

NMP (Figure 3-1). In contrast, in chloroform, Raman spectroscopy shows evidence of the presence of FLG only.

Scanning electron microscopy (SEM) was used to take a cross-section of pristine PIM-1 membrane, revealing a relatively smooth morphology (Figure 3-14a-b), in contrast to the jagged GPMMM structure (Figure 3-14e-f). This suggests that the presence of graphene layers affects the texture and morphology compared with pristine PIM-1 membrane. Graphene flakes could not be visualized by SEM.

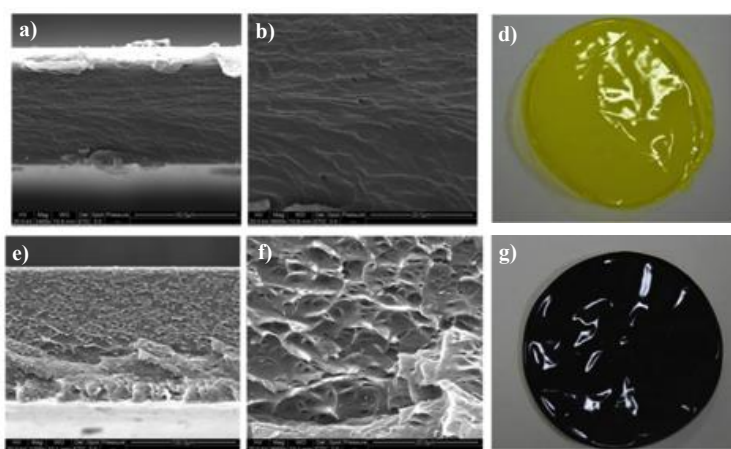


Figure 3-14. SEM images of pristine PIM-1 (KA1-4) and GPMMMs-3 (1). a) and b) are SEM images at two different magnifications of pristine PIM-1 membrane (d); e) and f) are the equivalent SEM images of GPMMM (g). Data were provided by Gonciaruk.

Yong and his coworkers⁵¹ produced SEM images of their pristine epoxy resin, showing its smooth structure (Figure 3-15a), whereas their graphene/epoxy composite, made by LPE in ethanol and drop-cast on silicon wafer, had a similar rough morphology (Figure 3-15b) to our GPMMM sample. In addition, a large block of aggregated graphene was found embedded in the epoxy matrix (Figure 3-15c). The rough morphology may be due to graphene inhibiting the fracturing of the composite.

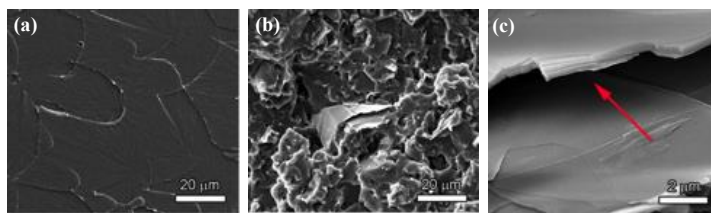


Figure 3-15. SEM image of pristine epoxy resin (a), graphene/epoxy composite (b) and a large block of aggregated graphene (c).⁵¹

SEM of GPMMM shows a relatively homogeneous dispersion of graphene in the polymer matrix. Therefore, the preparation of GPMMM from GEPS may have the advantage of avoiding large bloke aggregated graphene, which is an attractive property of composite preparation.

The resistance of PIM-1 to ultrasonic exposure is questionable, as high-energy ultrasonic exposure can lead to polymer decomposition. Therefore, GPC tests were performed on PIM-1 solution before and after ultrasonic treatment for 84 h (Figure 3-16). Treated PIM-1 showed a slight reduction in the high-molecular-weight region in comparison to original PIM-1 (*ca.* $1 \times 10^3 \text{ g mol}^{-1}$), without significant reduction in average molecular weight. It is worth mentioning that treating PIM-1 in an ultrasonic bath did not change its ability to form a flexible continuous film. The same results were obtained from KA1-4, which was examined after ultrasonic treatment for various lengths of time (Figure 3-17 and Table 3-7).

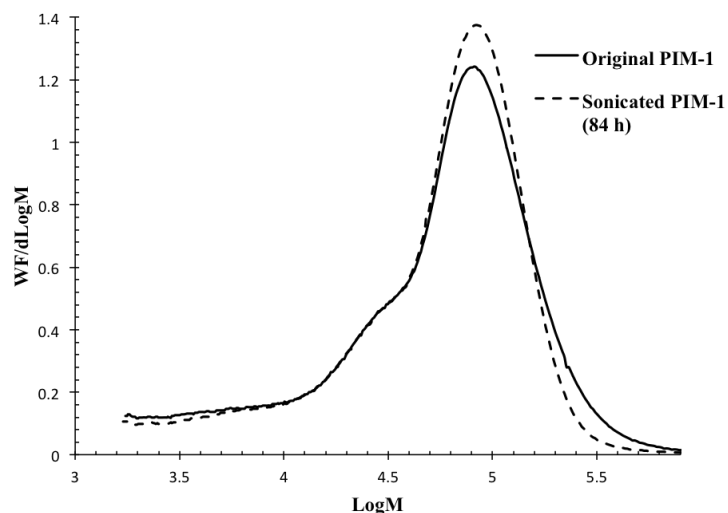


Figure 3-16. GPC graph of PIM-1 before and after ultrasonic treatment for 84 h. Before sonication, M_w , M_n and PDI were $78 \times 10^3 \text{ g mol}^{-1}$, $32 \times 10^3 \text{ g mol}^{-1}$ and 2.4; respectively. After sonication, M_w , M_n and PDI were $77 \times 10^3 \text{ g mol}^{-1}$, $22 \times 10^3 \text{ g mol}^{-1}$ and 3.4.

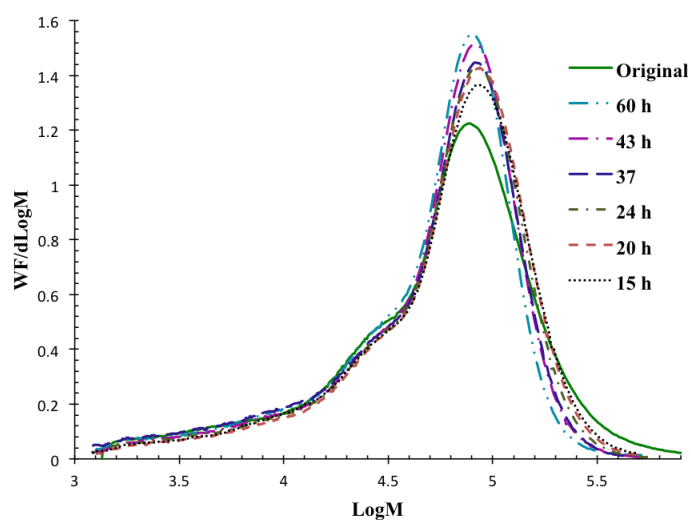


Figure 3-17. GPC graphs of KA1-4 (PIM-1) that was tested before and after ultrasonic treatment for various lengths of time.

Table 3-7. GPC data of KA1-4 (PIM-1) that was tested before and after ultrasonic treatment for various lengths of time.

Sample name	$M_w \times 10^3 \text{ g mol}^{-1}$	$M_n \times 10^3 \text{ g mol}^{-1}$	M_w/M_n
Original	92	24	3.8
15h	82	26	3.2
20h	82	28	2.9
24h	78	25	3.1
37h	72	22	3.3
43h	73	24	3
60h	69	23	3

3.5 Conclusions

In conclusion, graphene exfoliation in chloroform shows its validity to produce FLG in a relatively stable dispersion, as long as it is stored in an appropriate sealed container. However, low graphene concentration can be a disadvantage of this method. MMM preparation usually requires a large scale of graphene product in order to be applied. In addition, it is environmentally and commercially beneficial to reduce solvent usage, which is not the case in this method. In contrast, easier graphene characterization can be found with this method, as they are additive-free dispersions.

Graphene exfoliation in PIM-1 solution helps to increase the graphene content and avoid the mixing process between graphene and the polymer for composite preparation. The graphene content of this method was confirmed to be FLG by Raman spectroscopy. However, graphene characterization in fluorescent polymer composites is difficult, in comparison with pristine graphene dispersions. Therefore, advanced techniques are required for qualitative characterization.

Synthetic multi-layer graphene exfoliation exhibits a high level of dispersibility over natural graphene exfoliation. This helped in the preparation of a wide range of various graphene loadings, including those of higher graphene loadings than obtained loading with natural graphene exfoliation. Therefore, this method can be commercially beneficial and greener.

Other graphene products such as GO, RGO and BWGO were also exfoliated in PIM-1. They illustrate how hydrophobicity affects their dispersibility. In other words, as the hydrophobicity decreases, they exhibit lower dispersibility.

MMMs were prepared by two main methods. In the first, MMMs (Series 1 GPMMMs) were prepared via a mixing process. Other MMMs such as Series 2, 3 and 4 GPMMMs, were prepared by direct graphene exfoliation in PIM-1 solution. The second method has several advantages over the first method, such as high graphene concentration and homogeneous dispersion. Nevertheless, Raman spectroscopies of GPMMMs from direct graphene exfoliation in PIM-1 solution confirmed that the graphene obtained is FLG. However, GPMMMs from the mixing

method (Series 1 GPMMMs) shows a combination of FLG and graphite flakes (about 50% each).

3.6 References

- (1) Yi, M.; Shen, Z. *J. Mater. Chem. A* **2015**, 3, 11700.
- (2) Yu, J. G.; Yu, L. Y.; Yang, H.; Liu, Q.; Chen, X. H.; Jiang, X. Y.; Chen, X. Q.; Jiao, F. P. *Sci. Total Environ.* **2015**, 502, 70.
- (3) Ramesha, G. K.; Vijaya Kumara, a.; Muralidhara, H. B.; Sampath, S. *J. Colloid Interface Sci.* **2011**, 361, 270.
- (4) Stankovich, S.; Dikin, D.; Dommett, G. H. B.; Kohlhaas, K. M.; Zimney, E. J.; Stach, E.; Piner, R. D.; Nguyen, S. T.; Ruoff, R. S. *Nature* **2006**, 442, 282.
- (5) Zöpfl, A.; Lemberger, M. M.; König, M.; Ruhl, G.; Matysik, F. M.; Hirsch, T. *Faraday Discuss.* **2014**, 173, 403.
- (6) Kemp, K. C.; Seema, H.; Saleh, M.; Le, N. H.; Mahesh, K.; Chandra, V.; Kim, K. S. *Nanoscale* **2013**, 5, 3149.
- (7) Lü, K.; Zhao, G. X.; Wang, X. K. *Chinese Sci. Bull.* **2012**, 57, 1223.
- (8) Geim, A. K.; MacDonald, A. H. *Phys. Today.* **2007**, 60, 35.
- (9) Si, Y.; Samulski, E. T. *Nano Lett.* **2008**, 8, 1679.
- (10) Novoselov, K. S.; Geim, K.; Morozov, S. V.; Jiang, D.; Zhang, Y.; Dubonos, S. V.; Grigorieva, I. V.; Firsov, A. *Science* **2004**, 306, 666.
- (11) Novoselov, K. S.; Jiang, D.; Schedin, F.; Booth, T. J.; Khotkevich, V. V.; Morozov, S. V.; Geim, K. *Proc. Natl. Acad. Sci. U. S. A.* **2005**, 102, 10451.
- (12) Wei, T.; Luo, G.; Fan, Z.; Zheng, C.; Yan, J.; Yao, C.; Li, W.; Zhang, C. *Carbon N. Y.* **2009**, 47, 2296.
- (13) Kuilla, T.; Bhadra, S.; Yao, D.; Kim, N. H.; Bose, S.; Lee, J. H. *Prog. Polym. Sci.* **2010**, 35, 1350.
- (14) Stankovich, S.; Piner, R. D.; Nguyen, S. T.; Ruoff, R. S. *Carbon N. Y.* **2006**, 44, 3342.
- (15) Niyogi, S.; Niyogi, S.; Bekyarova, E.; Bekyarova, E.; Itkis, M. E.; Itkis, M. E.; McWilliams, J. L.; McWilliams, J. L.; Hamon, M. a; Hamon, M. a; Haddon, R. C.; Haddon, R. C. *J. Am. Chem. Soc.* **2006**, 128, 7720.
- (16) Ciesielski, A.; Samorì, P. *Chem. Soc. Rev.* **2014**, 43, 381.
- (17) Ravula, S.; Baker, S. N.; Kamath, G.; Baker, G. A. *Nanoscale* **2015**, 7, 4338.

- (18) Liang, Y. T.; Hersam, M. C. *J. Am. Chem. Soc.* **2010**, *132*, 17661.
- (19) Kang, M. S.; Kim, K. T.; Lee, J. U.; Jo, W. H. *J. Mater. Chem. C.* **2013**, *1*, 1870.
- (20) Zhang, R.; Zhang, B.; Sun, S. *RSC Adv.* **2015**, *5*, 44783.
- (21) Haar, S.; Ciesielski, A.; Clough, J.; Yang, H.; Mazzaro, R.; Richard, F.; Conti, S.; Merstorf, N.; Cecchini, M.; Morandi, V.; Casiraghi, C.; Samorì, P. *Small* **2014**, *11*, 1691.
- (22) Coleman, J. N. *Adv. Funct. Mater.* **2009**, *19*, 1.
- (23) Del Rio-Castillo, A. E.; Merino, C.; Díez-Barra, E.; Vázquez, E. *Nano Res.* **2014**, *7*, 963.
- (24) Han, J. T.; Jang, J. I.; Kim, H.; Hwang, J. Y.; Yoo, H. K.; Woo, J. S.; Choi, S.; Kim, H. Y.; Jeong, H. J.; Jeong, S. Y.; Baeg, K.-J.; Cho, K.; Lee, G.-W. *Sci. Rep.* **2014**, *4*, 5133.
- (25) Modesto-López, L. B.; Miettinen, M.; Riikonen, J.; Torvela, T.; Pfüller, C.; Lehto, V.-P.; Lähde, A.; Jokiniemi, J. *Aerosol Sci. Technol.* **2014**, *49*, 45.
- (26) Grandthyll, S.; Gsell, S.; Weinl, M.; Schreck, M.; Hüfner, S.; Müller, F. *J. Phys. Condens. Matter* **2012**, *24*, 314204.
- (27) Zheng, Q.; Zhang, B.; Lin, X.; Shen, X.; Yousefi, N.; Huang, Z. D.; Li, Z.; Kim, J. K. *J. Mater. Chem.*, **2012**, *22*, 25072.
- (28) Chakrabarti, A.; Lu, J.; Skrabutenas, J. C.; Xu, T.; Xiao, Z.; Maguire, J. A.; Hosmane, N. S. *J. Mater. Chem.* **2011**, *21*, 9491.
- (29) Coleman, K.; Edwards, R. S. *Nanoscale* **2013**, *5*, 38.
- (30) Zhao, J.; Guo, Y.; Li, Z.; Guo, Q.; Shi, J.; Wang, L.; Fan, J. *Carbon N. Y.* **2012**, *50* (13), 4939–4944.
- (31) Kelber, J. A.; Gaddam, S.; Vamala, C.; Eswaran, S.; Dowben, P. A. *Proc. SPIE* **2011**, *8100*, 81000.
- (32) King, M. K. *Proc. Combust. Inst.* **2002**, *29*, 2931.
- (33) Wick, P.; Louw-Gaume, A. E.; Kucki, M.; Krug, H. F.; Kostarelos, K.; Fadeel, B.; Dawson, K. a.; Salvati, A.; Vázquez, E.; Ballerini, L.; Tretiach, M.; Benfenati, F.; Flahaut, E.; Gauthier, L.; Prato, M.; Bianco, A. *Angew. Chemie - Int. Ed.* **2014**, *53*, 7714.
- (34) Bianco, A.; Cheng, H. M.; Enoki, T.; Gogotsi, Y.; Hurt, R. H.; Koratkar, N.; Kyotani, T.; Monthieux, M.; Park, C. R.; Tascon, J. M. D.; Zhang, J. *Carbon N. Y.* **2013**, *65*, 1.

- (35) Shornikova, O. N.; Kogan, E. V.; Sorokina, N. E.; Avdeev, V. V. *Russ. J. Phys. Chem. A* **2009**, 83, 1022.
- (36) Matte, H. S. S. R.; Subrahmanya, K. S.; Rao, C. N. R. *Nanotechnol. Nanomater.* **2011**, 1, 3.
- (37) Gadipelli, S.; Guo, Z. X. *Prog. Mater. Sci.* **2015**, 69, 1.
- (38) Diaz-chacon, L.; Metz, R.; Dieudonné, P.; Bantignies, J. L.; Tahir, S.; Hassanzadeh, M.; Sosa, E.; Atencio, R. *J. Mater. Sci. Chem. Eng.* **2015**, 3, 75.
- (39) Ferrari, A. C.; Basko, D. M. *Nat. Nanotechnol.* **2013**, 8, 235.
- (40) Hao, Y.; Wang, Y.; Wang, L.; Ni, Z.; Wang, Z.; Wang, R.; Koo, C. K.; Shen, Z.; Thong, J. T. L. *Small* **2010**, 6, 195.
- (41) Khan, U.; Neill, A. O.; Lotya, M.; De, S.; Coleman, J. N. *Small* **2010**, 6, 864.
- (42) Gong, L.; Young, R. J.; Kinloch, I. a.; Haigh, S. J.; Warner, J. H.; Hinks, J. a.; Xu, Z.; Li, L.; Ding, F.; Riaz, I.; Jalil, R.; Novoselov, K. S. *ACS Nano* **2013**, 7, 7287.
- (43) Sur, U. K.; Sung, S. H.; Stiles, P. L.; Dieringer, J. a; Shah, N. C.; Van Duyne, R. P. *Resonance* **2010**, 15, 154.
- (44) Rourke, J. P.; Pandey, P. a.; Moore, J. J.; Bates, M.; Kinloch, I. a.; Young, R. J.; Wilson, N. R. *Angew. Chemie - Int. Ed.* **2011**, 50, 3173.
- (45) O'Neill, A.; Khan, U.; Nirmalraj, P. N.; Boland, J.; Coleman, J. N. *J. Phys. Chem. C* **2011**, 115, 5422.
- (46) Khan, U.; O'Neill, A.; Porwal, H.; May, P.; Nawaz, K.; Coleman, J. N. *Carbon N. Y.* **2012**, 50, 470.
- (47) Gonciaruk, A.; Althumayri, K.; Harrison, W. J.; Budd, P. M.; Siperstein, F. R. *Microporous Mesoporous Mater.* **2015**, 209, 126.
- (48) Sun, Z. *Msc Diss. Univ. Manchester.* **2013**, 52.
- (49) Pei, S.; Cheng, H. M. *Carbon N. Y.* **2012**, 50, 3210.
- (50) Aroon, M. A.; Ismail, A. F.; Matsuura, T.; Montazer-Rahmati, M. M. *Sep. Purif. Technol.* **2010**, 75, 229.
- (51) Yang, Y.; Rigdon, W.; Huang, X.; Li, X. *Sci. Rep.* **2013**, 3, 2086.

Chapter 4 Gas separation by GPMMMs

4.1 Gas separation membranes

4.1.1 Introduction

The history of assessing the gas separation behaviour of polymer membranes began with an observation made in 1831 by John Mitchell.¹ His simplest demonstration of gas transport using natural rubber, which is mainly *cis*-poly(isoprene), was made by filling several balloons with hydrogen and letting them float to the ceiling of his lecture theatre, from which they descended over time. Further experiments showed that different gas species would undergo various rates of gas transport through a specific material. Eventually, the development of polymeric gas separation membranes started to be considered for commercialization in the 1970s.² The market for these membranes has grown significantly since then, and more are expected to be developed as technology progresses and applications increase.³

Polymer-based membranes are notable in providing an energy-efficient gas separation technique, as there is no need for a phase change, thermal regeneration or active moving parts in the process. Generally, the driving force for gas separation is a partial pressure difference across the membrane. Commercially attractive processes include hydrogen separation in ammonia production (especially H_2 from N_2) and in hydrocarbon processing (e.g. H_2 from CH_4), O_2 and N_2 enrichment of air, and natural gas purification (especially CO_2 from CH_4).⁴ Desirable performance in this technique requires both high productivity (i.e. high permeability) and high achievable separation (i.e. high selectivity). However, the trade-off between these two parameters is problematic in membrane gas separation. At present, gas separation is commercially based on polymers with low permeability and high selectivity. The lack of productivity is compensated by the use of a large membrane area.⁴

The trade-off for a given gas pair can be represented by a double logarithmic plot of the selectivity coefficient (i.e. the ratio of permeabilities) against the permeability coefficient (expressed as permeance multiplied by membrane thickness) of the fastest species (Figure 4-1). In 1991, Robeson illustrated the first empirical upper bound plots of such gas pairs, by which state-of-art performance can be utilized to compare polymers.⁵ As a result of significant developments in the area of gas

separation membranes, another upper bound was established in 2008. PIMs are competitive candidates in the separation of several gas pairs, some of which surpass the 2008 upper bound, as can be seen in Figure 4-1.

The upper bound has the following relationship:

$$P_i = k\alpha_{ij}^n \quad (4-1)$$

where P_i is the permeability of species i , α is selectivity of species i over j , n is the slope and k is a constant for a specific gas pair, named the front factor. Empirically, the slope $1/n$ is found to be in a linear relationship with the difference in diameters of a gas pair ($d_j - d_i$).⁶

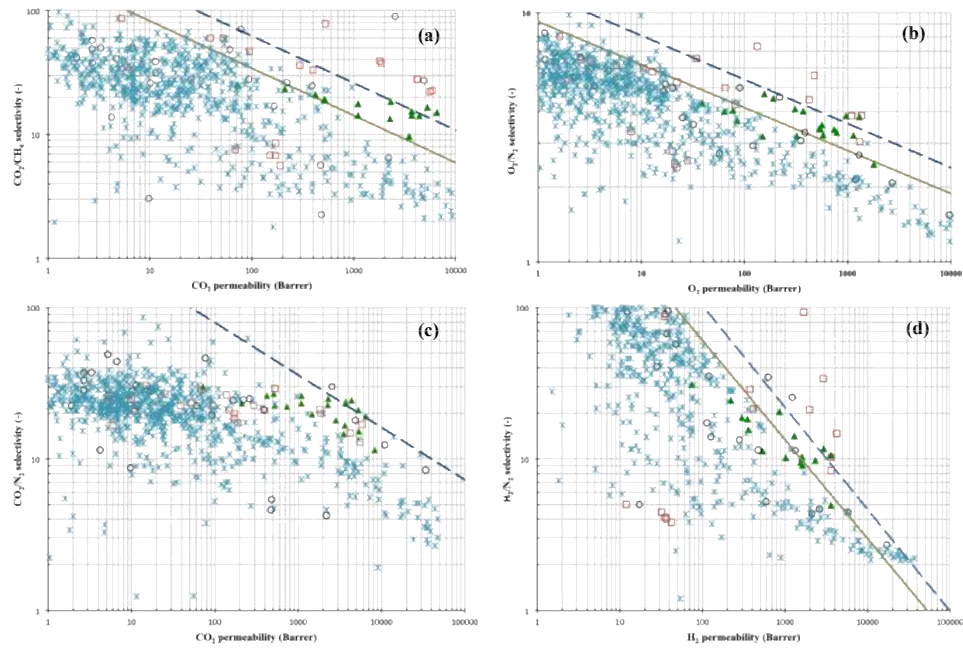


Figure 4-1. Robeson plots illustrating the correlation of permeability and permselectivity for various industrially important gas pairs: (a) CO₂/CH₄, (b) O₂/N₂, (c) CO₂/N₂ and (d) H₂/N₂. The solid brown line is the 1991 upper bound, the dashed blue line is the 2008 upper bound, filled green triangles indicate PIMs, non-filled red squares indicate thermal-rearranged polymers, non-filled circles indicate other high free-volume polymers and asterisks indicate various polymers.⁷

Significant developments in the area of synthetic polymers have supported the fundamental concept, which draws relationships between the polymer structure and gas permeation properties.⁸ In the case of glassy polymers, the sensitivity towards

chemical structure is very significant. For example, the permeability coefficient can be low for a polymer such as polyacrylonitrile ($P_{\text{CO}_2} = 0.0003$ barrer),⁹ whereas it can be high for one such as poly(trimethylsilyl)propyne (PTMSP) ($P_{\text{CO}_2} = 27000$ barrer).¹⁰ Some bulky chemical groups, such as $\text{Si}(\text{CH}_3)_3$, $\text{Ge}(\text{CH}_3)_3$ and $\text{CH}(\text{CH}_3)_2$, are suggested as useful components for increasing the permeation rate.¹¹ In addition, the presence of aromatic units in the polymer chains can determine the rigidity and high free volume that enhance the permeation rate. Moreover, glassy polymers have been found in general to offer a relatively good combination of selectivity and permeability,⁸ having the rigid structure and ineffective chain packing that provide the distinct size distribution of the free volume which is required to deliver the molecular sieving property. PIMs demonstrate the importance of these components in obtaining high performance membranes, as can be seen in Figure 4-1.

Membrane permeance is a key property in gas transport and can determine to what extent the membrane can be used for gas separation. It is determined by measuring the amount of gas that can pass through a certain effective membrane area under a given pressure difference. The permeability coefficient P can be obtained from Equation 4-2:

$$P = \frac{J \cdot l}{\Delta p} \quad (4-2)$$

where J is the flux, l is the membrane thickness and Δp is the pressure difference.

The gas transport mechanism plays a key role in determining the performance of gas separation membranes, which also depends on structural properties. In the case of nonporous or microporous polymeric membranes, gas transport is predominantly associated with the solution-diffusion mechanism proposed by Graham in 1866.¹² According to this model, transport starts when gas dissolves into the membrane surface on the high chemical potential feed side, followed by its diffusion through the membrane, and ends with its desorption from the low chemical potential permeate side of the membrane. Therefore, permeation is mainly governed by two factors, the diffusion and solubility coefficients, as Equation 4-3 shows.¹³

$$P = D * S \quad (4-3)$$

where S is the solubility coefficient. The permeability coefficient P is usually expressed in barrer, where $1 \text{ barrer} = 10^{-10} \text{ cm}^3 [\text{STP}] \text{ cm cm}^{-2} \text{ s}^{-1} \text{ cmHg}^{-1} = 10^5 \text{ Pa}$ (SI unit).

Another important factor in the gas transport process is the permselectivity coefficient (α_p) of a gas pair, given simply by the ratio of permeability coefficients (Equation 4-4). The ratio of the faster gas (A) to the slower gas (B) defines the permselectivity. Based on the contribution of both diffusion and solubility coefficients, permselectivity can be also given by Equation 4-5.

$$\alpha_p = \frac{P_A}{P_B} \quad (4-4)$$

$$\alpha_p = \frac{D_A}{D_B} * \frac{S_A}{S_B} \quad (4-5)$$

In general, glassy polymers exhibit permeability dominated by diffusion selectivity, as a consequence of their structural properties and free volume contributions. By contrast, gas transport through rubbery polymers is predominantly determined by sorption selectivity, making them interesting for condensable gases or vapour separation.¹⁴ However, exceptional polymers are not included in this general consideration. For instance, glassy polymers like perfluoropolymers exhibit high gas solubility compared to other polymers.⁶

The free volume in a polymer considerably enhances the diffusion coefficient, as predicted by the Cohen-Turnbull model. Equation 4-6 shows this relationship clearly.³

$$D = A \exp\left(\frac{\gamma^* v^*}{FFV}\right) \quad (4-6)$$

where A is a constant, γ is an overlap factor incorporated to avoid duplication in counting the fractional free volume, v^* is a factor related to permeant size and FFV is the fractional free volume. FFV is given by the following equation:

$$FFV = \frac{V_s - (1.3 \cdot V_w)}{V_s} \quad (4-7)$$

where V_s is the specific volume of the polymer and V_w is the van der Waals volume, multiplied here by 1.3 to give the potential efficient packing volume for a perfect crystal at zero temperature.³

Significant and simultaneous improvements in diffusion selectivity and sorption selectivity—and consequently permeability—are the remaining challenges for ideal membrane preparation. Recently, polymeric membranes of high gas separation performance have been developed from high free volume glassy polymers,⁸ starting with PTMSP, as reported by Masuda *et al.* in 1983.¹⁵ Those which followed include acetylene-based polymers (e.g. poly(4-methyl-2-pentene) (PMP) and poly(1-phenyl-1-propyne) (PPP)), involving various substituent groups.¹⁴ Moreover, a number of fluorinated polymers such as AF1600, AF2400, Hyflon AD and Cytop were commercially named for gas separation (Figure 4-2).³

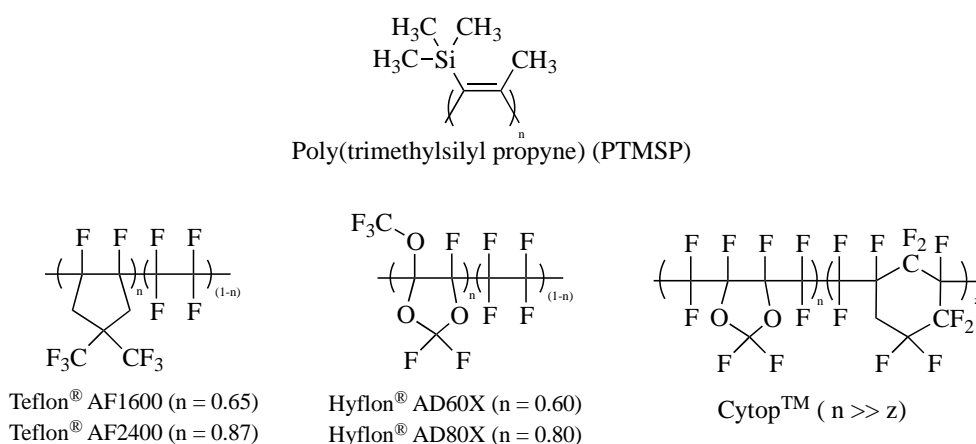


Figure 4-2. Examples of glassy polymers with high gas permeability.

In recent studies, high free volume polymers such as PIMs and thermally rearranged (TR) polymers have shown superior performance in gas separation. TR polymers can be obtained from polymer pyrolyzation, an example being polyimide

polymers pyrolyzed at 500-700 °C to give carbon membranes, or at lower temperatures to give polymeric membranes. Furthermore, incorporating –OH or –SH substituents in the ortho position of the imide can lead respectively to the formation of polybenzoxazoles and polybenzothiazoles (Figure 4-3),⁸ all of which yields significantly different gas transport properties from those of the original polyimides. However, the mechanical properties of TR polymers can be affected negatively by high processing temperature, in addition to the solubility properties, as TR polymers are insoluble.^{3, 8}

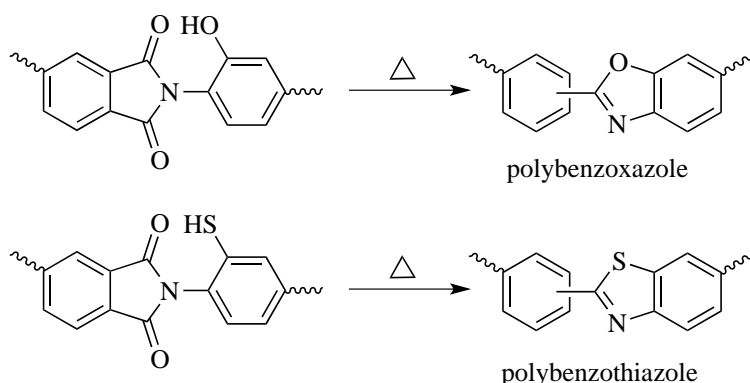


Figure 4-3. Examples of TR polymer preparation from polyimides. These examples are subjected to thermal treatment conditions with lower relative temperature, potential structural rearrangement from distinctive incorporation of –OH or –SH groups.

4.1.2 MMMs in gas separation

An emerging approach to enhancing the performance of polymeric gas separation membranes is considered to be the preparation of mixed matrix membranes (MMMs), consisting of organic polymers and inorganic fillers, schematically represented in Figure 4-4. This approach was established when many inorganic membranes such as carbon molecular sieves and zeolite membranes were found to surpass the upper bound.¹⁶ However, inorganic membrane applications were hindered by the high cost of preparation and difficulty in processing membranes in continuous and defect-free forms, as well as their fragility. The MMM approach is considered to overcome these problems, combining high gas transport performance with mechanical properties such as flexibility, in the case of choosing a flexible polymer.^{17, 18}

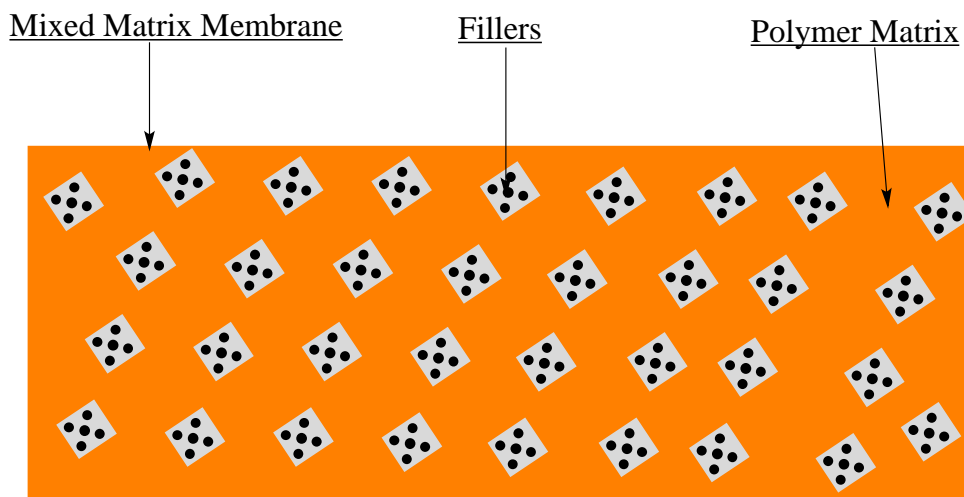


Figure 4-4. Schematic representation of an ideal MMM.

Substantial developments in MMM studies are based on tailoring polymer structure by incorporating inorganic fillers, which have unique surface chemistry, structure and mechanical properties. This combination can lead to the enhancement of separation capability. Therefore, MMMs have the potential for high performance gas separation, combining high selectivity with permeability.

In the first study of MMMs, in the 1970s, Paul and Kemp fabricated an MMM by incorporating zeolite-A5 into polydimethyl siloxane (PDMS), resulting in a significant increase in the diffusion time lag for CO_2 and CH_4 , relative to pure PDMS.¹⁹ In the 1980s, researchers at UOP LLC first reported the potential use of MMMs to obtain superior gas separation performance, initially examining an MMM of cellulose acetate (CA) and silicalite.¹⁸ However, among the many studies of MMMs, there have been repeated reports of fabrication difficulties, such as low component compatibility, leading to poor contact between filler and polymeric matrix, and poor filler distribution through the matrix. Other considerations are filler size, filler pore characteristics, amount of filler loading and polymer properties, all of which determine the properties of the resultant MMMs.

Tailoring desirable MMMs depends on the extent to which these aspects of MMM fabrication can be controlled to produce nanoscale modifications of morphology, particularly interface morphology. Six possible cases are proposed, when the fillers are sieves, as can be seen in Figure 4-5.

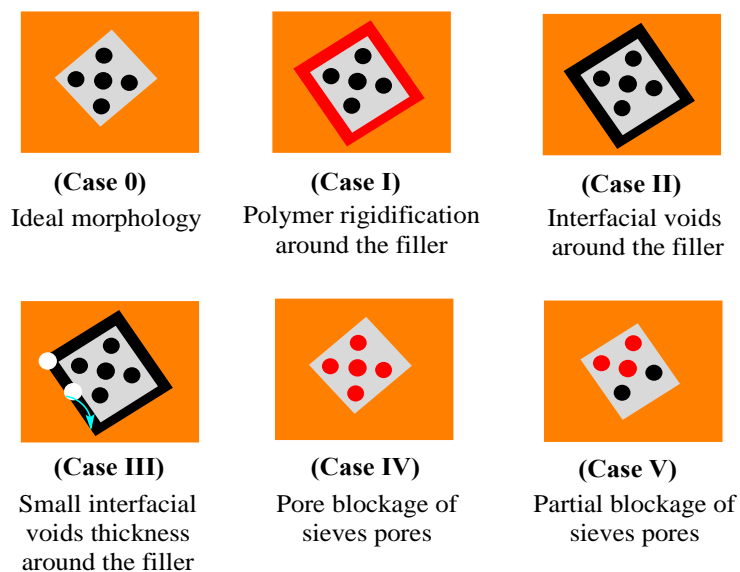


Figure 4-5. Six possible interfacial morphologies influencing gas transport properties.

Case 0 is the ideal case that can improve both permselectivity and permeability. In Case I, fillers are surrounded with rigid layers of polymer, reducing permeability. Case II illustrates the presence of interfacial voids between the polymer matrix and filler, inducing permeability. Case III is similar to case II, the difference being in the thickness of the voids, which is close to the permeant size. Cases IV and V involve sieve blockage, such as by the trapping of residual solvent, which hinders the permeation of gas through the sieves. In case IV the sieve pores are completely blocked; thus, there is no permeation. In case V, the sieves are partially blocked at the surface, which reduces permeability.²⁰

Moore and Koros have reported these cases in a comprehensive paper.²⁰ Their study shows the relationship between interfacial morphology and gas transport properties (Figure 4-6), based on Maxwell model predictions and experimental results, using MMMs prepared from components with well-characterized gas transport properties. The MMMs were prepared from zeolite A4 as filler and Ultem as polymeric matrix.

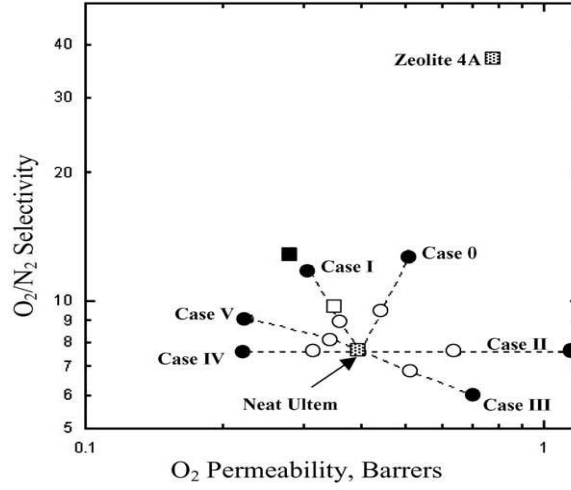


Figure 4-6. Plot adapted from Moore and Koros,²⁰ summarizing the relationship between various MMM morphologies and transport properties. Circles indicate predicted values; squares show experimental results. Filled markers are 35 vol.% Zeolite A4; non-filled markers are 15 vol.% 4A.

The Maxwell model is used to predict the effective permeability from ideal incorporation in the polymeric matrix of porous inorganic fillers, in small volume fractions. The model can be expressed in the following form:

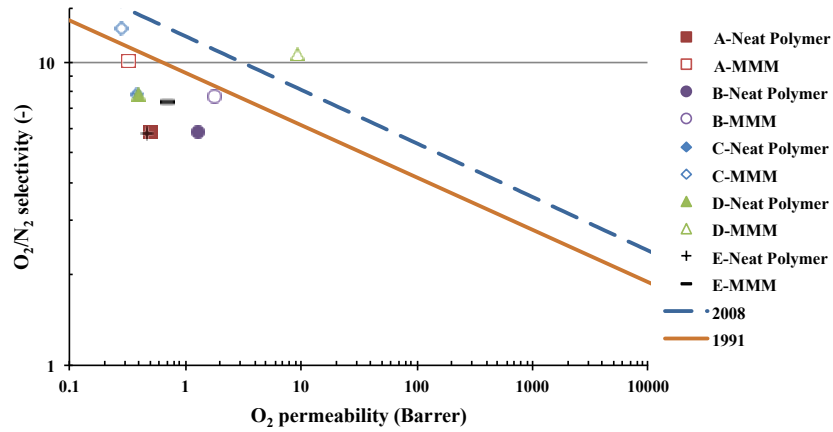
$$P_{\text{MMM}} = P_p \left[\frac{P_f + 2P_p - 2\phi_f(P_p - P_f)}{P_f + 2P_p + \phi_f(P_p - P_f)} \right] \quad (4-8)$$

where P_{MMM} is the effective permeability of the MMM, ϕ_f is the filler volume fraction, and P_p and P_f are the permeabilities of polymer and filler, respectively. This formula applies to an ideal case (case 0), where there are no defects and the individual phases exhibit uniform gas transport properties. In other cases, the Maxwell model equation requires modifications in order to calculate the effective MMM permeability of each individual case.^{17, 18, 20} The model notably does not take account of filler size distribution, filler shape or filler aggregations.

In general, MMMs can be prepared using porous or non-porous fillers. Porous fillers, as in the previously given example, have different influences on MMM performance, mainly based on pore size and structure. In general, porous fillers perform like molecular sieves in MMMs, separating the permeant gases based on filler shape and size. This approach is associated with conventional MMMs.¹⁸

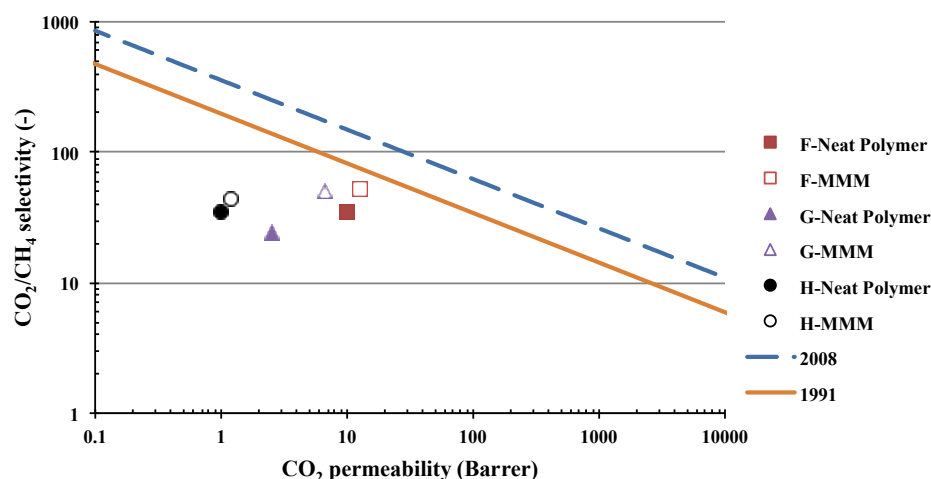
Moreover, both porous fillers and polymers have to be considered, based on their gas transport properties. Generally, porous fillers have better permselectivity than polymers. Nevertheless, small additions of porous filler to a polymer can result in significant improvement in its gas transport properties, as can be predicted from the Maxwell model. Table 4-1 illustrates several MMMs evaluated for N₂/O₂ separation, all of which have improved selectivity compared with the neat polymers. Table 4-2 shows several examples of MMMs with improved gas separation performance for CO₂/CH₄.

Table 4-1. Several MMM examples from the literature with improved O₂/N₂ separation.¹⁸



MMM	Polymer	Filler (loading)	Investigators (Ref.)
A-MMM	PVAc	4A zeolite (40 vol%)	Mahajan and Koros [21]
B-MMM	Psf	4A zeolite (25 wt%)	Wang et al. [22]
C-MMM	Ultem s PEI	4A zeolite (35 vol%)	Mahajan and Koros [23]
D-MMM	Ultem s PEI	H-SSZ-13 (14 wt%)	Kulkarni et al. [24]
E-MMM	PES	5A zeolite (50 wt%)	Li et al. [25]

Table 4-2. Several MMM examples from the literature with improved CO₂/CH₄ separation.¹⁸



MMM	Polymer	Filler (loading)	Investigators (Ref.)
F-MMM	Matrimids PI	CMS (36 vol%)	Vu et al. [²⁶]
G-MMM	ABS	AC (62.4 vol%)	Anson et al. [²⁷]
H-MMM	PES	A zeolite with silver ion exchange (50 wt%)	Li et al. [²⁸]

An unconventional type of MMM was introduced, comprising non-porous nano-inorganic fillers. Pinnau and He reported an increase in the permeability of glassy polymers after the addition of non-porous fillers such as fumed silica and carbon black.²⁹ These investigations led to the conclusion that fillers contribute by hindering the effective packing of polymer chains. Further studies on incorporating non-porous fillers, such as fumed silica, MgO and TiO₂, have shown that the resultant permeability of MMMs exceeded the predictions of the Maxwell or any other associated models.^{30, 31} This system provides a higher free volume content than that of unfilled polymers, resulting in significant permeability, despite the fact that the fillers are non-porous and impermeable. Moreover, gas transport properties are influenced directly by the modification of the free volume cavities that result from tailoring the size and shape of the micropores at the nanoscale level.

This chapter considers the influence of non-porous fillers, particularly graphene fillers, on the gas transport properties of PIM-1.

4.2 Experimental

4.2.1 Experimental setup

In this project, Dr. Paola Bernardo, Dr Gabriele Clarizia and Dr. Johannes Jansen performed all permeability measurements at the Institute on Membrane Technology (ITM), Italy, on an instrument made by GKSS (Germany), based on the time lag method. Each measurement was performed for a single gas, with the feed pressure set at 1 bar and the permeate side equipped with pneumatic valves controlled by a computer to create an operating system able to respond to a pressure increase in less than 0.1 seconds. Membranes were supported on stainless steel porous discs. Gases tested were He, H₂, N₂, O₂, CH₄, and CO₂ with a purity of 99.998% and each feed gas was at a fixed volume of 2 L (Figure 4-7).

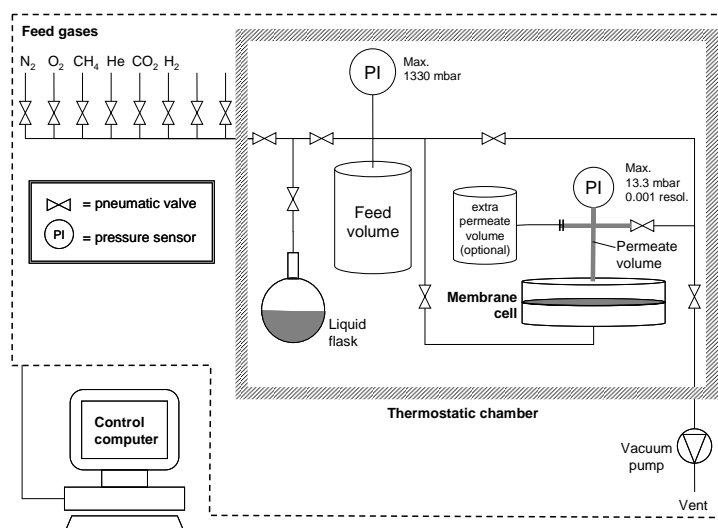


Figure 4-7: Schematic presentation of the permeation experiments performed at ITM.

These gases were tested on a perforated aluminium foil membrane to give time lags as shown in Figure 4-8. The instrumental time lag (θ) for each gas was determined by the intersection with the horizontal axis and found to be less than 0.1 seconds for all gases, as expected. These time lags were shorter than the shortest ones measured for microporous membranes (e.g. PIM-1) using the fastest gas, *i.e.* helium (Figure 4-9). Thus, the error in diffusion coefficient due to instrumental time lag is negligible for all measured gases. A proportional relationship between pressure increments and gas volume was noted for the perforated aluminium foil membrane.

This result also followed the trend of Knudsen diffusion. However, the permeation rates of these measurements ($>1 \text{ mbar s}^{-1}$) were significantly faster than those for common microporous membranes, which makes the instrumental transport resistance negligible.

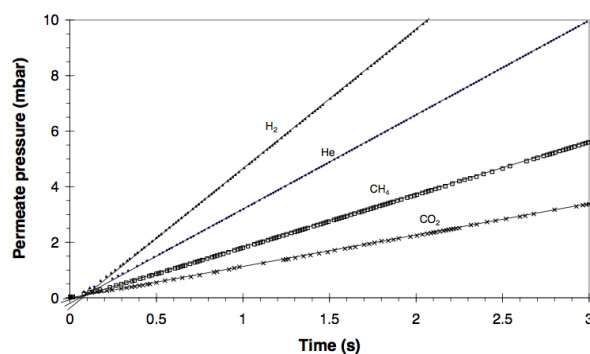


Figure 4-8. Time lag measurements on perforated aluminium foil for H_2 , He, CH_4 and CO_2 .³²

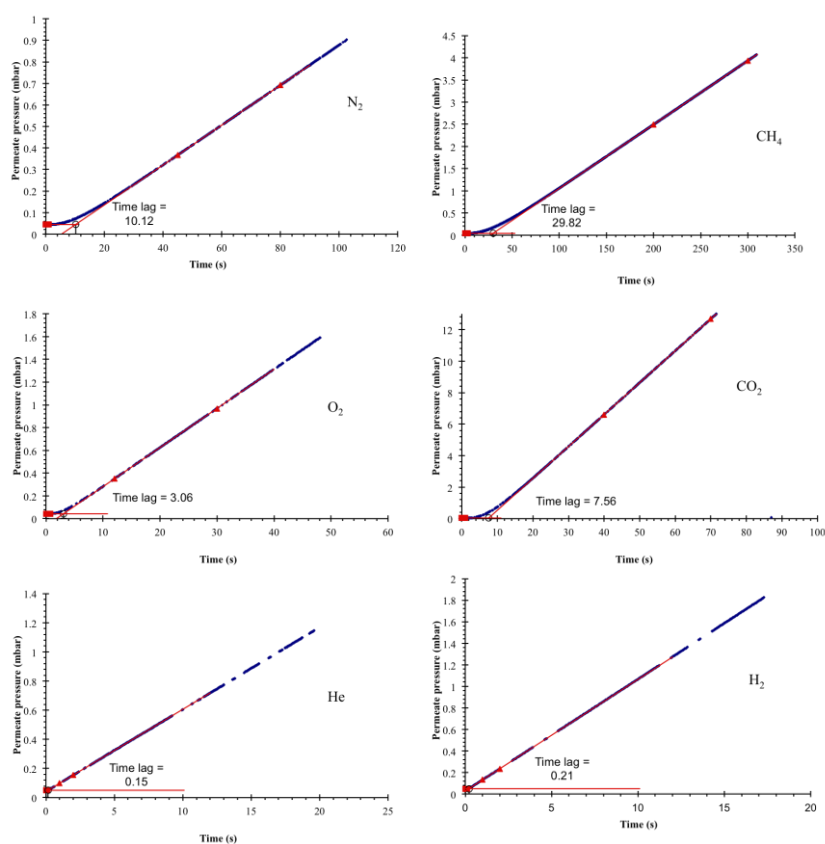


Figure 4-9. Permeate pressure versus time of various gases tested on a PIM-1 membrane as cast, determining the time lag for each gas.

Sample evacuation at 2-10 mbar was always performed before each experiment to ensure the removal of any dissolved gas species. Samples were measured as flat circular membranes with effective area of 2.14 cm² and membrane thickness was measured before each trial with a digital micrometer (Mitutoyo, Model IP65). Most membranes were tested as received and after methanol soaking followed by drying overnight in air at room temperature.

4.2.2 Determination of gas transport coefficients by time lag method

The diffusion coefficient (D) can be determined by the time lag method using Equation 4-9:

$$\theta = \frac{l^2}{6D} \quad (4-9)$$

where θ is the time lag and l is the membrane thickness.

The permeability coefficient (P) can then be calculated from the time lag results, using Equation 4-9:

$$P_t = P_0 + \left(\frac{dp}{dt}\right)_0 \cdot t + \frac{RT \cdot A \cdot l}{V_p \cdot V_m} P_f \cdot S \left(\frac{D \cdot t}{l^2} - \frac{1}{6} - \frac{2}{\pi^2} \sum_{n=1}^{\infty} \frac{(-1)^n}{n^2} \exp\left(-\frac{D \cdot \pi^2 \cdot n^2 \cdot t}{l^2}\right) \right) \quad (4-10)$$

where P_t is permeate pressure at time t , P_0 is permeate pressure at the initial time, $(dp/dt)_0$ is the baseline slope (empirically negligible if the sample is defect free), P_f is feed pressure, R is the universal gas constant, T is absolute temperature, A is effective membrane area, V_p and V_m are respectively the permeate volume and molar volume of the gas at standard temperature and pressure (0 °C, 1 atm), t is time.

This equation can be expressed as Equation 4-11, where the last term was added to correct the time lag (θ).

$$P_t = \frac{RT \cdot A}{V_p \cdot V_m} \cdot \frac{P_f \cdot S \cdot D}{l} \left(t - \frac{l^2}{6D} \right) \quad (4-11)$$

These equations express values that can be calculated from the time lag curve. Figure 4-10 illustrates more clearly their use in finding the permeation and diffusion coefficients. Once P and D have been obtained from the curve, the solubility coefficient can be calculated by Equation 2-9:

$$S = \frac{P}{D} \quad (4-12)$$

It is worth mentioning that this is a steady-state (i.e. stationary state) measurement. Therefore, there are transforming stages before equilibrium concentration takes place in the permeation route, as shown in Figure 4-10b. Equilibrium between the feed gas and the membrane surface can be reached immediately after the membrane is exposed to the feed gas. The penetrated gas then starts to diffuse into the membrane matrix and a linear concentration profile can be observed after some time. The speed with which the stationary state is reached depends on the diffusion coefficient.

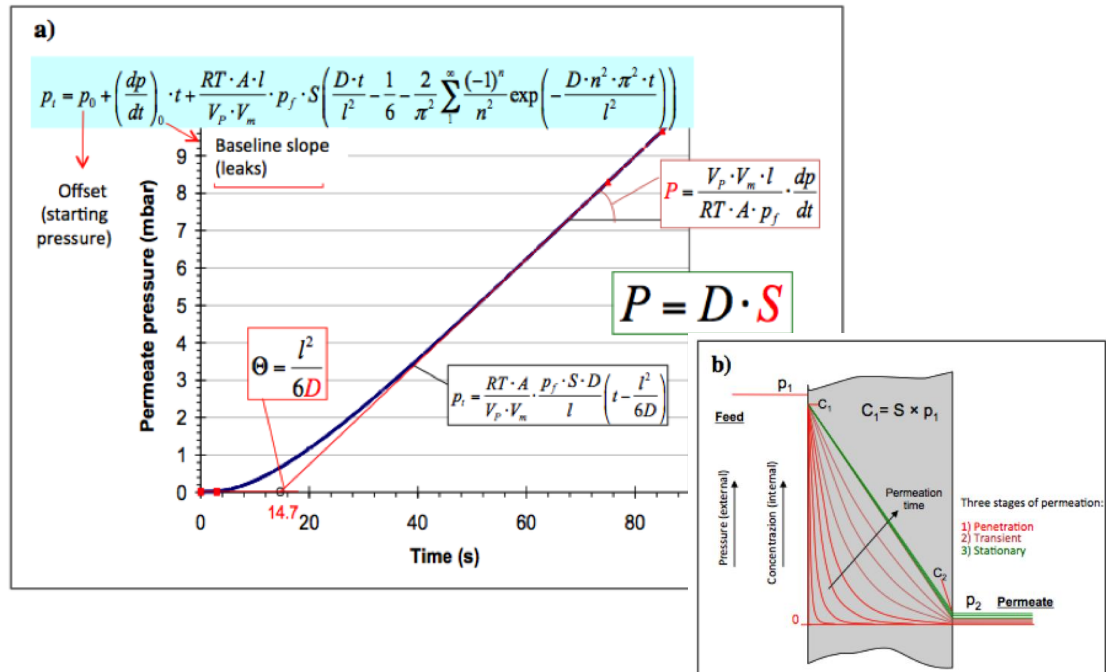


Figure 4-10. a) Illustration of the use of a permeation curve to find the permeation coefficient (P) and diffusion coefficient (D) from time lag (θ), as well as the indirect determination of solubility coefficient (S). b) Shows how the concentration profile can develop over time. This figure was produced by Johannes Jansen at ITM.

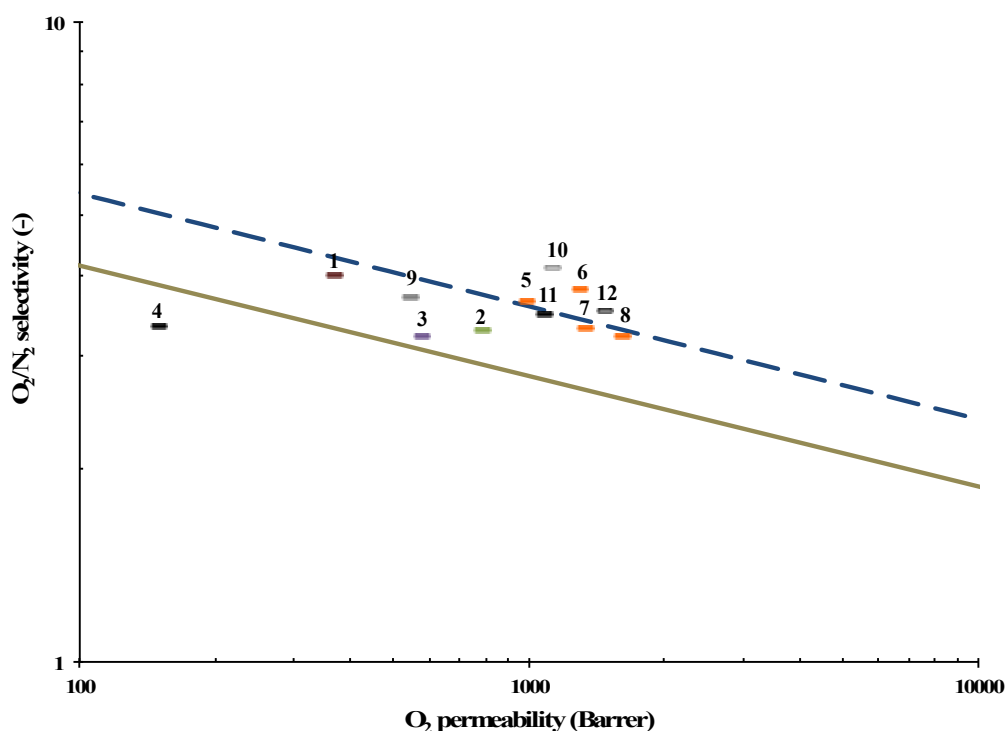
The margin of error of this measurement is considered to be within 5%. A number of MMMs were measured to compare their performance, using neat polymeric membranes as control samples. Additional measurements were carried out on these membranes after methanol treatment, and some after storage for known periods of time. Methanol treatment was performed by soaking the membrane in methanol overnight, before it was air-dried and placed in a vacuum oven overnight at 120 °C.

4.3 Results and discussion

4.3.1 Variation in gas transport properties among PIM-1 membranes

Gas transport properties are influenced directly by sample preparation, including solvent type and drying conditions.^{30,33} Table 4-3 shows various PIM-1 samples from the literature and from this work with different gas separation performances, correlated to different casting and treatment solvents.

Table 4-3. Variation of gas transport properties from different PIM-1 preparation conditions, using the example of O₂/N₂ separation. Data adapted from ref.



Example No.	Casting solvent / treatment	Reference	Example No.	Casting solvent / treatment	Reference
1	Tetrahydrofuran	Budd [34]	7	Chloroform / methanol	Ahn [35]
2	Dichloromethane	Staiger [36]	8	Chloroform / methanol	Budd [33]
3	Chloroform	Budd [33]	9	Chloroform	KA1-1 [this work]
4	Chloroform / water	Budd [33]	10	Chloroform / methanol	KA1-1 [this work]
5	Chloroform / methanol	Song [37]	11	Chloroform	KA1-4 [this work]
6	Chloroform / methanol	Tomas [38]	12	Chloroform / methanol	KA1-4 [this work]

Residual solvents can also influence gas transport properties, depending on the nature of the interactions between solvents molecules and the polymeric matrix. Solvent molecules can simply reduce the potential free volume and block a number of interconnecting pathways for gas transport. Therefore, strong interactions between solvent molecules and PIM-1 promote insufficient removal of these molecules by conventional processes such as exposure to heat or pressure. Residual water, for example, has a relatively strong hydrogen bond with PIM-1 and can therefore accumulate intrinsically in the PIM-1 matrix and reduce its permeability.³³ The same influence is expected from the presence of residual DMF or DMAc. Extensive water treatment is often used to remove DMF or DMAc.

Lower alcohols like methanol or ethanol have a particular effect on PIM-1, causing it to swell, which increases the interconnected free volume and thus the permeability. They can also aid in removing residual solvent. However, the extra free volume obtained by treatment with lower alcohols may not persist with time. Therefore, this phenomenon needs to be observed carefully.

The influence on PIM-1 performance of the abovementioned factors must be considered, along with others potentially arising from discrepancies in preparation or treatment which have not been well studied. Thus, the study of any series of PIM-1 membranes requires control samples to be included, to discount any confounding effects of sample preparation.

In this work, control samples of PIM-1 were tested along with filled PIM-1 membranes, in order to study the real effects on PIM-1 gas transport properties.

Control samples from two different batches showed significantly different permeability coefficients: KA1-1 can be described as a low-permeable PIM-1, relative to the high-permeable KA1-4. The low permeability of KA1-1 is associated with its residual water content from the preparation procedure. Conversely, the higher permeability coefficient of KA1-4 can be attributed to extensive methanol treatment of PIM-1 powder that reduced its water content. These observations are associated with permeation measurements of samples categorized as as-cast membranes. Figure 4-11 shows the difference in water content reflected in the ^1H NMR spectra.

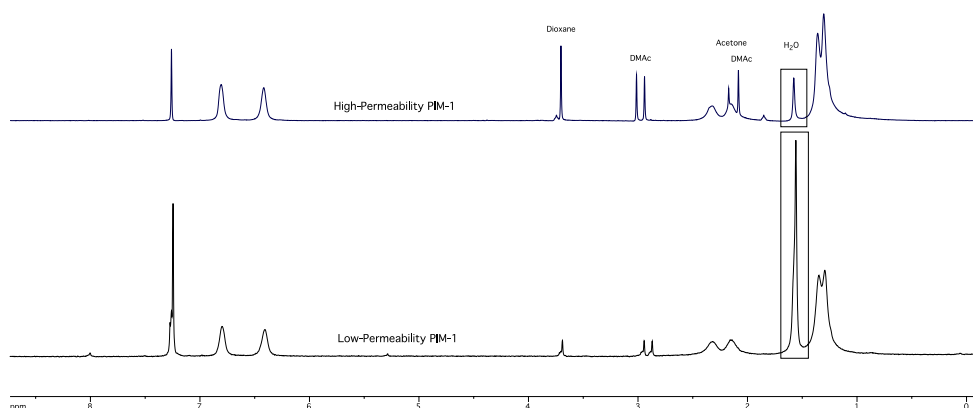


Figure 4-11. ^1H NMR spectra of low- and high- permeability PIM-1 batches (as powder in chloroform) (KA1-1 and KA1-4, respectively), showing a significant difference in water content.

4.3.2 Gas transport properties of GPMMMs

Series 2 GPMMMs, prepared as previously described, were tested before and after alcohol treatment; the results are shown in Table 4-4 and Table 4-5. Three of these membranes and the control PIM-1 (KA1-1) were also tested after being stored for approximately eight months (Table 4-6). Permeation data for Series 3 GPMMMs before and after methanol treatment are shown in Table 4-7 and Table 4-8, while Table 4-9 shows equivalent data for Series 4 GPMMMs as cast.

Table 4-4. Permeation data of Series 2 GPMMMs as cast.

Membrane	Graphene content (Wt. %)	Thickness (μm)	Permeability P (barrer)					
			CO ₂	H ₂	He	O ₂	CH ₄	N ₂
KA1-1	0	50.3	3120	1581	724	546	210	147
GPMMM-2 (6)	0.1	315.5	4784	1996	847	869	515	297
GPMMM-2 (4)	0.2	93.3	4494	2234	987	797	333	226
GPMMM-2 (3)	0.3	48	3774	1968	884	657	233	170
GPMMM-2 (2)	0.7	20.2	2701	2091	964	538	143	123
GPMMM-2 (1)	2.4	73.4	2142	1078	514	367	157	103

Table 4-5. Permeation data of Series 2 GPMMMs after methanol treatment.

Membrane	Graphene content (Wt. %)	Thickness (μm)	Permeability P (barrer)					
			CO ₂	H ₂	He	O ₂	CH ₄	N ₂
KA1-1	0	59	5119	3206	1609	1128	341	273
GPMMM-2 (6)	0.1	352	12699	4658	1771	2263	1451	869
GPMMM-2 (4)	0.2	100	9836	4734	1893	1852	801	569
GPMMM-2 (3)	0.3	52	7835	4472	1827	1563	551	415
GPMMM-2 (2)	0.7	24	3407	3863	1949	818	163	173
GPMMM-2 (1)	2.4	86	5151	3206	1387	1036	391	270

Table 4-6. Permeation data of Series 2 GPMMMs after ageing.

Membrane	Graphene content (Wt. %)	Age (Days)	Thickness (μm)	Permeability (barrer)					
				CO ₂	H ₂	He	O ₂	CH ₄	N ₂
KA1-1	0	244	57	3,700	2,700	1,200	730	200	160
GPMMM-2 (6)	0.1	226	351	9,200	4,000	1,600	1,800	980	620
GPMMM-2 (4)	0.2	236	94	6,700	3,500	1,400	1,300	460	340
GPMMM-2 (3)	0.3	236	50	5,700	3,200	1,400	1,100	330	260

Table 4-7. Permeation data of Series 3 GPMMMs as cast.

Membrane	Graphene content (Wt. %)	Thickness (μm)	Permeability (barrer)					
			CO ₂	H ₂	He	O ₂	CH ₄	N ₂
KA1-4	0	46	6327	2984	1240	1081	439	309
GPMMM-3 (14)	0.02	50	4625	2623	1160	846	309	226
GPMMM-3 (13)	0.03	39	5510.7	2868.1	1275	944	353	255
GPMMM-3 (12)	0.04	42	6637	3304	1366	1181	435	340
GPMMM-3 (11)	0.05	40	5463	2708	1144	944	353	255
GPMMM-3 (10)	0.07	41	5708	3023	1275	1023	374	275
GPMMM-3 (9)	0.1	40	4701	2470	1086	831	294	216
GPMMM-3 (8)	0.13	50	6687	3178	1301	1188	481	354
GPMMM-3 (6)	0.22	46	5903	2697	1133	1011	418	301
GPMMM-3 (5)	0.3	46	6311	3081	1289	1107	417	305
GPMMM-3 (3)	0.53	54	5536	2696	1139	966	383	274
GPMMM-3 (2)	0.7	53	2850	1638	792	505	192	137
GPMMM-3 (1)	1	48	4736	2421	1078	872	329	228

Table 4-8. Permeation data of Series 3 GPMMMs after methanol treatment.

Membrane	Graphene content (Wt. %)	Thickness (μm)	Permeability (barrer)					
			CO ₂	H ₂	He	O ₂	CH ₄	N ₂
KA1-4	0	46	7518	4079	1657	1473	510	415
GPMMM-3 (14)	0.02	50	6183	3376	1405	1103	404	328
GPMMM-3 (13)	0.03	44	7930	4049	1668	1409	548	394
GPMMM-3 (12)	0.04	42	8165	3950	1602	1480	600	427
GPMMM-3 (11)	0.05	40	5189	2731	1168	932	364	258
GPMMM-3 (10)	0.07	41	6352	3675	1530	1207	416	303
GPMMM-3 (9)	0.1	40	8774	4084	1650	1562	647	488
GPMMM-3 (8)	0.13	50	7392	3825	1561	1348	505	369
GPMMM-3 (6)	0.22	46	7787	3748	1532	1358	555	425
GPMMM-3 (5)	0.3	46	6842	3633	1514	1277	464	361
GPMMM-3 (3)	0.53	54	7708	3664	1483	1387	573	399
GPMMM-3 (2)	0.7	53	7203	9036	4760	289	3261	2376
GPMMM-3 (1)	1	48	6786	3438	1412	1262	502	366

Table 4-9. Permeation data of Series 4 GPMMMs as cast.

Membrane	Graphene content (Wt. %)	Thickness (μm)	Permeability P (barrer)					
			CO ₂	H ₂	He	O ₂	CH ₄	N ₂
KA1-4	0	46	6326.5	2984.4	1240.1	1081.02	438.59	309.39
GPMMM-4 (17)	0.04	37	5105.2	2727.7	1164.5	921.67	326.66	249.84
GPMMM-4 (15)	0.08	52	5269.7	28634	1247.2	959.97	356.04	259.68
GPMMM-4 (13)	0.13	62	6887.8	2927.1	1206.4	1150.6	523.07	352.99
GPMMM-4 (10)	0.31	44	5470.2	275	1172.8	952.5	356.69	262.93
GPMMM-4 (8)	0.56	63	5201.8	2217.8	938.9	853.24	399.06	267.744
GPMMM-4 (6)	1	51	3256.1	1628.2	725.2	567.63	239.74	169.78
GPMMM-4 (3)	2.38	51	2372	1136	536	377	171	111
GPMMM-4 (1)	4.22	55	1031	564	298	165	75	48

Graphene fillers are impermeable, yet they can induce permeability by prohibiting further potential packing of polymer chains, so that extra free volume can be gained from their incorporation. The phenomenon of permeability enhancement by addition of nanofillers has been observed in several low-loading MMMs, such as those comprising fused silica and functionalized multi-walled carbon nanotubes (f-MWCNTs) in PIM-1.^{30, 39, 40}

This study chose to target few-layer graphene nanofillers and to investigate their effects on the gas transport properties of PIM-1.

This work presents data on three series of GPMMMs. The Series 2 samples were prepared from relatively low-permeability PIM-1 (KA1-1), whereas Series 3 and 4 were prepared from high-permeability PIM-1 (KA1-4). Series 4 differs from the others in incorporating synthetic rather than exfoliated graphene. The discussion of the data includes some comparisons with data from the literature, notably on MMMs incorporating fused silica and f-MWCNTs.

Measurements of single gas permeability were carried out on all self-supported membranes and resulted in permeability values in the descending order of CO₂ > H₂ > He \approx O₂ > CH₄ > N₂. Measurements were also performed on membranes subjected to methanol soaking followed by drying, in order to remove residual solvent and reset their performance, which may have been influenced by previous membrane history. Based on the simplest gas transport model, the solution-diffusion model, the enhancement in diffusion coefficient D and solubility coefficient S leads to a direct

increase in the permeability coefficient P ($P = D * S$). With PIM-1, $P_{CO_2} > P_{H_2}$, this being attributed to the significant sorption coefficient of CO_2 . However, very strong sorption of CO_2 can lead to a reduction in permeability and restricted diffusion, which have been observed in amine-modified PIM-1.⁴¹

The results of permeation measurements for Series 2 were as expected. A low loading of graphene (< 0.34 wt.%) was sufficient to enhance the permeability coefficient for several gases (Figure 4-12) and methanol treatment was found to produce further enhancements. This increment in permeability resulted from expanded intrinsic free volume caused by graphene incorporation. However, no enhancement in permeability was achieved with high graphene loading (> 0.34 wt.%).

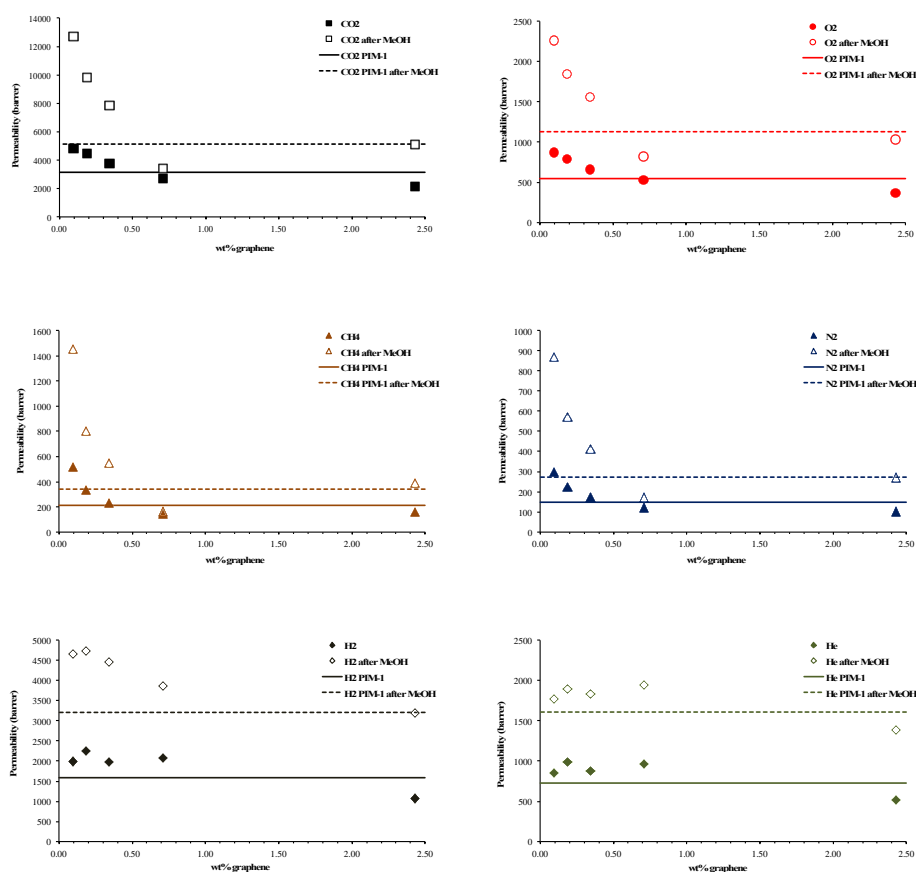


Figure 4-12. Permeability of several gases (CO_2 , H_2 , He , O_2 , CH_4 and N_2) in correlation with weight percent of graphene loading (GPMMS-2).

Permeability data from Ahn et. al.³⁰ for MMMs comprising hydrophobic fused silica (Cabosil TS 530) in PIM-1 and treated with methanol show a substantial

enhancement in permeability, which is not predicted by the Maxwell model (Figure 4-13). This increase in permeability was achieved with filler loadings of 7-24 vol.%. It was difficult to investigate loadings above 24 vol.% due to failure to obtain homogeneous dispersibility and flexible MMMs. The nanoparticle fillers were characterized with diameters in the range 11.1-13.3 nm, despite the fact that larger particle aggregations were observed in the MMMs. Filler density was reported to be 2.2 g cm⁻³.

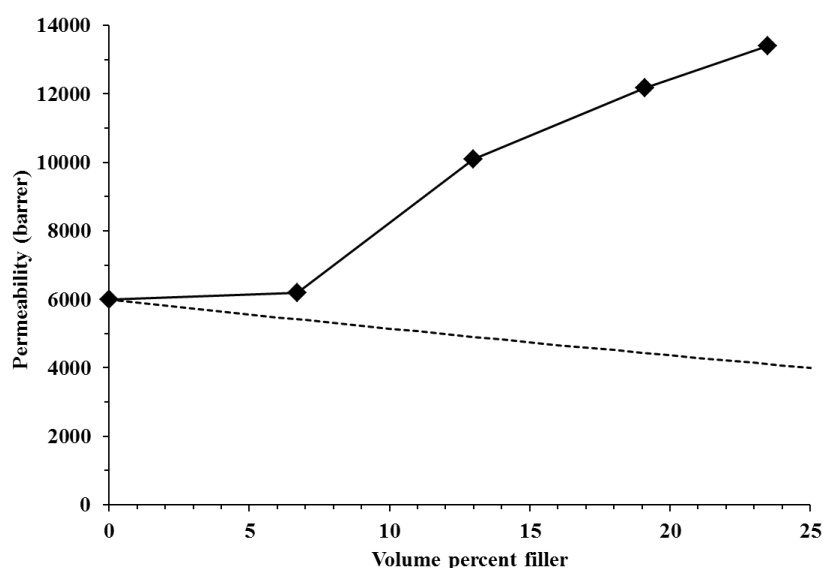


Figure 4-13. Correlation of CO₂ permeability and the loading of fused silica fillers for MMMs of PIM-1. The dashed line indicates the predication of the Maxwell model for an impermeable filler.

Khan et al.⁴⁰ report a similar trend of PIM-1 membranes comprising multi-walled carbon nanotubes functionalized with poly(ethylene glycol) fillers (f-MWCNTs/PIM-1-MMMs). For functionalization, they used MWCNTs having 8-12 walls and diameters ranging from 12 to 15 nm.

Figure 4-14 shows the correlation of CO₂ permeability and volume percent filler, as an example, for f-MWCNTs/PIM-1-MMMs, Series 2 GPMMMs. In order to calculate the volume fraction of filler, the respective densities of MWCNTs and graphene were assumed to be 2.1 and 2.2 g cm⁻³, respectively.

From this comparison, permeability can be seen to be enhanced by the incorporation of both graphene and f-MWCNT fillers at relatively low loading. The maximum enhancement was reached with graphene filler at a much lower loading

(0.05 vol%) than that of f-MWCNTs (1 vol%); this difference in optimum loading may be attributed to a topology effect. The topology effect can depend on the curvature of fillers, whether it is cylindrical in MWCNTs or planar in Graphene layers. In case of planar topology like graphene, the effect can be more pronounced, as the conformation freedom of polymer chains is more restricted than that in the case of curved surface (like MWCNTs). Therefore, the required optimum loading is expected to be higher in the case of cylindrical fillers than that of planar fillers.

Furthermore, it may be assumed that planar graphene can have higher exposed surface area for the polymer matrix, as an advantage of two exposed surfaces (i.e., the surfaces above and below the planar layer). In contrast, MWCNTs can have less exposed surface area, as the internal surface of MWCNTs is inaccessible to the polymer matrix. However, this assumption does not consider the variation of the specific surface area which can come from different numbers of stacking layers or walls.

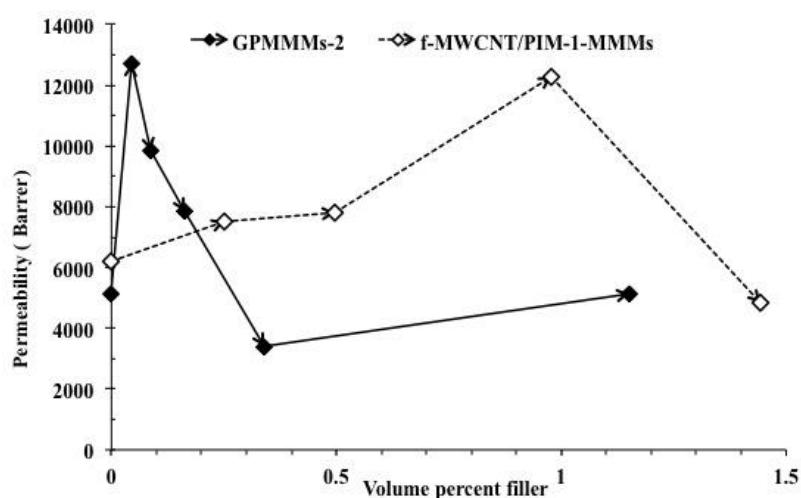


Figure 4-14. A graph shows the CO₂ permeability vs volume percent filler of graphene and f-MWCNTs, ⁴⁰ each comprising PIM-1 membranes.

Neither system fulfilled the Maxwell model prediction for impermeable fillers, which suggests that these fillers provided extra free volume to PIM-1. However, both fillers at high loading show reduction in permeability. This can be attributed to blockages of interconnected pathways in PIM-1.

Figure 4-15 shows the relationship between CO₂ permeability and graphene loading of Series 2 and 3 GPMMMs. From this comparison, the difference between the two series suggests that in Series 2 the graphene fillers aid to compensate the lack in permeability due to the presence of high water content. In contrast, Series 3 GPMMMs show scattered points of permeability without an obvious trend. This can be attributed to the fact that the corresponding PIM-1 batch (KA1-4) has high permeability coefficient, and graphene fillers have less contribution towards further permeability enhancement. This observation was true for both as-cast and methanol-treated membranes. Moreover, the presence of graphene filler did not prohibit the enhancement in permeability that is caused by methanol treatment.

Also Figure 4-15 shows that the Series 3 GPMMMs followed a different trend before and after methanol treatment from that of Series 2. Among those membranes measured as cast, only a few surpassed the permeability of PIM-1, while most were lower in permeability. After methanol treatment, almost all membranes showed enhanced permeability and more membranes significantly surpassed PIM-1 permeability after methanol treatment. These discrepancies in membrane performance can be attributed to the lack of controlling blockages or interfacial voids.

In the case of Series 3 GPMMMs, failure to control the flake size distribution or membrane preparation, using slow evaporation, may explain the discrepancies in observed permeability.

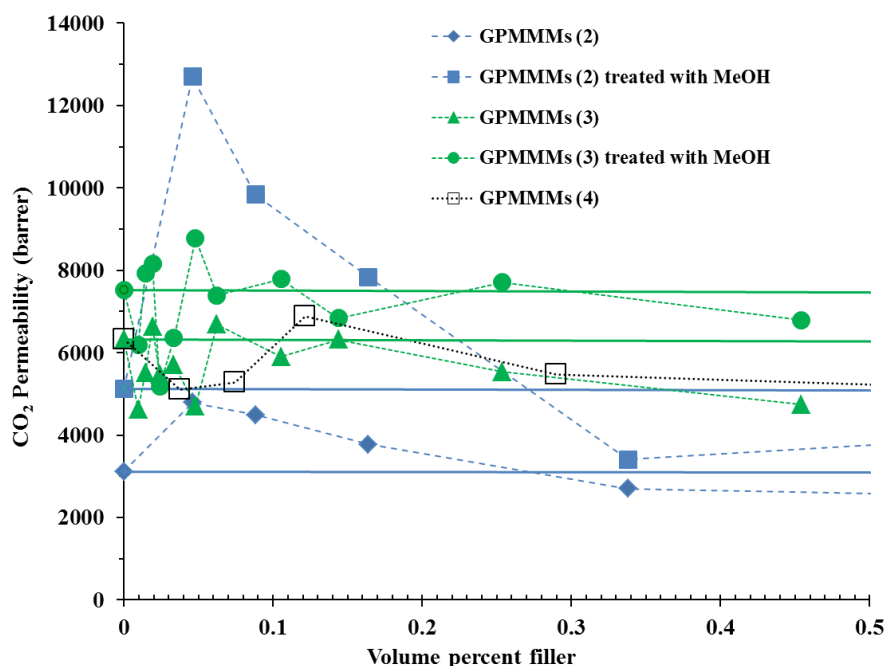


Figure 4-15. Correlations of CO₂ permeability and volume percent of graphene fillers of all samples as cast. Methanol treated are also included for most samples. Lines indicate Permeability of starting PIM-1.

The trade-off between permeability and selectivity is also an important consideration in membrane development. Figure 4-16 compares the effects of fused silica, f-MWCNTs and Series 2 and 3 GPMMMs on the gas transport properties of PIM-1, using O₂/N₂ separation as an example, plotting permeability against selectivity at different loading values. Fused silica shows a clear trade-off phenomenon: relatively high loading reduced selectivity below the upper bound of 1991. With f-MWCNTs, there was no enhancement beyond the upper bound of 2008, and there was still a trade-off. Series 2 GPMMMs exhibited a different relationship between graphene content and gas transport properties, whereby increasing the graphene content enhanced the selectivity of most membranes, the majority of which even exceeded the present upper bound. In series 3 GPMMMs, there were no major sacrifices in selectivity, and seven of the 12 membranes were relatively close to neat PIM-1. This relationship was even more pronounced in the case of CO₂/CH₄ separation (Figure 4-17).

Furthermore, maintaining relatively good selectivity suggests that further studies of the mechanical properties of GPMMMs would be useful, especially as they have the potential to perform above the present upper bound.

Series 4 GPMMMs incorporating synthetic graphene had the advantage of screening high graphene loading (up to 4.2 wt.%), which was achieved by neither Series 2 nor Series 3 GPMMMs. The effect is evident in Figure 4-18, which shows that permeability decreased in a relatively linear relationship as graphene content increased. This confirms the low permeability results of other GPMMMs at high loading. Moreover, there were almost no losses in selectivity, which confirms the stable character of the micropores.

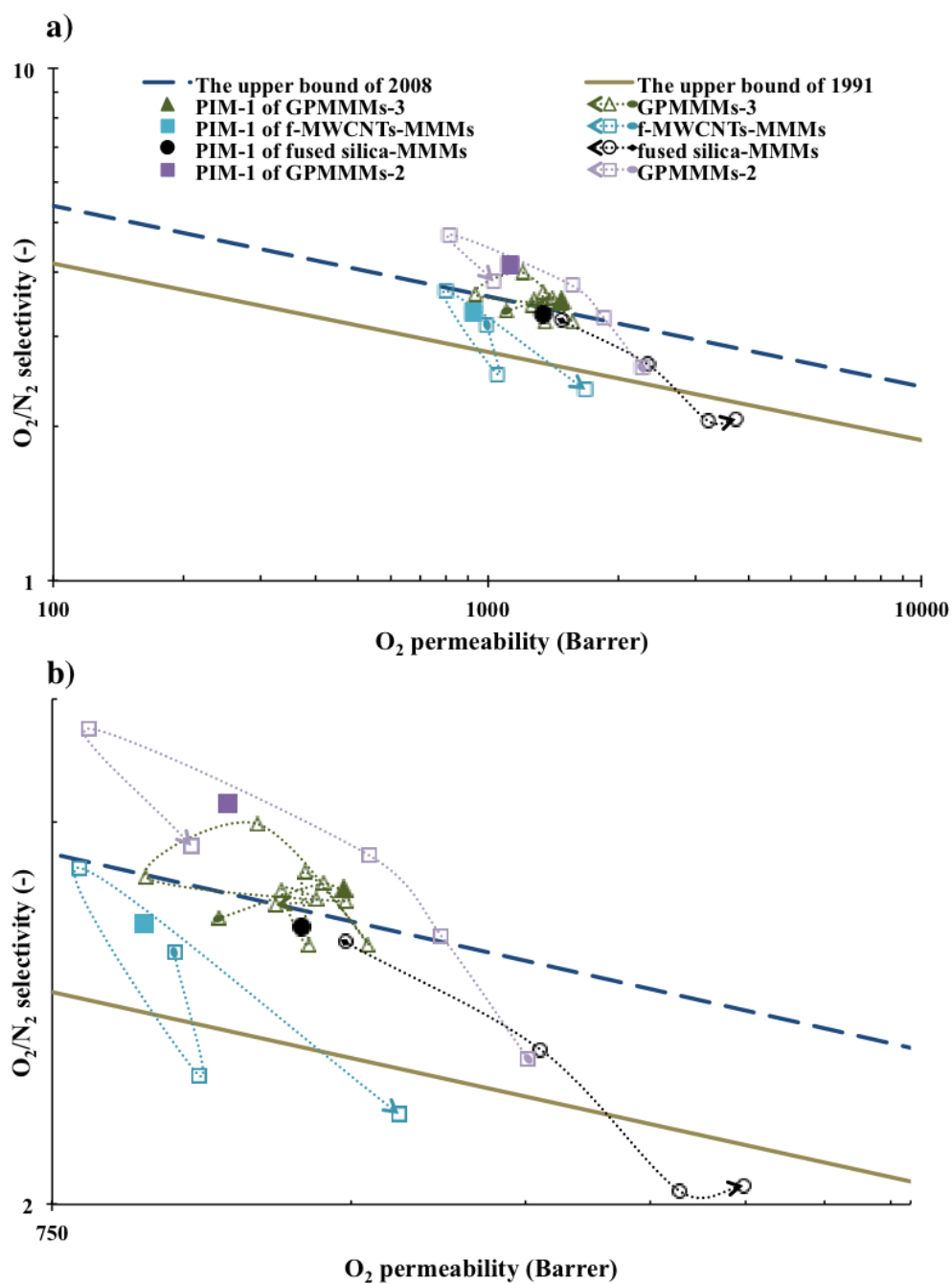


Figure 4-16. Correlation of O_2 permeability and O_2/N_2 selectivity for two series of GPMMMs, f-MWCNTs-MMMs and fused silica-MMMs. (b) is a zoomed-in image of (a) with highlighted regions for each series. Arrows indicate increased loading of nanofillers.

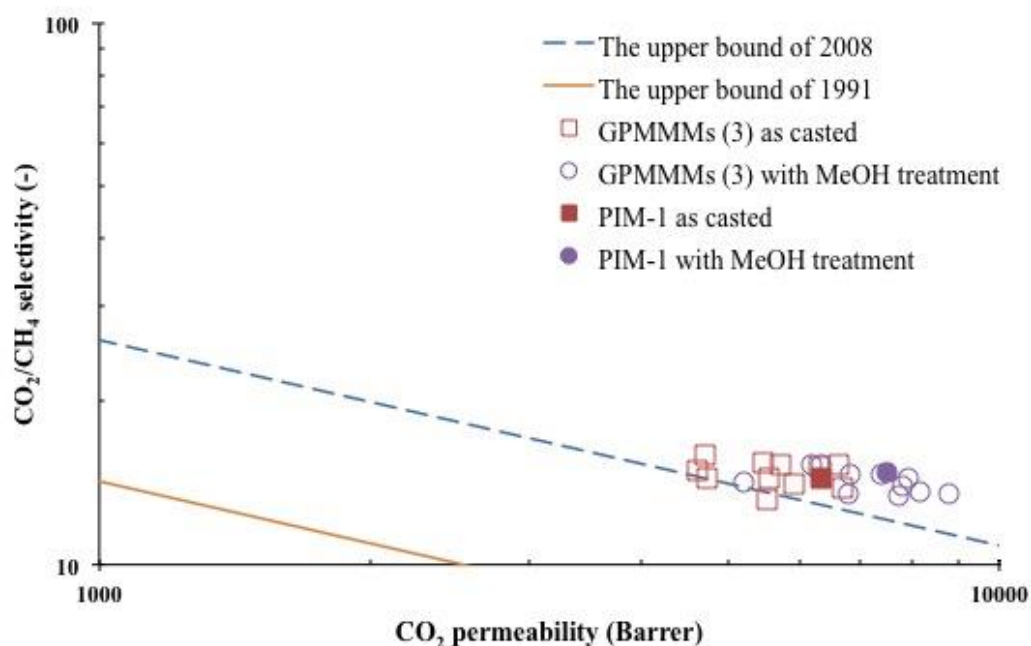


Figure 4-17. Effects of graphene fillers on CO_2/CH_4 separation of PIM-1. Filled squares indicate neat PIM-1 membrane measured as cast; unfilled squares indicate as-cast Series 3 GPMMMs; filled circles indicate PIM-1 membrane after methanol treatment; unfilled circles are Series 3 GPMMMs after methanol treatment.

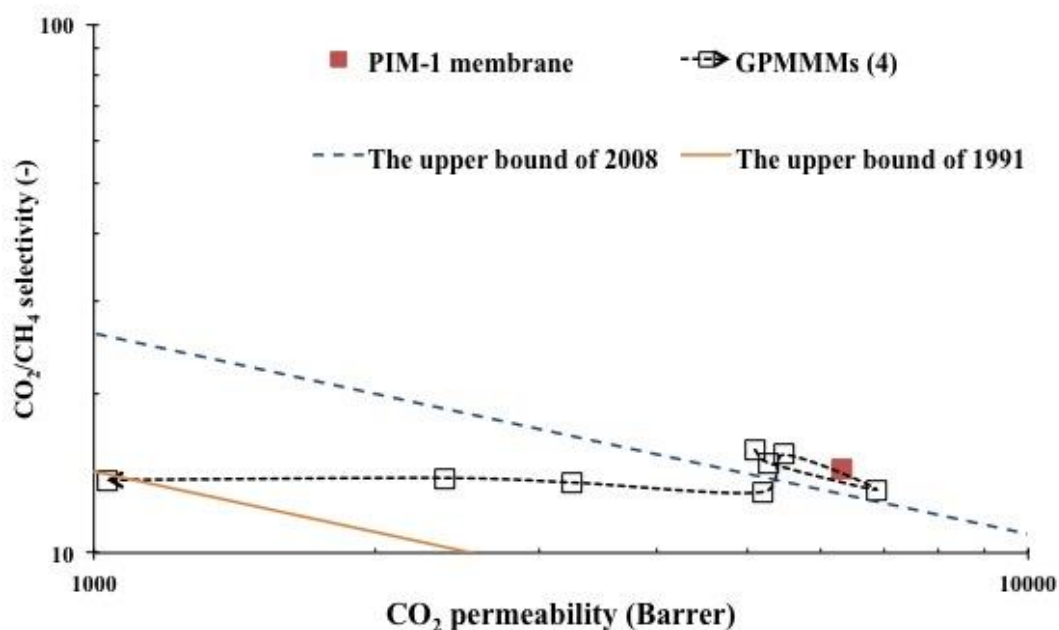


Figure 4-18. Effects of synthetic graphene fillers on CO_2/CH_4 separation of PIM-1. Filled square indicates neat PIM-1 membrane (as cast); unfilled squares indicate Series 4 GPMMMs (as cast). Arrows indicate increased filler.

Further graphs of different gas pairs are given in the Appendix, all of which show similar behaviour to those of the above examples.

Various measurements were carried out to investigate the effect of ageing on membranes. Figure 4-19 illustrates the performance of membranes with various graphene contents after approximately eight months storage. In all cases, a decrease in permeability was observed and the significant permeability enhancement from incorporating graphene was retained, so that permeability remained higher for all GPMMMs than for neat PIM-1. This is an important property for membrane applications.

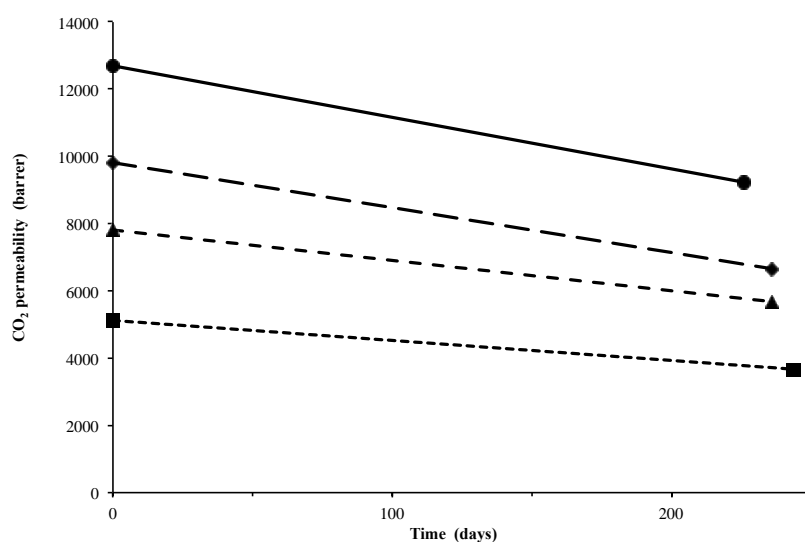


Figure 4-19. Effects of ageing for ca. 8 months on the CO₂ permeability of PIM-1 (■) and GPMMMs (Series 2) at nanofiller loadings of 0.046 vol.% (●), 0.088 vol.% (◆) and 0.164 vol.% (▲). The lines are guides to the eye.

4.4 Conclusion

A conclusion to be drawn from the above comparisons is that the gas transport properties of GPMMMs are sensitive to sample preparation and filler properties. The use of impermeable nanofillers can enhance gas transport by introducing extra free volume, which helps to induce diffusion and permeability. However, blockage of interconnected pores can reduce permeability. This phenomenon is more pronounced at higher graphene content.

Graphene fillers can contribute to significant enhancement in the case of using a PIM-1 batch of low-permeability (KA1-1). This contribution can have less potential in the case of a PIM-1 batch of high permeability.

The effects on the morphology—particularly the topology—of different carbon allotropes (graphene or MWCNTs) lead in turn to differences in the filler loading required for optimum permeability: a lower filler content is required for permeability enhancement in the case of graphene than of MWCNTs. The variation of topology effects from different nanofillers may result from different conformation freedom of polymer chains that are exposed to different surface curvatures.

The influence on permeability can be limited in the case of using high-permeability, low water content, PIM-1.

The permeability of GPMMMs decreases with age, as is the case for a pristine PIM-1 membrane. However, the permeability enhancement obtained from graphene incorporation was retained after ageing, so that GPMMM values remained higher than for unfilled PIM-1 membrane.

This work is believed to indicate an optimum approach for the preparation of MMMs using nano-impermeable fillers, as most GPMMMs performed above the present upper bound for gas separation.

4.5 References

- (1) Mitchell, J. K. *J. Memb. Sci.* **1995**, *100*, 11.
- (2) Koros, W. J.; Fleming, G. K. *J. Memb. Sci.* **1993**, *83*, 1.
- (3) Sanders, D. F.; Smith, Z. P.; Guo, R.; Robeson, L. M.; McGrath, J. E.; Paul, D. R.; Freeman, B. D. *Polymer (Guildf)*. **2013**, *54*, 4729.
- (4) McKeown, N. B. *ISRN Mater. Sci.* **2012**, *2012*, 16.
- (5) Robeson, L. M. *J. Memb. Sci.* **1991**, *62*, 165.
- (6) Robeson, L. M.; Smith, Z. P.; Freeman, B. D.; Paul, D. R. *J. Memb. Sci.* **2014**, *453*, 71.
- (7) The Membrane Society of Australasia <http://www.membrane-australasia.org/polymer-gas-separation-membranes/> (accessed Sep 22, 2015).
- (8) Yampolskii, Y. *Macromolecules* **2012**, *45*, 3298.

- (9) Allen, S. M.; Fujii, M.; Stannett, V. *J. Memb. Sci.* **1977**, *2*, 153.
- (10) Merkel, T. C.; Bondar, V.; Nagai, K.; Freeman, B. D. *J. Polym. Sci. Part B Polym. Phys.* **2000**, *38*, 273.
- (11) Nagai, K.; Masuda, T.; Nakagawa, T.; Freeman, B. D.; Pinnau, I. *Prog. Polym. Sci.* **2001**, *26*, 721.
- (12) Graham, T. *J. Memb. Sci.* **1995**, *100*, 27.
- (13) Ismail, Ahmad Fauzi, Hasbullah, Hasrinah; Mustafa, Azeman; Kusworol, T., *Proceeding of the 2005 Regional Conference on Engineering Education* **2005**, *12*, 155.
- (14) Lee, Y. M.; Han, S. H. *Recent High Performance Polymer Membranes for CO₂ Separation*; Drioli, E., Barbieri, G., Eds.; **2011**; *1*, pp 84-124.
- (15) Masuda, T.; Isobe, E.; Higashimura, T. *J. Am. Chem. Soc.* **1983**, *105*, 7473.
- (16) Singh, A.; Koros, W. J. *Ind. Eng. Chem. Res.* **1996**, *35*, 1231.
- (17) Aroon, M. A.; Ismail, A. F.; Matsuura, T.; Montazer-Rahmati, M. M. *Sep. Purif. Technol.* **2010**, *75*, 229.
- (18) Chung, T. S.; Jiang, L. Y.; Li, Y.; Kulprathipanja, S. *Prog. Polym. Sci.* **2007**, *32*, 483.
- (19) Paul, D. R.; Kemp, D. R. *J. Polym. Sci. Polym. Symp.* **1973**, *41*, 79.
- (20) Moore, T. T.; Koros, W. J. *J. Mol. Struct.* **2005**, *739*, 87.
- (21) Mahajan, R.; Koros, W. J. *Ind. Eng. Chem. Res.* **2000**, *39*, 2692.
- (22) Wang, H.; Holmberg, B. a.; Yan, Y. *J. Mater. Chem.* **2002**, *12*, 3640.
- (23) Mahajan, R.; Koros, W. J. *Polym. Eng. Sci.* **2002**, *42*, 1432.
- (24) Kulkarni, S.; David, H.; Corbin, D.; Patel, A. Gas separation membrane with organosilicon-treated molecular sieve. US6508860 B1, 2003.
- (25) Li, Y.; Chung, T. S.; Cao, C.; Kulprathipanja, S. *J. Memb. Sci.* **2005**, *260*, 45.
- (26) Vu, D. Q.; Koros, W. J.; Miller, S. J. *J. Memb. Sci.* **2003**, *211*, 311.
- (27) Anson, M.; Marchese, J.; Garis, E.; Ochoa, N.; Pagliero, C. *J. Memb. Sci.* **2004**, *243*, 19.
- (28) Li, Y.; Chung, T.; Kulprathipanja, S. *AIChE J.* **2007**, *53*, 610.
- (29) Pinnau, I.; He, Z. Filled superglassy membrane. US 6316684 B1, 2001.
- (30) Ahn, J.; Chung, W. J.; Pinnau, I.; Song, J.; Du, N.; Robertson, G. P.; Guiver, M. D. *J. Memb. Sci.* **2010**, *346*, 280.
- (31) Ahn, J.; Chung, W. J.; Pinnau, I.; Guiver, M. D. *J. Memb. Sci.* **2008**, *314*, 123.
- (32) Mason, C. R.; Maynard-Atem, L.; Al-Harbi, N. M.; Budd, P. M.; Bernardo,

- P.; Bazzarelli, F.; Clarizia, G.; Jansen, J. C. *Macromolecules* **2011**, *44*, 6471.
- (33) Budd, P. M.; McKeown, N. B.; Ghanem, B. S.; Msayib, K. J.; Fritsch, D.; Starannikova, L.; Belov, N.; Sanfirova, O.; Yampolskii, Y.; Shantarovich, V. *J. Memb. Sci.* **2008**, *325*, 851.
- (34) Budd, P.; Msayib, K.; Tattershall, C.; Ghanem, B.; Reynolds, K.; McKeown, N.; Fritsch, D. *J. Memb. Sci.* **2005**, *251*, 263.
- (35) Ahn, J.; Chung, W. J.; Pinna, I.; Song, J.; Du, N.; Robertson, G. P.; Guiver, M. D. *J. Memb. Sci.* **2010**, *346*, 280.
- (36) Staiger, C. L.; Pas, S. J.; Hill, A. J.; Cornelius, C. J. *Chem. Mater.* **2008**, *20*, 2606.
- (37) Song, J.; Du, N.; Dai, Y.; Robertson, G. P.; Guiver, M. D.; Thomas, S.; Pinna, I. *Macromolecules* **2008**, *41*, 7411.
- (38) Thomas, S.; Pinna, I.; Du, N.; Guiver, M. D. *J. Memb. Sci.* **2009**, *333*, 125.
- (39) Khan, M. M.; Filiz, V.; Bengtson, G.; Shishatskiy, S.; Rahman, M. M.; Abetz, V. *Nanoscale Res. Lett.* **2012**, *7*, 504.
- (40) Khan, M. M.; Filiz, V.; Bengtson, G.; Shishatskiy, S.; Rahman, M. M.; Lillepaerg, J.; Abetz, V. *J. Memb. Sci.* **2013**, *436*, 109.
- (41) Mason, C. R.; Maynard-Atem, L.; Heard, K. W. J.; Satilmis, B.; Budd, P. M.; Friess, K.; Lanč, M.; Bernardo, P.; Clarizia, G.; Jansen, J. C. *Macromolecules* **2014**, *47*, 1021.

Chapter 5 New polymers of intrinsic microporosity (PIMs)

5.1 Introduction

Owing to substantial interest in PIMs, exploring new PIM structures is important. As previously mentioned, the choice of appropriate monomers plays a key role in obtaining microporous properties. Spirobisindine-based monomers, for example, have emerged as candidates for introducing contortion and inefficient packing of polymer chains, allowing high free volume polymers to be obtained.

A similar approach that has been considered is to use the self-assembly property of supramolecular compounds, in order to obtain networks with intrinsic microporosity. Self-assembly can be promoted via special substituents that undergo noncovalent interactions such as hydrogen bonding or metal coordination, in order to control assemblies for the desired microporous construction.^{1,2,3,4,5} In this approach, the crystallization process is important for obtaining a particular network structure with cavities and interconnected porosity, hence pores of characteristic shape and size, offering potential selectivity towards guest molecules.

However, this approach can involve difficulties. An important factor is the simultaneous competition between directional and nondirectional noncovalent interactions, the latter usually being responsible for effective packing forces.² In the case of constructing large pores, self-interpenetration can take place, causing void filling.²

Recently, there has been substantial interest in hexaphenylbenzene (HPB) (Figure 5-1a), because of the number and types of its terminal substituents that can potentially be architecturally engineered. Moreover, HPB has a characteristic rigidity and shape-persistent structure, and the phenyl groups have intermolecular interactions, resulting in a propeller-like shape.

HPBs have been subjected to a wide range of applications such as electronic and photonic devices,^{6,7,8} crystal engineering,⁹ light-harvesting applications,¹⁰ and the preparation of graphene fragments¹¹ and microporous materials.^{12,13,14,15}

Various HPBs have been reported to have been engineered by the self-assembly approach. Figure 5-1 illustrates examples of HPBs that can construct a network structure using periphery substitutions, facilitating hydrogen bond interactions.⁴

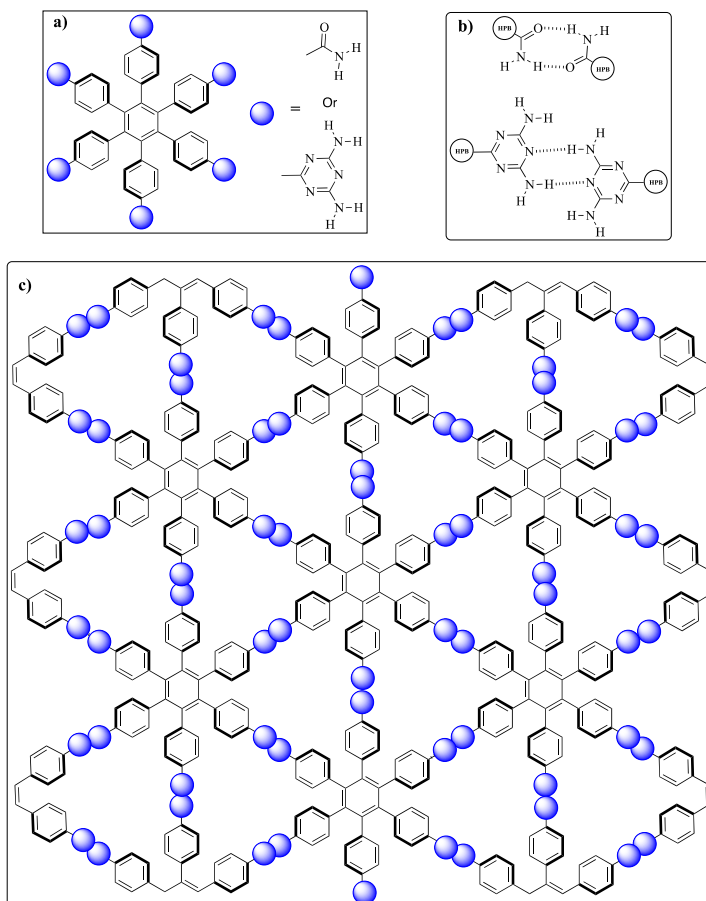
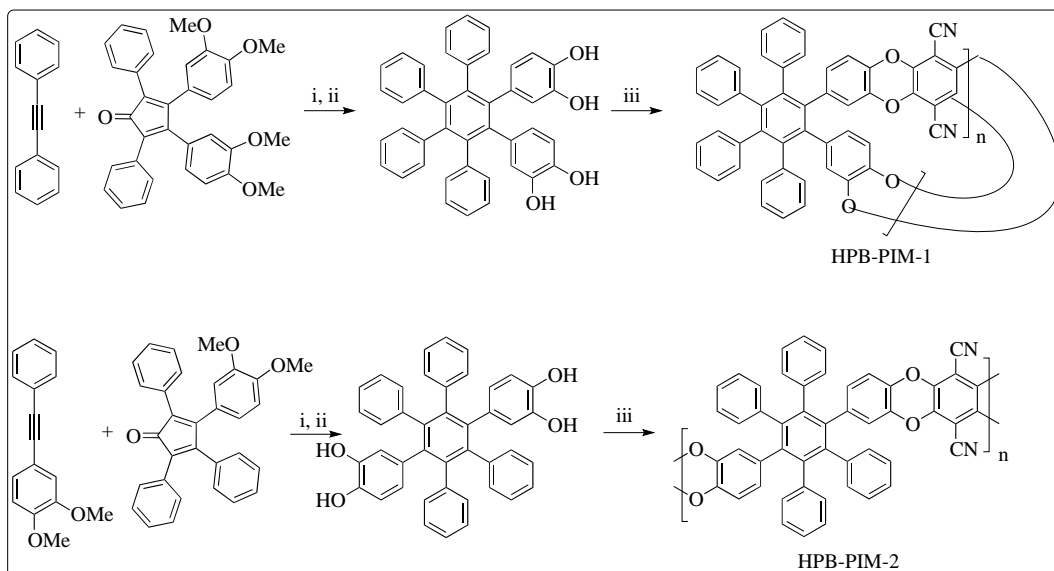


Figure 5-1. Illustrative examples of hexaphenylbenzene compounds (HPBs) that can construct pores by self-assembly: a) HPB with terminal functional groups, b) functional groups that facilitate hydrogen bond interactions, c) network structure of HPBs from self-assembly.⁴

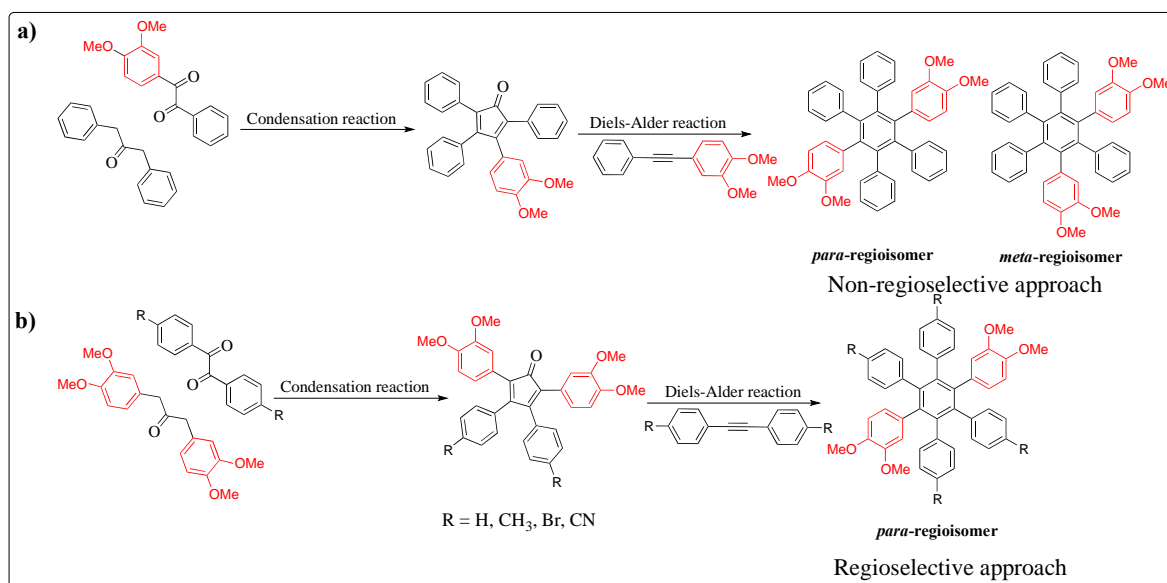
The incorporation of HPBs in polymerization can produce polymers that are predominantly either cyclic or linear, strongly influenced by the HPB structure. For example, McKeown et al.¹³ report two synthetic approaches in which HPB derivatives were incorporated in condensation polymerization (Scheme 5-1). Their work shows that using HPBs of different regioisomers produces predominantly either porous cyclic oligomers (HPB-PIM-1) or ladder polymers (HPB-PIM-2). The present approach to the synthesis of mono-regioisomers (Scheme 5-2) was adapted from this work.

In another continuing study, McKeown et al.¹⁴ followed a regioselective approach to the preparation of a *para* regioisomer of biscatechol HPB (Scheme 5-2b) for preparing ladder polymers such as PIM-HPB, PIM-CH₃-HPB, PIM-Br-HPB and PIM-CN-HPB. In this work, a number of *p*-bis(catechol) HPB derivatives were prepared using symmetrical benzils and diphenylacetylenes. In general, film forming

HPB-PIMs were reported with decent average molecular mass (M_w) ($65\text{--}400 \times 10^3 \text{ g mol}^{-1}$). A decrease in BET surface area was observed for these polymers in the following order: PIM-CH₃-HPB > PIM-HPB > PIM-CN-HPB > PIM-Br-HPB.

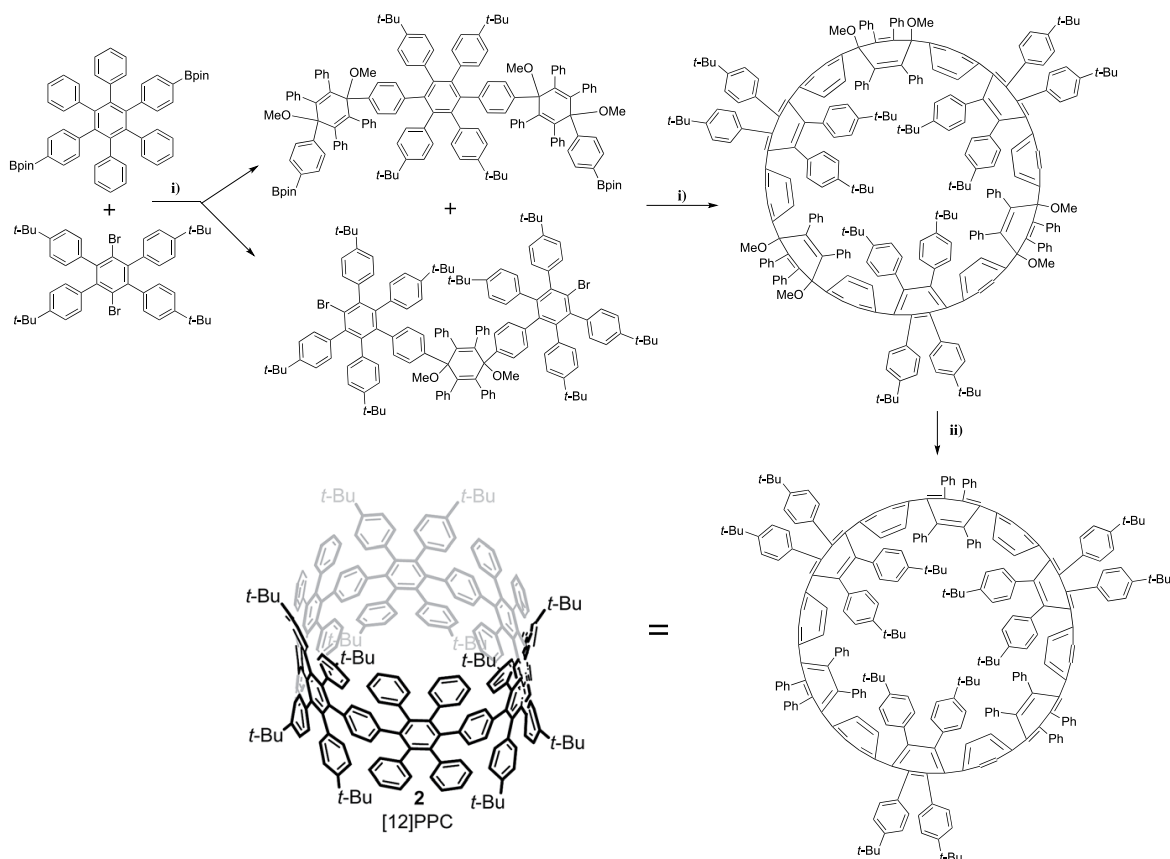


Scheme 5-1. Preparation of cyclic (top) and linear (bottom) HPB-PIMs. i) diphenyl ether, 250 °C; ii) BBr_3 , DCM, 20 °C; (iii) tetrafluoroterephthalonitrile, DMF, K_2CO_3 , 65 °C, 96 h.¹⁴



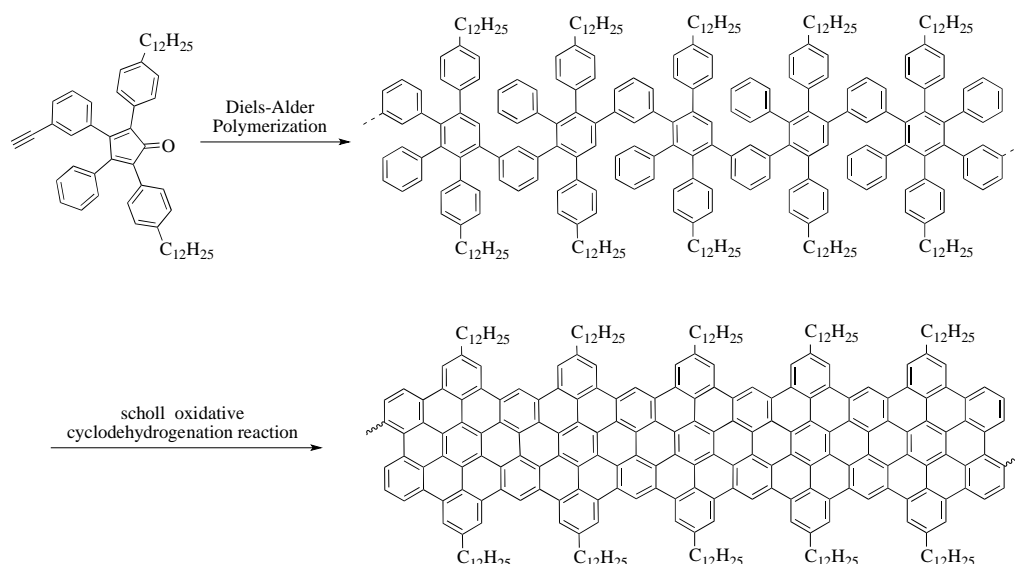
Scheme 5-2. Two different approaches for HPB monomer preparation, a) non-regioselective approach, b) regioselective approach. Adapted from McKeown et al.¹⁴

Recently, macrocycles derived from HPBs have been established as a route towards nano-engineered carbon nanotubes (CNTs). In this context, Müllen et al.¹⁶ report the synthesis of these materials. Scheme 5-3 illustrates an example, a so-called congested cyclic hexaphenylbenzene hexamer ([6] CCHPB 2). However, the production of CNTs of well-defined structure from CHPBs via cyclodehydrogenation is still limited.



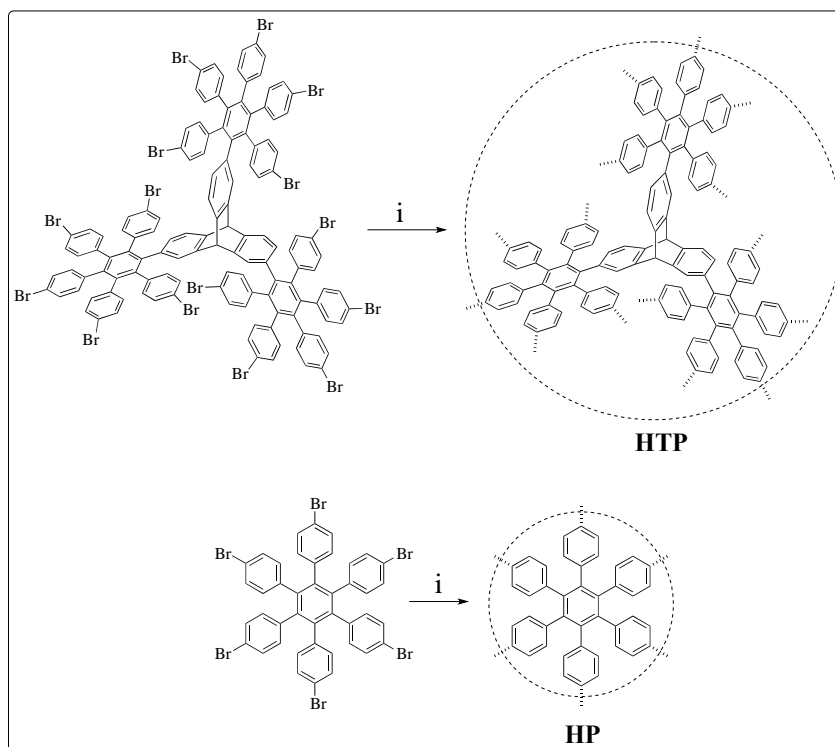
Scheme 5-3. Synthesis of [6] CCHPB 2 from HPB derivatives, i) Suzuki coupling reaction ($\text{Pd}(\text{PPh}_3)_4$, Cs_2CO_3 , 100 °C), ii) demethoxylation under reductive conditions (TiCl_4 , LiAlH_4 , 80 °C).¹⁶

In linear polymer preparation, pentaphenylbenzenes (PPBs), as compounds having the closest structures to HPBs and to polyphenylene precursors, were used in the preparation of polyphenylene-based polymers to produce graphene nanoribbons (GNRs). Müllen et al.¹⁷ report that these materials have high liquid-phase processability. Scheme 5-4 shows their approach to the synthesis of polyphenylene polymer followed by GNR preparation.



Scheme 5-4. Synthesis of GNRs from polyphenylene-based polymer.¹⁷

The interest in HPBs for constructing nanoporous frameworks has been extended to the preparation of novel crosslinked microporous polymers (CMPs), in which covalent bonds are dominant in forming intrinsic microporosity. Zhang et al.¹⁸ have reported examples of utilizing HPBs as building blocks in the preparation of organic microporous polymers. Scheme 5-5 shows these polymers (HP and HTP). HTP incorporates triptycenes and HPB, both of which have been used successfully to prepare polymers of high BET surface area. HP and HTP were prepared by a nickel-mediated reaction involving carbon-carbon homocoupling. HTP was found to have a higher BET surface area than HP, at 1151 and 675 m² g⁻¹ respectively. This observation was expected, as a result of the three-dimensional scaffold incorporating HPB or triptycene, in which effective packing is prohibited. Han et al.¹² have also reported CMPs in the form of so-called HPB-based porous organic polymers (HPOPs), which are more similar to HP. The difference between these polymers is that HPBs were joined with different aromatic linkages (Figure 5-2). Interestingly, these polymers show good porous properties, with a BET surface area up to 1148 m² g⁻¹.



Scheme 5-5. Preparation of HTP and HP. $i = 1,5$ -cyclooctadiene, bis(1,5-cyclooctadiene) nickel(0), 2,20- bipyridyl, DMF, 85 °C, 96 h.¹⁸

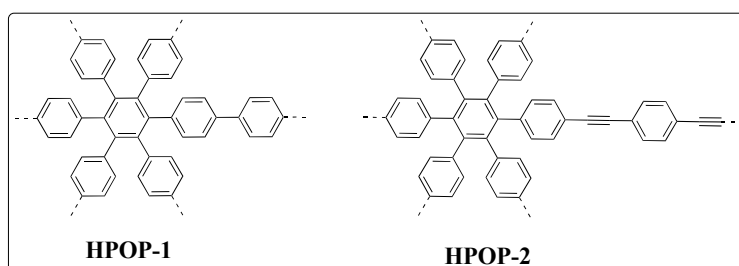


Figure 5-2. Chemical structures of HPOP-1 and HPOP-2.

As previously mentioned, HPBs are known for their three-dimensional structures, and in order to convert this structural property, planarization can be achieved via an oxidative cyclodehydrogenation reaction. Recently, Smaldone et al.¹⁵ have reported a series of HPB-based polymers named HEX-POPs, and their planar structures (HBC-POPs), with different functional groups. They found that porosity depended strongly on functionality. In general, the BET surface area of most of these polymers varied from 300 to 700 m² g⁻¹. However, the highest BET surface area (1140 m² g⁻¹) was recorded for HEX-POP-3, which has *tert*-butyl

substituents. Figure 5-3 summarizes the influence of functional groups on porous properties.¹⁵

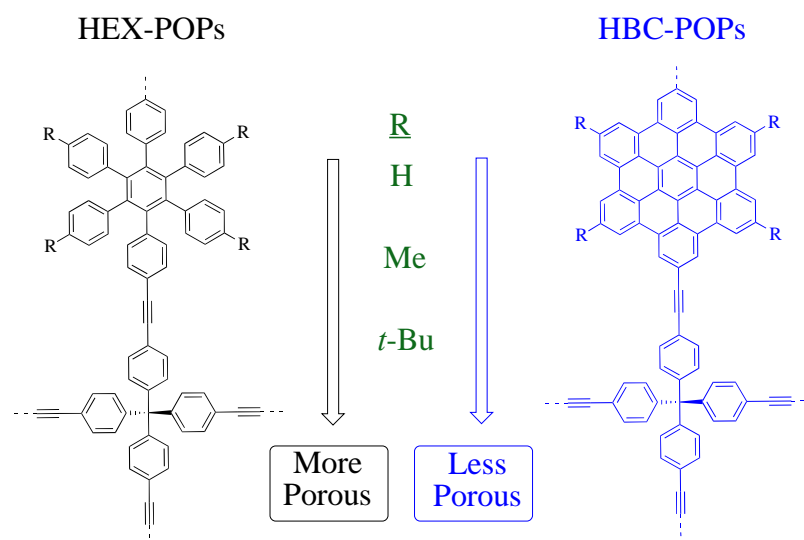


Figure 5-3. The relationship between porous properties and structure of HEX-POPs and HBC-POPs varying in structure, planarization and functional groups.¹⁵

The present study used HPBs as building blocks for novel polyphenylene-based polymers of intrinsic microporosity (PP-PIMs). There were two synthetic approaches. In the first, PP-PIMs were prepared by condensation polymerization, incorporating bis-catechol substituents in PP-PIM monomers in order to facilitate polymerization with tetrafluoroterephthalonitrile (TFTPN) monomer. These polymers can be classified as PP-PIMs produced by dibenzodioxin formation. There was also a novel PIM, synthesised by the same approach but differing by substituting the HPB building blocks in the monomer with biphenyl units, thus producing a biphenyl-based polymer of intrinsic microporosity (BP-PIM-1).

Another approach was to use [2-4] cycloaddition Diels-Alder polymerization to produce PP-PIMs. This required the preparation of two different PP-PIM monomers, one having two terminal tetraphenylcyclopentadienones (TPCPDs) and the other having two terminal phenylacetylenes.

5.2 Experimental

5.2.1 Materials

All chemical and reagents and solvents were used as received from Sigma-Aldrich. Dry solvents were prepared using 3 Å molecular sieves (10% m/v) for overnight. Anhydrous K₂CO₃ (99%, Fisher) was dried in an oven at 110 °C overnight before use. Anhydrous dimethylformamide (DMF), anhydrous dimethylacetamide (DMAc), toluene and methanol (MeOH) were purchased from Sigma-Aldrich and used as received. triflic anhydride (99 %, Apollo Scientific Ltd.) was used as received.

5.2.2 Methods

All NMR spectra were recorded at 400 MHz or 500 MHz using Bruker spectrometers and CDCl₃ as solvent, unless otherwise stated. For NMR sample preparation, \approx 5 mg was dissolved in CDCl₃ (Aldrich, 99.8% atom D) and transferred into a 5 mm NMR tube.

High-powered decoupling (Hpddec) magic angle spinning (MAS) solid-state ¹³C NMR spectra were obtained on a Bruker Avance III 400 MHz instrument using adamantane as reference. A spinning rate of \sim 10,000 Hz was used with powder samples packed into a 4 mm zirconia rotor. Spectra were compiled from 6000 scans using a repetition time of 10 seconds and a spectral width of 600 ppm.

All infrared spectra were recorded for solid samples using a Biorad FTS 6000 spectrometer with an attenuated total reflectance (ATR) accessory. Samples were measured with 16 times scans.

Thermogravimetric analysis (TGA) was carried out on a TGA Q5000 V3.15 Build 263, under atmospheric nitrogen at a heating rate of 10.00 °C min⁻¹ from 30 to 800 °C, using a pan of Platinum-HT.

UV-Vis absorption measurements were recorded on a Cary 60 UV-Vis spectrophotometer, in chloroform at room temperature.

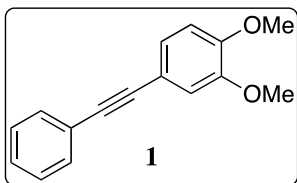
Elemental analysis was performed on a Carlo Erba Instruments EA1108 elemental analyzer.

N₂ adsorption/desorption isotherms and BET surface areas were obtained from powders at 77 K, using a Micromeritics ASAP 2020 instrument. Samples were degassed before measurement for 16 h at 120 °C under high vacuum. After cooling, degassed samples were reweighed, and placed in the analysis port. Further degassing was performed at sample run under high vacuum at 120 °C for 2 h. The apparent surface area was calculated from N₂ adsorption data by multi-point Brunauer-Emmet-Teller (BET) analysis. The free space of the samples tube was measured after analysis.

5.2.3 Polyphenylene-based polymers of intrinsic microporosity (PP-PIMs)

5.2.3.1 Synthesis of PP-PIM-1

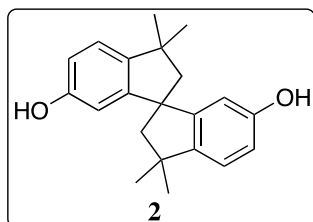
5.2.3.1.1 Synthesis of 1,2-dimethoxy-4-(phenylethynyl)benzene (**1**)



To a 100 mL round-bottomed flask were added 4-bromo-1,2-dimethoxybenzene (4.3 g, 20 mmol), PdCl₂(PPh₃)₂ (282 mg, 0.40 mmol), CuI (160 mg, 0.84 mmol) and diisopropylamine (60 mL) under nitrogen atmosphere. The mixture was stirred for 10 min, then phenylacetylene (2.1 g, 20 mmol) was added dropwise. The mixture was stirred continuously at 60 °C for 24 h. Thereafter, the work-up was carried out by water quenching and extraction with dichloromethane (DCM) (3 x 50 mL), then the product was washed three times with water (70 mL) and dried over magnesium sulphate. The solvent was removed using a rotary evaporator and further purification was achieved with column chromatography using a solvent system (1:40 ethyl acetate:hexane) to give a yellow crystalline powder (**1**) (4.72 g, 99%). M.p. 94-95 °C. ¹H NMR (400 MHz; CDCl₃): δ 7.54-7.51 (m, 2H), 7.37-7.31 (m, 3H), 7.15 (dd, *J* = 8.3, 1.9, 1H), 7.05 (d, *J* = 1.9, 1H), 6.84 (d, *J* = 8.3, 1H), 3.91 (s, 3H), 3.9 (s, 3H). ¹³C NMR (100 MHz, CDCl₃): δ 148.5 (C), 147.6 (C), 130.5 (CH), 127.3 (CH), 127.0 (CH), 123.9 (CH), 122.4 (CH), 114.4 (CH), 113.2 (CH), 110.0 (CH), 88.5 (C), 86.9 (C), 54.9 (CH₃). DEPT-135 (100 MHz,

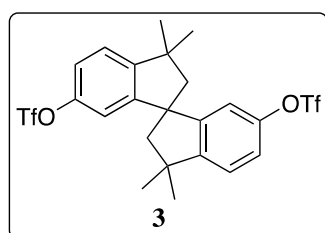
CDCl₃): δ 131.5 (CH), 128.4 (CH), 128.1 (CH), 124.9 (CH), 114.3 (CH), 111.0 (CH), 54.9 (CH₃). DEPT-90 (100 MHz, CDCl₃): δ 131.5 (CH), 128.4 (CH), 128.1 (CH), 124.9 (CH), 114.3 (CH), 111.0 (CH). Mass spectrometry (HRMS) m/z : 239.1330 [MH]⁺.

5.2.3.1.2 Synthesis of 3,3,3',3'-tetramethyl-2,2',3,3'-tetrahydro-1,1'-spirobi[indene]-6,6'-diol (**2**)



4,4'-(Propane-2,2-diyl)diphenol (4.963 g, 21.74 mmol) was dissolved in methanesulfonic acid (17.0 mL) and the solution was left stirring for four days at room temperature. Thereafter, the mixture was poured into ice water (250 mL) and stirred for two hours. The pink solid which formed was filtered and recrystallised from a 60% aqueous solution of ethanol. The final product (**2**) (2.15 g, 96%) was filtered and dried. ¹H NMR (500 MHz; DMSO-d₆): δ 9.01 (s, 2H), 7.00 (d, J = 8.2, 2H), 6.60 (dd, J = 8.2, 2.3, 2H), 6.10 (d, J = 2.2, 2H), 2.10 (d, J = 12.9, 2H), 2.6 (d, J = 12.9, 2H), 1.32 (s, 6H), 1.25 (s, 6H). ¹³C NMR (100 MHz; DMSO-d₆): δ 156.87 (C), 151.62 (C), 142.30 (C), 122.52 (CH), 114.49 (CH), 110.05 (CH), 59.48 (CH₂), 57.10 (C), 42.53 (C), 31.83 (CH₃), 30.67 (CH₃). DEPT-135 (100 MHz; DMSO-d₆): δ 122.85 (CH), 114.81 (CH), 110.37 (CH), 59.78 (CH₂), 32.12 (CH₃), 30.96 (CH₃). DEPT-90 (100 MHz; DMSO-d₆): δ 122.85 (CH), 114.81 (CH), 110.36 (CH). Mass spectrometry (ESI⁺) m/z : 309 [MH]⁺. Elemental analysis, calculated for C₂₁H₂₄O₂ (%): C, 81.78; H, 7.84. Found: C, 79.21; H, 7.76.

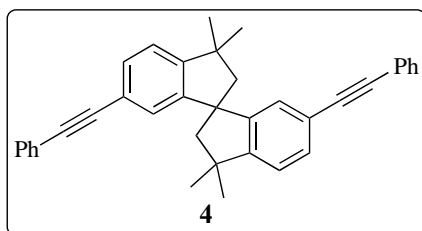
5.2.3.1.3 Synthesis of 3,3,3',3'-tetramethyl-2,2',3,3'-tetrahydro-1,1'-spirobi[indene]-6,6'-diyl bis(trifluoromethanesulfonate) (**3**)



To a round-bottomed flask, compound **2** (3.29 g, 5.7 mmol) was added, then dissolved in dry DCM under an inert atmosphere. Pyridine (10 mL) was added to the solution. Thereafter, the reaction mixture was cooled with an external ice-bath and triflic anhydride (1.95 mL, 13.8 mmol) was added dropwise within 10 minutes. The mixture was then allowed to warm up gradually to room temperature, with continuous stirring overnight. After

this, the mixture was purified via flash column chromatography (1:30 ethyl acetate:hexane) and concentrated via reduced pressure to yield compound **3** (2.2 g, 66%). ^1H NMR (500 MHz; CDCl_3): δ 7.25 (d, J = 8.4, 2H), 7.16 (dd, J = 8.4, 2.4, 2H), 6.63 (d, J = 2.4, 2H), 2.43 (d, J = 13.2, 2H), 2.25 (d, J = 13.2, 2H), 1.42 (s, 6H), 1.37 (s, 6H). ^{13}C NMR (100 MHz; CDCl_3): δ 152.40 (s, C), 151.81 (s, C), 149.12 (s, C), 123.74 (s, CH), 120.62 (s, CH), 116.91 (s, CH), 59.10 (s, CH_2), 57.54 (s, C), 43.44 (s, C), 31.45 (s, CH_3), 29.98 (s, CH_3). DEPT-135 (100 MHz; CDCl_3): δ 123.77 (s, CH), 120.66 (s, CH), 116.94 (s, CH), 59.12 (s, CH_2), 31.48 (s, CH_3), 30.01 (s, CH_3). DEPT-90 (100 MHz; CDCl_3): δ 123.77 (s, CH), 120.66 (s, CH), 116.94 (s, CH). ^{19}F NMR (400 MHz, CDCl_3): δ -74.6. Elemental analysis, calculated for $\text{C}_{23}\text{H}_{22}\text{F}_6\text{O}_6\text{S}_2$ (%): C, 48.21; H, 3.82. Found: C, 48.25; H, 3.87. Mass spectrometry (HRMS) m/z : calculated $[\text{MH}]^+$; 572.077. Found: 572.0755.

5.2.3.1.4 Synthesis of 3,3,3',3'-tetramethyl-6,6'-bis(phenylethynyl)-2,2',3,3'-tetrahydro-1,1'-spirobi[indene] (**4**)

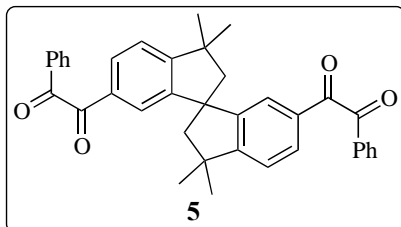


A solution of compound **3** (1.43 g, 2.6 mmol), $\text{PdCl}_2(\text{PPh}_3)_2$ (0.11 g, 0.15 mmol), phenylacetylene (0.77 g, 7.5 mmol) and triethylamine (6 mL, 43.13 mmol) was added to DMF (15 mL). The mixture was then heated to

80 °C for 17 hours under nitrogen. Thereafter, the work-up was carried out with water quenching and extraction with DCM (3 x 50 mL). The product was washed three times with water (70 ml) and dried over magnesium sulphate. The solvent was then removed using a rotary evaporator and further purification was achieved by column chromatography using a 1:30 ethyl acetate:hexane solvent system. White needle-like crystals were obtained (0.52 g, 42%). ^1H NMR (500 MHz; CDCl_3): δ 7.52-7.49 (m, 4H), 7.45 (dd, J = 7.9, 1.5, 2H), 7.35-7.31 (m, 6H), 7.21 (dd, J = 7.9, 0.4, 2H), 7.03 (d, J = 1.5, 2H), 2.41 (d, J = 13.1, 2H), 2.30 (d, J = 13.1, 2H), 1.46 (s, 6H), 1.39 (s, 6H). ^{13}C NMR (100 MHz; CDCl_3): δ 207.37 (C), 152.86 (C), 150.57 (C), 143.41 (C), 131.55 (CH), 130.82 (CH), 128.26 (CH), 127.62 (CH), 122.04 (CH), 89.84 (C), 88.64 (C), 59.20 (CH_2), 57.46 (C), 43.69 (C), 31.56 (CH_3), 29.99 (CH_3). DEPT-135 (100 MHz; CDCl_3): δ 131.53 (CH), 130.80 (CH), 128.26 (CH), 128.02 (CH), 127.61 (CH), 122.03 (CH), 59.20 (CH_2), 31.58 (CH_3), 30.02 (CH_3). DEPT-90

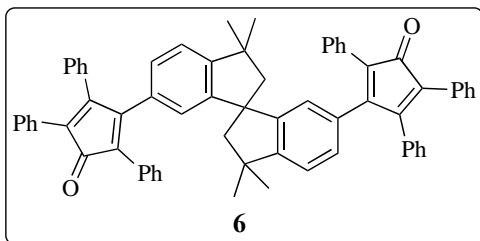
(100 MHz; CDCl₃): δ 131.52 (CH), 130.79 (CH), 128.25 (CH), 128.02 (CH), 127.61 (CH), 122.03 (CH). Mass spectrometry (APCI⁺) m/z : 476.65 [MH]⁺.

5.2.3.1.5 Synthesis of 2,2'-(3,3,3',3'-tetramethyl-2,2',3,3'-tetrahydro-1,1'-spirobi[indene]-6,6'-diyl)bis(1-phenylethane-1,2-dione) (5)



This synthesis was performed by Jafar Alkabli as follows. To a 100 mL round-bottomed flask, compound **4** (3.01 g, 6.32 mmol) and iodine (1.6 g, 6.32 mmol) were added in DMSO (40 mL) under a nitrogen atmosphere. The mixture was stirred overnight at 155 °C, then allowed to cool before being quenched with a saturated solution of sodium thiosulphate and extracted with DCM. Further washing with deionized water was performed, then the combined organic phase was dried over magnesium sulphate before solvent removal under reduced pressure. Purification was achieved using a chromatography column eluted with 1:7 DCM:hexane, to give the targeted compound (**5**) as a yellow solid (1.8g, 51%). ¹H NMR (400 MHz; CDCl₃): δ 7.97 (d, J = 7.3 Hz, 4H), 7.76 (d, J = 7.2 Hz, 2H), 7.66 (d, J = 7.1 Hz, 2H), 7.58 (d, J = 10.6 Hz, 2H), 7.52 (t, J = 7.4 Hz, 4H), 7.32 (d, J = 7.8 Hz, 2H), 2.45 (d, J = 13.2 Hz, 2H), 2.34 (d, J = 13.2 Hz, 2H), 1.46 (s, 6H), 1.40 (s, 6H). ¹³C NMR (100 MHz; CDCl₃): δ 194.6 (CO), 194.1 (CO), 160.0 (C), 151.1 (C), 134.6 (CH), 132.9 (C), 132.6 (C), 130.7 (CH), 129.7 (CH), 128.8 (CH), 124.9 (CH), 122.5 (CH), 58.9 (CH₂), 57.2 (C), 43.8 (C), 31.1 (CH₃), 29.4 (CH₃). DEPT-135 (100 MHz; CDCl₃): δ 134.8 (CH), 130.9 (CH), 130.0 (CH), 129.0 (CH), 125.1 (CH), 122.7 (CH), 59.1 (CH₂), 31.3 (CH₃), 29.6 (CH₃). Mass spectrometry (HRMS) m/z : 541.23 [MH]⁺.

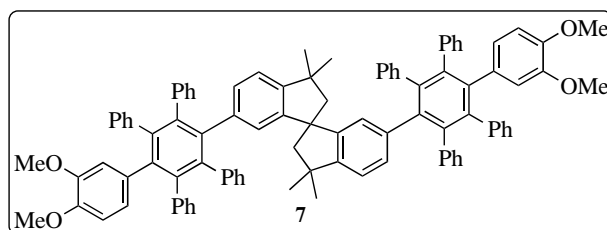
5.2.3.1.6 Synthesis of 4,4'-(3,3,3',3'-tetramethyl-2,2',3,3'-tetrahydro-1,1'-spirobi[indene]-6,6'-diyl)bis(2,3,5-triphenylcyclopenta-2,4-dienone) (6)



This synthesis was also performed by Alkabli, as follows. To a 100 mL round-bottomed flask was added potassium hydroxide (0.075 g, 60%) in ethanol (15 mL). Next, 1,3-diphenyl-2-propanone (0.8 g,

3.85 mmol) and compound **5** (1.04 g, 1.92 mmol) were added to the reaction mixture and stirred until dissolved. The mixture was heated at 80 °C for 2 hours. The product was precipitated with the aid of an ice bath and washed with ethanol before being recrystallized from 1:1 hexane:ethanol to give compound **6** (1.45 g, 85%) as a dark purple solid. ¹H NMR (400 MHz; CDCl₃): δ 7.29-7.12 (m, 30H), 6.92 (d, *J* = 7.9 Hz, 2H), 6.84 (d, *J* = 8.4 Hz, 4H), 6.75 (dd, *J* = 7.8, 1.6 Hz, 2H), 6.18 (d, *J* = 1.2 Hz, 2H), 2.20 (d, *J* = 13.1 Hz, 2H), 1.64 (d, *J* = 13.0 Hz, 2H), 1.29 (s, 6H), 1.18 (s, 6H). ¹³C NMR (100 MHz; CDCl₃): δ 200.5 (CO), 155.2 (C), 154.4 (C), 153.1 (C), 149.5 (C), 133.0 (C), 131.9 (C), 130.8 (C), 130.09 (CH), 130.05 (CH), 129.4 (CH), 128.6 (CH), 128.13 (CH), 128.06 (CH), 127.87 (CH), 127.80 (CH), 127.43 (CH), 127.33 (CH), 125.1 (C), 124.8 (CH), 121.4 (CH), 58.7 (CH₂), 57.5 (C), 43.2 (C), 31.5 (CH₃), 30.1 (CH₃). DEPT-135 (100 MHz; CDCl₃): δ 130.09 (CH), 130.05 (CH), 129.4 (CH), 128.6 (CH), 128.13 (CH), 128.07 (CH), 127.88 (CH), 127.80 (CH), 127.44 (CH), 127.33 (CH), 124.8 (CH), 121.4 (CH), 58.7 (CH₂), 31.5 (CH₃), 30.1 (CH₃). DEPT-90 (100 MHz; CDCl₃): δ 130.09 (CH), 130.05 (CH), 129.40 (CH), 128.56 (CH), 128.13 (CH), 128.07 (CH), 127.88 (CH), 127.80 (CH), 127.43 (CH), 127.33 (CH), 124.80 (CH), 121.44 (CH). Mass spectrometry (HRMS) *m/z*: 889.4 [MH]⁺.

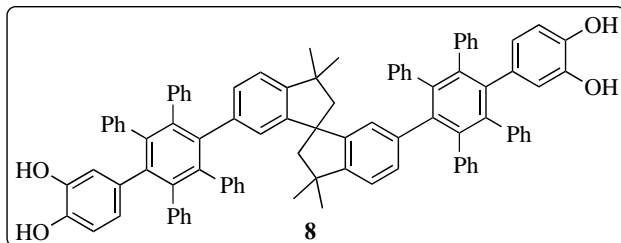
5.2.3.1.7 Synthesis of 6,6'-bis(6'-(3,4-dimethoxyphenyl)-4',5'-diphenyl-[1,1':2',1''-terphenyl]-3'-yl)-3,3',3',3'-tetramethyl-2,2',3,3'-tetrahydro-1,1'-spirobi[indene] (**7**)



Compound **6** (1.36 g, 1.5 mmol), compound **1** (0.60 g, 2.5 mmol) and diphenyl ether (4 mL) were added into a 25 mL round-bottomed flask. The mixture was

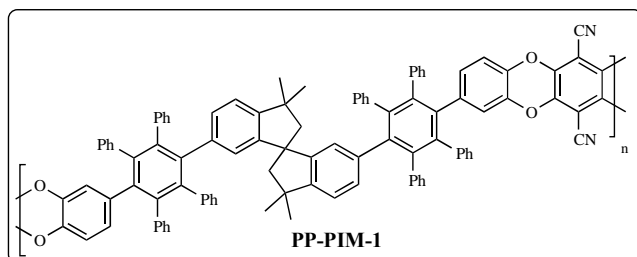
stirred and refluxed for 72 hours under a nitrogen atmosphere. The precipitate was collected by filtration and washed with ethanol and hexane. Compound **7** was obtained as a dark brown solid (1.58 g, 81%). ¹H NMR (400 MHz; CDCl₃): δ 6.94-6.92 (m, 2H), 6.88-6.72 (m, 32H), 6.62-6.58 (m, 6H), 6.54 (d, *J* = 7.8 Hz, 2H), 6.45-6.36 (m, 8H), 6.00 (s, 2H), 3.62 (s, 12H), 1.75 (dd, *J* = 13.0, 2.7 Hz, 2H), 1.20 (dd, *J* = 13.0, 4.8 Hz, 2H), 0.99 (s, 12H). ¹³C NMR (100 MHz; CDCl₃): δ 156.8, 149.4, 149.1, 140.97, 140.95, 140.4, 140.0, 139.2, 132.49, 132.44, 132.32, 131.61, 131.47, 131.33, 126.62, 126.59, 126.48, 124.9, 119.5, 112.14, 112.11, 112.08, 100.0, 58.5, 54.9, 42.8, 39.3, 31.5, 29.9. Mass spectrometry (HRMS) *m/z*: 1309.6190 [MH]⁺.

5.2.3.1.8 Synthesis of 4',4''''-(3,3,3',3'-tetramethyl-2,2',3,3'-tetrahydro-1,1'-spirobi[indene]-6,6'-diyl)bis(3',5',6'-triphenyl-[1,1':2',1''-terphenyl]-3,4-diol) (**8**)



In a 25 mL round-bottomed flask, compound **7** (0.66 g, 0.5 mmol) and dry DCM (12 mL) were added under nitrogen. The mixture was cooled to 0 °C, then boron tribromide (1 g, 4 mmol) was added dropwise. The mixture was left stirring overnight at room temperature, then quenched with methanol and extracted with ethyl acetate. The crude product was then flushed through a chromatography column to yield a pale brown powder (0.53 g, 85%). ¹H NMR (400 MHz; acetone-d₆): δ 7.43 (s, 4H), 7.02-6.74 (m, 38H), 6.68-6.61 (m, 6H), 6.49-6.22 (m, 6H), 6.10 (s, 2H), 1.84-1.81 (m, 2H), 1.34-1.30 (m, 2H), 1.06 (s, 12H). ¹³C NMR (101 MHz; acetone-d₆): δ 150.41 (C), 149.80 (C), 144.80 (C), 144.34 (C), 144.08 (C), 143.33 (C), 143.01 (C), 141.93 (C), 141.52 (C), 141.26 (C), 140.18 (C), 138.72 (C), 133.35 (C), 132.15 (C), 130.53 (CH), 129.03 (CH), 127.39 (CH), 126.71 (CH), 125.96 (C), 124.02 (CH), 120.40 (CH), 119.56 (CH), 119.34 (CH), 114.53 (CH), 59.23 (CH₂), 57.26 (C), 43.62 (C), 31.76 (CH₃), 29.46 (CH₃). DEPT-135 (100 MHz; acetone-d₆): δ 131.27 (CH), 129.66 (CH), 129.64 (CH), 128.14 (CH), 126.52 (CH), 125.82 (CH), 125.06 (CH), 123.26 (CH), 119.52 (CH), 118.67 (CH), 118.45 (CH), 113.65 (CH), 58.36 (CH₂), 30.93 (CH₃), 29.34 (CH₃). DEPT-90 (100 MHz; acetone-d₆): δ 131.25 (CH), 130.68 (CH), 129.61 (CH), 128.13 (CH), 126.50 (CH), 125.82 (CH), 125.05 (CH), 123.12 (CH), 119.51 (CH), 118.66 (CH), 118.45 (CH), 113.65 (CH). Mass spectrometry (HRMS) *m/z*: 1253.5509 [MH]⁺.

5.2.3.1.9 Synthesis of PP-PIM-1 from 6,6'-bis(1-(3,4-dihydroxyphenyl)-2,3,5,6-tetraphenylbenzyl)-3,3,3',3'-tetramethyl-1,1'-spirobisindane



PP-PIM-1(1): Compound **8** (0.252 g, 0.19 mmol), TFTP (0.038 g, 0.19 mmol) and potassium carbonate (0.208 g,

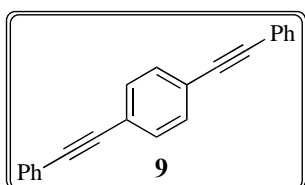
1.5 mmol) were added to a 7 ml screw-cap tube equipped with a bar stirrer. The system was vacuumed by syringe and nitrogen was injected in five cycles before the addition of DMF (4.5 mL). The reaction mixture was stirred at 65 °C for 48 h. Thereafter, the polymer was precipitated in water (7 mL), then filtered and washed with 50:50 acetone:water (20 mL). The mixture was dried overnight in a vacuum oven at 100 °C to give a yellow solid (205 g, 79%).

PP-PIM-1(2): Compound **8** (0.100 g, 0.08 mmol), TFTPn (0.016 g, 0.08 mmol) and potassium carbonate (0.066 g, 0.5 mmol) were added to a 7 ml screw-cap tube equipped with a bar stirrer. The system was vacuumed by syringe and nitrogen was injected in five cycles before the addition of DMF (1 mL) and toluene (0.3 mL). The reaction mixture was stirred at 125 °C for 1 h. Thereafter, the polymer was precipitated in water (7 mL), then filtered and washed with 50:50 acetone:water (30 mL). The mixture was dried overnight in a vacuum oven at 100 °C to give a yellow solid (0.064 g, 58%).

PP-PIM-1(3): Compound **8** (0.235g, 0.188 mmol), TFTPn (0.0375 g, 0.188 mmol) and potassium carbonate (0.155 g, 1.17 mmol) were added to a 7 ml screw-cap tube equipped with a bar stirrer. The system was vacuumed by syringe and nitrogen was injected in five cycles before the addition of DMF (1.3 mL) and toluene (0.3 mL). The reaction mixture was stirred at 145 °C for 30 minutes. Thereafter, the polymer was precipitated in methanol (5 mL), filtered, then washed with excess methanol and subsequently with deionized water and methanol. The mixture was then dried overnight in a vacuum oven at 100 °C to give a yellow solid (220 g, 85%). GPC - conc. 1 mg/mL, $M_w = 50 \times 10^3 \text{ g mol}^{-1}$, $M_n = 13.9 \times 10^3 \text{ g mol}^{-1}$, $M_w/M_n = 3.5$. $^1\text{H NMR}$ (400 MHz; CDCl_3): δ 6.88 (br, s, 52H), 1.74 (br, s, 4H), 1.02 (br, s, 12H). IR (ATR; cm^{-1}): 3100-2850, 2160, 1600, 1497, 1450, 1260, 741. UV-Vis (CHCl_3) λ_{max} (nm): 251, 288, 438.

5.2.3.2 Synthesis of PP-PIM-2

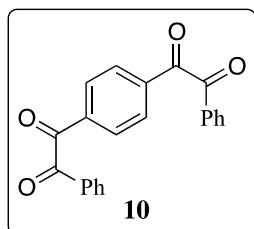
5.2.3.2.1 Synthesis of 1,4-bis (phenylethynyl)benzene (**9**)



This synthesis was performed by Alkabli, as follows. 1,4-diiodobenzene (10 g, 30 mmol), CuI (0.7 g, 1.8

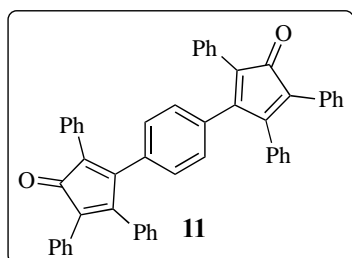
mmol) and $\text{Pd}(\text{PPh}_3)_2\text{Cl}_2$ (1.32 g, 1.8 mmol) were stirred for 20 min in DMF (60 mL) and triethylamine (45 mL) at 50 °C under nitrogen. Phenylacetylene (4 mL, 30 mmol) was added to the reaction mixture over the next 20 min and stirring was continued overnight at 70 °C. The mixture was extracted with diethylether, washed with water, then dried over Mg_2SO_4 and by reduced pressure. The residue was purified by column chromatography using 10:1 ethylacetate:hexane to give compound **9** as a white solid (3 g, 36 %). ^1H NMR (400 MHz; CDCl_3): δ 7.55-7.53 (m, 4H), 7.52 (s, 4H), 7.38-7.35 (m, 6H). ^{13}C NMR (100 MHz; CDCl_3): δ 131.63, 131.53, 128.46, 128.39, 123.09, 123.03, 91.2, 89.1. Mass spectrometry (HRMS) m/z : 279.1181 $[\text{MH}]^+$.

5.2.3.2.2 Synthesis of 2,2'-(1,4-phenylene)bis(1-phenylethane-1,2-dione) (**10**)



This synthesis was performed by Alkabli, as follows. Compound **9** (6 g, 21.5 mmol) was dissolved in DMSO (30 mL) before iodine (2.5 g, 10.75 mmol) was added. The reaction mixture was then stirred overnight at 155 °C under a nitrogen atmosphere. After cooling, it was quenched with a saturated solution of sodium thiosulphate, then extracted with DCM. The combined organic layers were washed five times with water, dried over magnesium sulphate and concentrated under vacuum. Purification was performed by column chromatography using a 1:7 DCM:hexane eluent, to yield the compound **10** as a yellow solid (3.2 g, 44%). ^1H NMR (400 MHz; CDCl_3): δ 8.11 (s, 4H), 7.97 (dd, J = 8.4, 1.2 Hz, 4H), 7.69 (tt, J = 7.5, 1.4 Hz, 2H), 7.53 (t, J = 7.8 Hz, 4H). ^{13}C NMR (100 MHz; CDCl_3): δ 193.43, 193.28, 137.1, 135.3, 132.6, 130.3, 130.0, 129.2. Mass spectrometry (HRMS) m/z : 541.2376 $[\text{MH}]^+$.

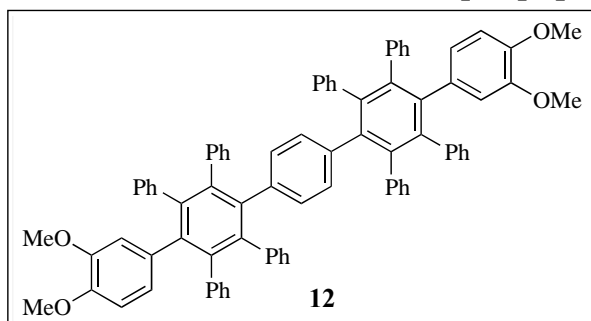
5.2.3.2.3 Synthesis of 4,4'-(1,4-phenylene)bis(2,3,5-triphenylcyclopenta-2,4-dienone) (**11**)



This synthesis was performed by Alkabli, as follows. To a solution of potassium hydroxide (0.1176 g, 2.1 mmol) in ethanol (15 mL) were added 1,3-diphenyl-2-propanone (0.886 g, 4.2 mmol) and

compound **10** (0.7 g, 2.1 mmol). The mixture was stirred for 2 h at 80 °C, then cooled and precipitation of the product was carried out with the aid of an ice bath. The product was washed with cooled ethanol and recrystallized by hexane:ethanol (1:1) to yield compound **11** (0.95 g, 65%). ¹H NMR (400 MHz; CDCl₃): δ 7.31-7.23 (m, 26H), 6.95 (d, *J* = 7.0 Hz, 4H), 6.81 (s, 4H). ¹³C NMR (100 MHz; CDCl₃): δ 200.1, 154.06, 153.87, 133.5, 132.9, 130.56, 130.49, 130.09, 130.03, 129.2, 129.0, 128.6, 128.06, 128.02, 127.99, 127.61, 127.56, 125.5, 125.2. Mass spectrometry (HRMS) *m/z*: 889.4040 [MH]⁺.

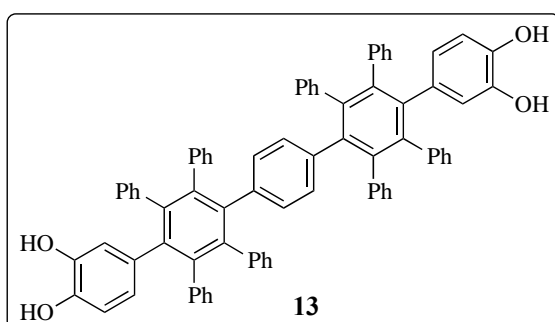
5.2.3.2.4 Synthesis of 3,3''',4,4'''-tetramethoxy-2',2''',3',3''',5',5''',6',6'''-octaphenyl-1,1':4,1'':4'',1''':4''',1''''-quinquephenyl (**12**)



This synthesis was performed by Alkabli, as follows. Compound **11** (1.5 g, 2.17 mmol), compound **1** (1.17 g, 4.8 mmol) and diphenyl ether (4 mL) were added into a 25 mL round-bottomed flask. The

mixture was stirred and refluxed for 72 hours under nitrogen. The precipitate was collected by filtration and washed with ethanol and hexane. Compound **12** was obtained as a dark brown solid. ¹H NMR (400 MHz; CDCl₃): δ 7.12-7.08 (m, 2H), 7.01 (dd, *J* = 8.7, 1.1 Hz, 2H), 6.92-6.66 (m, 40H), 6.33 (dd, *J* = 8.5, 1.9 Hz, 2H), 6.25 (s, 4H), 3.66 (s, 6H), 3.37 (s, 6H). ¹³C NMR (100 MHz; CDCl₃): δ 131.82, 131.79, 131.76, 131.73, 131.69, 131.62, 131.57, 131.55, 131.49, 131.44, 131.31, 130.35, 130.32, 130.1, 126.67, 126.60, 126.58, 126.55, 126.51, 126.49, 125.10, 125.07, 125.04, 109.4, 100.0, 55.5. Mass spectrometry (HRMS) *m/z*: 1111.4758 [MH]⁺.

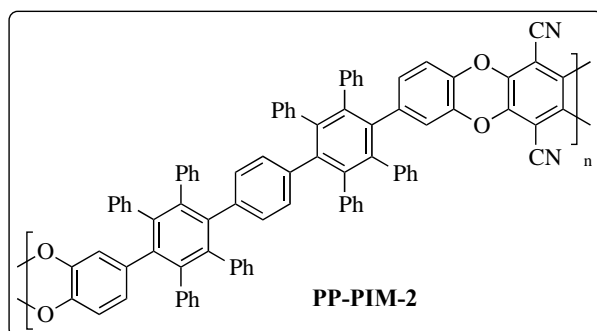
5.2.3.2.5 Synthesis of 2',2''',3',3''',5',5''',6',6'''-octaphenyl-[1,1':4,1'':4'',1''':4''',1''''-quinquephenyl]-3,3''',4,4'''-tetraol (**13**)



This synthesis was performed by Alkabli, as follows. In a 25 mL round-bottomed flask, compound **12** (1.3 g, 1.17 mmol) and dry DCM (25 mL)

were mixed under nitrogen. The mixture was cooled to 0 °C, then boron tribromide (1 g, 4 mmol) was added dropwise. The mixture was stirred overnight at room temperature, then quenched with methanol and extracted using ethyl acetate. The crude product was then flushed through a chromatography column to give a pale brown powder. ^1H NMR (400 MHz; acetone- d_6): δ 7.49-7.45 (m, 2H), 7.24-7.20 (m, 2H), 7.10-7.08 (m, 2H), 7.01-6.75 (m, 40H), 6.38-6.35 (m, 4H), 2.97 (s, 4H). ^{13}C NMR (100 MHz; acetone- d_6): δ 152.1, 132.03, 131.98, 131.92, 131.86, 130.7, 127.25, 127.11, 127.00, 125.7, 123.9, 119.3, 30.03, 29.84, 29.65. Mass spectrometry (HRMS) m/z : 1055.4084 $[\text{MH}]^+$.

5.2.3.2.6 Synthesis of PP-PIM-2 from 2',2''',3',3''',5',5''',6',6'''-octaphenyl-[1,1':4',1'':4'',1''':4''',1''':4'''-quinquephenyl]-3,3''',4,4'''-tetraol

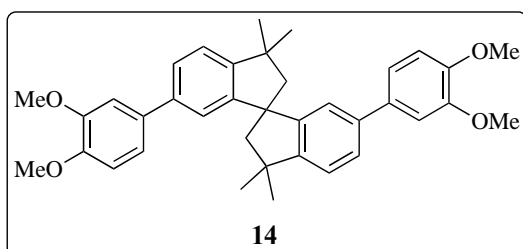


Compound **13** (0.2 g, 0.19 mmol), TFTPn (0.038 g, 0.19 mmol) and potassium carbonate (0.208 g, 1.5 mmol) were added to 4.5 mL DMF in a 10 mL round-bottomed flask under nitrogen. The mixture was stirred for 48 hours at

65 °C, then quenched with water (5 mL) and filtered with extensive washing with water. The polymer was washed with methanol before being filtered and dried in a vacuum oven at 100 °C to give a brownish solid (0.15 g, 59%). ^{13}C Solid-State NMR (100 MHz): δ 150-112.5 (br, Ar). IR (ATR; cm^{-1}): 3100-3000, 2240, 1599, 1451, 1262, 730. UV-Vis (CHCl_3) λ_{max} (nm): 248, 304, 413.

5.2.3.3 Biphenyl-based polymer of intrinsic microporosity (BP-PIM-1)

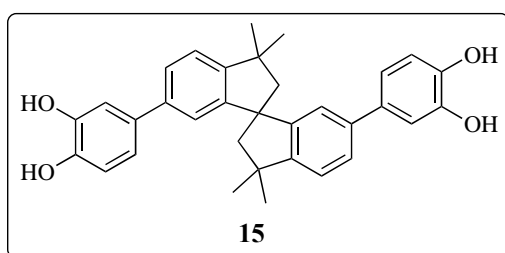
5.2.3.3.1 Synthesis of 6,6'-bis(3,4-dimethoxyphenyl)-3,3,3',3'-tetramethyl-2,2',3,3'-tetrahydro-1,1'-spirobi[indene] (**14**)



Compound **3** (4.69 g, 8.2 mmol), dimethoxyphenylboronic acid (3 g, 16.49 mmol), $\text{Pd}(\text{PPh}_3)_4$ (0.95 g, 0.825 mmol), toluene (72 mL), deionized water (108

mL), K_2CO_3 (30 g, 217 mmol) and aliquat 336[®] (5 drops) were added to a 250 mL round-bottomed flask. The mixture was degassed three times by the freeze-thaw method, then stirred overnight at 75 °C. The crude was worked up by organic layer extraction and the aqueous layer was washed with toluene (3 × 50 mL). The combined organic layer was washed further with water (2 × 70 mL) and brine (2 × 70 mL) before being dried over magnesium sulphate. The solvent was removed under reduced pressure and the crude was purified using column chromatography, eluted with 2:5 ethyl acetate:hexane to give a white solid (**14**) (3.72 g, 83%). ¹H NMR (400 MHz; CDCl_3): δ 7.43 (dd, J = 7.9, 1.8, 2H), 7.26 (d, J = 7.6 2H), 7.00 (dd, J = 7.5, 1.5, 6H), 6.85 (dd, J = 3.6, 1.2 2H), 3.87 (d, J = 2.0, 12H), 2.43 (d, J = 13.1, 2H), 2.37 (d, J = 13.1, 2H), 1.46 (s, 6H), 1.41 (s, 6H). ¹³C NMR (100 MHz; CDCl_3): δ 151.20 (C), 151.16 (C), 148.93 (C), 148.32 (C), 140.52 (C), 134.73 (C), 126.13 (CH), 122.84 (CH), 122.15 (CH), 119.49 (CH), 111.27 (CH), 110.69 (CH), 59.66 (CH_2), 57.90 (C), 55.95 (CH_3), 43.27 (C), 31.66 (CH_3), 30.38 (CH_3). DEPT-135 (100 MHz; CDCl_3): δ 126.13 (CH), 122.84 (CH), 122.15 (CH), 119.48 (CH), 111.26 (CH), 110.67 (CH), 59.65 (CH_2), 55.94 (CH_3), 31.66 (CH_3), 30.38 (CH_3). DEPT-90 (100 MHz; CDCl_3): δ 126.13 (CH), 122.84 (CH), 122.14 (CH), 119.48 (CH), 111.26 (CH), 110.67 (CH). Mass spectrometry (APCI⁺) m/z : 549.3 [MH]⁺.

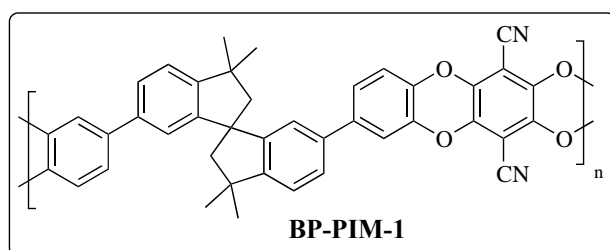
5.2.3.3.2 Synthesis of 4,4'-(3,3',3'-tetramethyl-2,2',3,3'-tetrahydro-1,1'-spirobi[indene]-6,6'-diyl)bis(benzene-1,2-diol) (**15**)



Compound **14** (2.68 g, 4.89 mmol) was added to a 50 mL round-bottomed flask equipped with a bar stirrer, then degassed and refilled with nitrogen for three cycles. Thereafter, dry DCM (33 mL) was added, then the mixture was dried overnight over molecular sieve 3 Å. Boron tribromide (3.7 mL) was next added dropwise at 0 °C and the reaction mixture was left stirring overnight at room temperature. Finally, the reaction was quenched with water and the crude product extracted with ethyl acetate before being evaporated and dried to give **15**. ¹H NMR (500 MHz; CDCl_3): δ 7.99 (s, 4H), 7.52 (dd, J = 7.9, 1.8, 2H), 7.37 (dd, J = 8.0, 0.5, 2H), 7.07-7.05 (m, 4H), 6.95 (dd, J = 8.2, 2.2, 2H), 6.89 (d, J = 8.2, 2H), 2.53 (d, J = 13.0, 2H), 2.43 (d, J = 13.0, 2H),

1.55 (s, 6H), 1.48 (s, 6H). ^{13}C NMR (100 MHz; CDCl_3): δ 156.42 (C), 155.86 (C), 150.38 (C), 149.77 (C), 145.62 (C), 138.62 (C), 130.81 (CH), 127.36 (CH), 127.07 (CH), 123.49 (CH), 120.76 (CH), 118.89 (CH), 64.79 (CH_2), 62.91 (C), 48.21 (C), 36.28 (CH_3), 34.91 (CH_3). DEPT-135 (100 MHz; CDCl_3): δ 130.81 (CH), 127.36 (CH), 127.07 (CH), 123.49 (CH), 120.76 (CH), 118.89 (CH), 64.78 (CH_2), 36.28 (CH_3), 34.92 (CH_3). DEPT-90 (100 MHz; CDCl_3): δ 130.82 (CH), 127.37 (CH), 127.08 (CH), 123.50 (CH), 120.77 (CH), 118.90 (CH). Mass spectrometry (APCI $^+$) m/z : 493.5 $[\text{MH}]^+$.

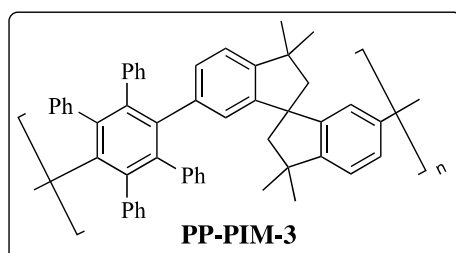
5.2.3.3.3 Synthesis of BP-PIM-1 from 4,4'-(3,3,3',3'-tetramethyl-2,2',3,3'-tetrahydro-1,1'-spirobi[indene]-6,6'-diyl)bis(benzene-1,2-diol)



To a 7 mL screw cap tube equipped with a magnetic stirrer, compound **15** (0.29 g, 0.59 mmol), TFTP (0.1776 g, 0.59 mmol), potassium carbonate (0.486 g, 3.5

mmol) and DMF (2 mL) were added under nitrogen. The mixture was stirred for 30 min at 145 °C, then quenched with methanol (5 mL) and filtered with extensive washing with water and methanol. It was dried in a vacuum oven at 100 °C to give a yellowish solid (0.32 g, 89%). ^1H NMR (500 MHz; CD_2Cl_2): δ 7.68-6.71 (br, m, 12H), 2.49 (br, s, 2H), 2.35 (br, s, 2H), 1.50 (br, s, 6H), 1.43 (br, s, 6H). ^{13}C Solid-State NMR (100 MHz): δ 151.06 (br, Ar), 138.41 (br, Ar), 122.70 (br, Ar), 115.47 (br, Ar), 93.73 (br, Ar), 57.58 (br, CH_2), 42.23 (br, C), 29.30 (br, CH_3). IR (ATR; cm^{-1}): 3050-2850, 2240, 1600, 1500, 1450, 1260, 1010, 748. UV-Vis (CHCl_3) λ_{max} (nm): 255, 297, 439.

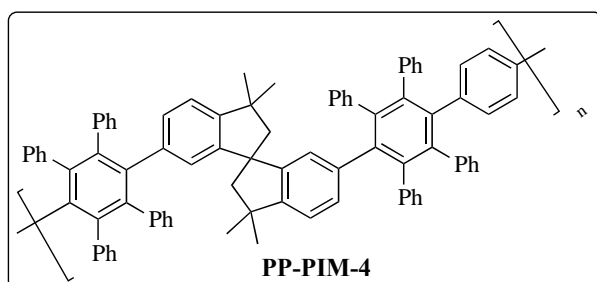
5.2.3.4 Synthesis of PP-PIM-3



This polymerization was performed by Alkabli, as follows. Compound **6** (80 mg, 0.0899 mmol), compound **4** (42 mg, 0.0899 mmol) and diphenylether (0.3 mL) were added to a 7 mL screw-cap tube. The reaction

mixture was degassed and left stirring for 10 days at 255 °C. The initial purple colour of the mixture turned to pale yellow by the 8th day, after which 2,3,4,5-tetraphenylcyclopenta-2,4-dienone (0.2 eq.) was added as an end-capping agent. After the 9th day, diphenylacetylene (0.2 eq.) was added. The reaction mixture was cooled to room temperature, then the targeted polymer was precipitated with methanol, collected by filtration, washed with hexane and dried under high vacuum to give a pale brownish polymer (86.2 mg, 65% yield). GPC - conc. 1 mg mL⁻¹, $M_w = 53 \times 10^3$ g mol⁻¹, $M_n = 13 \times 10^3$ g mol⁻¹, $M_w/M_n = 4.2$. ¹H NMR (500 MHz; CDCl₃): δ 6.77 (br, s, 26H), 1.57 (br, s, 4H), 0.99 (br, s, 12H). ¹³C NMR (100 MHz; CDCl₃): δ 150.2-147.7 (br, Ar), 141.6-138.6 (br, Ar) 133.4-123.4 (br, Ar), 120.4-118.8 (br, Ar), 58.4 (CH₂), 42.6 (C), 31.3 (CH₃), 30.0 (CH₃). IR (ATR; cm⁻¹): 3100-3000, 2952-2861, 1600, 1495, 1441, 697. UV-Vis (CHCl₃) λ_{max} (nm): 240, 256, 281, 313.

5.2.3.5 Synthesis of PP-PIM-4



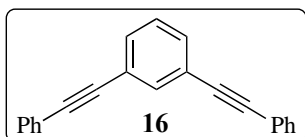
This polymerization was performed by Alkabli, as follows. Compound **11** (80 mg, 0.115 mmol), compound **4** (55 mg, 0.115 mmol) and diphenylether (0.3 mL) were added to a 7 mL screw-cap

tube. The reaction mixture was degassed and left stirring at 255 °C for 10 days. The initial purple colour of the mixture turned to pale yellow by the 8th day, after which 2,3,4,5-tetraphenylcyclopenta-2,4-dienone (0.2 eq.) was added as an end-capping agent. After the 9th day, diphenylacetylene (0.2 eq.) was added as well. The reaction mixture was cooled to room temperature, then the targeted polymer was precipitated with methanol, collected by filtration, washed with hexane and dried under high vacuum to give a pale brownish polymer (122 mg, 82% yield). GPC - conc. 1 mg mL⁻¹, $M_w = 75 \times 10^3$ g mol⁻¹, $M_n = 15 \times 10^3$ g mol⁻¹, $M_w/M_n = 4.9$. ¹H NMR (500 MHz; CD₂Cl₂): δ 6.79 (br, s, 50H), 1.74 (br, s, 4H), 1.01 (br, s, 12H). ¹³C NMR (100 MHz; CD₂Cl₂): δ 140.95 (CH), 131.49 (CH), 130.13 (CH), 126.64 (CH), 125.29 (CH), 123.01 (CH), 43.17 (CH₂), 31.46 (CH₃), 29.78 (CH₃). IR (ATR; cm⁻¹): 3100-

3000, 2930-2850, 1600, 1496, 1442, 696. UV-Vis (CHCl_3) λ_{max} (nm): 241, 258, 284, 313.

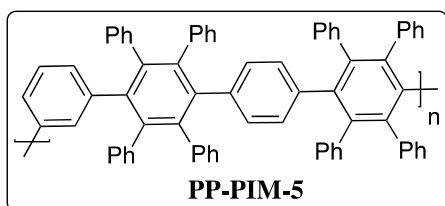
5.2.3.6 Synthesis of PP-PIM-5

5.2.3.6.1 Synthesis of 1,3-bis(phenylethynyl)benzene (**16**)



This synthesis was performed by Alkabli, as follows. 1,3-diiodobenzene (3.5 g, 10 mmol), CuI (0.12 g, 0.6 mmol) and $\text{Pd}(\text{PPh}_3)_2\text{Cl}_2$ (0.47 g, 0.6 mmol) were stirred in DMF (25 mL) and TEA (15 mL) at 50 °C under nitrogen for 20 min. Phenylacetylene (2.05 mL, 20 mmol) was then added to the reaction mixture over 10 min and stirring was continued overnight at 70 °C. The mixture was extracted with diethylether and water, dried over Mg_2SO_4 , then dried under reduced pressure. The residue was purified on a silica gel column with 10:1 ethylacetate:hexane, to yield a white solid compound (0.83 g, 30%). MP = 113 °C. ^1H NMR (400 MHz; CDCl_3): 7.33-7.40 (m, 7H), 7.50-7.52 (m, 2H), 7.55-7.57 (m, 4H), 7.74 (dt, J = 1.6 and 0.4 Hz, 1H). ^{13}C NMR (100 MHz, CDCl_3): 88.7, 90.1, 123.1, 123.8, 128.5, 128.6, 131.4, 131.8, 134.7. Mass spectrometry (HRMS) m/z : 279.1164 $[\text{MH}]^+$.

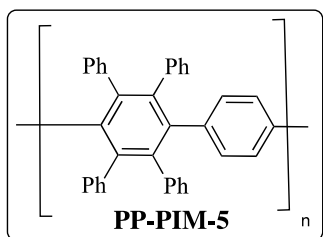
5.2.3.6.2 Synthesis of PP-PIM-5



This polymerization was performed by Alkabli, as follows. Compound **11** (80 mg, 0.0899 mmol), compound **16** (25 mg, 0.0899 mmol) and diphenylether (0.3 mL) were added to a 7 mL screw-cap tube. The reaction mixture was degassed and left stirring for 10 days at 255 °C. The initial purple colour of the mixture turned to pale yellow by the 8th day, after which 2,3,4,5-tetraphenylcyclopenta-2,4-dienone (0.2 eq.) was added as end-capping agent. After the 9th day, diphenylacetylene (0.2 eq.) was added as well. The reaction mixture was cooled to room temperature, then the targeted polymer was precipitated with methanol, collected by filtration, washed with hexane and dried under high vacuum to give a pale brownish polymer (44 mg, 40% yield). GPC - conc. 1 mg mL⁻¹, $M_w = 29 \times 10^3$ g mol⁻¹, $M_n = 7.3 \times 10^3$ g mol⁻¹, $M_w/M_n = 3.9$. ^1H

NMR (500 MHz; CDCl₃): δ 8.26-5.88 (m, Ar). ¹³C NMR (100 MHz; CDCl₃): δ 141.03, 140.99, 140.8, 140.56, 140.39, 139.9, 139.0, 131.6, 131.1, 130.89, 130.73, 130.3, 129.96, 129.88, 129.1, 126.5, 124.9. IR (ATR; cm⁻¹): 3100-3000, 1599, 1494, 1441, 695. UV-Vis (CHCl₃) λ_{max} (nm): 241, 267, 305, 359.

5.2.3.7 Synthesis of PP-PIM-6



This polymerization was performed by Alkabli, as follows. Compound **11** (80 mg, 0.115 mmol), compound **9** (55 mg, 0.115 mmol) and diphenylether (0.3 mL) were added to a 7 mL screw-cap tube. The mixture was degassed and left stirring for 10 days at 255 °C. Its initial purple colour turned to pale yellow by the 8th day, after which 2,3,4,5-tetraphenylcyclopenta-2,4-dienone (0.2 eq.) was added as end-capping agent. After the 9th day, diphenylacetylene (0.2 eq.) was added as well. The reaction mixture was cooled to room temperature, then the targeted polymer was precipitated with methanol, collected by filtration, washed with hexane and dried under high vacuum to give a pale brownish polymer (62 mg, 51% yield). GPC - conc. 1 mg mL⁻¹, $M_w = 4.5 \times 10^3$ g mol⁻¹, $M_n = 1.4 \times 10^3$ g mol⁻¹, $M_w/M_n = 3.3$. ¹H NMR (500 MHz; CD₂Cl₂): δ 7.32 (br, Ar). ¹³C NMR (100 MHz; CDCl₃): δ 132-125 (br, m, CH). IR (ATR; cm⁻¹): 3100-3000, 2159, 1667, 1596, 1488, 1446, 1416, 696. UV-Vis (CHCl₃) λ_{max} (nm): 241, 261, 299, 312.

5.3 Results and discussion

5.3.1 Synthesis of polyphenylene-based polymers of intrinsic microporosity (PP-PIMs)

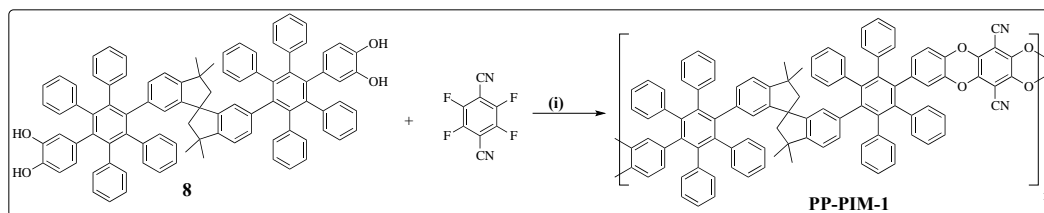
In this work, new polymers were synthesized in order to investigate the structural properties arising from combining two building blocks of HPBs and spirobisindanes, both of which have three-dimensional structures with high potential for inefficient packing in the solid state. PP-PIMs with novel porous properties were expected from incorporating these building blocks. In addition, studies were made of

the synthesis of various PP-PIMs which differed in the number of phenyl substituents, polymer backbone contortion and polymer linkages; in particular, dioxane-forming and benzene-forming PP-PIMs. In general, this work was based on the experience of the Budd and Gardiner research groups. Alkabli was involved in this work, as his project focused on the synthesis and characterization of novel polyphenylene dendrimers. Alkabli prepared nine of the organic precursors required for the preparation of PP-PIM-1 and PP-PIM-2. He also prepared four polymers via Diels-Alder polymerization.

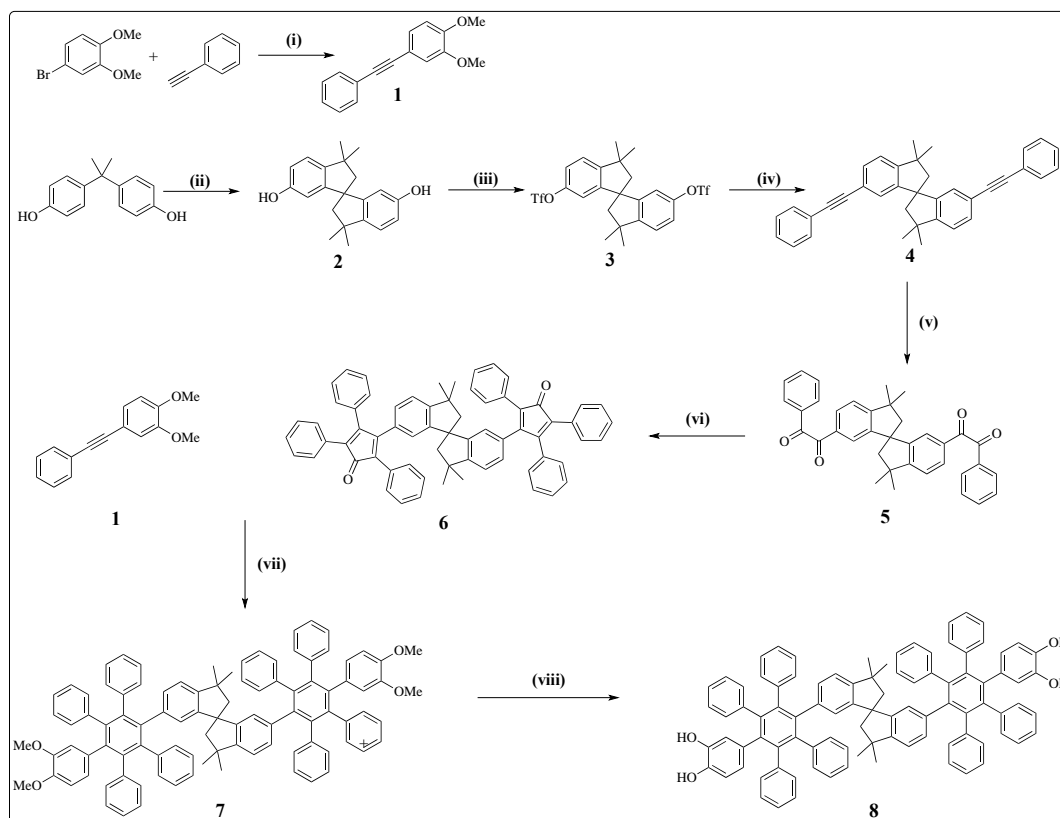
5.3.1.1 PP-PIMs via condensation polymerization

5.3.1.1.1 Synthesis of PP-PIM-1

The synthesis of PP-PIM-1 required a novel monomer (compound **8**), in order to perform condensation polymerization (Scheme 5-6). For the synthesis of compound **8**, a number of precursors were synthesized in series, as outlined in Scheme 5-7, beginning with the Sonogashira coupling reaction for the synthesis of compound **1**. In this reaction, carbon-carbon coupling between phenylacetylene and 4-bromoveratole was facilitated by the presence of a palladium catalyst. Compound **6** was prepared in order to react it with compound **1** for the preparation of compound **8**. The synthesis of compound **6** began with the preparation of spirobisindane compound **2**, which was performed in the acidic medium of methanesulfonic acid.¹⁹ The triflation of compound **2**, using triflic anhydride and pyridine as base, yielded compound **3**. Sonogashira coupling was performed between phenylacetylene and compound **3** to give compound **4**, in which triflate substituents (-OTf) act as good leaving groups. The resulting compound (**4**) underwent oxidation to form a benzil derivative (**5**), which was then condensed with 1,3-diphenyl-2-propanone to give the bis-TPCPD compound **6**. Thereafter, the Diels-Alder reaction between compounds **1** and **6** was used to prepare compound **7**. Finally, the monomer **8** was synthesized from compound **7** by demethylation.



Scheme 5-6. Synthesis of PP-PIM-1 from **8**. i) K_2CO_3 , DMF, toluene, 145 °C, 30 min.



Scheme 5-7. Synthesis of **8**. i) $\text{PdCl}_2(\text{PPh}_3)_2$, CuI, DMF, diisopropylamine, 60 °C, 24 h; ii) $\text{CH}_3\text{SO}_3\text{H}$, RT, 4 days; iii) $(\text{CF}_3\text{SO}_2)_2\text{O}$, DCM, pyridine, RT, 18 h; iv) Phenylacetylene, $\text{PdCl}_2(\text{PPh}_3)_2$, CuI, DMF, Et_3N , 80 °C, 17 h; v) I_2 , DMSO, 155 °C, 18 h; vi) 1,3-diphenyl-2-propanone, KOH, EtOH, 80 °C, 2 h; vii) Diphenyl ether, 255 °C, 3 days; viii) BBr_3 , DCM, RT, 18 h.

Three different polymerization conditions were applied using compound **8** and TFTP as monomers. The first condition, PP-PIM-1 (1), was adapted from the low-temperature method (LTM) followed by McKeown et al.¹³ in preparing HPB-PIM-2. The polymerization did not produce a high molar mass polymer; dissolution in acetone and methanol were observed. GPC confirmed that the products were oligomers (Figure 5-4).

PP-PIM-1 (2) was the second attempt to prepare this polymer. The conditions were adapted to follow the high temperature method (HTM): the polymerization temperature was set at 125 °C. However, the product yielded was similar to that of PP-PIM-1 (1) in terms of solubility in acetone and methanol, while the GPC results were not significantly different from those of PP-PIM-1 (1) (Figure 5-4).

The third attempt was the preparation of PP-PIM-1 (3). This also followed the HTM, but the temperature was set at 145 °C. After 30 min of the reaction, stirring was ceased because the reaction mixture was becoming viscous. This time, the polymerization mixture was precipitated in methanol, indicating a higher molar mass polymer than in the cases of PP-PIM-1 (1) and PP-PIM-1 (2). The GPC graph in Figure 5-4 shows the higher molar mass of PP-PIM-1 (3). Although sufficient molar mass for a film-forming polymer was still not reached, this work indicates that this polymer can be prepared with a high molar mass using the HTM. Polymerization could probably be optimized towards a high molar mass polymer via large-scale production involving a mechanical stirrer for effective mixing. It is worth mentioning that compound **8** has a high molecular weight, which may have inhibited the polymerization of the small molecules of the TFTP_N monomer.

The structure of PP-PIM-1 was confirmed by ¹H NMR in chloroform solution, as shown in Figure 5-5. MALDI-ToF mass spectrometry showed the presence of cyclic oligomers of PP-PIM-1 (C₂-C₇) that were produced in this polymerization (Figure 5-6). This result confirms that cyclization occurred in this polymerization, as in the case of PIM-1 preparation.

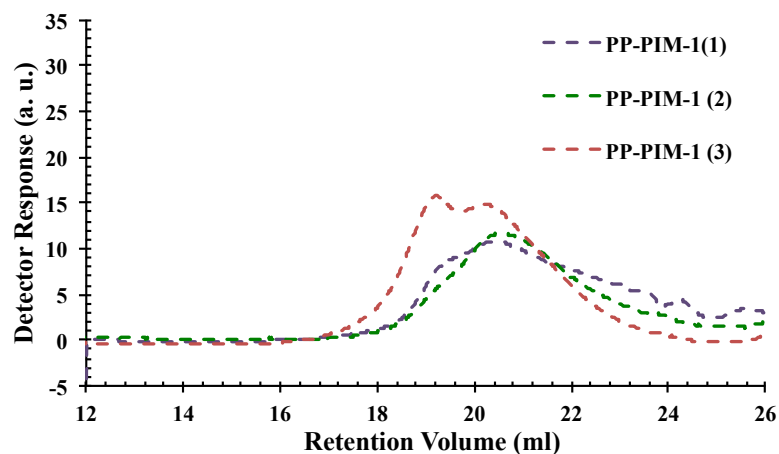


Figure 5-4. GPC plots of three batches of PP-PIM-1 polymerization. PP-PIM-1 (1) was via LTM, PP-PIM-1 (2) and PP-PIM-1 (3) via HTM, at 125 °C and 145 °C respectively.

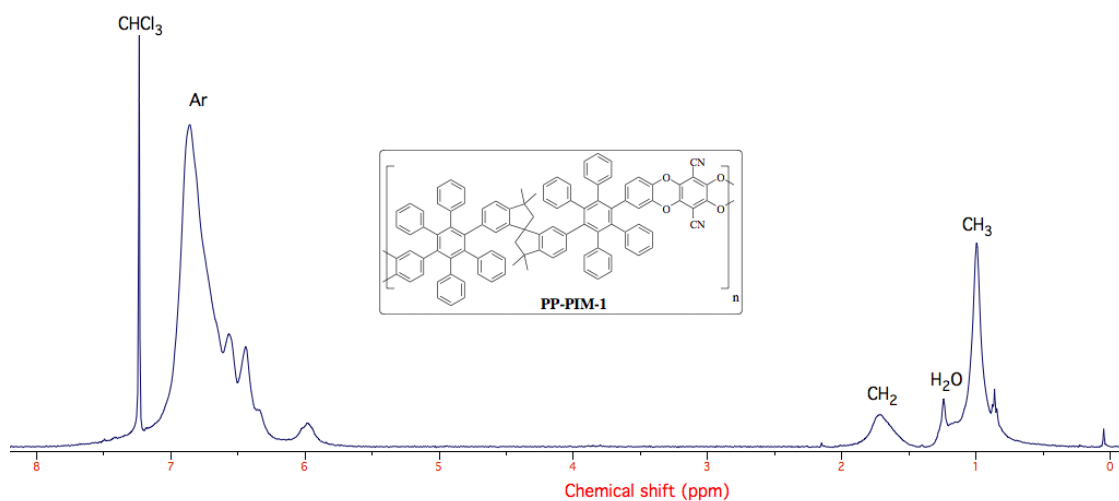


Figure 5-5. ^1H NMR spectroscopy of PP-PIM-1 in CDCl_3 .

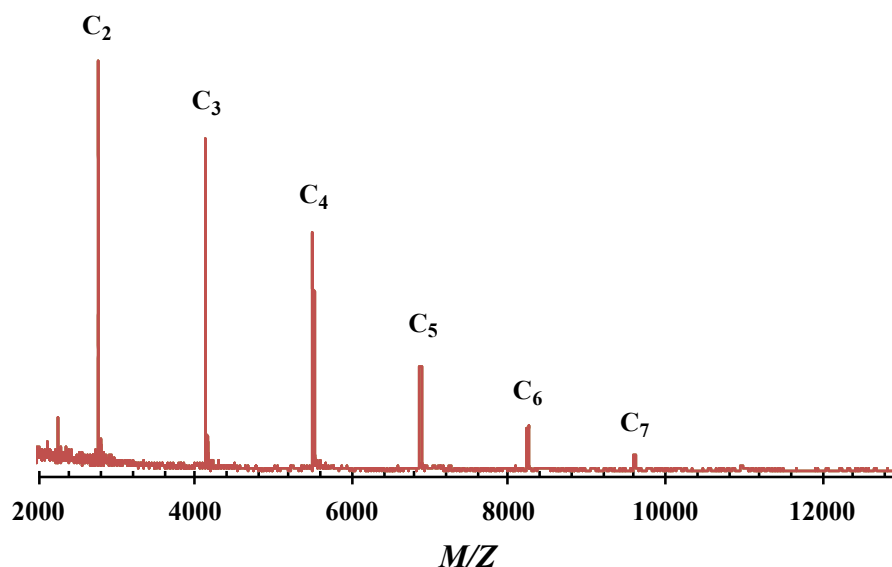


Figure 5-6. MALDI-ToF spectrum of PP-PIM-1 produced by HTM (batch PP-PIM-1 (3)), showing cyclic-PP-PIM-1 oligomers. Cyclic-PP-PIM-1 = $C_n = 1373.6 \times n + 23$.

The porous properties of PP-PIM-1 were investigated. The nitrogen sorption isotherm of PP-PIM-1 (3) showed an apparent BET surface area of $326 \text{ m}^2 \text{ g}^{-1}$ (Figure 5-7). Significant adsorption at low relative pressure ($P/P^\circ < 0.01$) indicates that PP-PIM-1 is a microporous polymer. However, the value of BET surface area is considerably lower than what was found for PIM-1 ($700 \text{ m}^2 \text{ g}^{-1}$).

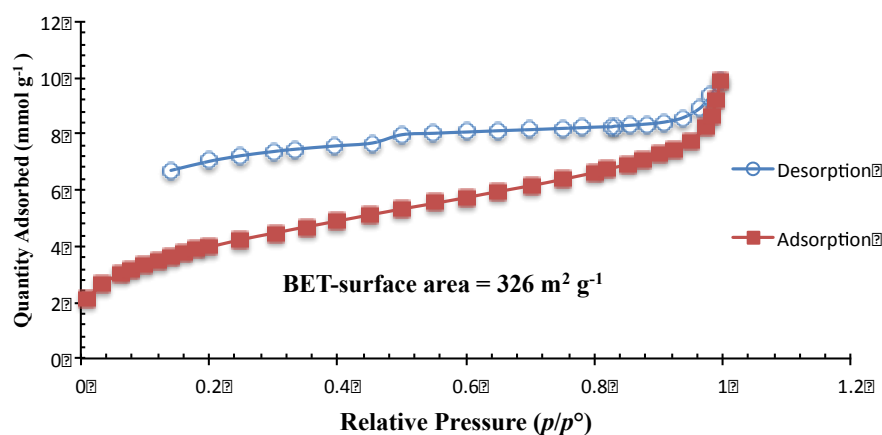
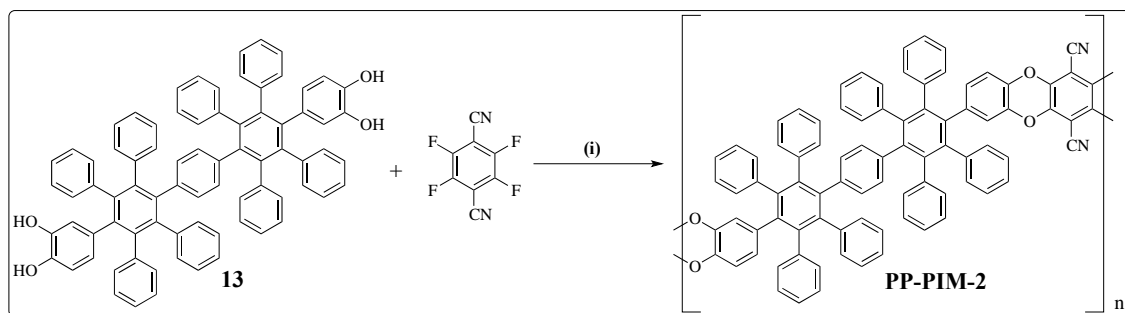


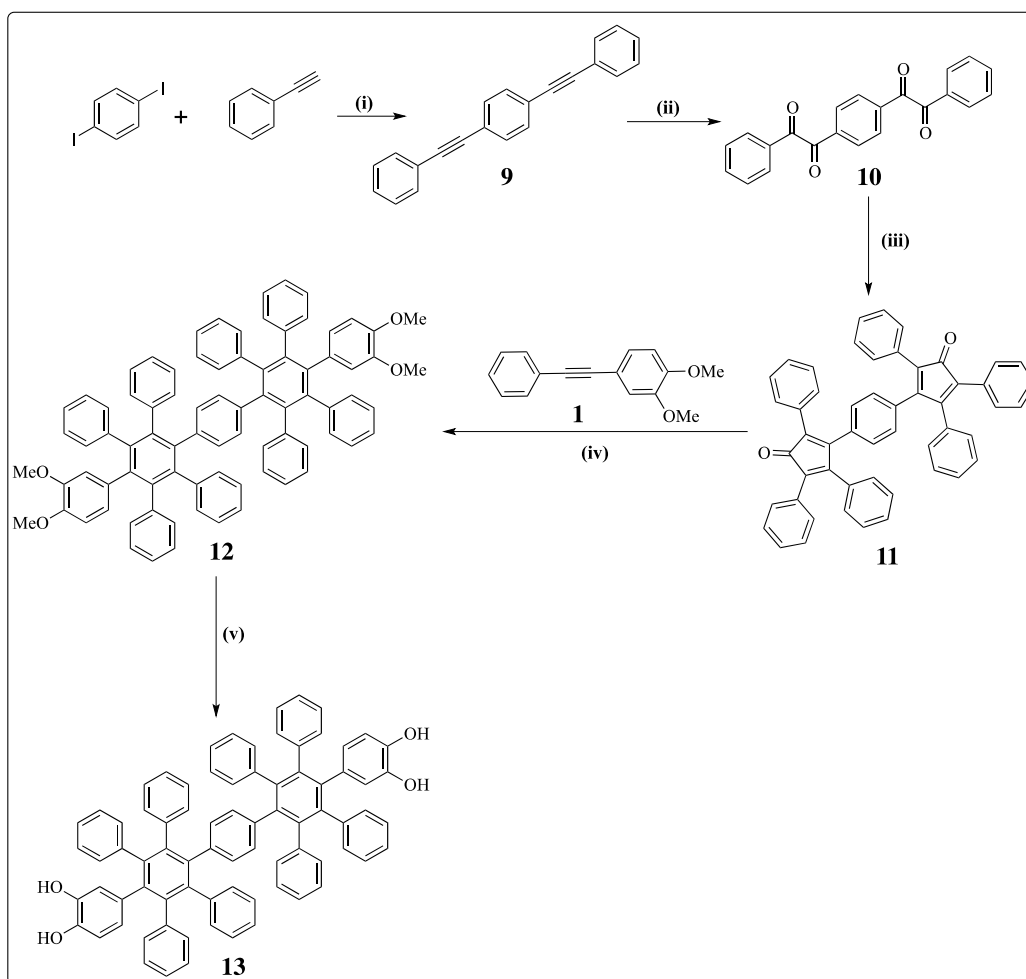
Figure 5-7. Nitrogen sorption isotherm of PP-PIM-1 at 77 K; nitrogen adsorption (filled squares) and desorption (empty circles).

5.3.1.1.2 Synthesis of PP-PIM-2

The absence of spirobisindine units in PP-PIM-2 is one of the key differences between this polymer and PP-PIM-1. PP-PIM-2 was synthesized from compound **13** as a monomer via condensation polymerization (Scheme 5-8). The preparation of compound **13** was carried out via a number of organic reactions, as outlined in Scheme 5-9. Compound **9** was synthesised by Sonogashira coupling between 1,4-diiodobenzene and phenylacetylene, catalyzed with a palladium compound. Compound **9** was then converted to benzil derivative **10**, followed by condensation to form compound **11**. Thereafter, a cycloaddition reaction gave compound **12**, which was basically the targeted monomer, but protected with methyl substituents. In order to deprotect this compound for polymerization purposes, boron tribromide was used for demethylation and synthesis of the monomer of compound **13**. The BET surface area was measured by means of the nitrogen isotherm at $290 \text{ m}^2 \text{ g}^{-1}$ (Figure 5-8). This value is also lower than the PIM-1 value of $700 \text{ m}^2 \text{ g}^{-1}$.



Scheme 5-8. Synthesis of PP-PIM-2 from **13**, i) K_2CO_3 , DMF, 65°C , 48 h.



Scheme 5-9. Synthesis of **13**, i) PdCl₂(PPh₃)₂, CuI, DMF, Et₃N, 50 °C, 18 h; ii) I₂, DMSO, 155 °C, 18 h; iii) 1,3-diphenyl-2-propanone, KOH, EtOH, 80 °C, 2 h; iv) Diphenyl ether, 255 °C, 3 days; v) BBr₃, DCM, RT, 18 h.

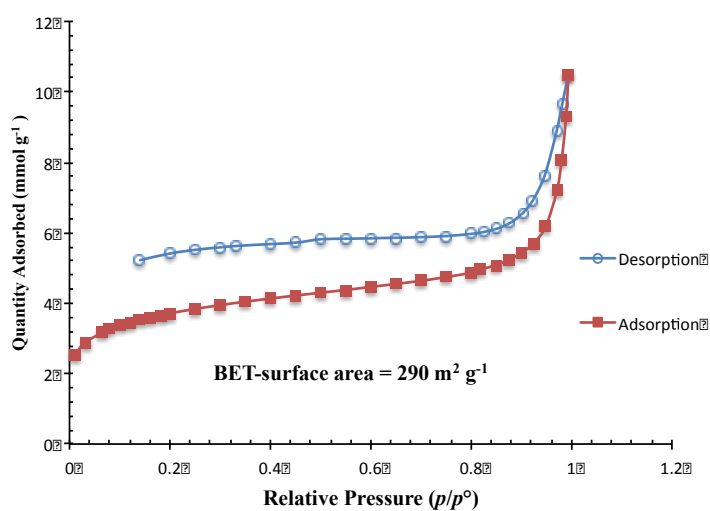


Figure 5-8. Nitrogen sorption isotherm of PP-PIM-2 at 77 K; nitrogen adsorption (filled squares) and desorption (empty circles).

PP-PIM-2 was brownish in colour in the powder form and was not soluble in any organic solvent such as chloroform, tetrahydrofuran, DCM, DMF, dimethylacetamide, DMSO and 1,4-dichlorobenzene. However, there were small traces of oligomers that were soluble to give a greenish fluorescent solution (Figure 5-9). This greenish colour is known to be due to fluorophore units. Soluble fractions in d_6 -DMSO were measured in ^1H NMR, producing broad peaks in the region between 6.5 and 7 ppm (Figure 5-10). Solid-state ^{13}C NMR confirmed the structure, as broad peaks of aromatic carbons were observed (Figure 5-11). In contrast, PP-PIM-1 showed the same peaks of aromatic carbon, but with alkane carbons of spirobisindine. Another comparison between PP-PIM-1 and PP-PIM-2, using IR spectra, shows the absence of alkane C-H stretch peaks in PP-PIM-2 (Figure 5-12).

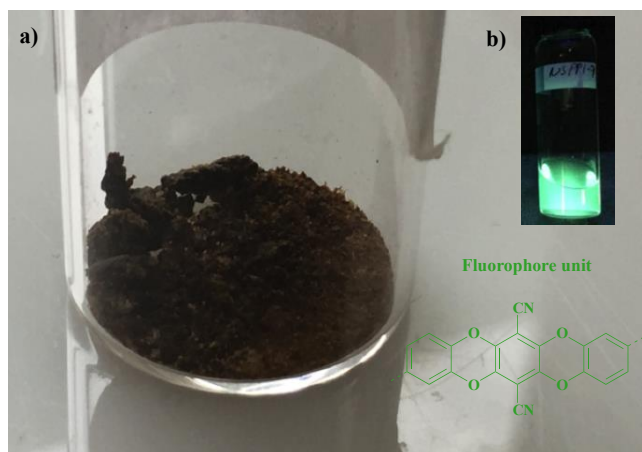


Figure 5-9. Photograph of PP-PIM-2 powder (a) and oligomer solution in chloroform under a UV lamp at 365 nm (b).

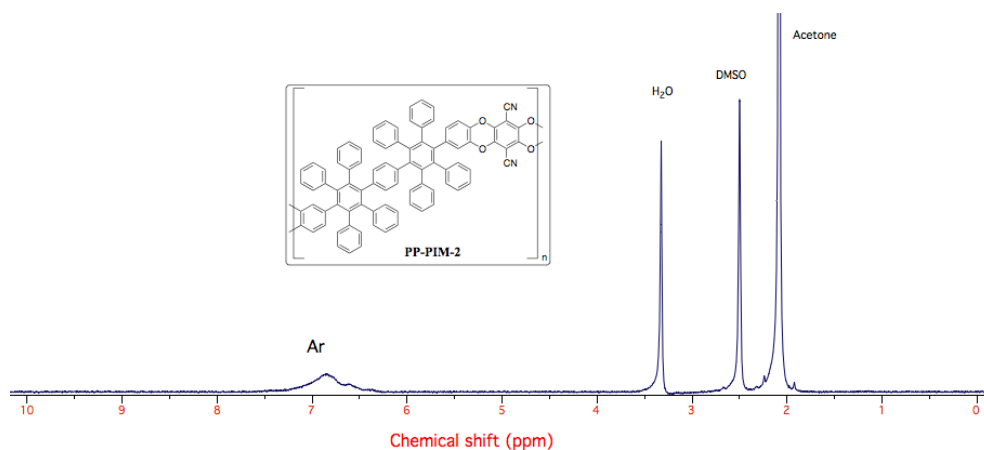


Figure 5-10. ^1H NMR spectroscopy of soluble fractions of PP-PIM-2 in d_6 -DMSO.

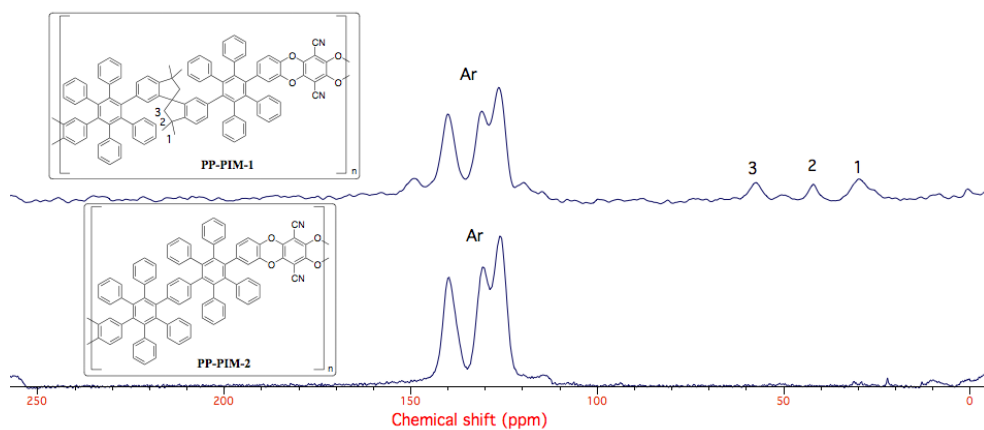


Figure 5-11. ^{13}C solid-state NMR spectroscopy of PP-PIM-1 (top) and PP-PIM-2 (bottom). Data provided by Bann Dawood.

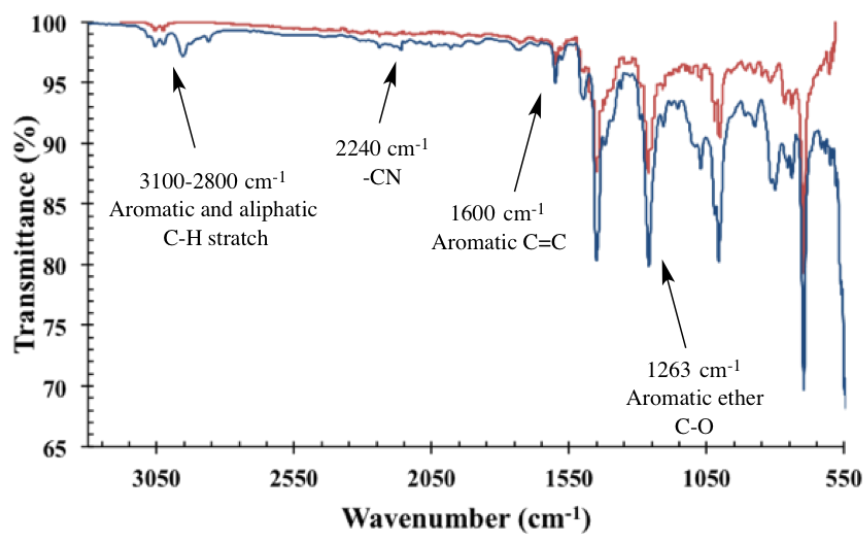
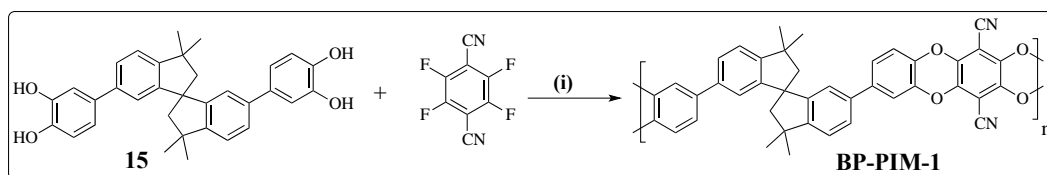


Figure 5-12. ATR-IR spectra of PP-PIM-2 (top) and PP-PIM-1 (bottom).

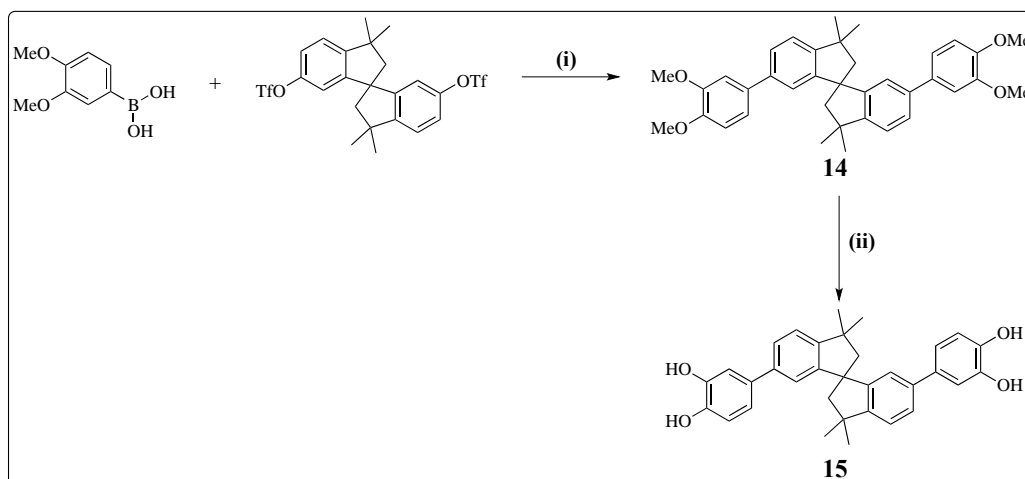
5.3.1.1.3 Synthesis of BP-PIM-1

BP-PIM-1 was synthesised by condensation polymerization between compound **15** and TFTPn, as shown in Scheme 5-10. The polymer structure has significantly fewer phenyl substituents compared to the shape-persistent structures of PP-PIM-1 and PP-PIM-2. Spirobisindane units may introduce contortion to the polymer chains, allowing more free voids to form. However, phenyl-phenyl single bonds in the biphenyl units are expected to possess more conformational freedom than that of PIM-1.



Scheme 5-10. Synthesis of BP-PIM-1 from **15**.

In order to prepare BP-PIM-1, compound **15** was synthesised by the route shown in Scheme 5-11, beginning with Suzuki coupling between a triflated spirobisindane precursor and 3,4-dimethoxyphenylboronic acid, in the presence of a palladium catalyst. This reaction successfully produced compound **14**, which was converted to active monomer **15** by boron-mediated demethylation.



Scheme 5-11. Synthesis of compound **15**. i) $\text{Pd}(\text{PPh}_3)_4$, K_2CO_3 , toluene/ H_2O , aliquat 336[®], 75 °C, 18 h; ii) BBr_3 , DCM, RT, 18 h.

The polymerization conditions, adapted from HTM, gave a yellowish powder (Figure 5-13a). This polymer was not soluble in chloroform, tetrahydrofuran, DCM, DMSO or 1,4-dichlorobenzene. Only oligomer traces were soluble in organic solvents such as chloroform, tetrahydrofuran and DCM. Figure 5-13b shows a solution of BP-PIM-1 oligomers that is fluorescent under a UV lamp, in a very similar way to PIM-1 solution. Interestingly, MALDI-ToF mass spectrometry shows peaks correlated to cyclic oligomers of BP-PIM-1 ranging from C₂ to C₇ (Figure 5-14).

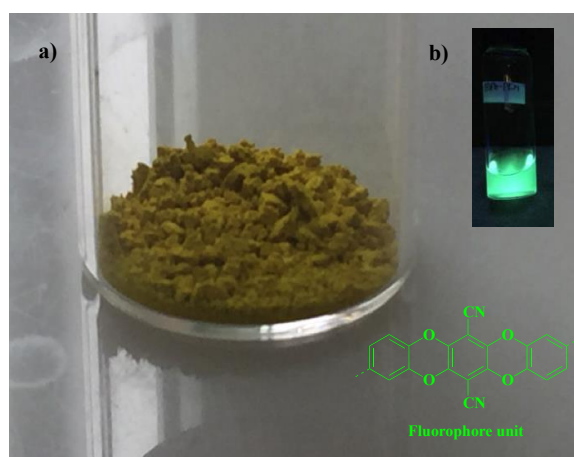


Figure 5-13. Photograph of BP-PIM-1 powder (a) and oligomer solution in chloroform under UV lamp at 365 nm (b).

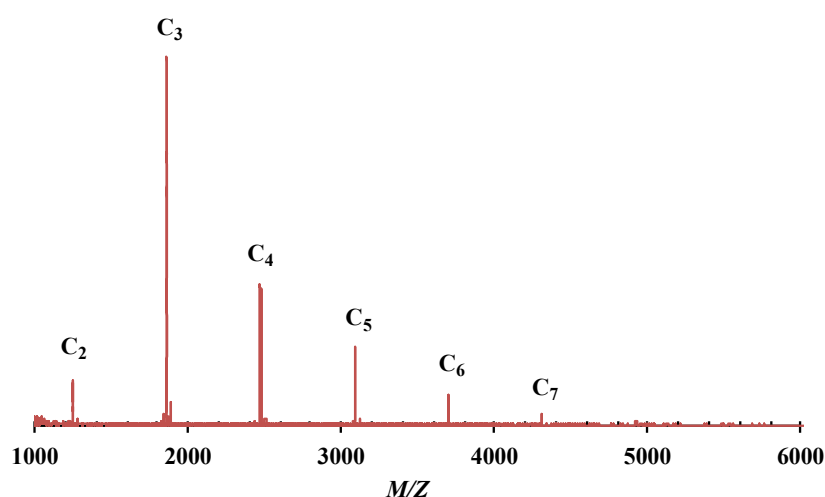


Figure 5-14. MALDI-ToF spectrum of BP-PIM-1, showing peaks of cyclic-PP-PIM-1 oligomers. Cyclic-PP-PIM-1 = C_n = 612.2 × n + 23.

^1H NMR spectroscopy of BP-PIM-1 (soluble fractions) showed broad peaks of aromatic protons between 7.7 and 6.7 ppm (Figure 5-15). There were also broad alkane peaks of CH_2 and CH_3 between 2.6 and 1 ppm.

Because BP-PIM-1 was not totally soluble, it was subjected to ^{13}C solid-state NMR. Comparison between BP-PIM-1 and PIM-1 spectra shows different patterns of aromatic carbon peaks (Figure 5-16). However, carbon peaks correlated to nitrile and alkane groups are similar. This result was expected, as the differences are based mainly on aromatic carbons. The IR spectrum (Figure 5-17) showed absorption at 2240 cm^{-1} corresponding to nitrile groups, as well as aromatic and aliphatic C-H stretch in the range of $2800\text{--}3100\text{ cm}^{-1}$ and aromatic $\text{C}=\text{C}$ at 1600 cm^{-1} .

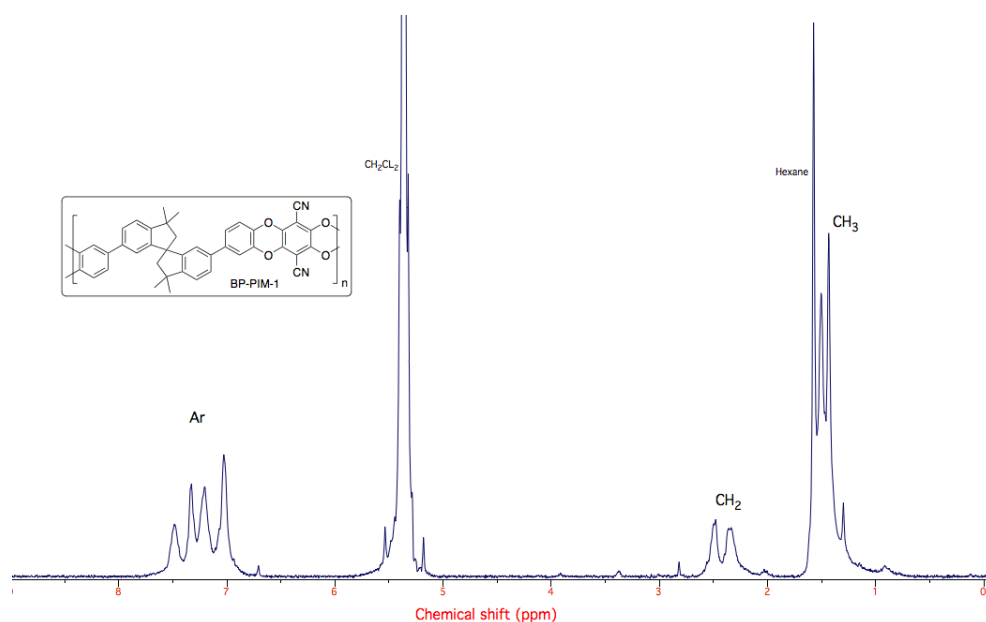


Figure 5-15. ^1H NMR spectroscopy of BP-PIM-1 in CD_2Cl_2 .

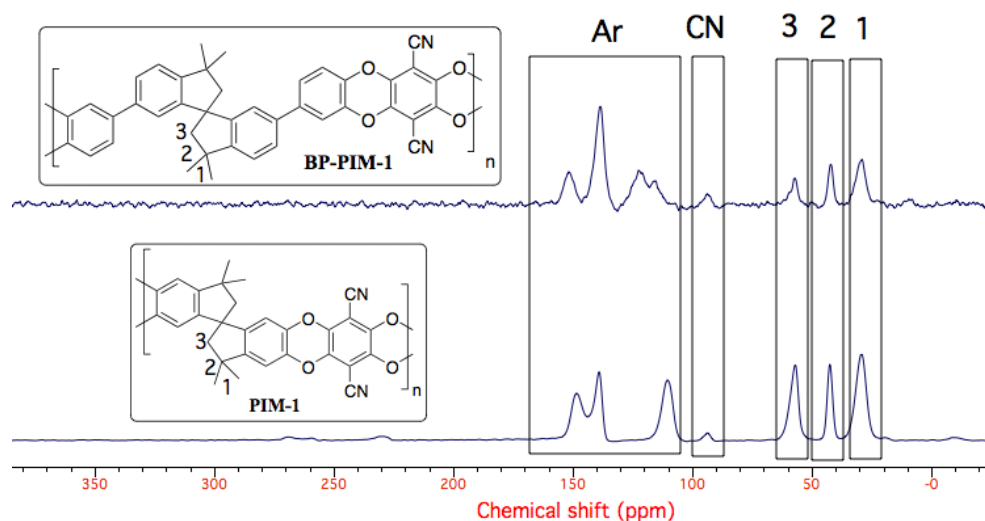


Figure 5-16. ^{13}C solid-state NMR spectra of BP-PIM-1 (top) and PIM-1 (bottom). Data provided by Bann Dawood.

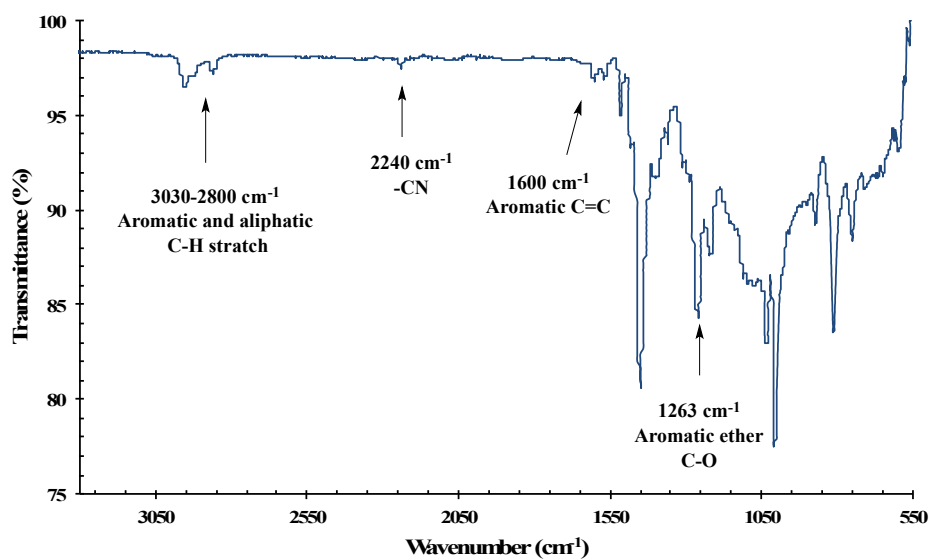


Figure 5-17. ATR-IR spectrum of BP-PIM-1.

BP-PIM-1 had a BET surface area of $443 \text{ m}^2 \text{ g}^{-1}$, calculated from the nitrogen isotherm (Figure 5-18). This value is lower than PIM-1 ($700 \text{ m}^2 \text{ g}^{-1}$), which can be ascribed to the higher conformational freedom of the backbone in BP-PIM-1.

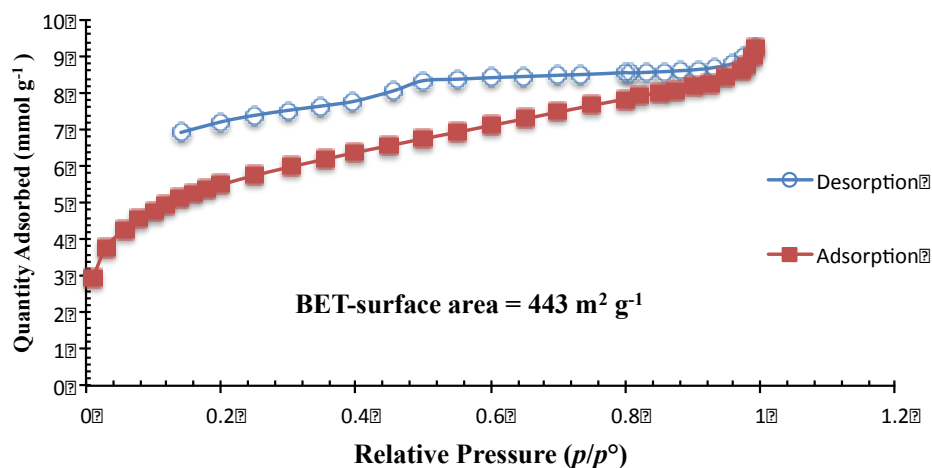


Figure 5-18. Nitrogen sorption isotherm of BP-PIM-1 at 77 K; nitrogen adsorption (filled squares) and desorption (empty circles).

UV-Vis absorptions of this sample and others of dibenzodioxin-forming polymers were measured (Figure 5-19), all of which showed absorption typical of phenyl groups ($\lambda_{\text{max}} \approx 250$ nm), in addition to that of dibenzodioxin substituents at around 440 nm.

The TGA thermogram (Figure 5-20) shows that PP-PIM-1 is similar to PIM-1 in tending to degrade above ca. 450 °C, whereas BP-PIM-1 degrades at a lower temperature, above ca. 390 °C, and PP-PIM-2 at a higher temperature than PIM-1 and PP-PIM-1.

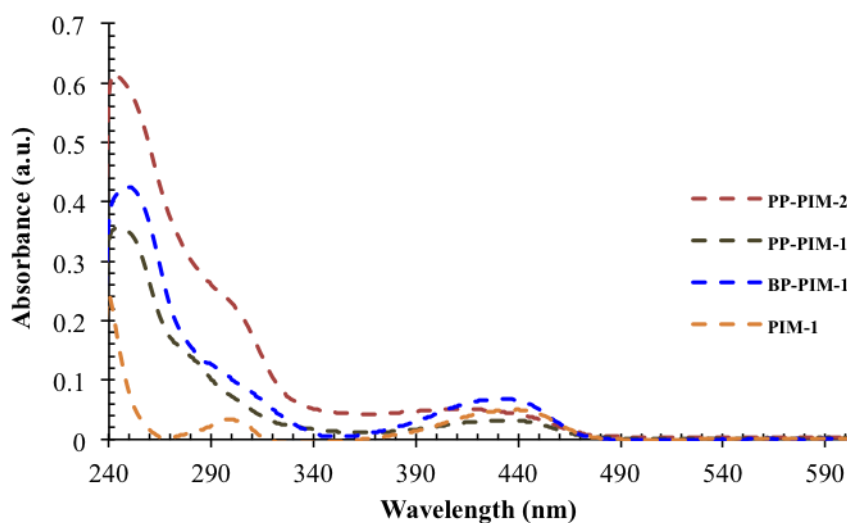


Figure 5-19. UV-Vis spectra of PP-PIMs from condensation polymerization.

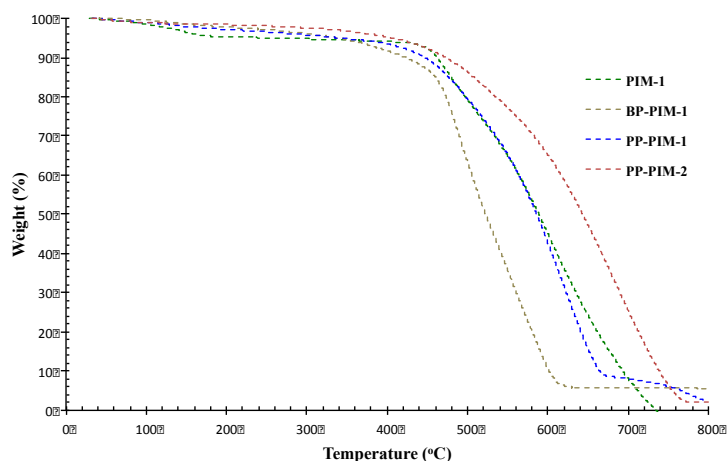
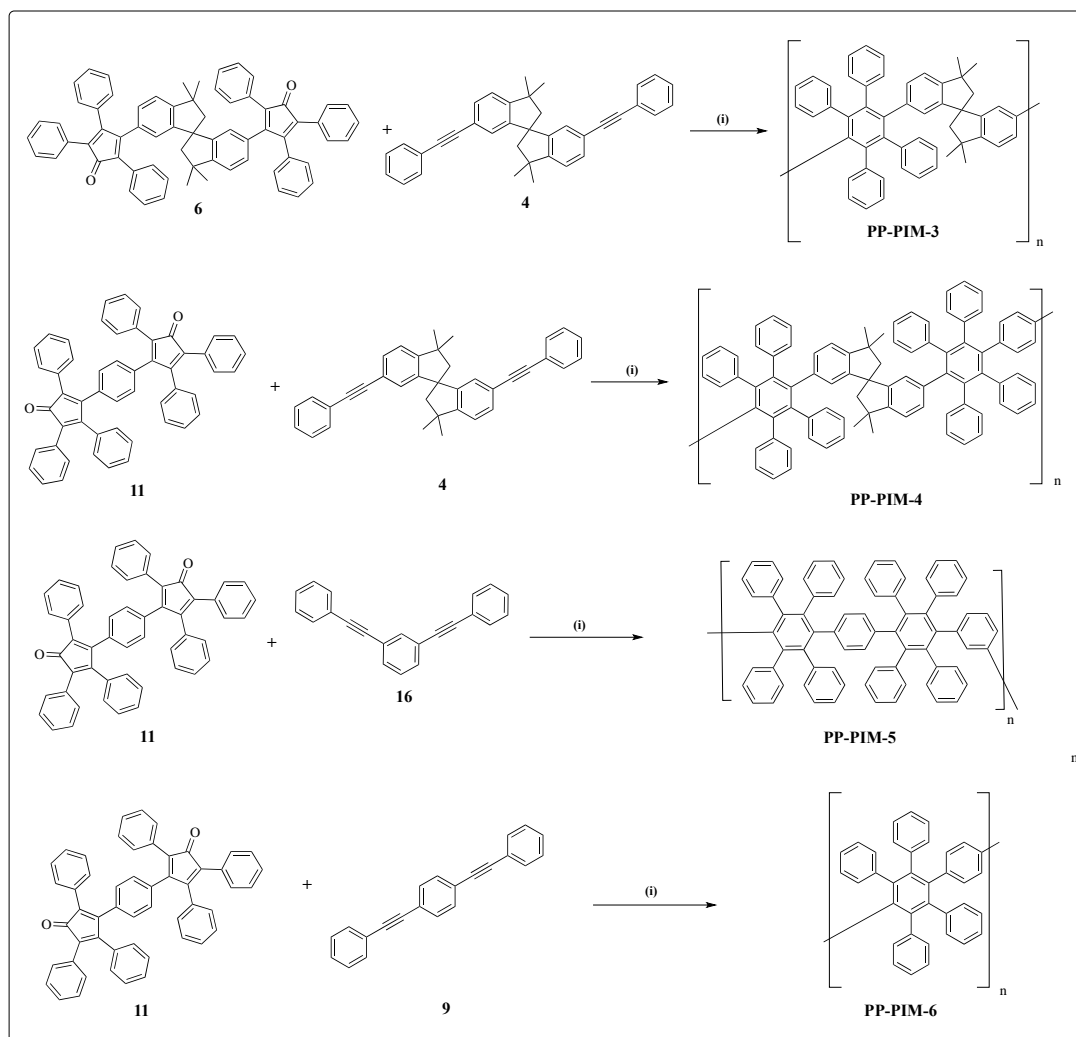


Figure 5-20. TGA thermogram of PP-PIMs from condensation polymerization.

5.3.1.2 PP-PIMs via Diels-Alder polymerization

Synthesis of PP-PIM-3, PP-PIM-4, PP-PIM-5 and PP-PIM-6 were performed by Alkabli, as outlined in Scheme 5-12. These syntheses are based on [2-4] cycloaddition Diels-Alder polymerization, in which A-A and B-B type monomers were required to form six-membered ring linkages. This is a metal-free reaction. The monomers were subjected to a high temperature condition (255 °C), so diphenylether was used as solvent for its high decomposition temperature.



Scheme 5-12. Synthesis of PP-PIMs from Diels Alder polymerization. i) diphenyl ether, 255 °C, 8 days. These polymerizations were performed by Alkabli.

This approach yielded polyphenylene-based polymers with relatively rigid structures consisting only of carbon and hydrogen atoms. The capability of polyphenylene as a building block to prohibit efficient polymer packing can lead to polymers with intrinsic microporosity.¹⁴ Therefore, these polymers are of interest in PIM applications such as gas separation or sensing.

GPC results (Table 5-1) show potential polymerization tendencies. PP-PIM-3 and PP-PIM-4 were higher in molar mass than PP-PIM-6 and PP-PIM-5. It seems that the presence of spirobisindine in the polymer backbone causes polymerization to tend towards high molar mass polymers. However, further study is needed to optimize the polymerization conditions. BET surface areas were measured by nitrogen adsorption isotherms (Figure 5-21) for PP-PIM-3, PP-PIM-4 and PP-PIM-5,

all of which had values significantly lower than PIM-1 ($700 \text{ m}^2 \text{ g}^{-1}$), as can be seen in Table 5-1. These polymers also showed little variation in their BET surface area values. It is worth mentioning, however, that their isotherms exhibit the properties of microporous polymers (Figure 5-21).

Table 5-1. Properties of PP-PIMs prepared via Diels Alder polymerization.

Polymer name	Mw (g mol^{-1})	Mn (g mol^{-1})	PDI	Yield (%)	BET surface area ($\text{m}^2 \text{ g}^{-1}$)
PP-PIM-3	57×10^3	12×10^3	4.5	65	358
PP-PIM-4	83×10^3	13×10^3	6.6	82	363
PP-PIM-5	29×10^3	7×10^3	3.9	40	393
PP-PIM-6	5.2×10^3	1.3×10^3	3.8	51	-

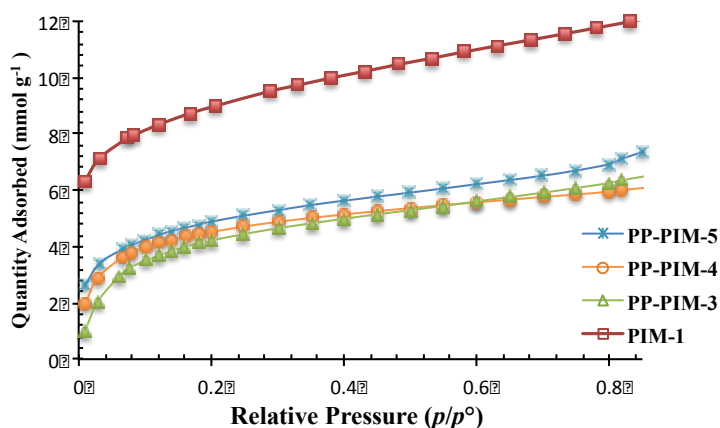


Figure 5-21. Nitrogen adsorption isotherm at 77 K; for PIM-1, PP-PIM-3, PP-PIM-4 and PP-PIM-6.

These polymers were confirmed with ^1H and ^{13}C NMR spectra (Figure 5-22). In addition, TGA thermograms show increasing decomposition with increasing phenyl substituents in the polymer backbone (Figure 5-23). In the case of PP-PIM-6, a different trend was seen, which may be due to its significantly lower molar mass. UV-Vis spectra show absorptions typical of phenyl groups (Figure 5-24).

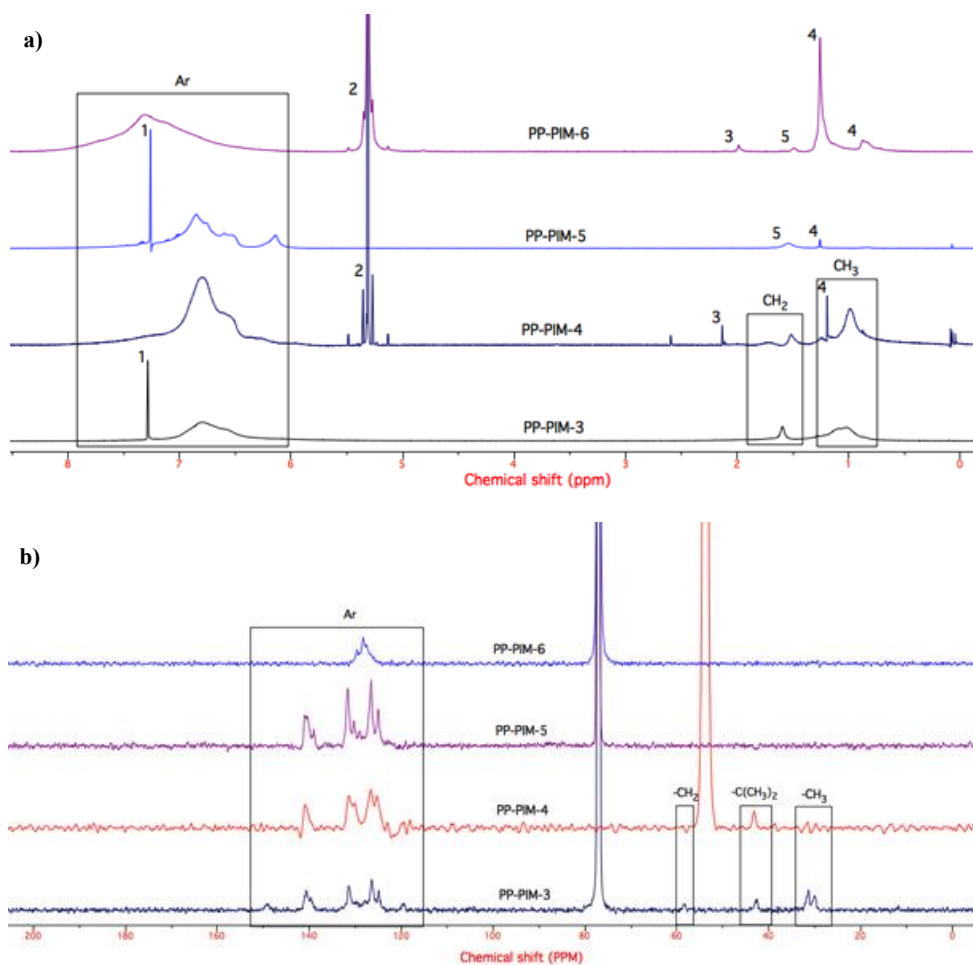


Figure 5-22. ^1H NMR (a) and ^{13}C NMR (b) spectra of PP-PIM-3, PP-PIM-5, PP-PIM-6 (in CDCl_3) and PP-PIM-4 (in CD_2Cl_2). In ^1H NMR solvent traces were labelled as follows: 1) CHCl_3 , 2) CH_2Cl_2 3) acetone, 4) *n*-hexane, 5) H_2O .

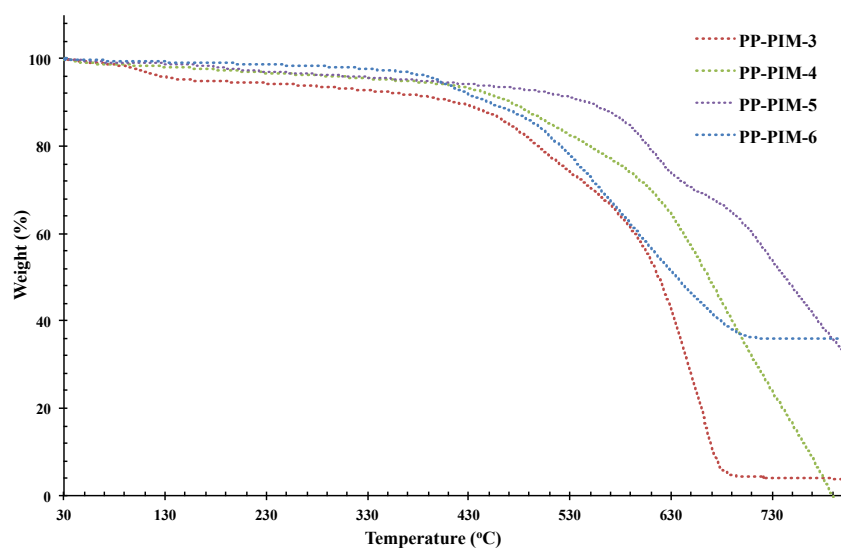


Figure 5-23. TGA thermogram of PP-PIMs from Diels Alder polymerization.

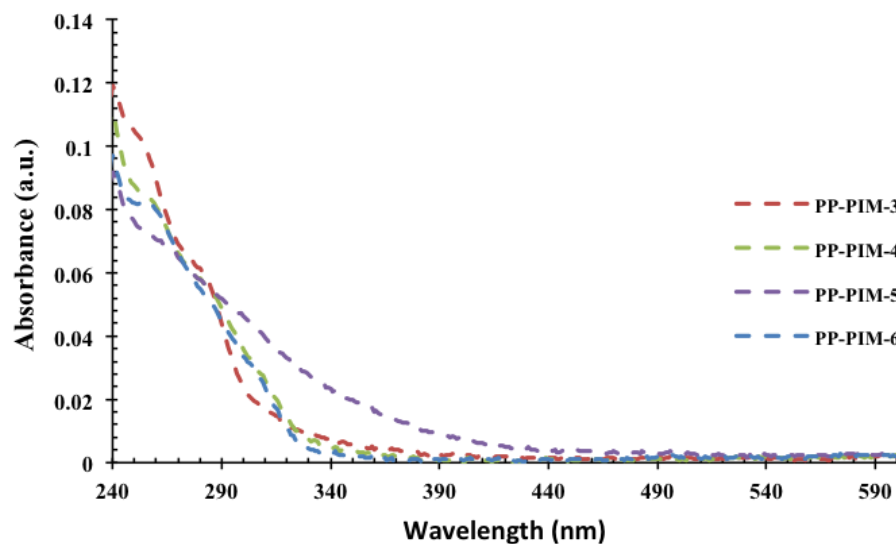


Figure 5-24. UV-Vis spectra of PP-PIMs from Diels Alder polymerization.

Interestingly, the MALDI-ToF spectrum of PP-PIM-4 showed evidence of cyclic oligomers in the C_2 - C_4 peaks (Figure 5-25).

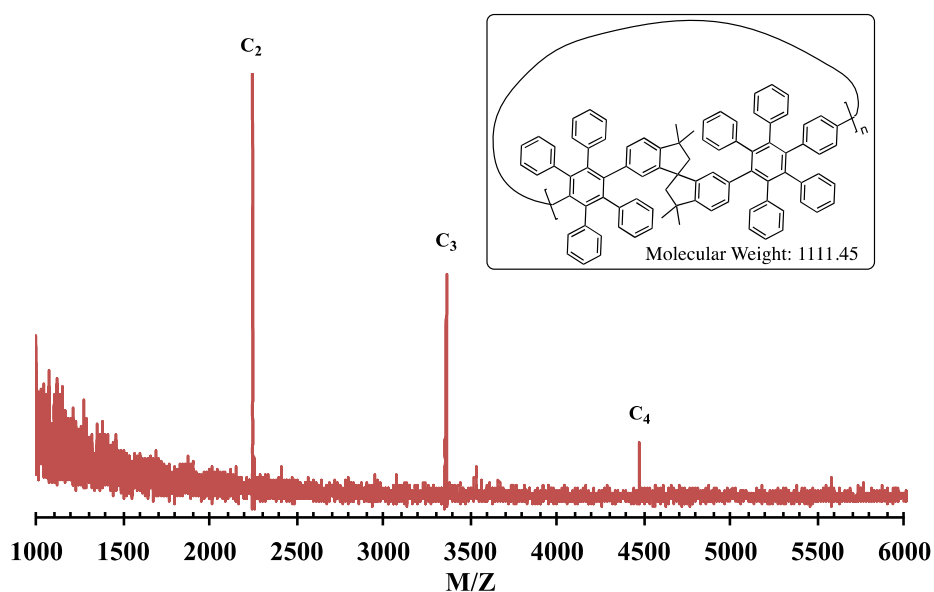


Figure 5-25. MALDI-ToF spectrum of PP-PIM-4, showing cyclic-PP-PIM-4 oligomers. Cyclic-PP-PIM-4 = $C_n = 1111.45 \times n + 23$.

5.4 Conclusions

In summary, two approaches were used in the preparation of new PIMs. In the first, condensation polymerization was used to produce three different dibenzodioxin-forming PIMs. One of these (PP-PIM-1) exhibited good solubility in common organic solvents such as chloroform and tetrahydrofuran, whereas PP-PIM-2 and BP-PIM-1 had poor solubility. All three polymers had a lower apparent BET surface area (290-443 m² g⁻¹) than PIM-1 (700 m² g⁻¹).

In the other new approach, PIMs were prepared with microporous properties, as an alternative to dibenzodioxin-forming PIMs. This synthesis, based on Diels Alder polymerization, yielded four polymers. PP-PIM-3, PP-PIM-4 and PP-PIM-5 had microporous properties, as determined by nitrogen isotherms, but all had apparent surface areas significantly lower than PIM-1.

This approach needs more study so that polymerization conditions can be optimised in order to obtain higher molar mass polymers suitable for membrane-based gas separation.

All polymers were characterized when possible with techniques such as NMR, TGA, UV-Vis and GPC.

5.5 References

- (1) Zhang, R.; Wang, L. C.; Li, M.; Zhang, X. M.; Li, Y. B.; Shen, Y. T.; Zheng, Q. Y.; Zeng, Q. D.; Wang, C. *Nanoscale* **2011**, 3, 3755.
- (2) Kobayashi, K.; Sato, A.; Sakamoto, S.; Yamaguchi, K. *J. Am. Chem. Soc* **2003**, 125, 3035.
- (3) Kobayashi, K.; Shirasaka, T.; Sato, A.; Horn, E.; Furukawa, N. *Angew. Chemie - Int. Ed.* **1999**, 38, 3483.
- (4) Maly, K. E.; Gagnon, E.; Maris, T.; Wuest, J. D. *J. Am. Chem. Soc.* **2007**, 129, 4306.
- (5) Gagnon, E.; Maris, T.; Arseneault, P. M.; Maly, K. E.; Wuest, J. D. *Cryst. Growth Des.* **2010**, 10, 648.
- (6) Shin, H.; Wang, Y. F.; Kim, J. H.; Lee, J.; Kay, K. Y.; Park, J. *Nanoscale Res. Lett.* **2013**, 8, 421.

- (7) Li, Z.; Ye, S.; Liu, Y.; Yu, G.; Wu, W.; Qin, J.; Li, Z., *J. Phys. Chem. B* **2010**, *114*, 9101.
- (8) Labidi, H.; Sonnet, P.; Riedel, D. *J. Phys. Chem. C* **2013**, *117*, 13663.
- (9) Gagnon, E.; Halperin, S. D.; Métivaud, V.; Maly, K. E.; Wuest, J. D. *J. Org. Chem.* **2010**, *75*, 399.
- (10) Pramanik, S.; Bhalla, V.; Kumar, M. *ACS Appl. Mater. Interfaces* **2015**, *7*, 22786.
- (11) Pisula, W.; Feng, X.; Mullen, K. *Chem. Mater.* **2011**, *23*, 554.
- (12) Chen, Q.; Luo, M.; Wang, T.; Wang, J. X.; Zhou, D.; Han, Y.; Zhang, C. S.; Yan, C. G.; Han, B. H. *Macromolecules* **2011**, *44*, 5573.
- (13) Short, R.; Carta, M.; Bezzu, C. G.; Fritsch, D.; Kariuki, B. M.; McKeown, N. B. *Chem. Commun.* **2011**, *47*, 6822.
- (14) Carta, M.; Bernardo, P.; Clarizia, G.; Jansen, J. C.; McKeown, N. B. *Macromolecules* **2014**, *47*, 8320.
- (15) Thompson, C. M.; McCandless, G. T.; Wijenayake, S. N.; Alfarawati, O.; Jahangiri, M.; Kokash, A.; Tran, Z.; Smaldone, R. A. *Macromolecules* **2014**, *47*, 8645.
- (16) Golling, F. E.; Osella, S.; Quernheim, M.; Wagner, M.; Beljonne, D.; Müllen, K. *Chem. Sci.* **2015**, *6*, 7072.
- (17) Narita, A.; Feng, X.; Hernandez, Y.; Jensen, S. A.; Bonn, M.; Yang, H.; Verzhbitskiy, I. A.; Casiraghi, C.; Hansen, M. R.; Koch, A. H. R.; Fytas, G.; Ivasenko, O.; Li, B.; Mali, K. S.; Balandina, T.; Mahesh, S.; De Feyter, S.; Müllen, K. *Nat. Chem.* **2014**, *6*, 126.
- (18) Zhang, C.; Peng, L. H.; Li, B.; Liu, Y.; Zhu, P. C.; Wang, Z.; Zhan, D. H.; Tan, B.; Yang, X. L.; Xu, H. B. *Polym. Chem.* **2013**, *4*, 3663.
- (19) Chen, W. F.; Lin, H. Y.; Dai, S. A., *Org. Lett.* **2004**, *6*, 2341.

Chapter 6 Conclusions

The development of membranes for gas separation is an area of strong commercial interest. This thesis has made a modest contribution to investigating novel gas separation membranes. Thus, the incorporation of graphene in PIM-1 to produce novel mixed matrix membranes (GPMMMs) was studied via a number of preparation methods. This part of the study investigated the production of graphene from natural graphite via liquid phase exfoliation, assessing the effects of solvent efficiency, sonication power and centrifugation speed. The enhancement of graphene exfoliation by adding PIM-1 was also evaluated. This was followed by the fabrication of GPMMMs, considering the limitations of graphene loading in PIM-1. A wide range of GPMMMs were prepared with graphene content ranging from 0.02 to 2.43 wt%. Graphene synthesised by the bottom-up approach was also used in GPMMM preparation, yielding the highest graphene content (4 wt%). Parallel work was done to assess the applicability to GPMMM preparation of various graphene moieties such as graphene oxide, reduced graphene oxide and base-washed graphene oxide.

The GPMMMs were characterised using Raman spectroscopy and SEM. This study showed that graphene exfoliation in PIM-1 produced few-layer graphene. GPC results for PIM-1 exposed to the same preparation condition as the GPMMMs showed that PIM-1 underwent no significant reduction in molar mass. The influence of graphene in PIM-1 gas separation was evaluated and found to depend strongly on the permeability of PIM-1. In the case of low-permeability PIM-1, the enhancements in gas permeability were significant with low graphene content. In contrast, these enhancements were limited in high-permeability PIM-1.

In the same scope of developing membrane materials, a number of new polymers were prepared and investigated. This work predominately relied on incorporating polyphenylene substituents based on hexaphenylbenzene as building units in order to prepare PP-PIMs. The two approaches followed were based respectively on condensation polymerization and on Diels Alder polymerization. None of the polymers produced had an apparent BET surface area as high as that of PIM-1. Further optimization of polymerization conditions is required in order to obtain membrane-forming polymers of high molar mass, whose gas transport properties can then be investigated.

Chapter 7 Appendixes

Appendix A. Permeation data of GMMMs.

Table 7-1. Permeation data of Series 2 GPMMMs as cast.

Membrane	Graphene content (Wt. %)	Thickness (μm)	Permeability P (barrer)						Diffusivity D ($\times 10^{-12} \text{ m}^2 \text{ s}^{-1}$)						Solubility S ($\times 10 \text{ cm}^3 \text{ (STP) / cm}^3 \text{ of polymer bar}$)					
			CO ₂	H ₂	He	O ₂	CH ₄	N ₂	CO ₂	H ₂	He	O ₂	CH ₄	N ₂	CO ₂	H ₂	He	O ₂	CH ₄	N ₂
KA1-1	0	50.3	3120	1581	724	546	210	147	55.8	1980.6	2820.6	137.6	14.1	41.7	42	0.6	0.2	3	11.2	2.7
GPMMM-2 (6)	0.1	315.5	4784	1996	847	869	515	297	111.46	3276.8	5091.5	217.7	33.7	76.3	32.2	0.5	0.1	3	11.5	2.9
GPMMM-2 (4)	0.2	93.3	4494	2234	987	797	333	226	75.7	3146.8	15856.2	188.2	19.2	57.1	44.5	0.5	0.1	3.2	13	3
GPMMM-2 (3)	0.3	48	3774	1968	884	657	233	170	58.6	2121.7	2890.6	150.7	13.9	44	48.3	0.7	0.2	3.3	12.6	2.9
GPMMM-2 (2)	0.7	20.2	2701	2091	964	538	143	123	35.32	705.5	861.2	97.2	7.5	26.3	57.4	2.2	0.8	4.2	14.4	3.5
GPMMM-2 (1)	2.4	73.4	2142	1078	514	367	157	103	37	1810	3111	97	11	33	43	0.5	0.1	2.8	11.1	2.3

Table 7-2. Permeation data of Series 2 GPMMMs after methanol treatment.

Membrane	Graphene content (Wt. %)	Thickness (μm)	Permeability P (barrer)						Diffusivity D ($\times 10^{-12} \text{ m}^2 \text{ s}^{-1}$)						Solubility S ($\times 10 \text{ cm}^3 \text{ (STP) / cm}^3 \text{ of polymer bar}$)					
			CO ₂	H ₂	He	O ₂	CH ₄	N ₂	CO ₂	H ₂	He	O ₂	CH ₄	N ₂	CO ₂	H ₂	He	O ₂	CH ₄	N ₂
KA1-1	0	59	5119	3206	1609	1128	341	273	69.1	3234	4144	204.3	13.3	51.6	55.6	0.9	0.3	4.1	19.3	4
GPMMM-2 (6)	0.1	352	12699	4658	1771	2263	1451	869	206.1	6395.5	8406.2	485.6	75	171.7	46.2	0.5	0.16	3.5	14.5	3.8
GPMMM-2 (4)	0.2	100	9836	4734	1893	1852	801	569	143.4	5118.6	6718.38	367.43	37	107.8	51.4	0.7	0.2	3.8	16.2	4
GPMMM-2 (3)	0.3	52	7835	4472	1827	1563	551	415	105	2960	3589	277	22	78	56.1	1.1	0.4	4.2	18.7	4
GPMMM-2 (2)	0.7	24	3407	3863	1949	818	163	173	31.8	1115.9	1329.5	112.5	6.3	23.5	80.4	2.6	1.1	5.5	19.3	5.5
GPMMM-2 (1)	2.4	86	5151	3206	1387	1036	391	270	75	3804	5038.1	201.7	17.1	53.5	51.5	0.6	0.2	3.9	17.1	3.8

Table 7-3. .Permeation data of Series 2 GPMMMs after ageing.

Membrane	Graphene content (Wt. %)	Age (Days)	Thickness (μm)	Permeability (barrer)						Diffusivity D ($\times 10^{-12} \text{ m}^2 \text{ s}^{-1}$)						Solubility S ($\times 10 \text{ cm}^3 \text{ (STP) / cm}^3 \text{ of polymer bar}$)					
				CO ₂	H ₂	He	O ₂	CH ₄	N ₂	CO ₂	H ₂	He	O ₂	CH ₄	N ₂	CO ₂	H ₂	He	O ₂	CH ₄	N ₂
KA1-1	0	244	57	3,7	2,7	1,2	73	200	160	51.2	2566	3548	136.3	10.2	31.4	53.8	0.8	0.3	4	14.9	3.8
GPMMM-2 (6)	0.1	226	351	9,2	4	1,6	1,8	980	620	186.6	5507	7355	382.3	53.2	133.5	37.1	0.5	0.2	3.5	13.8	3.5
GPMMM-2 (4)	0.2	236	94	6,7	3,5	1,4	1,3	460	340	95.0	3878	5374	239.8	22.8	69.4	52.6	0.7	0.2	3.9	15	3.7
GPMMM-2 (2)	0.3	236	50	5,7	3,2	1,4	1,1	330	260	79.2	2483	3066	207.1	17.3	55.8	53.8	1	0.3	3.9	14.3	3.6

Table 7-4. Permeation data of Series 3 GPMMMs as cast.

Membrane	Graphene content (Wt. %)	Thickness (μm)	Permeability (barrer)						Diffusivity D ($\times 10^{-12} \text{ m}^2 \text{ s}^{-1}$)						Solubility S ($\times 10 \text{ cm}^3 \text{ (STP) / cm}^3 \text{ of polymer bar}$)					
			CO ₂	H ₂	He	O ₂	CH ₄	N ₂	CO ₂	H ₂	He	O ₂	CH ₄	N ₂	CO ₂	H ₂	He	O ₂	CH ₄	N ₂
KA1-4	0	46	6327	2984	1240	1081	439	309	93.7	2285.5	2906.1	228.9	24.4	72.	50.7	1	0.3	3.5	13.5	3.2
GPMMM-3 (14)	0.02	50	4625	2623	1160	846	309	226	69.8	2360.7	3087.6	177.4	16.6	49.9	49.7	0.8	0.3	3.6	14	3.4
GPMMM-3 (13)	0.03	39	5510.7	2868.1	1275	944	353	255	76.7	492.8	465.7	198.1	20.8	72.6	53.9	4.4	2.1	3.9	15	3.6
GPMMM-3 (12)	0.04	42	6637	3304	1366	1181	435	340	96	2216	2637	232	23	75	51.8	1.1	0.4	3.8	14.2	3.4
GPMMM-3 (11)	0.05	40	5463	2708	1144	944	353	255	74.8	1760.3	2273.5	176.5	17.5	53.	54.8	1.2	0.4	4	15.1	3.6
GPMMM-3 (10)	0.07	41	5708	3023	1275	1023	374	275	79	2037.4	2470.3	196.8	18.8	57	54.2	1.1	0.4	3.9	14.9	3.6
GPMMM-3 (9)	0.1	40	4701	2470	1086	831	294	216	67.4	1999.7	2157	166.6	15.4	47.7	52.3	0.9	0.4	3.8	14.3	3.4
GPMMM-3 (8)	0.13	50	6687	3178	1301	1188	481	354	96.2	2597.1	3325.2	238.7	24	76	52.1	0.9	0.3	3.7	15.1	3.5
GPMMM-3 (6)	0.22	46	5903	2697	1133	1011	418	301	91.4	2271.9	2747.4	215.5	24.2	70.7	48.4	0.9	0.3	3.5	12.9	3.2
GPMMM-3 (5)	0.3	46	6311	3081	1289	1107	417	305	91.9	2329.2	2707	229.2	22.1	67.8	51.5	1	0.36	3.6	14.1	3.4
GPMMM-3 (3)	0.53	54	5536	2696	1139	966	383	274	84.8	2570.1	3436.7	204.8	20.5	61.6	49	0.8	0.3	3.5	14	3.3
GPMMM-3 (2)	0.7	53	2850	1638	792	505	192	137	52.04	1912.5	2907	126.9	13.2	40.4	41.1	0.6	0.2	3	11	2.6
GPMMM-3 (1)	1	48	4736	2421	1078	872	329	228	73.5	2210.5	2724.1	192.6	18.4	54.3	48.3	0.8	0.3	3.4	13.4	3.2

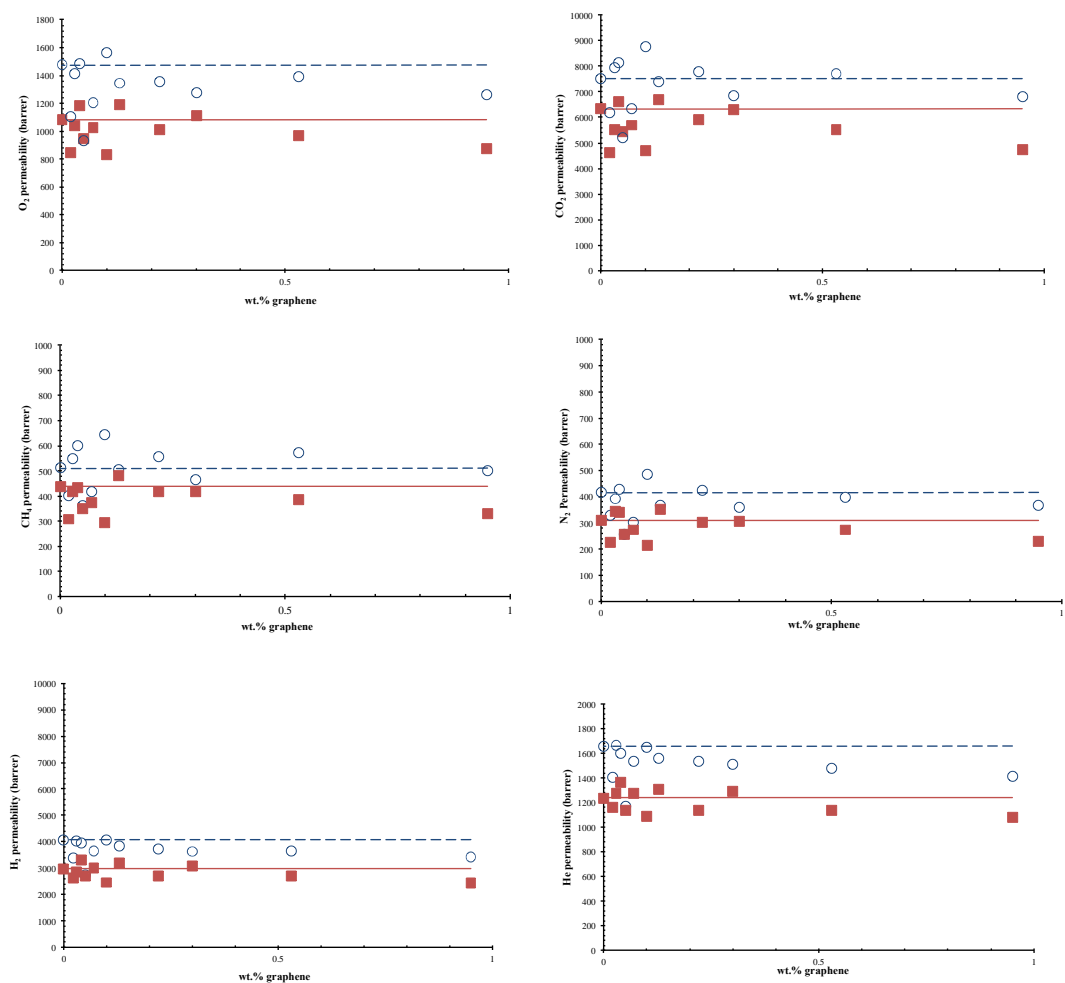
Table 7-5. Permeation data of Series 3 GPMMMs after methanol treatment.

Membrane	Graphene content (Wt. %)	Thickness (μm)	Permeability (barrer)						Diffusivity D ($\times 10^{-12} \text{ m}^2 \text{ s}^{-1}$)						Solubility S ($\times 10 \text{ cm}^3 \text{ (STP)} / \text{cm}^3 \text{ of polymer bar}$)					
			CO ₂	H ₂	He	O ₂	CH ₄	N ₂	CO ₂	H ₂	He	O ₂	CH ₄	N ₂	CO ₂	H ₂	He	O ₂	CH ₄	N ₂
KA1-4	0	46	7518	4079	1657	1473	510	415	96.5	2559	3092	271.9	25.99	85.7	58.4	1.2	0.4	4.1	14.7	3.6
GPMMM-3 (14)	0.02	50	6183	3376	1405	1103	404	328	89	2829	3993	237	24	78	51.9	0.9	0.3	3.5	12.6	3.1
GPMMM-3 (13)	0.03	44	7930	4049	1668	1409	548	394	101.9	2372.3	2992.6	262.4	26.31	85	58.4	1.3	0.4	4	15.6	3.5
GPMMM-3 (12)	0.04	42	8165	3950	1602	1480	600	427	109.6	2486.2	3093.7	282.4	27.96	86.1	55.9	1.2	0.4	3.9	16.1	3.7
GPMMM-3 (11)	0.05	40	5189	2731	1168	932	364	258	78.8	2242.2	28001	194.6	19.3	57.8	49.4	0.9	0.3	3.6	14.2	3.3
GPMMM-3 (10)	0.07	41	6352	3675	1530	1207	416	303	73.2	1990.2	2461.4	197.8	18.4	54.5	65.1	1.4	0.5	4.6	17	4.2
GPMMM-3 (9)	0.1	40	8774	4084	1650	1562	647	488	112.5	2398.8	2970.1	282	31.9	95.1	58.5	1.3	0.4	4.2	15.2	3.9
GPMMM-3 (8)	0.13	50	7392	3825	1561	1348	505	369	90.7	2669.8	3155.6	229.5	21.7	66.2	61.1	1.1	0.4	4.4	17.4	4.2
GPMMM-3 (6)	0.22	46	7787	3748	1532	1358	555	425	104	2798	3479	252	25	81	56.4	1	0.3	4	16.5	3.9
GPMMM-3 (5)	0.3	46	6842	3633	1514	1277	464	361	83.8	2154.8	2554.3	225.3	22.6	72.59	61.2	1.3	0.5	4.3	15.4	3.7
GPMMM-3 (3)	0.53	54	7708	3664	1483	1387	573	399	95.6	2676.5	3222.3	251.3	26.5	78	60.5	1	0.4	4.1	16.2	3.8
GPMMM-3 (2)	0.7	53	7203	9036	4760	289	3261	2376	100.7	1160.3	1055.9	1521.5	766.3	565.4	53.7	5.8	3.4	0.1	3.2	3.2
GPMMM-3 (1)	1	48	6786	3438	1412	1262	502	366	88.2	2399.4	3012.4	234.3	23.8	73.44	57.7	1.1	0.4	4	15.8	3.7

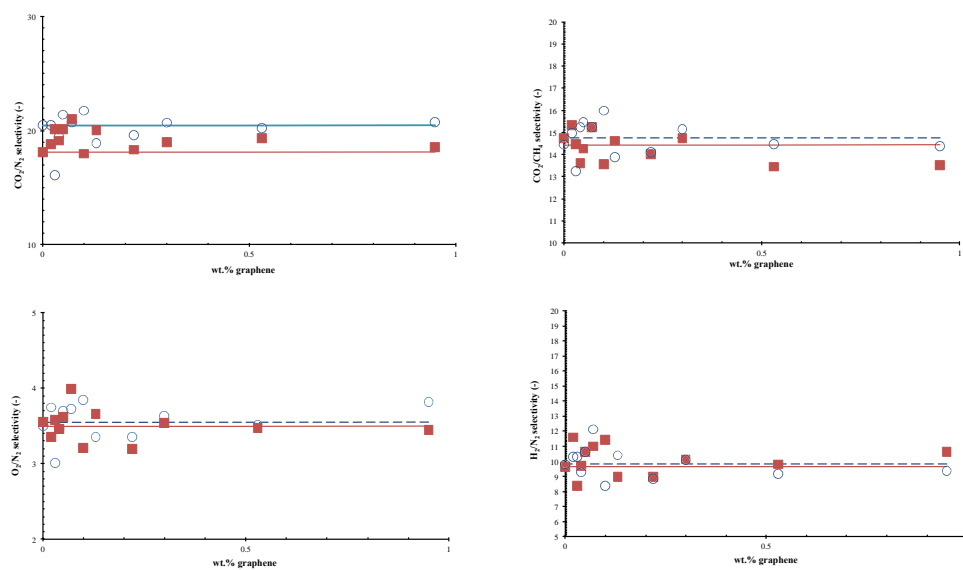
Table 7-6. Permeation data of Series 4 GPMMMs as cast.

Membrane	Graphene content (Wt. %)	Thickness (μm)	Permeability P (barrer)						Diffusivity D ($\times 10^{-12} \text{ m}^2 \text{ s}^{-1}$)						Solubility S ($\times 10 \text{ cm}^3 \text{ (STP) / cm}^3 \text{ of polymer bar}$)					
			CO ₂	H ₂	He	O ₂	CH ₄	N ₂	CO ₂	H ₂	He	O ₂	CH ₄	N ₂	CO ₂	H ₂	He	O ₂	CH ₄	N ₂
PIM-1	0	46	6326.5	2984.4	1240.1	1081.02	438.59	309.39	93.66	2285.53	2906.1	228.9	24.42	71.98	50.67	0.98	0.32	3.54	13.47	3.22
GPMMM-4 (17)	0.04	37	5105.2	2727.7	1164.5	921.67	326.66	249.84	74	1709	2093	182	17	54	51.64	1.2	0.42	3.8	14.31	3.45
GPMMM-4 (15)	0.08	52	5269.7	28634	1247.2	959.97	356.04	259.68	78.29	2629.99	3382.3	200.42	19.35	58.56	50.49	0.82	0.28	3.59	13.8	3.33
GPMMM-4 (13)	0.13	62	6887.8	2927.1	1206.4	1150.6	523.07	352.99	107.9	2994.54	3968.2	250.16	27.93	79.24	47.88	0.73	0.23	3.45	14.05	3.34
GPMMM-4 (10)	0.31	44	5470.2	275	1172.8	952.5	356.69	262.93	88.04	2257.85	3014.2	216.42	20.3	62.36	46.6	0.91	0.3	3.3	13.18	3.16
GPMMM-4 (8)	0.56	63	5201.8	2217.8	938.9	853.24	399.06	267.744	83.59	2595.71	3965.5	196.06	22.31	64.24	46.67	0.64	0.18	3.26	13.42	3.13
GPMMM-4 (6)	1	51	3256.1	1628.2	725.2	567.63	239.74	169.78	56.22	1893.09	2784.8	131.24	13.49	41.77	43.44	0.65	0.2	3.24	13.33	3.05
GPMMM-4 (3)	2.38	51	2372	1136	536	377	171	111	45.47	1661.81	2639	103.43	11.83	34.33	39.13	0.51	0.15	2.74	10.86	2.43
GPMMM-4 (1)	4.22	55	1031	564	298	165	75	48	27.74	1116.37	2387.4	58.29	7	19.92	27.89	0.38	0.09	2.12	8.04	1.82

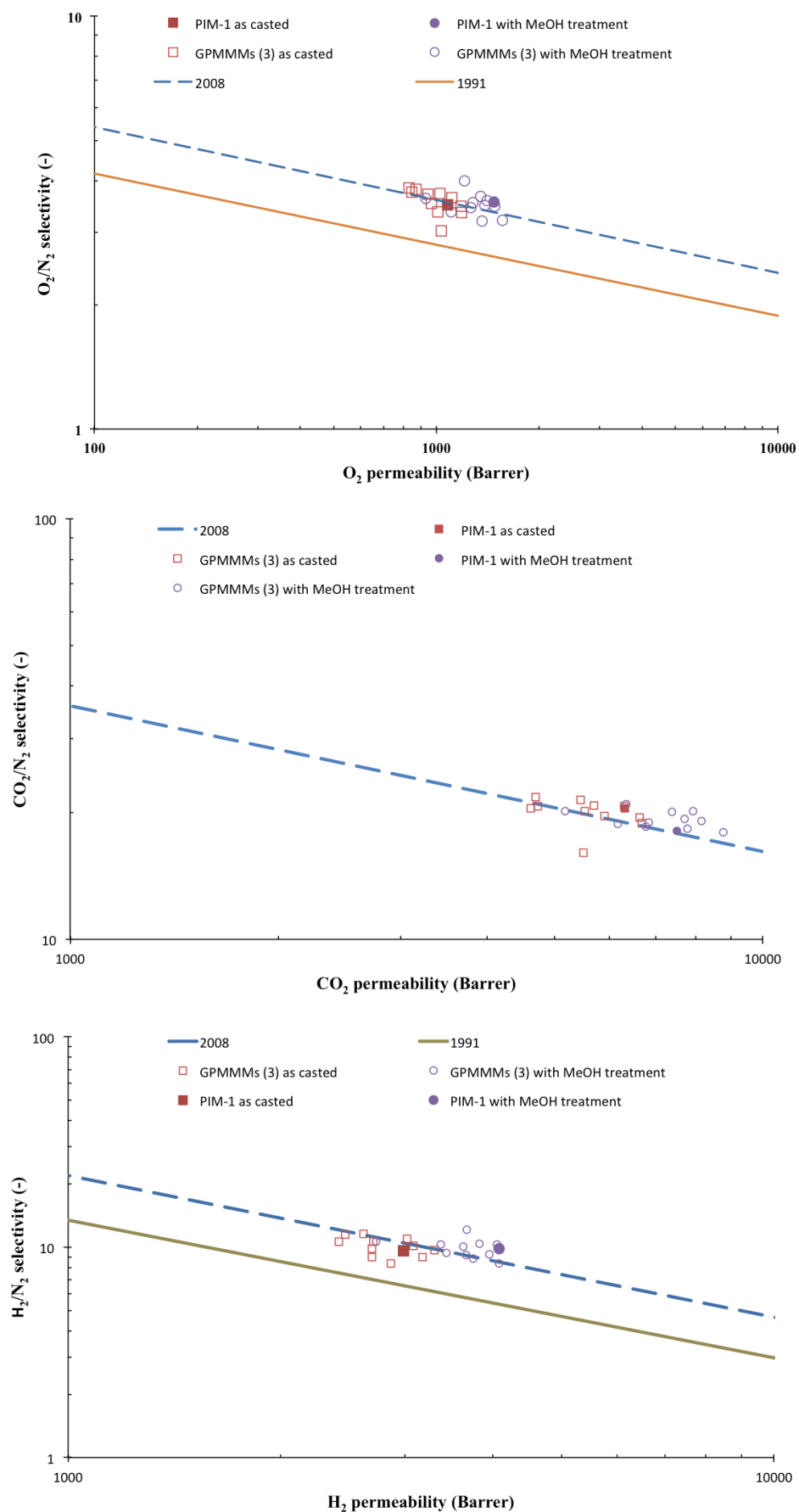
Appendix B. Effects of graphene (GPMMMs-3) in the permeability (O_2 , CO_2 , CH_4 , N_2 , H_2 and He). Squares as casted membranes, circles indicate methanol treated membranes, line indicates PIM-1 as casted membrane, and dashed line indicates PIM-1 methanol treated membrane.



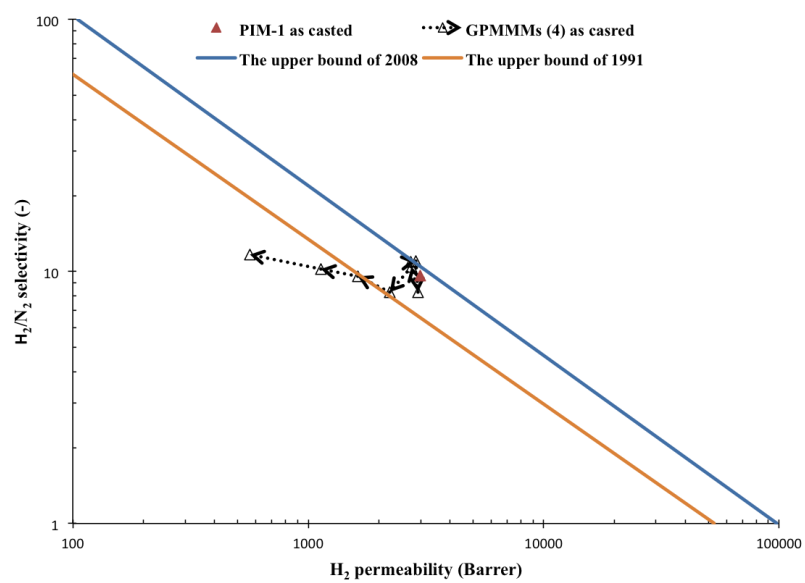
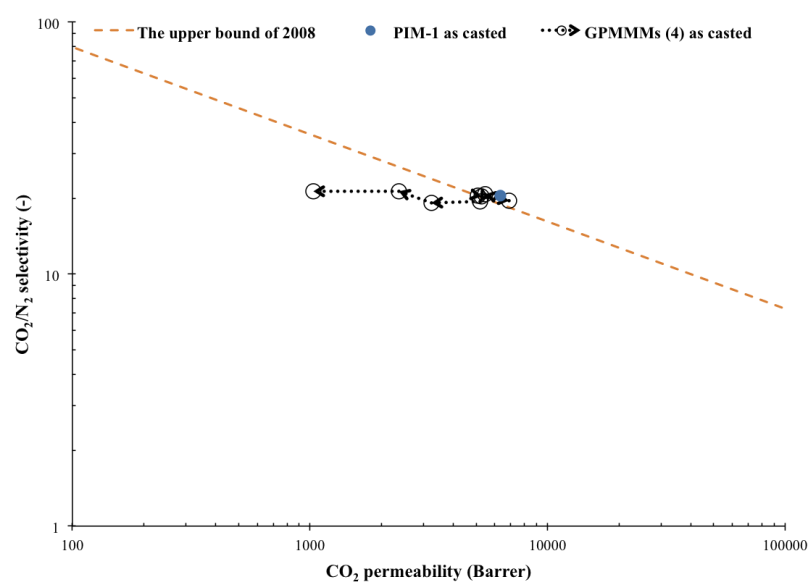
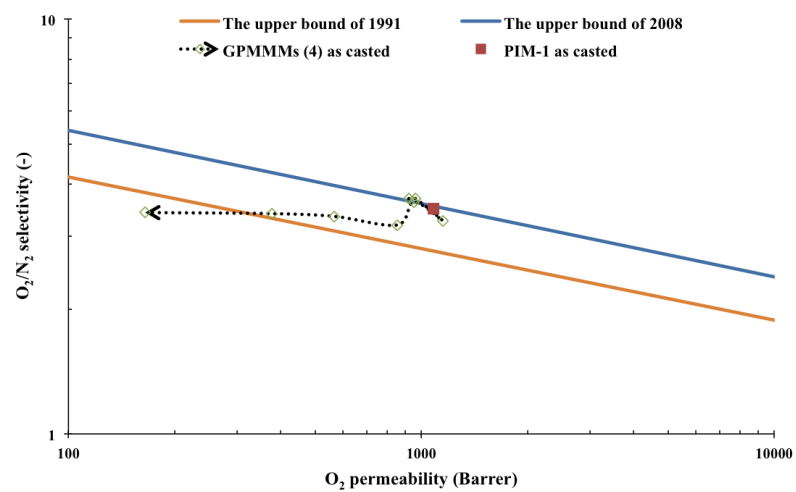
Appendix C. Effects of graphene (GPMMMs-3) in the selectivity (CO_2/N_2 , CO_2/CH_4 , O_2/N_2 and H_2/N_2). Squares as casted membranes, circles indicate methanol treated membranes, line indicates PIM-1 as casted membrane, and dashed line indicates PIM-1 methanol treated membrane.



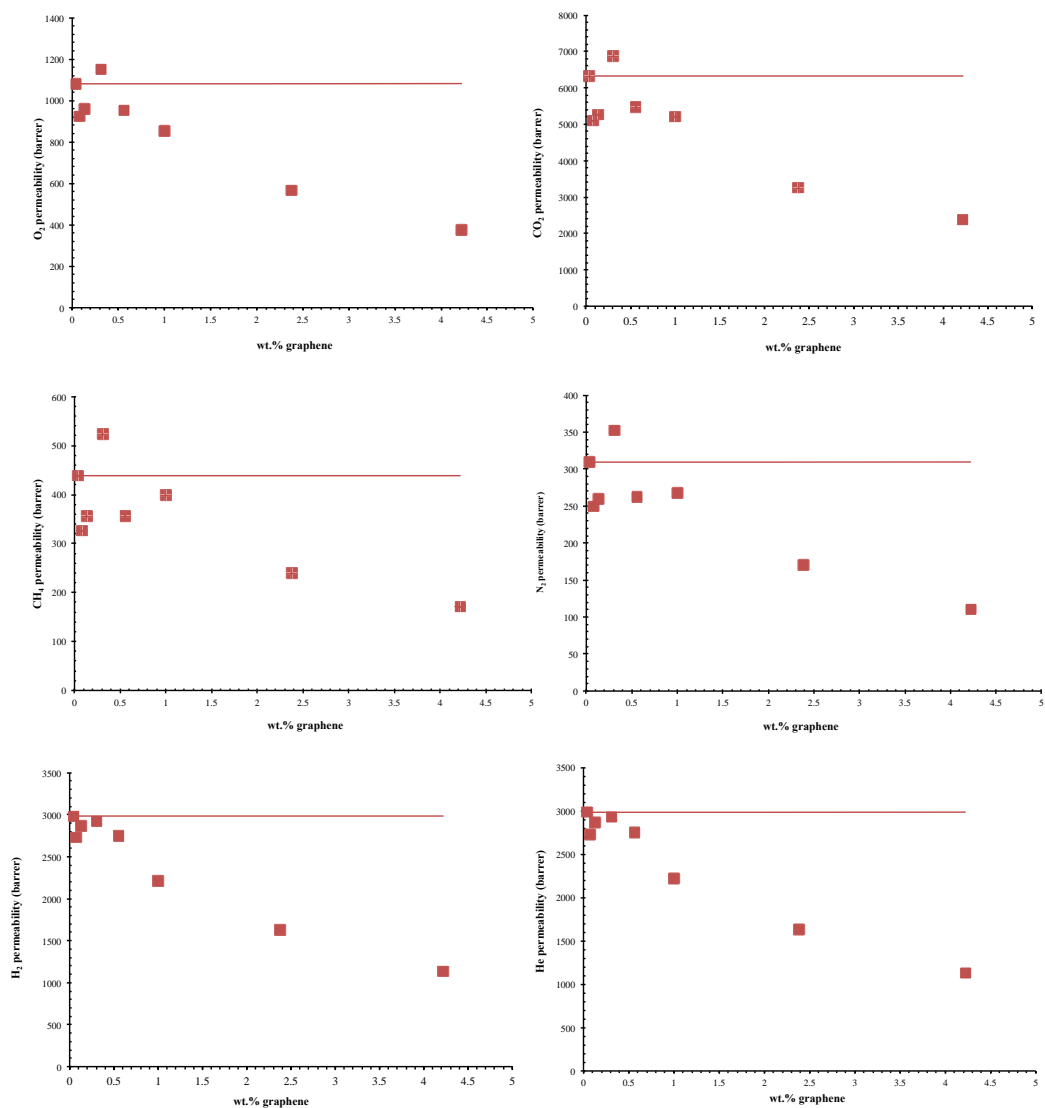
Appendix D. Robeson plots of GPMMMs Series 3.



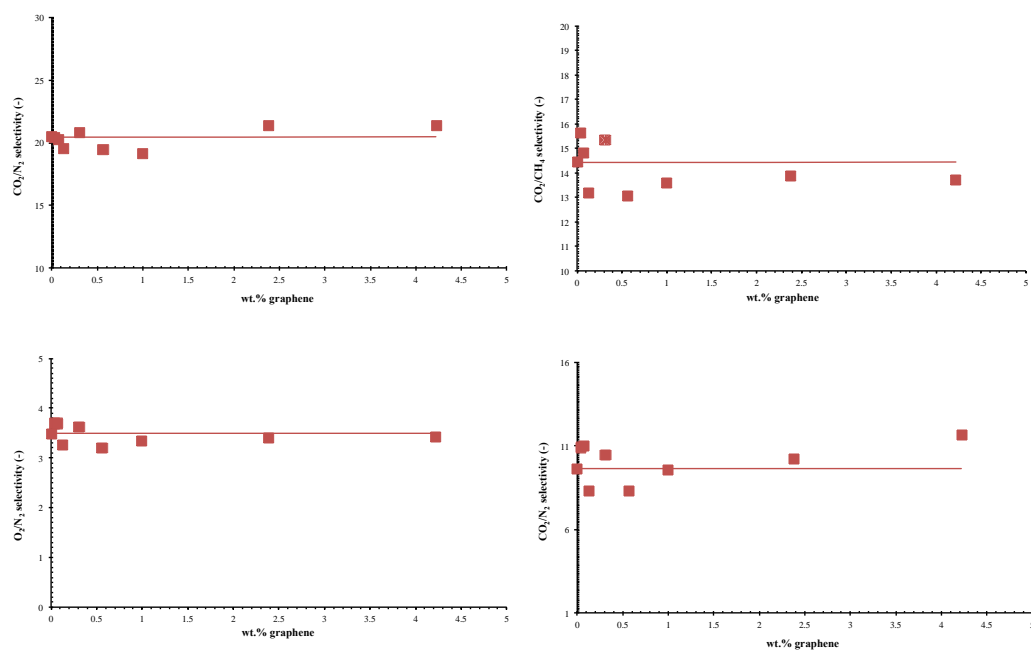
Appendix E. Robeson plots of GPMMMs Series 4.



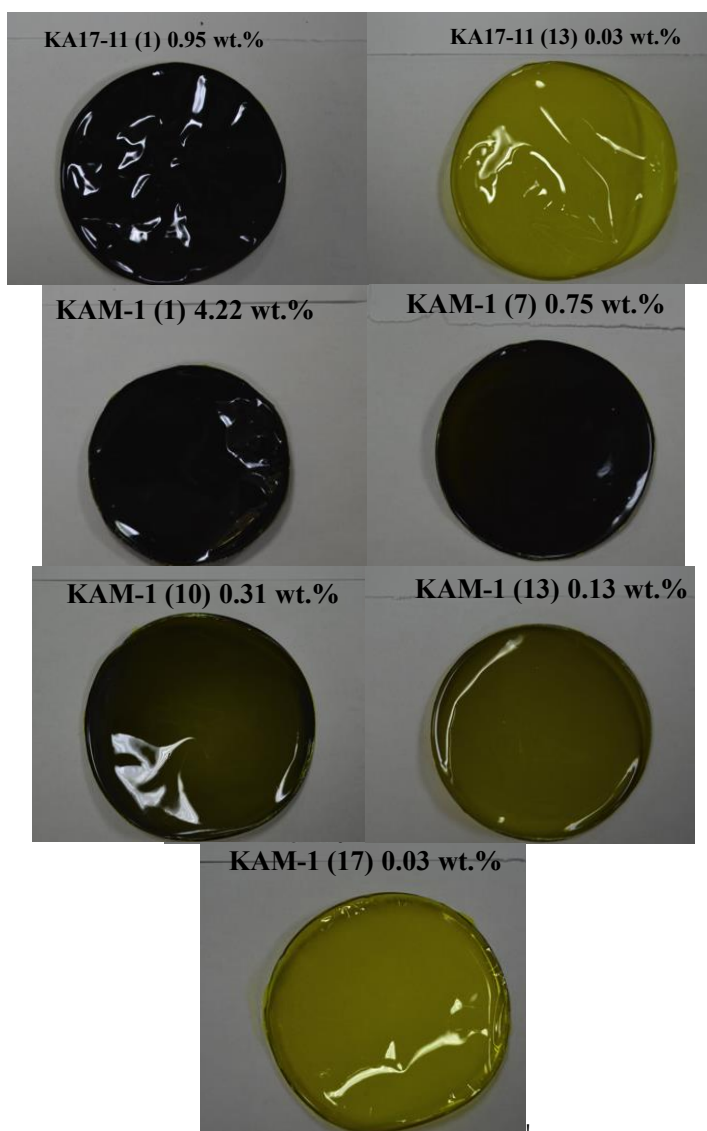
Appendix F. Effects of graphene (GPMMMs -4) in the permeability (O_2 , CO_2 , CH_4 , N_2 , H_2 and He). Squares as casted membranes, line indicates PIM-1 as casted membrane.



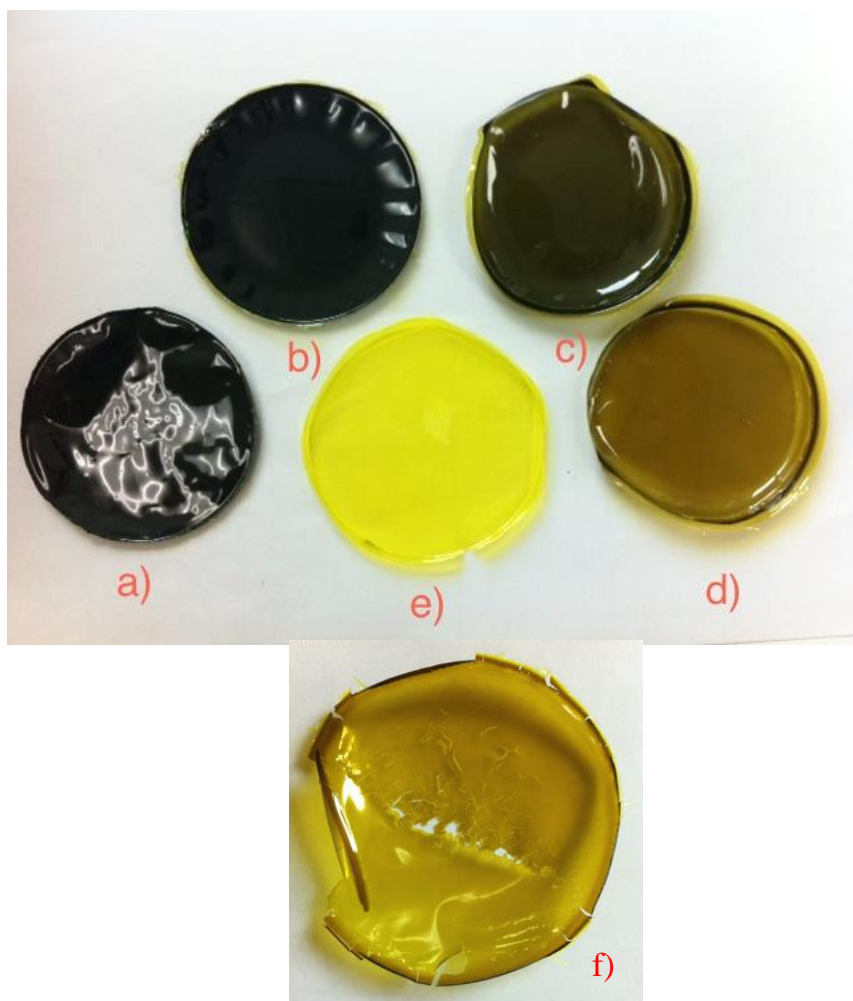
Appendix G. Effects of graphene (GPMMMs-4) in the selectivity (CO_2/N_2 , CO_2/CH_4 , O_2/N_2 and H_2/N_2). Squares as casted membranes, circles indicate methanol treated membranes, line indicates PIM-1 as casted membrane.



Appendix H. Digital images of Series 3 and 4 GPMMMs.



Appendix I. Digital images of GPMMMs that made from Graphene exfoliation of various sources, a) from natural graphite, b) from synthetic multilayers graphene, c) from reduced graphene oxide (r-GO), d) from base washed graphene oxide (BWGO), e) from pristine PIM-1 and f) from graphene oxide (GO).



Appendix J. Sample names and Experimental codes

Sample name	Experimental code	Sample name	Experimental code
GEOS-1	KA7-2	GEPS-9	KA17-13
GEOS-2	KA7-4	GEPS-10	KAM-1
GEOS-3	KA7-7-1	Graphene/ PIM-1 mixed matrix membranes-2 (GPMMMs-2)	
GEOS-4	KA7-7-2	GPMMM-2 (1)	KA1-7-12(3)
GEOS-5	KA7-8-1	GPMMM-2 (2)	KA1-7(1)
GEOS-6	KA7-8-2	GPMMM-2 (3)	KA1-7(2)
GEOS-7	KA7-9-1	GPMMM-2 (4)	KA1-7(3)
GEOS-8	KA7-9-2	GPMMM-2 (5)	KA1-7(5)
GEOS-9	KA7-9-3	GPMMM-2 (6)	KA1-7(6)
GEOS-10	KA7-9-4	Graphene/ PIM-1 mixed matrix membranes-3 (GPMMMs-3)	
GEOS-11	KA7-10	GPMMM-3 (1)	KA17-11 (1)
GEOS-12	KA7-6	GPMMM-3 (2)	KA17-11 (2)
GEOS-13	KA15	GPMMM-3 (3)	KA17-11 (3)
Graphene/ PIM-1 mixed matrix membranes-1 (GPMMMs-1)		GPMMM-3 (4)	KA17-11 (4)
GPMMM-1 (0.02%)	GPIM-1 (0.02%)	GPMMM-3 (5)	KA17-11 (5)
GPMMM-1 (0.05%)	GPIM-1 (0.05%)	GPMMM-3 (6)	KA17-11 (6)
GPMMM-1 (0.08%)	GPIM-1 (0.08%)	GPMMM-3 (7)	KA17-11 (7)
GPMMM-1 (0.1%)	GPIM-1 (0.1%)	GPMMM-3 (8)	KA17-11 (8)
GPMMM-1 (0.12%)	GPIM-1 (0.12%)	GPMMM-3 (9)	KA17-11 (9)
GPMMM-1 (0.15%)	GPIM-1 (0.15%)	GPMMM-3 (10)	KA17-11 (10)
GPMMM-1 (0.18%)	GPIM-1 (0.18%)	GPMMM-3 (11)	KA17-11 (11)
GPMMM-1 (0.2%)	GPIM-1 (0.2%)	GPMMM-3 (12)	KA17-11 (12)
GPMMM-1 (0.22%)	GPIM-1 (0.22%)	GPMMM-3 (13)	KA17-11 (13)
GPMMM-1 (0.28%)	GPIM-1 (0.28%)	GPMMM-3 (14)	KA17-11 (14)
GPMMM-1 (0.3%)	GPIM-1 (0.3%)	Graphene/ PIM-1 mixed matrix membranes-4 (GPMMMs-4)	
GPMMM-1 (0.32%)	GPIM-1 (0.32%)	GPMMM-4 (1)	KAM-1 (1)
GPMMM-1 (0.35%)	GPIM-1 (0.35%)	GPMMM-4 (2)	KAM-1 (2)
GPMMM-1 (0.38%)	GPIM-1 (0.38%)	GPMMM-4 (3)	KAM-1 (3)
GPMMM-1 (0.45%)	GPIM-1 (0.45%)	GPMMM-4 (4)	KAM-1 (4)
GPMMM-1 (0.48%)	GPIM-1 (0.48%)	GPMMM-4 (5)	KAM-1 (5)
GPMMM-1 (0.1%)	GPIM-1(3) (0.1%)	GPMMM-4 (6)	KAM-1 (6)
GPMMM-1 (0.03%)	GPIM-1(3) (0.03%)	GPMMM-4 (7)	KAM-1 (7)
GPMMM-1 (0.01%)	GPIM-1(3) (0.01%)	GPMMM-4 (8)	KAM-1 (8)
GPMMM-1 (0.18%)	GPIM-1(1) (0.18%)	GPMMM-4 (9)	KAM-1 (9)
Graphene exfoliation in PIM-1 solutions (GEPSs)		GPMMM-4 (10)	KAM-1 (10)
GEPS-1	KA1-7 (12)	GPMMM-4 (11)	KAM-1 (11)
GEPS-2	KA17-1	GPMMM-4 (12)	KAM-1 (12)
GEPS-3	KA17-2	GPMMM-4 (13)	KAM-1 (13)
GEPS-4	KA17-4	GPMMM-4 (14)	KAM-1 (14)
GEPS-5	KA17-5	GPMMM-4 (15)	KAM-1 (15)
GEPS-6	KA17-8	GPMMM-4 (16)	KAM-1 (16)
GEPS-7	KA17-10	GPMMM-4 (17)	KAM-1 (17)
GEPS-8	KA17-11		